UNIVERSITY OF CALGARY

Optical Quantum Memory and Signal Processing Using a Rare-earth-ion-doped Waveguide

by

Neil James Sinclair

A THESIS

SUBMITTED TO THE FACULTY OF GRADUATE STUDIES

IN PARTIAL FULFILLMENT OF THE REQUIREMENTS FOR THE

DEGREE OF DOCTOR OF PHILOSOPHY

PHYSICS AND ASTRONOMY

CALGARY, ALBERTA

April, 2016

Abstract

Advanced applications of quantum information science, such as long-distance quantum communication based on quantum repeaters, require photons to be interfaced with different devices. These devices, such as single photon detectors, quantum memories, quantum signal processors, and linear optical elements, may be integrated on a single chip to enable efficient, robust and scalable implementations. With aim of constructing a quantum repeater, and towards realizing integrated optical quantum memories and signal processors in general, we experimentally develop quantum light-matter interfaces using a cryogenically-cooled rare-earth-ion-doped waveguide, namely thulium-doped lithium niobate (Tm^{3+}:$LiNbO_3$).

As the basis for our work, we describe a quantum repeater architecture that uses spectral multiplexing and quantum memories that operate with a fixed storage time. Our repeater architecture promises efficient operation, is compatible with the properties of cryogenically-cooled rare-earth-ion-doped crystals, and simplifies the demands of quantum memories compared to other architectures.

To demonstrate the feasibility of our repeater design, we utilize our light-matter interface as a quantum memory to perform several experimental demonstrations. These include high-fidelity storage and retrieval of 26 spectrally-multiplexed quantum bits encoded into single-photon-level laser pulses, high-fidelity storage and retrieval of single and entangled photons derived from a photon-pair source, and high-visibility two-photon interference between weak laser pulses that are stored in one or two, separate, quantum memories.

The unique properties of our light-matter interface allow us to demonstrate additional protocols that further highlight its promise for integrated quantum signal processing. By combining our Tm^{3+}:$LiNbO_3$ waveguide with a $LiNbO_3$ waveguide phase modulator,

we demonstrate operations such as sequencing, filtering, interference, and compression of laser pulses attenuated to the single-photon level. In another experiment, we measure the cross-phase modulation between strong pulses, by which we demonstrate photon-photon interactions that point towards non-destructive measurements of quantum bits.

Since the performance of all aforementioned protocols, and future light-matter applications, hinge on the basic spectroscopic properties of our waveguide, we measure these properties at temperatures as low as 800 millikelvin.

Our findings, discussed over several attached publications, usher the development of integrated quantum memories and processors for multi-component optical quantum information applications such as repeaters and networks.

Preface

Below is a list of papers that are included in this thesis. Papers are listed according to the order they are introduced in Chapter 5 and the Appendix.

1. "Spectral multiplexing for scalable quantum photonics using an atomic frequency comb quantum memory and feed-forward control", N. Sinclair, E. Saglamyurek, H. Mallahzadeh, J. A. Slater, M. George, R. Ricken, M. Hedges, D. Oblak, C. Simon, W. Sohler, and W. Tittel, Physical Review Letters 113(5): 053603 (2014).

2. "Conditional detection of pure quantum states of light after storage in a Tm-doped waveguide", E. Saglamyurek, N. Sinclair, J. Jin, J. A. Slater, D. Oblak, F. Bussières, M. George, R. Ricken, W. Sohler, and W. Tittel, Physical Review Letters, 108(8): 083602 (2012).

3. "Broadband waveguide quantum memory for entangled photons", E. Saglamyurek, N. Sinclair, J. Jin, J. A. Slater, D. Oblak, F. Bussières, M. George, R. Ricken, W. Sohler, and W. Tittel, Nature, 469 (7331): 512 (2011).

4. "Two-photon interference of weak coherent laser pulses recalled from separate solid-state quantum memories", J. Jin, J. A. Slater, E. Saglamyurek, N. Sinclair, M. George, R. Ricken, D. Oblak, W. Sohler, and W. Tittel, Nature Communications 4: 2386 (2013).

5. "An integrated processor for photonic quantum states using a broadband light-matter interface", E. Saglamyurek, N. Sinclair, J. A. Slater, K. Heshami, D. Oblak, and W. Tittel, New Journal of Physics 16(6): 065019 (2014).

6. "Cross-phase modulation of a probe stored in a waveguide for non-destructive detection of photonic qubits", N. Sinclair, K. Heshami, C. Deshmukh, D. Oblak, C. Simon,

and W. Tittel, arXiv:1510.01164, to be submitted (2016).

7. "A rare-earth-ion-doped waveguide based on a standard photonics technology for quantum signal processing", N. Sinclair, D. Oblak, C. W. Thiel, R. L. Cone, and W. Tittel, to be submitted (2016).

Acknowledgements

To formulate a compact list of people who contributed to this work would be an injustice to those who were not mentioned. I want to acknowledge those who have been a part of my life along the road to this thesis; starting from the very beginnings in childhood, all the way up to my last frantic minute of preparations before my defense. I reserve a special recognition for those who have made sacrifices for me – thank you. I will always be indebted to your efforts, and you will never be forgotten.

Table of Contents

List of Tables

List of Figures and Illustrations

Chapter 1

Background

1.1 Introduction

It is well-known that science has been perpetually linked with technology [1]. However, applications of quantum physics took time to be realized after the initial development of quantum theory in the early 20th century. This was partially due to the misconception that quantum uncertainty restricted any utility [1]. Today quantum physics-based science is widely researched and has led to significant technological developments [2]. The goal of one area of research is to perform information processing tasks that are not possible within the exclusive framework of classical physics [3]. This field is often referred to as quantum information science and technology [2, 3].

The basic unit of classical information is a bit, i.e. binary values of 0 or 1. Similarly, the basic unit of quantum information, the qubit, is a superposition of bits: $\alpha|0\rangle + \beta|1\rangle$, where $|0\rangle$ and $|1\rangle$ represent orthogonal physical (basis) states of a system, and $|\alpha|^2+|\beta|^2 = 1$ [3]. For example, two distinct times-of-arrival of a photon could define the orthogonal states, e.g. an 'early' ('late') arrival time would correspond to $|0\rangle(|1\rangle)$, creating a so-called time-bin qubit [4]. In this thesis we generally utilize time-bin qubits to encode quantum information [3, 5].

Beyond the single qubit, scientists utilize more complex multi-particle states such as entangled states to perform novel tasks [2, 3, 6, 7]. Entangled systems are those that cannot be completely described by considering their sub-systems individually, but only by the system as a whole [6, 7]. Such systems are discussed in this thesis. Quantum computing, a branch of quantum information science and technology, exploits the paral-

lelism inherent in entangled states, and promises to outperform any classical computer with respect to certain problems, such as database searches and factoring [3]. Since the security of internet cryptosystems is based on the the inability of classical computers to efficiently factor large numbers [8, 9], quantum computers might endanger the secrecy of sensitive information transferred over the internet. Fortunately, quantum cryptography, another quantum information technology, offers a solution to overcome this potential security problem [10, 11].

1.2 Quantum cryptography and key distribution

The goal of quantum cryptography is to secure information, transferred over a public communication channel, from an adversary or eavesdropper [10, 11]. Quantum cryptography is based on the property that a measurement of a quantum system can change its state – a different foundation than that of classical cryptosystems – allowing the parties to detect an eavesdropper [10, 11]. To understand how this works, we can consider an example where, say, Alice and Bob wish to communicate securely. If they share identical copies of a random string of bits (the key), they can use the one-time pad – an informationally-secure method – to render their communications secret [12]. To use the one-time pad, Alice's message is written as a string of bits, added (modulo two) with the key, and sent publicly to Bob. Bob then receives the encoded message and adds it with the key, thus decoding the message. The challenge of this method is for Alice and Bob, usually separated from each other by a long-distance, to obtain a shared secret key initially – this is where quantum key distribution (QKD) is utilized [10, 11].

There exists many QKD protocols [13], however, here we focus on a QKD protocol that requires Alice and Bob to share an entangled state [11, 14]. Measurement of the entangled state, in conjunction with classical post-processing, enables Alice and Bob to

share correlated random bits [11, 14]. To illustrate, imagine that Alice generates a pair of photons in an entangled state $|\phi^+\rangle = (|ee\rangle + |ll\rangle)/\sqrt{2}$, where $|e\rangle(|l\rangle)$ corresponds to a photon arriving early (late). Alice sends one photon over a channel to Bob. Next, Alice and Bob measure their photons with respect to a set of conjugate bases such as those defined by e/l and $+/-$ states, where $|\pm\rangle = (|e\rangle \pm |l\rangle)/\sqrt{2}$. This can be done using a simple interferometric setup and single-photon detection. For a given basis, a different bit is ascribed to each measurement outcome (i.e. bit 0(1) is ascribed to both $e(l)$ and $+(-)$) to define the (potential) key Alice and Bob will share. Alice and Bob record both the basis used and the resultant bit for each measurement. After many events, they publicly announce the bases that they used for their measurements, keeping only the bits corresponding to identical choices of bases. Provided no eavesdropping (or other errors) have taken place, their bits form a key for one-time pad encryption.

If an eavesdropper (Eve) intercepts and measures any of the qubits, she will alter the entangled state, introducing errors into Alice and Bob's key [11, 15]. Thus, the final stage of the protocol is for Alice and Bob to publicly disclose a randomly-chosen sub-set of their key, so that they can estimate an error rate. Provided it is below a certain threshold, they perform classical error-correction and privacy amplification post-processing to eliminate any possible information obtained by an eavesdropper, and otherwise they abort [11]. QKD has advanced much further beyond our simple description, for example with respect to protocols and different attacks [13, 15], and has resulted in commercial enterprises [16].

1.3 Quantum repeaters

QKD is effective only up to a certain distance since we cannot differentiate between errors due to eavesdropping and system noise [11]. The current distance record is $\sim$200 km in a laboratory setting [17]. The range of QKD can be extended via trusted parties, and

has been demonstrated in network architectures (see Ref. [18] and references therein). However, this 'trusted node' architecture may not be desirable or available for some applications. The telecommunication industry uses repeaters that amplify bits encoded into strong pulses of light, thereby extending the communication distance of classical signals [19]. These classical repeaters rely on inverted atomic media to produce amplification via stimulated emission. Since stimulated emission is invariably accompanied by spontaneous emission, amplification results in additional noise and, if used for single photons and QKD, Bob detecting uncorrelated photons that introduce errors into the key [20]. Inverted atomic media can be viewed as imperfect cloning machines for qubits encoded into single photons. It has been shown that it is impossible to produce identical clones of states that are used for QKD [21, 22]. This is crucial to the success of QKD, as it means that Eve cannot copy the state, wait until Alice and Bob announce their bases, then measure her clones in the basis that matches that selected by Bob to produce an identical copy of the key [11]. One way to achieve long-distance QKD without trusted nodes relies on quantum repeaters [23, 24]. Quantum repeaters, as we will introduce below, rely on quantum memories [20, 25, 26, 27] and the processes of entanglement swapping (sometimes referred to as quantum teleportation of entanglement) [28, 29, 30].

Quantum teleportation allows, via classical information obtained from a Bell-state measurement [3], the transfer of a quantum state from Alice to Bob without directly transmitting any particle [28, 29]. Fig. 1.1 illustrates how a single qubit is teleported. Note that the Bell states are $|\phi^{\pm}\rangle = (|00\rangle \pm |11\rangle)/\sqrt{2}$ and $|\psi^{\pm}\rangle = (|01\rangle \pm |10\rangle)/\sqrt{2}$ where $|0\rangle$ and $|1\rangle$ define the single-qubit basis. The Bell states are basis states for the two-qubit system, thus a Bell-state measurement is a measurement with respect to the Bell basis [3].

As an extension to teleporting a single qubit, entanglement swapping is the teleportation of an entangled state comprised of usually two qubits [30]. In a quantum repeater,

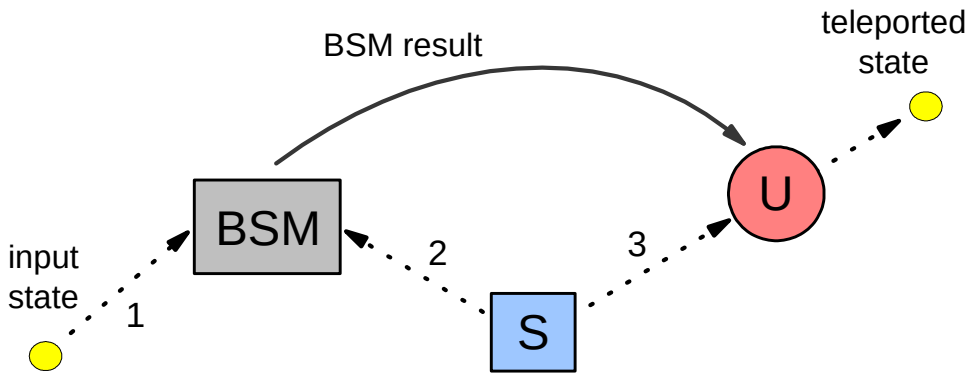

Figure 1.1: Quantum teleportation. A photon (yellow circle) occupies mode 1 and carries the quantum state (denoted as input state) to be teleported. A source (S) emits a pair of photons in a Bell state into modes 2 and 3. A Bell-state measurement (BSM) is performed using the photons occupying modes 1 and 2. The result of the BSM is publicly announced. The remaining photon occupying mode 3 is then submitted to a unitary transformation (U) that is determined by the BSM result. This process results in the teleportation of the quantum state encoded into the photon of mode 1 (input state) onto the photon of mode 3 (yellow circle; teleported state).

entanglement swapping is used to distribute a Bell state between Alice and Bob [23, 24]. To understand how this can be done, consider the long, lossy channel between Alice and Bob to be formed by an array of shorter elementary links. See Fig. 1.2 and its caption for a description. Photons encoded into Bell states are transmitted over each elementary link. A Bell-state measurement is performed at each connection-point between links. Provided all entanglement swapping events occur simultaneously, Alice and Bob share a Bell state and, consequently, they can perform QKD without relying on trusted nodes. However entanglement swapping on its own is not a solution, as it is no more efficient than sending an entangled photon directly. This is because all entangled pairs must participate in the teleportation i.e. they must synchronously arrive at the nodes. Since there is channel loss, the sequence of teleportation events is broken, and Alice and Bob will obtain uncorrelated results. For example, if the probability of transmitting a photon over the ith link is $e^{-\alpha l_i}$, where α is the attenuation coefficient of the channel and

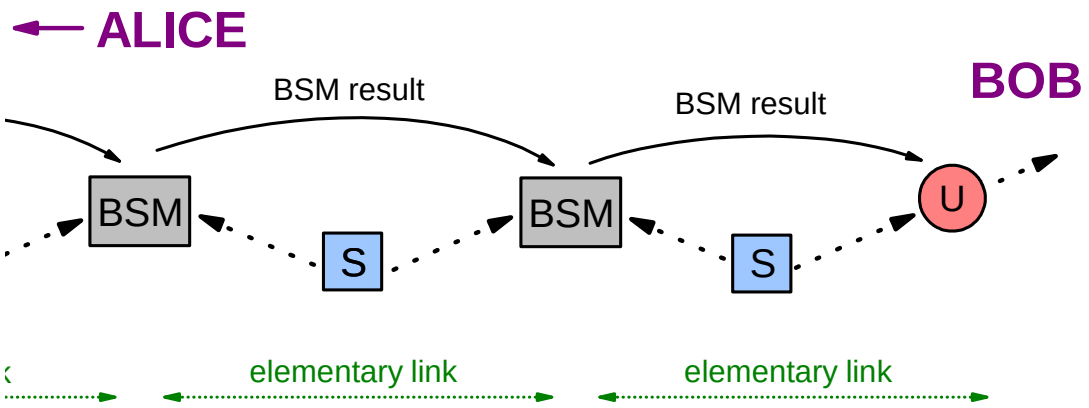

Figure 1.2: Entanglement swapping. A pair of entangled photons encoded into Bell states are emitted from each source (S). The photon pairs are transmitted over a distance defined by each elementary link (green dotted arrows). Bell-state measurements (BSMs) are performed on photons derived from different sources. The results of the BSMs are publicly announced. A unitary transformation, that is determined by all the BSM results, is performed by Bob. The process results in entangled photons shared by Alice (not shown) and Bob in a known Bell state.

the link length is l_i, then the probability of transmitting the photon over the channel is $\prod_i e^{-\alpha l_i} = e^{-\alpha L}$ where the total channel length is $L = \sum_i l_i$.

On-demand quantum memories [20, 25, 26, 27] – devices that store and allow one to retrieve quantum states when desired – can be utilized to allow photons to arrive synchronously for efficient entanglement swapping steps in a quantum repeater [23, 24]. A quantum repeater, like the one depicted in Fig. A.1, relies on the creation of heralded entanglement of quantum memories that is established via a publicly-announced BSM result. See the caption of Fig. A.1 for more details. Each source emits an entangled photon pair such that one photon from each pair is stored in a quantum memory, and the other is transmitted over half of an elementary link for entanglement swapping. Entangled photons are subsequently released from the quantum memories on-demand when all Bell-state measurements have succeeded. Here, on-demand refers to memories that output their stored states when triggered to do so. This allows the next steps of

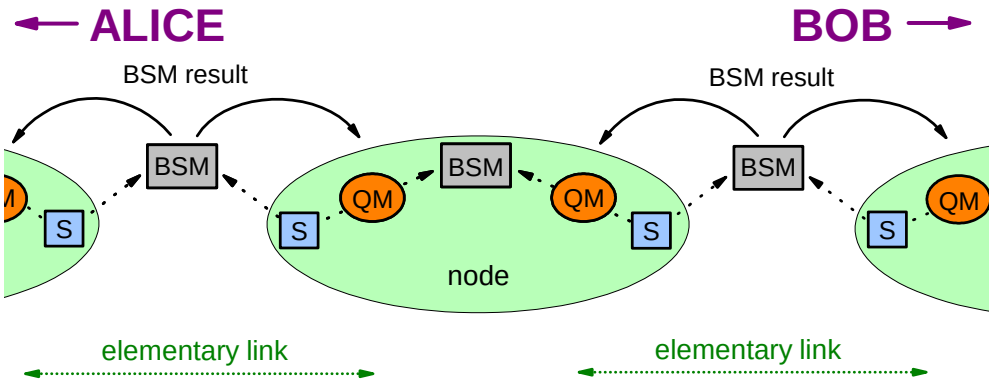

Figure 1.3: Quantum repeater. A pair of entangled photons prepared in a Bell state is emitted from each source (S). One member of each pair is stored in a quantum memory (QM) at the node while the other is transmitted over half of an elementary link (indicated by the green dotted arrows) to a Bell-state measurement (BSM) station. Once a BSM is achieved, its outcome is communicated to the adjacent nodes. After both BSM results have arrived from adjacent BSM stations, the memories are triggered to release their stored photons. This allows entanglement swapping, facilitated by the BSM at each node, to occur. This results in a Bell state established between Alice and Bob (both not shown).

entanglement swapping (that occurring at the nodes in Fig. A.1) to succeed provided there is no additional loss. Many quantum repeaters rely on multiplexing, i.e. utilize multiple copies of entangled qubits, to increase distribution rates [24, 31] or to facilitate certain designs of quantum repeaters that do not require on-demand memories, but those with a fixed and pre-established storage time [32].

Although the motive of quantum repeaters, as discussed here, is to overcome the effect of loss, decoherence of Bell states during transmission must be considered [3]. Repeaters in conjunction with entanglement purification – an approach relying on basic elements of quantum computers – is a way for Alice and Bob to share a high-fidelity Bell-state extracted from many shared copies of low-fidelity states [33, 34]. However, many experimental efforts, including from our group, do not yet consider this step. This is because errors produced over small links are remedied via classical error correction at

the final step of QKD [11]. The price we pay is that our approach is not scalable to longer distances, or applicable if high-fidelity entanglement is required.

Quantum repeaters are a widely-explored theoretical and experimental topic, with many different approaches and protocols, each requiring different systems and elements [24, 35, 36, 37]. Our approach is discussed further in Paper 1. To distinguish what constitutes a quantum repeater, a precise definition has been recently suggested by Takeoka, Guha and Wilde [38]; if a protocol can distribute a quantum key over a general quantum channel with a rate that scales better than that given by a bound (the TGW bound) then that protocol is a quantum repeater. The TGW bound is derived with the assumption of no trusted nodes. Note that a follow-up work by Pirandola, Laurenza, Ottaviani, and Banchi gives a tighter bound assuming a pure-loss channel [39].

Quantum repeaters and QKD are part of the more general field of quantum communication [40], and comprises an important part of a future quantum internet [41] – where quantum states are distributed between (computing) nodes – a preeminent application of quantum communication, and pursued research objective.

1.4 Light-matter interfaces for quantum memories

Quantum memories are designed to keep quantum states stationary for a certain duration. Thus, most memories are based on atomic transitions in matter, with optical transitions garnering a lot of investigation for quantum repeaters [20, 26, 27]. Many quantum memories are created to be so-called 'reversible' quantum memories. Reversible quantum memories for light are those that map externally-provided qubits (which are encoded into light) onto matter (storage), and subsequently back onto light (retrieval). These memories are of focus in this thesis. Note that there are other types of quantum memories, e.g. atomic ensembles that are prepared, via laser excitation, in a state that

is entangled with a photon [42, 43].

Since quantum memories for light rely on light-atom interaction, many quantum memory protocols are closely related to procedures used for spectroscopic measurements, yet with different goals. In spectroscopy, an input light field interrogates an atomic system, the system undergoes a process, and light is emitted with properties that differ from the input. It is hence necessary that the light is sensitive to the internal mechanisms affecting the atomic state. Consequently, a method is chosen such that the output field is measurably different from the input, dictated by the atomic process under question. For memories however, it is desirable to have the output state of light to be invariant from the input. If atoms experience decoherence, this effect is mapped onto the retrieved photons and generally leads to reduced performance of the memory for applications, e.g., the photon is lost or any encoded information becomes corrupted. Thus, the performance of quantum memories are dependent upon the protocol and atomic system employed.

There is a set of figures of merit that define how 'well' a memory performs [20, 44, 45]. They have been defined to benchmark demonstrations, i.e. define the state-of-the-art, and guide development. Note that figures of merit may be defined according to the task. Here we highlight figures of merit that are generally important for building workable quantum repeaters.

1.4.1 Figures of merit

- Fidelity – Quantifies how close the output quantum state $|\psi_{output}\rangle$ is to the input state $|\psi_{input}\rangle$. Generally $|\psi\rangle$ is described by all degrees-of-freedom of the photon. This is discussed in Paper 4. In all of the work presented in this thesis, we consider events where a single photon (which the qubit is encoded into) is detected, so fidelity is defined here as $|\langle\psi_{input}|\psi_{output}\rangle|^2$ with respect to the encoded quantum information (i.e. we consider the post-selected fidelity in this thesis). Unit fidelity is desired by definition.

The maximum fidelity of a classical memory for single qubits is 2/3, thus achieving a fidelity above this value is important.

- Efficiency – Given our context of single-photon encoding, this is the probability of storage and retrieval. Its classical analogue is the ratio of energy input to energy output. Unit efficiency is desired.

- Storage time – The required storage time is application-dependent. For certain repeaters, the storage time is dictated by the distance between nodes – this is typically assumed to be around 100 km to align with that used by classical repeaters. In fiber, this corresponds to a storage time of 500 μs. In other quantum repeater architectures, the required storage times can vary from $\sim$ 10 ms to seconds [24]. For the memories that we consider, storage time is inherently connected with efficiency due to time-dependent decoherence. The longer the storage time, the less coherent the atoms become. Consequently, the atoms may not all coherently participate in emission (in phase), thus reducing the retrieval probability.

- Bandwidth – Dictates the communication rates achievable as larger bandwidths corresponds to shorter durations of qubits. Several GHz bandwidths are desirable to align with classical communication standards.

- Multimode capacity – Sometimes referred to as multiplexing capacity. It bounds the number of qubits that can be stored simultaneously. Unless storage is performed using multiple spatial modes, the temporal (spectral) multiplexing capacity is approximately equal to the ratio of storage time to qubit duration (total bandwidth to qubit spectral width). Multiplexing is important for overcoming the effect of loss, but leads to increased complexity. A closely-related quantity to the temporal multiplexing capacity is the storage 'time-bandwidth product', however, this figure of merit is typically quoted in the cases where the memory protocol itself may only allow storage of a few modes.

- Complexity and practicality – Quantum memories may be created on-chip or designed for efficient interfacing with other components. Protocols and materials used for memories may limit usefulness. For example, memories utilizing off-resonant Raman scattering creates memory-photon entanglement directly, however the wavelength of the emitted photon is defined by the properties of the memory itself. Memories storing externally-provided photons can allow each photon from an entangled pair to be prepared at a wavelength suitable for either storage or transmission. Room-temperature memories generally are desirable, yet other components such as single-photon detectors may require cryogenics, thus implementations must also be considered in design.

Quantum memory research goes beyond repeater applications. For example, memories can be used to produce heralded single photons from a probabilistic photon pair source [46], or used for synchronizing processing steps in a quantum computer [27]. There are also varying types of memory protocols and systems used for storage [20, 26, 27, 44, 45]. Different protocols and systems used for state-of-the-art reversible optical quantum memories are introduced in Chapter 2.

It is important to mention that classical storage devices cannot be used as quantum memories. Classical memories are designed to only store classical information. One may try to use a classical memory to store quantum information by measuring a quantum state, and store the appropriate classical bits describing the measurement outcome. However this would only be useful if one had infinitely-many copies of the state [47]. Given the no-cloning theorem, a qubit-copying strategy is not possible for arbitrary input states [21].

Quantum memories can be viewed, more abstractly, as devices that map qubits from (occupying) one temporal mode to another. For example, if a qubit $|\psi\rangle$ is stored at time t_1 and emitted at time t_2, then a memory performs the operation $|\psi(t_1)\rangle \mapsto |\psi(t_2)\rangle$. As mentioned in the last section, an on-demand quantum memory is defined so that its stor-

age time, $t_2 - t_1$, is decided during the interval (t_1, t_2). Concerning the aforementioned figures of merit, it is desirable to have a memory of unit fidelity, $|\langle\psi(t_1)|\psi(t_2)\rangle|^2 = 1$. One may imagine extending the qubit mapping to other degrees of freedom such as frequency and space – $|\psi(t_1, \omega_1, z_1)\rangle \mapsto |\psi(t_2, \omega_2, z_2)\rangle$ with $|\langle\psi(t_1, \omega_1, z_1)|\psi(t_2, \omega_2, z_2)\rangle|^2 = 1$. Note that the qubit itself must be encoded into a degree of freedom not altered during the mode-mapping process, we could use polarization in this example. Thus, an on-demand quantum memory is a special case of a generalized qubit-mapping device; work in this thesis involves establishment and implementation of this idea. In conjunction with multiplexing, a generalized qubit-mapping device can be used in a quantum repeater instead of an on-demand quantum memory provided the device performs an on-demand mapping with respect to at least one other degree of freedom (see Paper 1). Furthermore, other applications requiring on-demand memories may be replaced by generalized qubit-mapping devices, and by doing so may both reduce the impact of various system constraints, and lead to new protocols and approaches.

1.5 Photonic quantum-state processing and storage

One utilization of light-matter interfaces is within the context of quantum state processing and manipulation [48]. Single photons are a workhorse for further development of quantum information science, thus it is important to tailor their properties to suit the systems of interest. It is possible to expand the use of a light-matter interface from qubit mapping to qubit manipulation [49]. This allows such an interface to perform tasks such as photon spectrum or temporal envelope modification, carrier-frequency shifting, or even qubit projection measurements (in conjunction with single-photon detection). For a quantum internet, photon processing may be integral for efficient interfacing between different nodes. Atomic media have long been employed for manipulation of classical light,

and many classical approaches can be straightforwardly adapted to single quanta (e.g. a prism will disperse single photons), but this adaptation does not hold in general. It is natural to combine quantum processing with storage in a single device to reduce complexity. Single-device quantum storage and manipulation is currently being researched in different systems and contexts [27, 45, 49, 50]. A rare-earth-doped waveguide implementation is discussed in Paper 5 of this thesis.

Atomic ensembles can be used not only to directly manipulate single photons, but also serve as an intermediary such that a single photon can controllably manipulate another [27, 45, 50, 51, 52]. Photons, on their own, do not directly alter the quantum state of other photons. One mechanism to facilitate photon-photon interactions is to use off-resonant non-linear interactions. Some approaches require many photons (strong fields) to achieve the desired interactions. There has been a great amount of work in achieving single photon non-linearities by enhancing the atom-light interaction (see Refs. [50, 51, 52] and references therein). A lot of this work has been motivated by achieving controlled photon-photon operations for quantum computers.

One approach to achieve photon-photon interaction is to have an atomic medium absorb a photon (probe), mapping its properties (e.g. its phase) onto the stationary atoms. Next, another photon (signal) is sent to off-resonantly interact with the atoms, thereby influencing the properties of the atomic state, without being demolished. If the ensemble is created as a quantum memory, the probe photon is retrieved with properties of the signal photon mapped onto it. For example, the presence of the signal can change the phase of the probe via a cross-phase modulation interaction. As mentioned in Section 1.4, photons emitted from a quantum memory are good probes of the internal atomic state. The challenge of this method is to strongly interact a signal photon with the atomic state (map properties onto the atoms) without disturbing the signal itself – in this case without losing the signal photon (and in some cases, to preserve any quantum

information encoded into it) [50].

The probe-signal cross-phase interaction described above can be used to perform a quantum non-destructive (QND) measurement to extract information about a quantum state without destroying it [53, 54]. Note that a classical memory, in conjunction with strong probe pulses, could substitute for the quantum memory in our aforementioned protocol, but with added complexity due to the requirement of spectrally filtering noise produced by the memory. QND is a desired objective for quantum information processing in general [3, 48]. In many applications, a goal is to quantify the number of photons (or even the presence of at least a photon) in a signal mode, without altering the qubit-state encoded (see Ref. [51] and references therein). This so-called qubit QND measurement does not defy quantum uncertainty as the qubit is encoded into an observable that commutes with that impacted by the QND. Qubit QND has applications for quantum repeaters, as it would allow heralding the arrival of an entangled photon after propagating through a lossy channel [55]. Progress towards a qubit-QND measurement is reported in Paper 6 of this thesis.

Chapter 2

Light-matter interaction

This thesis involves coherent interaction between light and matter. A brief overview of the physics governing this interaction is provided in this chapter. Following a common approach (e.g. see Ref. [56]), we derive the equations of motion of a two-level atomic system excited by a classical field. We will write these equations in the form of the Bloch equations. To take into account propagation of light through an atomic ensemble, we use the wave equation in combination with the Bloch equations to derive the Maxwell-Bloch equations. The Maxwell-Bloch equations are the starting point for mathematically depicting many light-atom effects. Later in the chapter we discuss two specific light-matter interactions that concern this thesis, namely spectral hole burning and photon echo [56].

2.1 Maxwell-Bloch equations

2.1.1 Bloch equations

Light-matter interaction is governed by the coupling between an atom, described by the transition dipole operator $\vec{d}\hat{\sigma}_1$, and the electric-component of an applied electromagnetic (light) field $\vec{E}(t)$. The operator $\hat{\sigma}_1$ is one of the three Pauli matrices $\hat{\sigma}_i$ where $i \in \{1, 2, 3\}$. The description of this interaction is quantified by the Hamiltonian

$$\hat{H}_I(t) = -\vec{d} \cdot \vec{E}\hat{\sigma}_1. \tag{2.1}$$

The total Hamiltonian of the system is

$$\hat{H} = \hat{H}_a + \hat{H}_I, \tag{2.2}$$

where $\hat{H}_a = \frac{\hbar\omega_0}{2}\hat{\sigma}_3$ is the Hamiltonian of a two-level atom that is comprised of a ground state $|g\rangle$ and an excited state $|e\rangle$, which differ in energy by $\hbar\omega_0$. The time evolution of the system can be described by evolving each of the Pauli operators using the Heisenberg equation of motion

$$i\hbar\dot{\hat{\sigma}}_i = [\hat{\sigma}_i, \hat{H}]. \tag{2.3}$$

This results in the following Bloch equations

$$\begin{aligned} \dot{\hat{\sigma}}_1 &= -\omega_0\hat{\sigma}_2, \\ \dot{\hat{\sigma}}_2 &= \omega_0\hat{\sigma}_1 + \frac{2}{\hbar}\vec{d}\cdot\vec{E}\hat{\sigma}_3, \\ \dot{\hat{\sigma}}_3 &= -\frac{2}{\hbar}\vec{d}\cdot\vec{E}\hat{\sigma}_2. \end{aligned} \tag{2.4}$$

Next we can relate these equations to the density matrix elements of the atomic state. We define a 3-vector $\vec{s} = \sum_i^3 s_i\vec{e}_i$ whose components are defined by the expectation values of each Pauli matrix $s_i = \mathrm{Tr}(\hat{\sigma}_i\rho)$, where ρ is the density matrix of the atomic state. This so-called Bloch vector allows interpreting the atomic state as a vector on a sphere. The coherence terms are s_1 and s_2, and s_3 describes the inversion probability.

Since $\hat{\sigma}_i$ is not explicitly time-dependent, we can use $i\hbar\dot{s}_i = \mathrm{Tr}(\rho[\hat{\sigma}_i, \hat{H}])$ [3] in conjunction with Eqs. 2.3 and 2.4 to re-write the Bloch equations describing the atomic state as

$$\begin{aligned} \dot{s}_1 &= -\omega_0 s_2, \\ \dot{s}_2 &= \omega_0 s_1 + \kappa E s_3, \\ \dot{s}_3 &= -\kappa E s_2, \end{aligned} \tag{2.5}$$

where we assume that the polarization of the field is parallel to that of the atomic dipole:

$\frac{2}{\hbar}\vec{d}\cdot\vec{E} = \kappa E$. The driving field can be simply defined as $E(t) = \mathcal{E}(t)[e^{i\omega t} + c.c.]$, giving

$$\begin{aligned} \dot{s}_1 &= -\omega_0 s_2, \\ \dot{s}_2 &= \omega_0 s_1 + 2\kappa\mathcal{E}\cos(\omega t)s_3, \\ \dot{s}_3 &= -2\kappa\mathcal{E}\cos(\omega t)s_2. \end{aligned} \tag{2.6}$$

Next we invoke the rotating-wave approximation. This allows us to easily find an analytical solution of the atomic dynamics. One way to do this is to move into a frame rotating at frequency ω about an axis defined by s_3. This is invoked by the following change of coordinates:

$$\begin{pmatrix} u \\ v \\ w \end{pmatrix} = \begin{pmatrix} \cos(\omega t) & \sin(\omega t) & 0 \\ -\sin(\omega t) & \cos(\omega t) & 0 \\ 0 & 0 & 1 \end{pmatrix} \begin{pmatrix} s_1 \\ s_2 \\ s_3 \end{pmatrix}.$$

We neglect the terms in the rotating frame that are rotating at 2ω, and define the detuning of the field with respect to the atom to be $\Delta = \omega_0 - \omega$. This gives

$$\begin{aligned} \dot{u} &= -\Delta v, \\ \dot{v} &= \Delta u + \kappa\mathcal{E}w, \\ \dot{w} &= -\kappa\mathcal{E}v. \end{aligned} \tag{2.7}$$

The Bloch equations can then be written in the compact form

$$\dot{\vec{\rho}} = \vec{\Omega} \times \vec{\rho}, \tag{2.8}$$

where $\vec{\rho} = (u, v, w)$, and $\vec{\Omega} = (-\kappa\mathcal{E}, 0, \Delta)$ is the Rabi frequency. This equation shows that, when coherent radiation interacts with a two level atom, the Bloch-vector (i.e. the atomic state) precesses around $\vec{\Omega}$ at a rate proportional to its length $||\vec{\Omega}|| = \sqrt{\Delta^2 + (\kappa\mathcal{E})^2}$. For example, consider an atom in the ground state $\vec{\rho} = (0, 0, -1)$ that is resonantly driven ($\Delta = 0$). If $\vec{\Omega}/||\vec{\Omega}|| = (-1, 0, 0)$ then the atomic state will rotate around v causing the

atom to evolve from the ground into the excited state and back again in oscillation. This phenomenon, called Rabi oscillation, happens with frequency Ω. Thus, a larger light-atom coupling strength corresponds to larger oscillation frequencies.

To quantify how much an atomic state changes with on-resonant excitation of an electric field for time t, the 'pulse area' can be defined as

$$\Theta = \int_0^t \kappa \mathcal{E}(t')dt', \tag{2.9}$$

which corresponds to the angle by which the Bloch-vector rotates during atom-light interaction. For example, a π pulse, having $\Theta = \pi$, causes a 180° rotation of the Bloch vector.

The Bloch equations so far do not include the possibility of decoherence or atomic decay. These effects can be included phenomenonologically. We modify the equations to read as

$$\begin{aligned} \dot{u} &= -\Delta v - \frac{u}{T_2}, \\ \dot{v} &= \Delta u - \frac{v}{T_2} + \kappa \mathcal{E} w, \\ \dot{w} &= -\frac{w+1}{T_1} - \kappa \mathcal{E} v, \end{aligned} \tag{2.10}$$

where $T_2(T_1)$ is the coherence (population) lifetime. We discuss these quantities more in Chapter 5.

2.1.2 Electromagnetic wave propagation

The starting point for the description of light as an electromagnetic wave is the set of equations known as Maxwell's equations (see any advanced electromagnetics textbook, e.g. Ref. [56]). The absence of free currents or charges allows Maxwell's equations to be simplified and combined into a wave equation

$$\frac{\partial^2}{\partial z^2} E(z,t) - \mu_0 \epsilon_0 \ddot{E}(z,t) = \mu_0 \ddot{P}(z,t), \tag{2.11}$$

where the second time-derivative is denoted by a 'double-dot', and we write the equation in 1-D. The electric field is $E(z,t)$, the atomic polarization (dipole moment per unit volume) is $P(z,t)$, $\epsilon_0\mu_0 = 1/c^2$, and c is the speed of light in vacuum.

Many basic light-matter effects can be observed assuming a linear material where $P = \epsilon_0\chi E$ and χ is the electric susceptibility. This is the case when there is very weak excitation. In this case, the solution to Eq. 2.11 is a plane wave

$$E(z,t) = E_0 e^{-i(\omega t - kz)} + c.c., \tag{2.12}$$

where E_0 is a constant amplitude, and $(\omega/k)^2 = (c/[1+\chi])^2$. In general, the susceptibility can be frequency-dependent and complex-valued with the real (complex) part describing dispersion (absorption).

Most experiments do not employ plane waves, but rather fields contained by an envelope function $\mathcal{E}(z,t)$,

$$E(z,t) = \mathcal{E}(z,t) e^{-i(\omega t - kz)} + c.c., \tag{2.13}$$

such as a laser pulse. This field produces a polarization having the same form, $P(z,t) = \mathcal{P}(z,t)e^{-i(\omega t - kz)} + c.c.$ We are interested in describing the evolution of $\mathcal{E}(z,t)$ and $\mathcal{P}(z,t)$ as the field passes through a medium. To derive an analytical solution of the dynamics, we invoke the slowly-varying envelope approximation: the field envelope varies slowly compared to the optical period and the wavelength. Mathematically, this is described by $\frac{\partial \mathcal{E}}{\partial z}/\mathcal{E} << k$ and $\dot{\mathcal{E}}/\mathcal{E} << \omega$. The polarization is approximated the same way. This results in Eq 2.11 taking the form

$$\Big(\frac{\partial}{\partial z} + \frac{1}{c}\frac{\partial}{\partial t}\Big)\mathcal{E} = \frac{i\omega}{2\epsilon_0 c}\mathcal{P} \tag{2.14}$$

where we have used $c^2 = \omega/k$ here, with k being the vacuum wavevector. As a result, the dispersion and absorption is dictated by $\mathcal{P}$.

2.1.3 Bloch equations with field propagation

The aim of this section is to relate the macroscopic polarization described in Eq. 2.14 with the relevant Bloch vectors, thereby deriving the Maxwell-Bloch equations.

First we note that, in many cases (and in the case of this thesis), the atomic ensemble is an inhomogeneously broadened array of two-level atoms. The absorption profile can be described by a distribution function $g(\Delta)$ satisfying

$$\int_{-\infty}^{\infty} d\Delta g(\Delta) = 1 \tag{2.15}$$

where Δ is the detuning of the atomic transition from the light carrier frequency. The medium can be thought of as a continuum of atoms with a corresponding Bloch-vector at each position z, and for each detuning Δ, distributed according to $g(\Delta)$.

The slowly-varying polarization of one frequency class of ions within the medium can be written as

$$\mathcal{P}(z,t) = Nd\langle\sigma_1(t,z)\rangle, \tag{2.16}$$

where N is the atomic density, and d is the dipole moment as defined in Eq. 2.1. By including inhomogeneous broadening, the slowly-varying polarization of the medium takes the form

$$\mathcal{P}(z,t) = Nd\int_{-\infty}^{\infty} d\Delta g(\Delta) Re\Big\{u(z,t,\Delta) + iv(z,t,\Delta)\Big\}, \tag{2.17}$$

where we have used the Bloch vectors in the rotating-wave approximation $\langle\sigma_1(t,z)\rangle = Re\{u+iv\}$. We combine Eqs. 2.14 and 2.17 to give

$$\Big(\frac{\partial}{\partial z} + \frac{1}{c}\frac{\partial}{\partial t}\Big)\mathcal{E} = \frac{i\omega Nd}{2\epsilon_0 c}\int_{-\infty}^{\infty} d\Delta g(\Delta) Re\Big\{u(z,t,\Delta) + iv(z,t,\Delta)\Big\}. \tag{2.18}$$

This equation relates the atomic dynamics, given by the Bloch equations, with wave propagation given by the Maxwell's equation. If we define $D = u + iv$, and use $z = ct$,

all Bloch equations may be written more compactly as

$$\begin{aligned} \dot{D} &= i\Delta D - \frac{D}{T_2} + ik\mathcal{E}w, \\ \dot{w} &= -\frac{w+1}{T_1} - \kappa\mathcal{E}Im\{D\}, \\ \frac{\partial\mathcal{E}}{\partial z} &= ia\int_{-\infty}^{\infty} Re\{D\}g(\Delta)d\Delta, \end{aligned} \tag{2.19}$$

where $a = \frac{\omega N d}{\epsilon_0 c}$ is related to the optical depth. These equations are a common starting point for many descriptions of light-atom dynamics.

2.2 Spectral hole burning

An inhomogeneously-broadened absorption line is composed of a large number of atomic transitions, each with their own individual linewidth and resonance frequency [56, 57]. Thus, with a narrowband light source, it is possible to excite a specific sub-ensemble of two-level atoms (or ions) absorbing at the source frequency. This interaction transfers atoms from their ground level into their excited level. In other words, inverting the Bloch-vector component w from -1 towards +1. Since absorption is proportional to the difference between the number of atoms in the ground and excited levels, atomic excitation causes a decrease in absorption at the frequency of excitation. Consequently, this results in a spectral hole in the inhomogeneously broadened profile, see Fig. 2.1 [56, 57, 58]. If the light source irradiates the ensemble longer than their characteristic coherence and population lifetimes T_2 and T_1, respectively, an equal distribution of population between the ground and excited levels is created. This effect can be derived from the Maxwell-Bloch equations in the limit $t >> T_2, T_1$, resulting in a set of rate equations (e.g. see Ref. [56]). If a third level is available, i.e. a Λ system, atoms may decay into this level rather than going back to the ground level. A so-called persistent spectral hole may be created on the transition between the ground and excited levels due to trapping

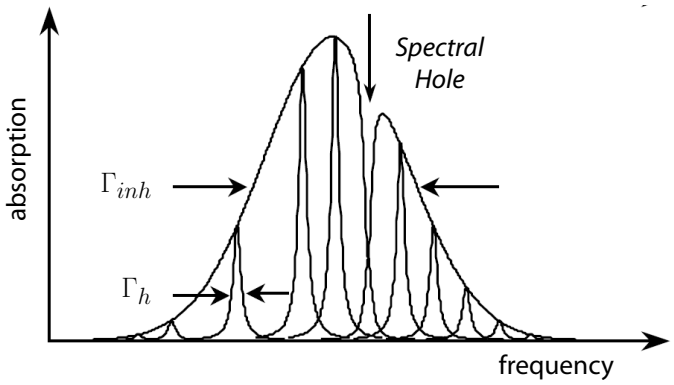

Figure 2.1: Line broadening and spectral hole burning. The envelope over the ensemble of atoms, each having individual linewidth Γ_h, is denoted by Γ_{inh}. A spectral hole is created at the laser frequency and can be seen as a reduction in absorption. Figure taken from Ref. [59].

of atomic population in the third level, whose population lifetime should be much longer than T_1 of the excited state.

If there are multiple atomic levels, for example hyperfine ground levels with energy-level differences much smaller than the inhomogeneous linewidth, a narrowband light source will be resonant with all hyperfine transitions [57]. A hole burning measurement will result in a population redistribution among all available sub-levels, see Fig. 2.2. Consequently, an increase or decrease of absorption may be measured, leading to a modification of the inhomogeneous lineshape at frequencies detuned from the spectral hole, i.e. a pattern of persistent side-holes and anti-holes. If there are several sub-levels comprising the excited level, 'side-holes' will appear at frequencies corresponding to each of the transitions from the ground-state level with depleted population, in addition to the hole at the burning frequency. 'Anti-holes', i.e. increased absorption, will occur at frequencies corresponding to transitions from the ground state hyperfine levels with increased population, i.e. levels into which ions have decayed.

Atomic decay leads to population dynamics, thus time-resolved spectral hole measurements are a useful spectroscopic tool [57]. Important properties of a material may

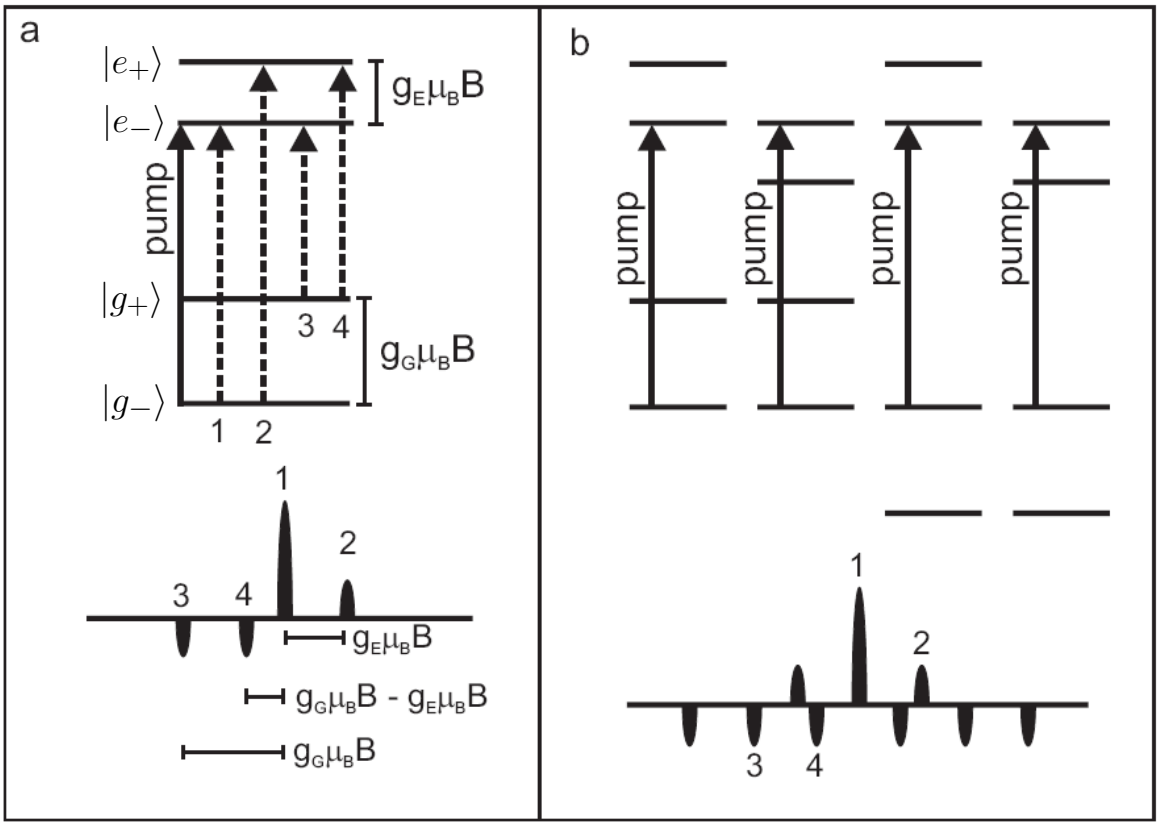

Figure 2.2: a. Four-level hole burning spectrum (Zeeman levels) for the class of ions for which the laser is in resonance with the $|g_-\rangle$ to $|e_-\rangle$ transition. B is the applied magnetic field, g_i and μ_B are constants. The laser pump transition (solid line) and possible laser probe transitions (dashed lines) between the four levels are shown in the energy diagram and labeled on the corresponding transmission spectrum of holes and anti-holes. b. Four-level hole burning spectrum with inhomogeneous broadening. Figure is taken from Ref. [60].

be established by performing time-resolved spectral hole burning, and by measuring hole and anti-hole properties as a function of parameters such as temperature or magnetic field. We employ spectral hole burning spectroscopy in Paper 7.

Varying the carrier frequency and intensity of a narrowband light source allows tailoring of the inhomogeneous line [57, 61, 62]. For an ensemble of two-level atoms, arbitrary frequency-dependent absorption profiles may be created. If a hyperfine structure exists, the sub-level splitting limits the structures that can be created [61]. However, many hyperfine levels are long-lived, and thus are beneficial for preparing persistent spectral features [57]. Spectral tailoring is employed to create many of the persistent spectral features that underpin the operation of absorptive quantum memories [62]. Spectral tailoring can be used for other applications such as frequency domain classical data storage [63] in which occurrence or absence of a hole defines logical zero or one, or frequency stabilization of lasers [59].

2.3 Photon echo

Typically, hole burning involves incoherent light-matter interaction, and is concerned with population transfer, i.e. change of the Bloch vector component w. This section focuses on photon echoes [56, 64, 65]. They arise from coherent light-matter interactions i.e. modifications of the u and v components of the Bloch vector. For this reason, photon echoes underpin the operation of many quantum memories, and comprise an important part of the quantification of atomic coherence properties [57, 27, 62]. A photon echo is produced if an ensemble of atoms coherently oscillate in phase at a certain time after an initial coherent excitation. Atoms that oscillate coherently, i.e. in-phase, produce strong coherent radiation. This is in contrast to the radiation emitted spontaneously by atoms with a random distribution of phases.

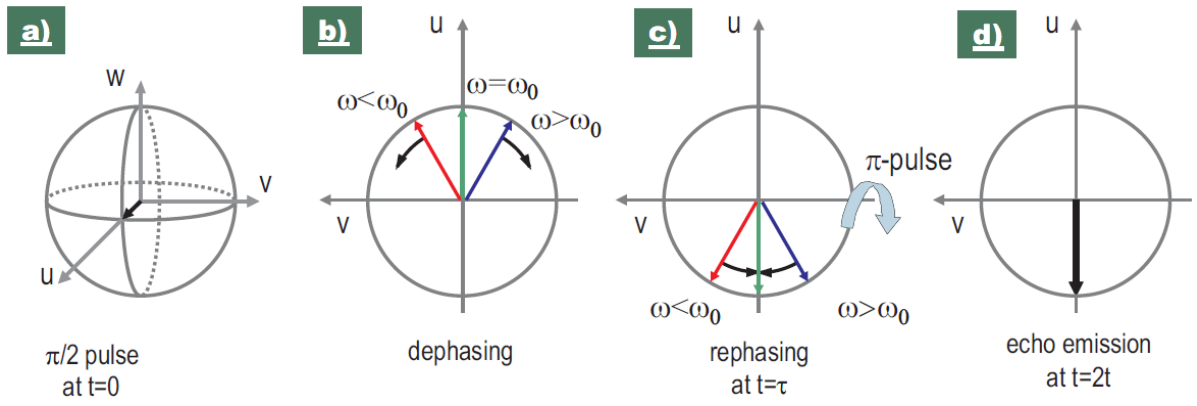

Figure 2.3: Two-pulse photon echo process. a) shows the Bloch-vector on the Bloch sphere after applying the first pulse, b)-d) show the evolution of the Bloch-vector on the equator of the Bloch sphere during the two-pulse echo protocol. The laser frequency is ω_{L}. Figure is taken from Ref. [62].

A simple way to produce a photon echo is to use a so-called two-pulse photon echo sequence [56]. It is observed after two strong brief laser pulses, separated by time τ, excite an inhomogeneously broadened absorption line (see Fig. 2.3). The first pulse creates coherence between the ground and the excited level. Ideally, this should be a $\frac{\pi}{2}$-pulse, placing the Bloch vector parallel to the u-axis of the Bloch sphere (see Fig. 2.3 a). Initially, all the atoms are phase aligned with the excitation light, with their Bloch-vectors all pointing in the same direction. Due to the inhomogeneous broadening, the atoms dephase (i.e. acquire a phase difference relative to the laser that is proportional with their detuning). The second pulse rotates the phase of the atomic states by π. Atoms that have acquired a negative phase difference relative to that of the laser will now have a positive phase, which starts to decrease (Fig. 2.3 c). At a time 2τ after the initial $\frac{\pi}{2}$-pulse, all atoms again oscillate with the same phase (in a forward propagating frame), which re-establishes the original dipole moment and causes the emission of light – the photon echo (Fig. 2.3 d).

The two pulse photon echo allows measuring decoherence, i.e. T_2, see Eq. 2.20. Since the echo intensity is proportional to the magnitude of u and v [57], the echo intensity will

decrease as the time delay between the two excitation pulses is increased. This method is used to quantify coherence properties of a rare-earth-ion doped waveguide in Paper 7.

If the second π-pulse comprising the two-pulse echo sequence is split into two time-delayed $\pi/2$-pulses, the resultant excitation produces a so-called three-pulse photon echo [57]. It begins with the first pulse creating an atomic excitation parallel to the u-axis. After a time delay τ, a second pulse is applied that rotates the quantum state into the plane defined by the ground and excited levels. The third pulse causes the atoms to be rotated into the u-v plane as in the two-pulse case. At that point rephasing occurs and an echo is emitted a time τ after the third pulse. The effect of the first two excitation pulses is to create a frequency-dependent periodic modulation of the population in the ground and excited levels, i.e. a population grating containing full information about the relative phase and time separation between the two excitation pulses. The period of the grating, inversely proportional to the time interval between the first two pulses, τ, dictates the delay time of the echo.

Two- and three-pulse photon echo protocols are not appropriate for quantum memory due to spontaneous emission produced by excited-level population decay that decreases the fidelity of the quantum information encoded into the emitted photon [66, 67]. The atomic frequency comb [68] quantum memory protocol (employed in this thesis and described in Chapter 3) is a way to achieve the storage and re-emission of individual photons without the addition of noise.

Chapter 3

State-of-the-art optical reversible quantum memories

There has been a great amount of work towards developing optical quantum memories for quantum information storage and processing tasks. For an extensive summary, these reviews [20, 26, 27, 44, 45] cover the subject well. In this chapter we briefly describe a few protocols that have led to state-of-the-art experiments giving the best performance with respect to the figures of merit introduced in Section 1.4.1. We restrict our discussion to post-selected, reversible, ensemble-based memories that have been used to perform experiments with light at the single-photon level. By reversible we are referring to memories that store and retrieve externally-provided quantum states. We note that, beyond the scope of this chapter, there have been many experiments of classical light storage using quantum memory protocols, measurements of spectroscopic properties that have shown promise for development of quantum memories, and demonstrations employing (non-reversible) memories based on off-resonant Raman scattering [20, 26, 27, 44, 45].

As discussed in Ref. [27], most atomic ensemble-based approaches to quantum memory may be grouped into two categories: optically-controlled or engineered-absorption-based memories. The former requires intense laser pulses (referred to as control pulses) to reversibly map a photonic qubit onto an atomic state of an ensemble. The latter relies on direct absorption of a photon to achieve the mapping onto the ensemble, and a tailored static, or dynamic, absorption line in order to control the re-emission of the photon. Many schemes employ a combination of both approaches to achieve optimal memory performance. We note that there has been research exploring similarities between both categories of protocols [27].

The protocols we consider here are based on electromagnetically-induced transparency

(EIT) [69], off-resonant Raman interaction [70, 71], gradient-echo memory (GEM) [72, 73], and atomic frequency comb (AFC) [68]. To implement any one of the four protocols, between three and four atomic levels are typically required. For proof-of-principle demonstrations, some of these protocols can be implemented using only two atomic levels. However, due to restrictions based on atomic properties or the protocol itself, a multi-level implementation of the protocol may be necessary for practical applications. In most experimental demonstrations of the aforementioned protocols, the ground levels are hyperfine or spin-levels that are long-lived and closely spaced in energy compared to the energy difference between any of the ground and excited levels. See Fig. 3.1 for a diagram. A photon carrying quantum information, a signal field, is interfaced on- or off-resonantly with the optical transitions and a control field converts the optical to ground-level coherence. An auxiliary ground level is used to store atomic population as required for many absorptive quantum memories (see descriptions in sub-sections 3.3 and 3.4 describing GEM and AFC respectively).

3.1 Electromagnetically-induced transparency

A basic EIT scheme uses a control field to interface the signal state with the memory [69], see Fig. 3.2. The detuning of the signal is much less than the inhomogeneous linewidth of the transition itself. Without the control field the signal is absorbed. However, if the control field is applied with the correct strength and detuning, a sharp dip in the absorption profile – the electromagnetically-induced transparency – is experienced by the signal photon. Due to the Kramers-Kronig relations [74], the sharp absorption dip results in strong dispersion of the signal, and a reduction of its group velocity. In this way, EIT can be used as a 'slow-light' memory. To increase the storage time beyond that given by the transit time of the signal, the control field is slowly reduced (i.e. ramped down) to

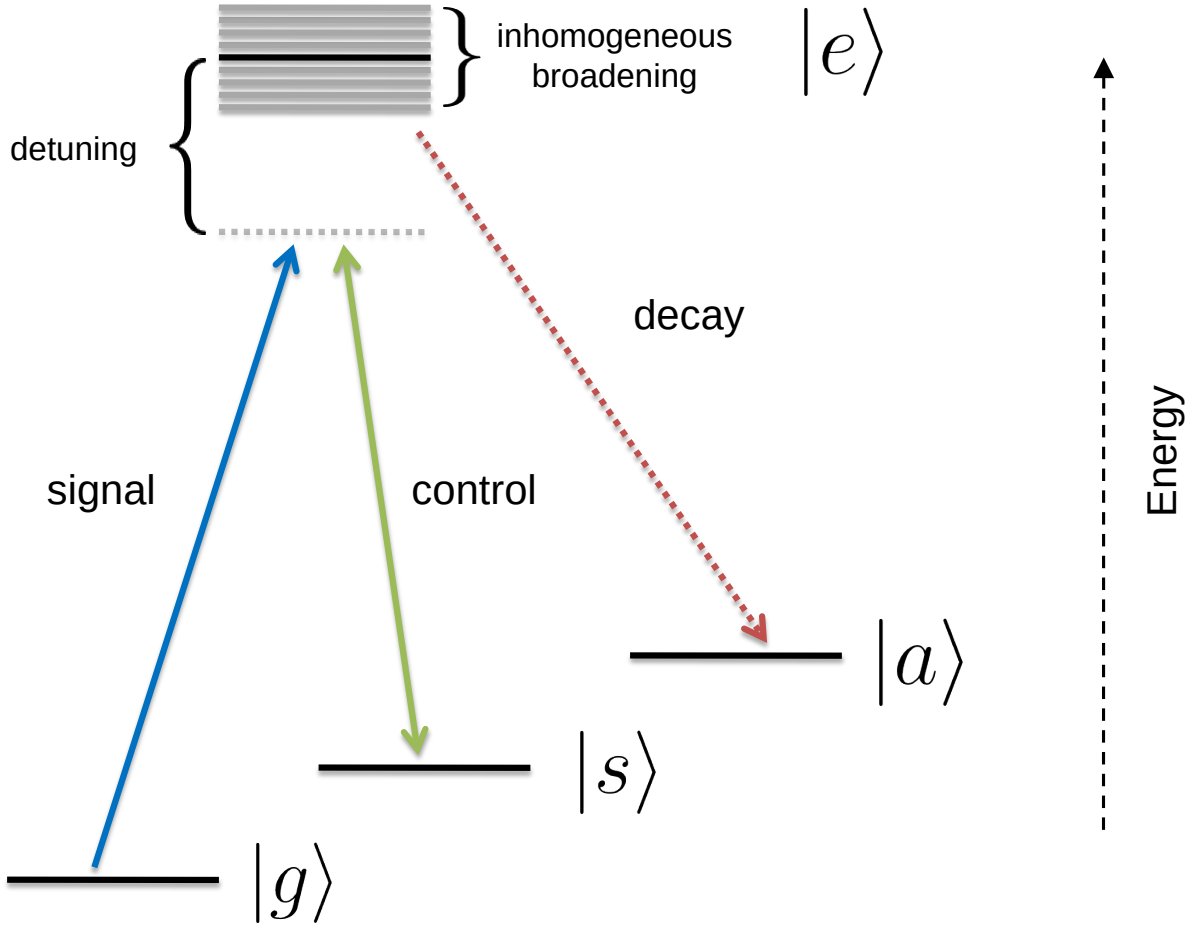

Figure 3.1: Level diagram suitable for many quantum memory protocols. The ground levels, each differing in energies given typically by MHz to GHz frequencies, are labeled $|g\rangle$, $|s\rangle$ and $|a\rangle$. The ground levels are separated by optical frequencies from an excited level $|e\rangle$. Inhomogeneous broadening of the optical transition is indicated by grey lines in the excited level. Quantum information is encoded into a photon (the signal; blue arrow), which on- or off-resonantly drives the $|g\rangle \rightarrow |e\rangle$ transition. A control field (green arrow) coherently maps the signal state onto the $|g\rangle \rightarrow |s\rangle$ transition. Absorptive memories require optical tailoring of the inhomogeneous broadening. This can be accomplished by optical pumping, i.e. optical excitation of population from $|g\rangle$ to $|e\rangle$ followed by population decay (dotted red arrow) to the level $|a\rangle$.

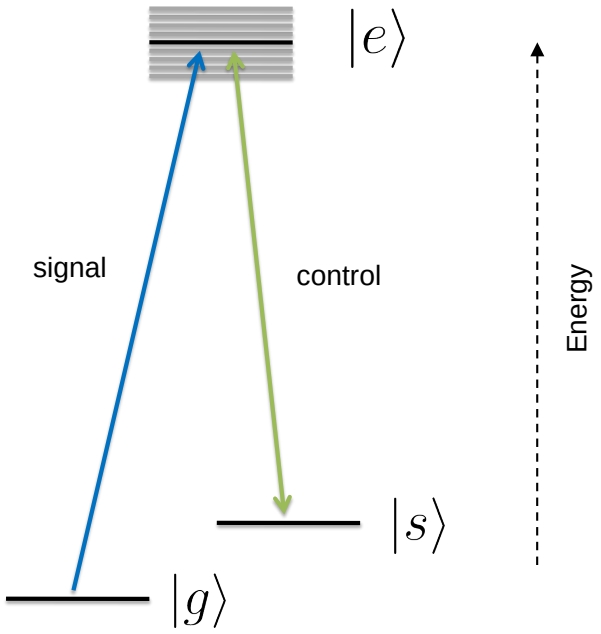

Figure 3.2: Simplified level structure for EIT.

zero. This maps the signal to the ground-level atomic coherence. To retrieve the signal, the control field is slowly increased, subsequently mapping the ground-level coherence back to slow-light.

Although EIT is a widely-explored approach for quantum memory, in its simplest form it is not one that points to satisfying all figures of merit in a single system [27]. First, the memory bandwidth is proportional to the control field intensity [69]. Since strong control fields may introduce fluorescence noise, only up to ∼MHz memory bandwidths are generally achievable [27].

Furthermore, the temporal multimode storage capacity scales with the square-root of the optical depth [75]. This scaling is unfavourable compared to what is achievable using other memories such as those based on GEM or AFC (discussed in Sections 3.3 and 3.4, respectively). Recently, a cold-atom EIT memory for polarization qubits has shown better than 80% fidelity for several millisecond storage times but with efficiency of only a

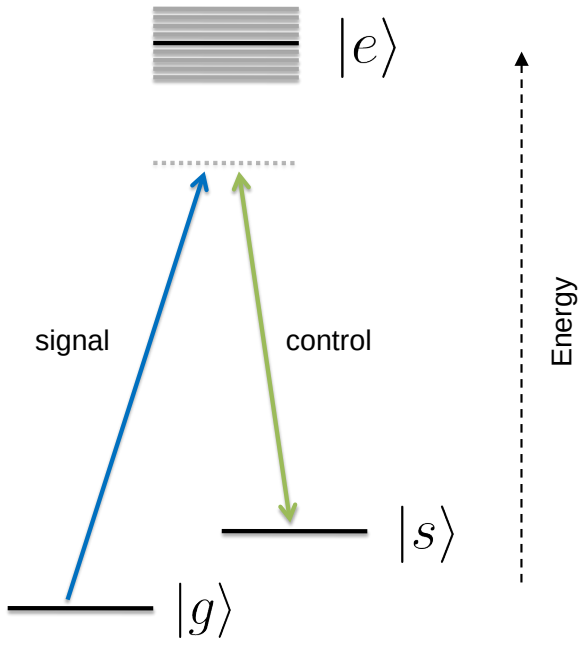

Figure 3.3: Simplified level structure for an off-resonant Raman-based memory.

few percent [76]. These storage times are the longest observed using reversible-memories (note that similar performance has been observed with an AFC memory [77]).

3.2 Off-resonant Raman

In contrast to EIT, a simple Raman scheme has both the signal and the control beam off-resonant from the excited level [70, 71], see Fig. 3.3. The signal and control pulses together create an effective optical two-level system comprised of the ground levels (a Raman absorption line). The control is turned on when absorption of the signal is desired. Once the signal is absorbed, the control is turned off, resulting in the signal qubit being mapped to the ground levels. Turning the control field on again retrieves the signal. One advantage of this method compared to EIT is its possibility for broadband storage of single photons. Despite requiring stronger control fields than EIT for efficient storage,

Raman implementations suffer less from fluorescence noise when compared to EIT (for a fixed control-field intensity) since the control is far off-resonant, however other effects such as spontaneous four-wave mixing can add noise [27].

Despite its possibility for broadband utility, the temporal multimode capacity of Raman memories scales with optical depth in the same way as EIT [75]. Recently, room-temperature Raman memories have stored heralded single photons of several-THz bandwidth in optical-phonon modes of diamond [78]. This work demonstrates the largest memory bandwidth achieved to-date, but with storage times of a few picoseconds, limited by the decay time of the optical phonon. Consequently, this memory is unusable for quantum repeaters, but is suitable for synchronization of photons in high-rate applications. There have been other demonstrations using off-resonant Raman memories, mainly in warm Cs gas, that have simultaneously shown the possibility of GHz-bandwidth storage (see Ref. [80] and references therein).

3.3 Gradient echo

GEM, sometimes called longitudinal controlled reversible inhomogeneous broadening (CRIB) [81], is categorized under engineered-absorption [72, 73]. A narrow absorption line is prepared from an inhomogeneously-broadened line by optical pumping of (typically) ions into the auxiliary level $|a\rangle$. See Fig. 3.4. The absorption line is longitudinally broadened (i.e. detuned along the propagation direction of the signal) via its coupling to an external field gradient. For example, a longitudinally-varying DC electric field results in a corresponding longitudinally-dependent Stark shift. See Fig. 3.4. At this stage, the signal is absorbed by the broadened line, resulting in a de-localized excitation over N atoms as described by the Dicke state,

$$\sum_{j=1}^{N} c_j e^{i\ 2\pi\delta_j t} e^{-ikz_j} |g_1 ... e_j ... g_N\rangle, \tag{3.1}$$

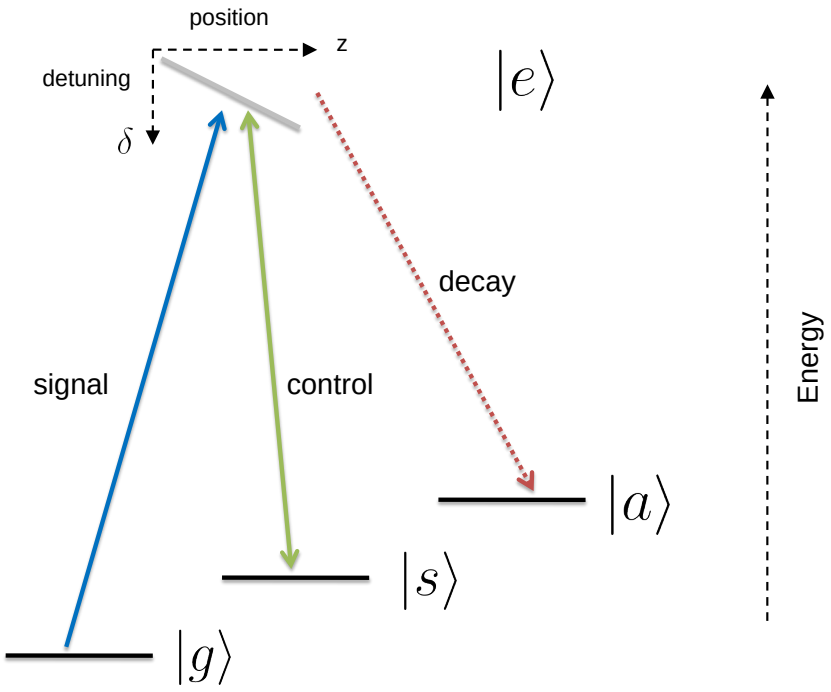

Figure 3.4: Simplified level structure of a GEM/CRIB memory.

where z_j is the position of atom j, k is the wave number of the signal, δ_j is the detuning of the atom with respect to the carrier frequency of the signal, t is the time elapsed after absorption, and the amplitudes c_j depend on the frequency and on the position of the jth atom. After storage, each term in Eq. 3.1 acquires the frequency-dependent phase $\delta_j t$. To re-emit the photon, one reverses the sign of the applied field at time t_r; consequently reversing the detuning of each atom. This results in each term in Eq. 3.1 acquiring the phase $-\delta_j(t - t_r)$, rendering a zero phase shift at $t = 2t_r$ and emission of the signal. The spatially-dependent frequency shift guarantees no possibility of re-absorption in the medium.

If it is not possible to generate a longitudinal gradient, it is sufficient to broaden the initially prepared line with a spatially-inhomogeneous external field (this is straightforward to achieve in experiment) to produce a fixed but arbitrary frequency shift of the

absorption line at each position z within the medium (i.e. transversal broadening of the absorption line). Reversing the sign of the field results in the desired frequency-dependent phase matching and retrieval. This protocol requires an additional spatial phase matching step to eliminate re-absorption. This can be achieved with counter-propagating control fields that reversibly map optical to spin-level coherence before the sign of the field is reversed. See Fig. 3.4. This results in the retrieved photon propagating in the backwards direction. This modified version of GEM/longitudinal CRIB is referred to as transverse CRIB [81]. Note that the temporal multimode capacity of CRIB and GEM scale linearly with the optical depth; an improvement over the EIT and Raman schemes [75].

As it is done in many experiments (see Ref. [82] and references therein), our description of GEM can be combined with the off-resonant Raman memory developed earlier. In this case, there is no initial preparation of an absorption line, but rather the natural line of the ground-state spin transition is used. A magnetic field gradient longitudinally-broadens this transition, see Fig. 3.5. A strong control field maps the signal state onto the broadened line. Sign reversal of the field results in the required re-phasing, and application of the control field results in emission of the signal. This type of GEM was used to demonstrate 87% quantum memory efficiency – the highest efficiency yet observed – with a cold Rb cloud, but with an acceptance bandwidth of only a few hundred kHz [82]. Storage times greater than 1 millisecond have be achieved without significant deterioration of storage fidelity, despite the observation of non-zero four-wave mixing noise [82].

3.4 Atomic frequency comb

AFC is another type of engineered-absorption quantum memory [68]. Instead of preparing a single absorption line as is done for GEM or CRIB, many identical spectral lines, each

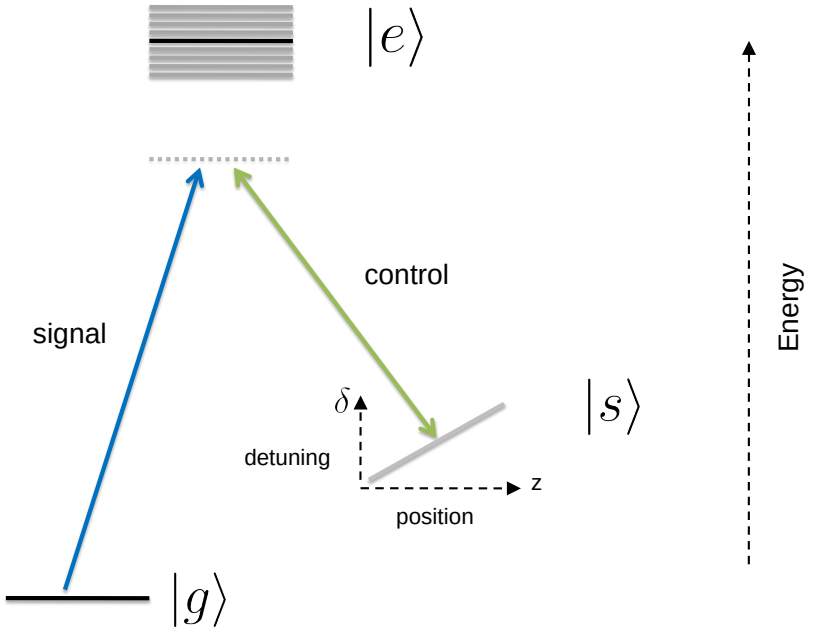

Figure 3.5: Simplified level structure of an Raman-GEM memory.

separated from their nearest-neighbour by frequency Δ, are created, i.e. a frequency 'comb' of absorption lines is created. See Fig. 3.6. A photon of bandwidth greater than Δ but less than the overall width of the comb is absorbed, creating the Dicke state of Eq. 3.1. Re-emission of the photon occurs automatically at a time given by $1/\Delta$ due to re-phasing of the atomic excitations. This is due to the periodicity of the comb; it guarantees that $\delta_j = m\Delta$ where m is an integer, and hence for $t = 1/\Delta$, $2\pi\delta_j t = 2\pi m$. Thus, the storage time is established before absorption (engineered absorption before storage). Given the description above, AFC does not allow on-demand retrieval. Despite this apparent limitation, as mentioned in Chapter 1 (and discussed further in Paper 1) storage, and mode-selective retrieval, of photons encoded into other degrees of freedom allows AFCs with fixed storage times to be utilized in quantum repeaters. Nevertheless, for on-demand retrieval, counter-propagating control fields allow reversible and on-demand mapping of the signal to the ground-state with the additional benefit of phase matching

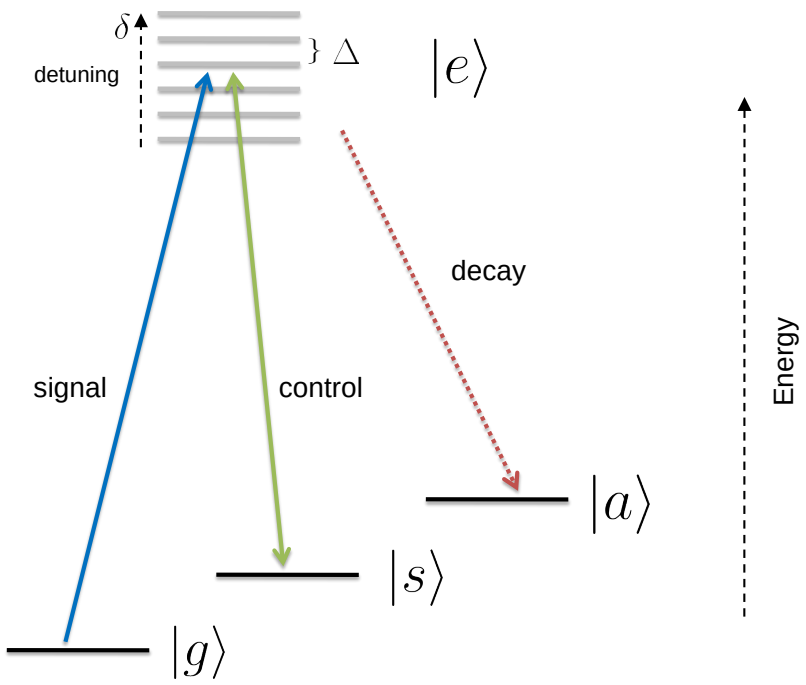

Figure 3.6: Simplified level structure of an AFC memory.

for efficient (backwards) retrieval (as similar to CRIB). The efficiency of an AFC featuring Gaussian-shaped teeth and phase-matched retrieval in the backwards direction is given by

$$\eta = (1 - e^{-d/F})^2 e^{-7/F^2}, \tag{3.2}$$

where d is the peak optical depth of each tooth, and $F = \gamma/\Delta$, where γ is the linewidth of each tooth and F is the comb finesse. Thus near-unit efficiency is possible with high optical depth and finesse. We note that one promising avenue to achieve both phase-matching and high efficiency relies on impedance-matched cavities [83, 84].

Notably, the temporal multimode capacity of AFC is independent of optical depth, rendering AFC more promising than GEM, Raman or EIT in this respect [75]. AFC is used for all quantum memories developed in this thesis. Due to our quantum repeater architecture, the limited number of atomic ground states of our storage material and other

experimental restrictions, we restrict our studies to AFC operating with a fixed delay (not on-demand) and without the longitudinal phase-matching step (i.e. forward retrieval). In the case of forward-retrieval, the efficiency is given by $\eta = (d/F)^2 e^{-d/F} e^{-7/F^2}$ for a comb with Gaussian-shaped teeth [85]. The maximum efficiency of this type of AFC memory is limited to 54% due to re-absorption [86].

AFC has resulted in several benchmark demonstrations of quantum memory (see Ref. [27] and references therein). These include millisecond timescale on-demand storage of weak pulses [77], up to 99.9% fidelities [87], multimode storage of single photons created in 100 temporal modes [88] and GHz-scale bandwidths (see Paper 3). Most AFC work has utilized the properties of cryogenically-cooled rare-earth-ion-doped crystals. All quantum memories used for this thesis employ AFC memory in a thulium-doped $LiNbO_3$ waveguide.

Chapter 4

Properties of rare-earth-ion doped crystals

The experiments presented in this thesis employ a titanium-indiffused Tm^{3+}:$LiNbO_3$ waveguide (Ti^{4+}:Tm^{3+}:$LiNbO_3$) cooled to temperatures of less than 4 Kelvin for AFC quantum memory. Titanium is used to raise the index of refraction of Tm^{3+}:$LiNbO_3$ to allow wave guiding. A photograph showing many of our Tm^{3+}:$LiNbO_3$ waveguides is presented in Fig. B.2.

In this chapter we outline some properties of rare-earth-ion-doped crystals that are important for the development of quantum light-matter devices based on rare-earth-ion-doped crystals. Cryogenic cooling partially removes the negative impacts of thermally-activated lattice vibrations (phonons), and thus allows rare-earth atomic ensembles to possess desirable properties. These properties include ions being initialized in well-defined ground states, having long-lived sub-level structure that allows for spectral tailoring, long coherence lifetimes, and an inhomogeneously-broadened optically-addressable absorption line [57, 89].

The rare-earth elements are comprised of 14 elements from Lanthanum (atomic number 57) to Ytterbium (atomic number 70). When doped into crystals, they generally occur as triply-positive ions. All rare-earth elements have similar bonding electrons, specifically those occupying the 6s shell. The 4f-4f transitions are those utilized by absorptive optical memories. Since the 4f shell is closer to the nucleus than the 6s, 5s and 5p shells, the 4f-4f transitions are shielded from the dynamic crystal environment, allowing these transitions to feature low decoherence at cryogenic temperatures [57, 89]. Selection rules for a free ion dictate the 4f-4f transitions to be forbidden. However, selection rules are weakly broken due to mixing of the atomic states by the electrostatic field of the host crystal

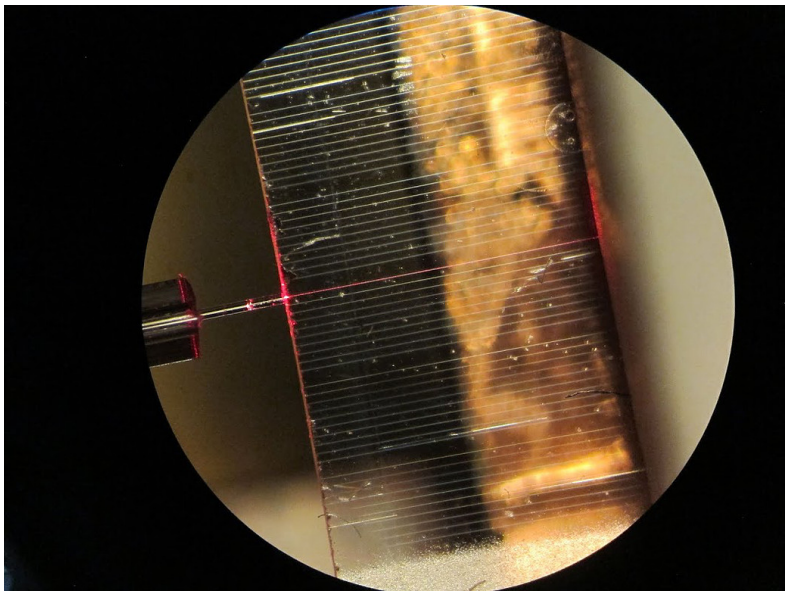

Figure 4.1: Tm^{3+}:$LiNbO_3$ waveguides. Waveguides are seen in white due to ambient-light scattering. A single waveguide is illuminated with red light from a butt-coupled fibre held by a capillary.

[90]. Since the crystal field acts as a perturbation, only very weak dipole moments exist and hence, long excited level population lifetimes can be obtained. Low decoherence and long population lifetimes at cryogenic temperatures are one of the reasons why optical transitions of rare-earth ion doped crystals are used for quantum storage and processing applications [62]. We point out that although the level structure of a specific rare-earth ion only weakly depends on its host crystal, its coherence properties may be influenced by host ions and other impurities (see Section 4.2) [89].

The magnetic properties of a rare-earth ion are strongly dependent on whether it has an even or odd number of f-orbital electrons [57, 89]. Rare-earth-ions with an odd number of 4f electrons are called Kramers ions. Due to their unpaired electron, they tend to have large magnetic moments and paramagnetic properties. Non-Kramers ions are those with an even number of electrons and occupy crystal sites with lower than axial symmetry. Each class of ions (Kramers or non-Kramers) tend to share properties.

For example, Kramers ions can induce large magnetic dipole-dipole interactions that can influence decoherence. Next we introduce more detailed spectroscopic properties of rare-earth-ion doped crystals. We also summarize important parameters of the Tm^{3+}:$LiNbO_3$ waveguide that we have utilized for our AFC demonstrations.

4.1 Level structure

The free-ion level structure is dictated by the Coulomb and spin-orbit interactions. Each level is denoted by a term symbol $^{2S+1}L_J$, where S is the total spin quantum number, J is the total angular momentum quantum number, and L is the total orbital angular momentum quantum number (e.g L= 1 refers to P). These levels are commonly split by optical frequencies. A set of energy levels having the same values of L, S and J, are generally split into at most 2J+1 'Stark levels' by the electrostatic crystal field, with level separations typically around 0.1-1 THz. Specifically, the number of Stark levels and energy-level separations are dictated by the rare-earth and the symmetry of the site it occupies. The labeling of levels by their free ion description (e.g. $^3H_4$), although used in literature, is slightly misleading due to perturbations introduced by the crystal field [57, 89].

If an ion is excited to a higher-energy level within the same Stark manifold, it generally relaxes rapidly (10^{-9}-10^{-12}s timescales) with phonon emission to the lowest-energy Stark level. In this thesis, and most other work, only the transition from the lowest Stark level of the electronic ground state to the lowest level of an optically excited state is used. This transition is referred to as the 'zero phonon line' as it does not involve the absorption or emission of phonons at cryogenic temperatures.

It is important to note that calculating the level structure, and the properties, of a rare-earth-ion doped crystal is challenging. Thus, it is important to study many proper-

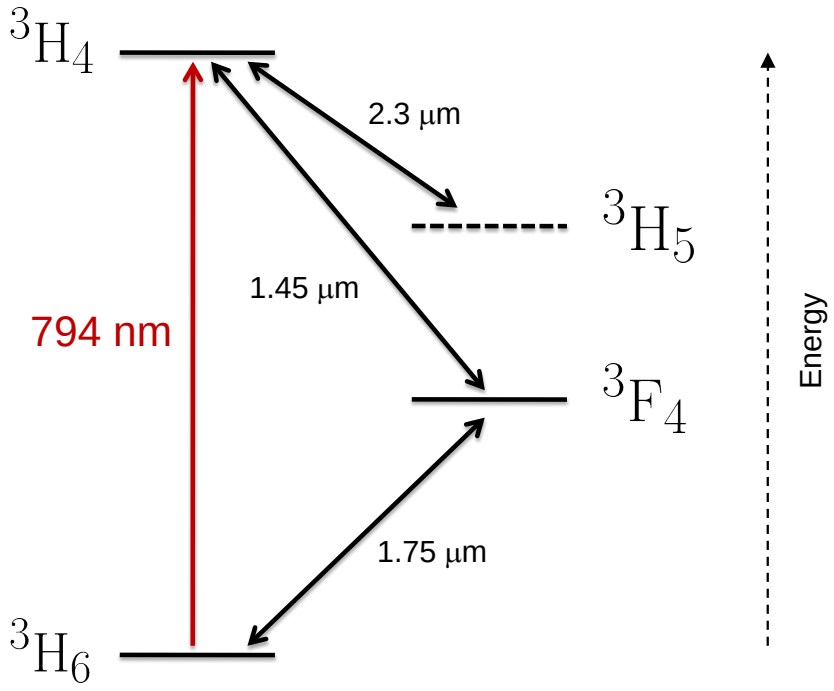

Figure 4.2: Simplified electronic structure of Tm^{3+}:$LiNbO_3$.

ties of new materials before employing them for applications. For this thesis, we employ the $^3H_6$ to $^3H_4$, 795 nm transition, of Tm^{3+}:$LiNbO_3$ [91]. See Fig. 4.2 for a simplified level diagram. The $^3H_5$ level is short-lived in comparison to the $^3F_4$ level, thus it is usually neglected in literature.

4.1.1 Sub-level splitting

The next level of detail in the level structure beyond the crystal field splitting comes from the magnetic hyperfine interaction. The nature of the hyperfine levels are dependent on the ion and crystal, e.g. Kramers or non-Kramers, site symmetry, etc. A general discussion of the hyperfine structure of rare-earth-doped crystals can be found in Refs. [57, 89]. For certain non-Kramers ions (e.g. Tm^{3+}:$LiNbO_3$), the levels are electronic singlets and the angular momentum is said to be quenched by the crystal field, resulting

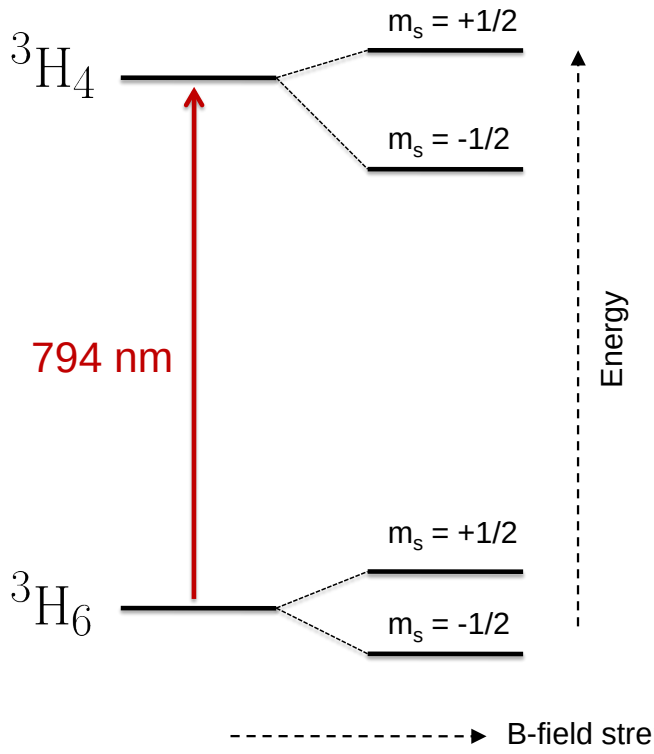

Figure 4.3: Simplified hyperfine level structure of Tm^{3+}:$LiNbO_3$.

in no first order hyperfine interaction ($I \cdot J = 0$). In this case, the hyperfine levels are described by weak nuclear quadrupole and spin interactions. For the I= 1/2 nuclear spin of Tm, quadrupole and second-order magnetic hyperfine interactions vanish in zero magnetic field. When an external magnetic field is applied, nuclear Zeeman and electronic Zeeman interactions combine with a second-order hyperfine interaction to split the ground and excited states into a pair ($m_s = \pm 1/2$) of hyperfine levels. We refer to these levels as hyperfine or 'nuclear Zeeman' levels [57]. See Fig. 4.3 for a simplified diagram. For Tm^{3+}:$LiNbO_3$, both the $^3H_4$ and $^3H_6$ are each split into two Zeeman levels. The difference of splitting between the excited- and ground-level Zeeman levels is approximately 1.4 GHz/T [92, 93, 94]. This is a relatively large value for a non-Kramers ion.

For applications, ground state hyperfine levels are commonly used for population

storage, or mapping of optical coherences, as relaxation between hyperfine levels is slow (depending on the crystal, temperature, field, etc.). The relaxation may involve a spin-exchange with the surrounding nuclei, or a phonon-assisted process. At 3 K, our Tm^{3+}:$LiNbO_3$ waveguide features a 1 second-long hyperfine population lifetime [91] that increases to several hours below 1 K (see Paper 7).

Next lowest in energy are superhyperfine splittings, which are due to the additional energy of the interaction between the ion and the nuclear magnetic moment of the surrounding atoms in the host material [57, 92]. For Tm^{3+}:$LiNbO_3$, ^{7}Li and ^{93}Nb spins tend to have the strongest effect and may influence spectral tailoring (see Paper 6).

4.2 Line broadening

After an atom is excited, there is a non-zero probability it will decay. Thus, any resonance feature has an associated non-zero spectral linewidth. Considering rare-earth-ions doped into crystals, the width and central frequency of a spectral line depends largely on the ion and the ion's environment. For this work, it is important to discuss mechanisms behind spectral line broadening to understand how it affects the performance of light-matter devices. Two important broadening mechanisms are prevalent in rare-earths doped into crystals: homogeneous and inhomogeneous broadening [57, 89].

4.2.1 Homogeneous broadening

The homogeneous linewidth defines the intrinsic spectral linewidth of an ion in the rare-earth ensemble, and is the same for all rare-earth ions. The homogeneous linewidth, Γ_h, is related to the coherence lifetime, T_2, of an ion through the time-frequency Fourier transform:

$$\Gamma_h = \frac{1}{\pi T_2} = \frac{1}{2\pi T_1} + \frac{1}{\pi T_2^*}. \tag{4.1}$$

Included here is the relationship between the coherence lifetime T_2, the population lifetime T_1 and a time T_2^* that quantifies the amount of linewidth broadening beyond that given by the population lifetime [89]. Optical coherence lifetimes are reduced by mechanisms such as coupling of levels by emission, absorption, or scattering of lattice phonons, or by spectral diffusion (see below). At low temperatures, the number of phonons is small. However, more phonons will contribute to decoherence if the temperature is increased above a few Kelvin, consequently limiting T_2 to nanoseconds at best. In the absence of any decoherence, the minimum homogeneous linewidth is determined by spontaneous relaxation alone; $2T_1 \geq T_2$.

Homogeneous linewidths approaching the lifetime limit has been observed in some materials, such as in Er^{3+}:Y_2SiO_5, where the narrowest optical resonance, 73 Hz (T_2 = 4.38 ms), in any solid-state material was measured (compare to T_1 = 11.4 ms, giving a linewidth of 14 Hz) [59]. For Tm^{3+}:$LiNbO_3$ waveguides, coherence lifetimes of 1.6 μs have been measured at 3 Kelvin [91]. Coherence lifetimes increase to more than 100 μs at temperatures less than 1 Kelvin, mainly due to the reduction of phonon-induced decoherence (see Paper 7).

Random energy-level shifts due to a dynamically varying crystal environment is another source of decoherence. This type of decoherence is called spectral diffusion. Spectral diffusion is time-dependent and, in many cases, may be reduced with an applied magnetic field [57, 89]. For example, host spin-spin energy exchange leads to magnetic field variations adjacent to a rare-earth ion, creating spectral diffusion. Application of a magnetic field renders a rare-earth ion to have a strong magnetic moment that detunes nearest spins from each other and others in the surrounding lattice, reducing spectral diffusion. This is called the frozen core effect. Spectral diffusion may be further minimized by choosing host materials in which all host atoms have small or zero nuclear magnetic moments, e.g. silicates such as Y_2SiO_5 [89].

At 3 Kelvin, measurements using our Tm^{3+}:$LiNbO_3$ waveguide show ∼MHz linewidths at time delays of a few ms [91]. The impact of spectral diffusion is reduced at temperatures less than 1 Kelvin, giving homogeneous linewidths of ∼50 kHz at ms time delays under similar conditions [94].

Another mechanism known to broaden homogeneous lines is called instantaneous, or excitation-induced, spectral diffusion (ISD or EID) [95]. This occurs when an ion changes state via optical excitation or decay, which in turn changes their electric dipole moment. Consequently, the electric or magnetic environment experienced by neighbouring ions will change, leading to a shift of the resonance frequency of these ions. To limit the effects of instantaneous spectral diffusion, one may decrease the dopant concentration in the crystal, thus increasing the average distance between the rare-earth ions. It is important that spectroscopic measurements and preparation of quantum memories should employ the lowest power feasible to reduce the impact of ISD [96].

4.2.2 Inhomogeneous broadening

Rare-earth ions reside in different local crystalline environments due to lattice imperfections and strain. Consequently, each rare-earth ion experiences (unique) local fields, leading to a fixed shift of the resonance frequency of an ion. For an ensemble of rare-earth ions, this variation in resonance frequency from ion-to-ion leads to inhomogeneous broadening of an absorption line [57]. Since the position of, and perturbation due to, each defect can vary randomly, there are generally no spectral correlations between ions that reside at two different locations in the crystal. However specialized growth techniques, e.g those aiming at producing stoichiometric compositions, can reduce the number of defects, resulting in very high spectral densities [89].

At cryogenic temperatures, the homogeneous broadening is much smaller than the inhomogeneous broadening, thus the absorption profile can be seen as the sum of the

homogeneously broadened lines of the individual ions. See Fig. 2.1. A distinguishing and attractive feature of rare-earth-ion doped crystals is the ability to have both inhomogeneous and homogeneous broadening. Inhomogeneous broadening, in conjunction with a photon-echo protocol, allows wide-band photons to be absorbed and emitted, while narrow homogeneous linewidths provide good coherence properties to develop efficient and long-lasting memories.

In rare-earth crystals with a low doping concentration, the inhomogeneous widths of absorption lines are generally a few GHz, but can range from $\sim$10 MHz up to hundreds of GHz depending on the crystal [89]. Measurements have shown the inhomogeneous line of the $^3H_6$ to $^3H_4$ transition of our waveguide to be $\sim$1 THz [91]. This is due to both the nature of the crystal, and the relatively large ion doping concentration of 0.7%. We note that other rare-earth transitions, such as hyperfine transitions, can be inhomogeneously broadened [57]. This broadening may impact the ability to efficiently optically pump ions, or reduce the efficiency of protocols that rely on spin-state mapping [61]. Spin inhomogeneous broadening in our waveguide has been shown to be up to 1/2 of the difference between the Zeeman splittings in the excited state and the ground state [94].

Chapter 5

This thesis

The aim of this chapter is to briefly summarize, and describe my contribution to, each of the papers presented in the Appendix to this thesis. These papers encompass my thesis work.

One of the objectives of my Ph.D. research, and that of my supervisor and other group members, is to experimentally develop a functional quantum repeater. To this end, one of our goals is to develop workable quantum memories. Our quantum memories are based on rare-earth-ion doped materials cooled to cryogenic temperatures. Moreover, we are interested in developing rare-earth-ion doped materials for other quantum signal processing tasks such as QND measurements. My primary contribution was to develop quantum memories and signal processing devices using Tm^{3+}:$LiNbO_3$ waveguides. This material was used for all experiments described in the papers attached to this thesis. My specific contributions to each paper are mentioned in italic font.

5.1 Summary of papers

Paper 1 – We describe a new quantum repeater architecture based on spectral multiplexing. This quantum repeater design lays the foundation for work described in papers 2-4 and is closely-related with the work described in papers 5-7. This paper also introduces how quantum memories operating as delay lines (not on-demand) are sufficient for quantum repeaters provided another degree-of-freedom (we use the example of frequency) is utilized for qubit mode-mapping. Frequency is chosen here not only for technical reasons, but also because this approach exploits the broad inhomogeneous lines

of rare-earth-ion-doped crystals. To show how a quantum memory is interfaced with our spectrally-multiplexed repeater, we demonstrate high-fidelity storage and retrieval of 26 spectrally multimode qubits. The fidelity measurement utilizes decoy states, a commonly employed approach in QKD. This method is a new and resourceful way to characterize the behavior of a memory if single photons are not available or less practical to employ. *My contribution involved the co-development of initial theoretical ideas concerning spectral multiplexing and quantum memories, formulation of the measurements, design and development of the experiment, implementation of the measurements, and analysis and interpretation of the results. Concerning the manuscript, I wrote its first draft, edited it in conjunction with all other co-authors, and managed the editing, submission and publishing steps.*

Paper 2 – We demonstrate high-fidelity storage and retrieval of a qubit encoded into a single photon generated from a photon pair source. Our measurement is conditional on detection of the other member of the pair, thus is closely related to the heralding required for a quantum repeater. It is important to show that photon pairs can be interfaced with (rare-earth-ion-doped) quantum memories as it is a necessary building-block for many quantum repeaters. *Along with some co-authors, I focused on the development of the quantum memory experimental setup and its interface with the photon-pair source. I also participated in the troubleshooting of the photon-pair source and photon-detection apparatus. I, along with other co-authors, developed and performed the measurements and analysis, and wrote the manuscript.*

Paper 3 – We extend the experiment of Paper 2 to storage and retrieval of a photon from an entangled pair. This experiment is of both fundamental and practical importance. We demonstrate that, within uncertainty, no decoherence of quantum information is introduced by the quantum memory during storage. This is quantified by measuring and comparing the density matrix, an invariance of an entanglement witness, and the amount

of violation of a Bell inequality before and after storage. *My contributions are similar to that described for Paper 2.*

Paper 4 – Bell-state measurements, which are needed for entanglement swapping, require two-photon indistinguishability. We show that storage and retrieval of an attenuated laser pulse (at the single photon level) does not render it distinguishable from another identically-prepared pulse. This result is stronger than simply achieving a high-fidelity memory with respect to encoded quantum information because indistinguishability concerns all degrees-of-freedom of the photon. Our result is quantified via the visibility of a Hong-Ou-Mandel interference fringe between pulses of which only one has been stored, or both have been stored, and for reference, in which both have not been stored. To verify our conclusion, we perform a high-fidelity Bell-state measurement between time-bin qubits encoded into laser pulses of mean photon number less than one, of which one qubit has been stored in the memory. *I participated in the formulation of the measurements, the design and development of the experiment, implementation of the measurements, analysis and interpretation of the results, and writing of the manuscript.*

Paper 5 – Rare-earth-ion-doped crystals can be used as both storage and processing devices. We demonstrate this possibility, with direction to integrability, using $LiNbO_3$ waveguide phase modulators operated at room temperature in conjunction with our Tm^{3+}:$LiNbO_3$-based AFC quantum memory at cryogenic temperatures. Using laser pulses attenuated to the few photon level, we perform tasks such as pulse sequencing, time-to-frequency multiplexing and demultiplexing, splitting, interference, temporal and spectral filtering, compressing and stretching as well as selective delaying. *I engaged in the formulation of the initial theoretical ideas and measurements, development of the experiment, implementation of the measurements, analysis of the results, and writing of the manuscript.*

Paper 6 – Towards another hybrid memory-processor device, we both propose and im-

plement an experiment showing a cross-phase modulation between a signal qubit and a probe pulse, which is stored and retrieved from a quantum memory. Although performed with strong pulses, this experiment lays the groundwork for implementing qubit QND for photons using a solid-state device. The approach is general for rare-earth-ion-based quantum memories, however its possibility for single-photon level implementation relies on the unique properties of both Tm:$LiNbO_3$ and the waveguide dimensions. *My contribution concentrated on leading the experimental effort. This includes the formulation of theoretical ideas into measurements, design and development of the experiment, performing the measurements, and the analysis and interpretation of the results. I also participated in the writing and publication steps of the manuscript.*

Paper 7 – Spectroscopic properties of a material dictate its suitability and performance for quantum information applications such as quantum memory. This work quantifies important parameters such as the optical coherence lifetime, sub-level lifetime, and the magnitude of the transition dipole moment all of which strongly govern the magnitude of cross-phase modulation for Tm^{3+}:$LiNbO_3$-based QND measurements. The aforementioned properties of our waveguide exceed those measured at 3 K, and match or surpass those measured in both a non-waveguiding Tm:$LiNbO_3$ crystal at temperatures less than 1 Kelvin and other rare-earth-ion-based waveguides. *I led the development of all aspects of the paper. With help from other co-authors, I formulated the initial idea, developed the experiment, performed the measurements, analyzed the results, and wrote the manuscript.*

Chapter 6

Outlook

The work described in my thesis marks a significant advance in the development of quantum repeaters, quantum memories, signal processors and other quantum light-matter devices. Yet substantial theoretical and experimental work remains before these applications can be used in practice.

For our quantum repeater application, ideal single-pair entangled photon sources have to be used if resources should remain reasonable [97]. Emitters, such as those based on parametric down-conversion or four-wave mixing, are convenient for initial demonstrations, but introduce multi-photon events that reduce fidelities [98]. Some promising pair-sources that would be suitable in this regard rely on quantum dots [99] or QND devices in conjunction with spontaneous emitters. However, these pair sources have yet to show other important attributes such as high efficiencies and wavelength compatibility with respect to other devices that comprise quantum repeaters [88]. Concerning quantum memories, further testing and development of rare-earth-ion-doped crystals is needed to identify candidate materials that offer narrow homogeneous linewidths, suitable and long-lived hyperfine levels, low spectral diffusion, and broad inhomogeneous lines suitable for spectral multiplexing. The recently-investigated Tm^{3+}:$Y_3Ga_5O_{12}$ crystal may be a promising candidate [100, 101]. Efficient repeater components with increased multiplexing capacities must also be developed. Memory efficiencies must be enhanced; for example using impedance-matched cavities [83, 84]. However, these cavities must be compatible with the multiplexing employed, and may be challenging to implement in waveguides due to propagation loss. The Bell-state measurement efficiency can be increased if implemented through controlled-phase quantum gates [3] or auxiliary photons [102]. Gates

could be implemented using optical-to-microwave conversion protocols, thereby benefiting from superconducting quantum circuits [103, 104]. Increased multiplexing requires advanced mode discriminators and qubit-mode shifting techniques. Spectrally-multiplexed multimode detection could be accomplished with wavelength-division multiplexers, although devices that feature memory-compatible (narrow-band) channel widths are not currently employed in industry [19]. Temporal or spatial qubit mode translation could be accomplished by micro-electrical-mechanical switch array technology [105].

Pertaining to our QND application, the greatest challenge is to increase the magnitude of the phase shift per photon without destroying the signal qubit. First, the resolution of our measurement needs to be improved to the standard quantum (shot-noise) limit [74]. Towards this end, classical phase noise, mostly due to laser phase noise on timescales of the storage time and electronic noise of the detector, must be eliminated. The impact of technical noise of the laser may be reduced with frequency stabilization and possibly using shorter memory storage times. Once operating at the shot-noise limit, phase resolution is governed by the number of photons contained within the probe. This cannot be increased arbitrarily as considerations such as total number of atoms, scattering-induced heating, or spontaneous-emission noise may become relevant. Second, the magnitude of the cross-phase modulation must be increased. A significant improvement would be achieved by decreasing the interaction area, i.e. the transverse mode volume of the signal and probe light, to the limit dictated by the optical wavelength of $\sim$1 μm. This is possible with precision fabrication techniques such as ion-beam milling [107] or femtosecond laser writing [108]. The interaction strength also benefits from a large ratio of radiative to homogeneous linewidth. Moreover, loss of the signal must be avoided. Off-resonant absorption of the signal by the memory can be avoided by significantly detuning the signal. The ensuing reduction in cross-phase shift must in-turn be compensated by a signal multi-pass configuration. We predict that with the aforementioned improvements,

the phase shift per photon will be of order 10^{-4} radians, which would allow single-shot detection of individual photons [106] (see Paper 6).

More generally, we must explore ways to improve device performances, e.g. with new protocols or systems, but also consider the possibility that a quantum device will never achieve its desired performance. Since advanced quantum applications will be comprised of multiple components, it is likely that certain devices will need to compensate for the drawbacks of others; perhaps resulting in a trade-off of overall performance [109]. Consequently, much work needs to be done towards developing both new approaches and optimizing a system's performance given the limitations of the devices available. As many of these limitations are technical or system-specific, such details may be known only by specialists. Hence, the described optimization problem is challenging and possibly even open-ended.

Partially fuelled by the growing need of a connected society, further research of quantum-enabled networks and technologies sets the stage for a bright future of both fundamental and practical discoveries. This research will bring together scientists, engineers, those in governments and industry, and researchers in other disciplines; likely generating new opportunities, ideas, and avenues for innovation, while simultaneously garnering public awareness of the exciting natural world at the quantum level.

Bibliography

[1] L. Cormack and A. Ede. A History of Science in Society: From Philosophy to Utility. University of Toronto Press, Higher Education Division (2012).

[2] Quantum Information. Nature. [accessed 2016 March]. http://www.nature.com/subjects/quantum-information.

[3] M. Nielsen and I. L. Chuang. Quantum Computation and Quantum Information. Cambridge (2000).

[4] J. Brendel, N. Gisin, W. Tittel, and H. Zbinden, Phys. Rev. Lett. 82, 2594 (1999).

[5] S. L. Braunstein and P. van Loock, Rev. Mod. Phys. 77, 513 (2005).

[6] A. Einstein et al., Phys. Rev. 47, 777 (1935).

[7] R. Horodecki et al., Rev. Mod. Phys. 81, 865 (2009).

[8] R. Rivest et al., Communications of the ACM 21, 120 (1978).

[9] P. W. Shor, Algorithms for quantum computation: discrete logarithms and factoring. in Proc. 35th Ann. Symp. Found. Comp. Sci. (ed. Goldwasser, S.) 124 (1994).

[10] C. H. Bennett, and G. Brassard, 1984, in Proceedings of the IEEE International Conference on Computers, Systems and Signal Processing, Bangalore, India, (IEEE, New York), pp. 175.

[11] N. Gisin et al., Rev. Mod. Phys. 74, 145 (2002).

[12] F. Miller, Telegraphic Code to Insure Privacy and Secrecy in the Transmission of Telegrams. New York: Charles M. Cornwell (1882). G. S. Vernam, Journal of the IEEE 55, 109 (1926).

[13] H.-K. Lo et al., Nat. Photon. 8, 595 (2014).

[14] A. K. Ekert, Phys. Rev. Lett. 67, 661 (1991).

[15] N. Jain et al., Contemporary Physics (2016).

[16] See for example, id Quantique, MagiQ, QuintessenceLabs, and SeQureNet.

[17] Y.-L. Tang et al., Phys. Rev. Lett. 114, 069901 (2015).

[18] S. Wang et al., Optics Express 22, 21739 (2014).

[19] G. Keiser. Optical Fiber Communications. McGraw-Hill Education (2010).

[20] A. I. Lvovsky et al., Nat. Photon. 3, 706 (2009).

[21] W. K. Wootters, and W. H. Zurek, Nature 299, 802 (1982).

[22] V. Scarani et al., Rev. Mod. Phys. 77, 1225 (2005).

[23] H. Briegel et al., Phys. Rev. Lett. 81, 5932 (1998).

[24] N. Sangouard et al., Rev. Mod. Phys. 83, 33 (2011).

[25] B. Julsgaard et al., Nature 432, 482 (2004).

[26] K. Hammerer et al., Rev. Mod. Phys. 82, 1041 (2010).

[27] K. Heshami et al., Journal of Modern Optics 63, S42 (2016).

[28] C. H. Bennett et al., Phys. Rev. Lett. 70, 1895 (1993).

[29] D. Bouwmeester et al., Nature 390, 575 (1997).

[30] M. Zukowski et al., Phys. Rev. Lett. 71, 4287 (1993).

[31] C. Simon et al., Phys. Rev. Lett. 98, 190503 (2007).

[32] N. Sinclair et al., Phys. Rev. Lett. 113, 053603 (2014).

[33] C. Bennett et al., Phys. Rev. A 53, 2046 (1996).

[34] C. Bennett et al., Phys. Rev. Lett. 76, 722 (1996).

[35] W. J. Munro et al., Nat. Photon. 6, 777 (2012).

[36] K. Azuma et al., Nat. Communications 6, 6787 (2014) and references therein.

[37] S. Muralidharan et al., Scientific Reports 6, 20463 (2016) and references therein.

[38] M. Takeoka et al., Nat. Communications 5, 5235 (2014).

[39] S. Pirandola et al., arXiv:1510.08863 (2015).

[40] N. Gisin and R. Thew, Nature Photonics 1, 165 (2007).

[41] H. J. Kimble, Nature 453, 1023 (2008).

[42] L. Duan et al., Nature 414, 413 (2001).

[43] P. M. Ledingham et al., Phys. Rev. Lett. 109, 093602 (2012).

[44] C. Simon et al., Euro. Phys. J. D 58, 1 (2010).

[45] F. Bussières et al., J. Mod. Opt. 60, 1519 (2013).

[46] J. Nunn et al., Phys. Rev. Lett. 110,133601 (2013).

[47] S. Massar and S. Popescu, Phys. Rev. Lett. 74, 1259 (1995).

[48] J. L. OBrien et al., Nat. Photon. 3, 687 (2009).

[49] M. Hosseini et al., Nature 461, 241 (2009).

[50] D. Chang et al., Nat. Photon. 8, 685 (2014).

[51] N. Kalb et al., Phys. Rev. Lett. 114, 220501 (2015).

[52] A. Feizpour et al., Nature Physics 11, 905 (2015).

[53] N. Imoto et al., Physical Review A, 32, 2287 (1985).

[54] P. Grangier et al., Nature 396, 537 (1998).

[55] K. Boone et al., Phys. Rev. A 91, 052325 (2015).

[56] D. Allen and J. Eberly. Optical resonace and two-level atoms. Wiley, New York (1975).

[57] R. M. Macfarlane and R. M. Shelby in: A.A. Kaplyanskii, R.M. Macfarlane (Eds.), Spectroscopy of Solids Containing Rare Earth Ions, North-Holland, Amsterdam (1987).

[58] W. E. Moerner et al., Persistent spectral hole-burning: Science and applications, Moerner, W. E. (Ed.), Springer-Verlag, Berlin (1988).

[59] T. Böttger, Ph.D. Thesis, Montana State University (2002).

[60] S. Hastings-Simon, Ph.D. Thesis, University of Geneva (2008).

[61] M. Nilsson et al., Phys. Rev. B 70, 214116 (2004).

[62] W. Tittel et al., Laser Photon. Rev. 4, 244 (2009).

[63] A. Szabo, Frequency selective optical memory, U.S. Patent No. 3,896,420 (1975).

[64] U. Kh. Kopvillem and V. R. Nagibarov, Fiz. Metall. Metalloved 2, 313 (1963).

[65] N. A. Kurnit et al., Phys. Rev. Lett. 13, 567 (1964).

[66] J. Ruggiero et al., Phys. Rev. A 79, 053851 (2009).

[67] N. Sangouard et al., Phys. Rev. A 81, 062333 (2010).

[68] M. Afzelius et al., Phys. Rev. A 79, 052329 (2009).

[69] S. E. Harris et al., Phys. Rev. A 46, R29(R) (1992).

[70] A. E. Kozhekin et al., Phys. Rev. A 62, 033809 (2000).

[71] J. Nunn et al., Phys. Rev. A 75, 011401(R) (2007).

[72] A. L. Alexander et al., Phys. Rev. Lett. 96, 043602 (2006).

[73] G. Hétet et al., Phys. Rev. Lett. 100, 023601 (2008).

[74] P. Meystre and M. Sargent, Elements of Quantum Optics, Springer-Verlag (1989).

[75] J. Nunn et al., Phys. Rev. Lett. 101, 260502 (2008).

[76] Z. Xu et al., Phys. Rev. Lett. 111, 240503 (2013).

[77] P. Jobez et al., Phys. Rev. Lett. 114, 230502 (2015).

[78] D. G. England et al., Phys. Rev. Lett. 114, 053602 (2015).

[79] K. F. Reim et al., Nat. Photon. 4, 218 (2010).

[80] D.J. Saunders et al., Phys. Rev. Lett. 116, 090501 (2016).

[81] B. Kraus et al., Phys. Rev. A 73, 020302 (2006).

[82] Y.-W. Cho et al., Optica 3, 100 (2016).

[83] M. Afzelius et al., Phys. Rev. A 82, 022310 (2010).

[84] S. A. Moiseev et al., Phys. Rev. A 82, 022311 (2010).

[85] H. de Riedmatten et al., Nature 456, 773 (2008).

[86] H. Sõnajalg and P. Saari, J. Opt. Soc. Am. B 11, 372 (1994).

[87] Z.-Q. Zhou et al., Phys. Rev. Lett. 108, 190505 (2012).

[88] J.-S. Tang et al., Nat. Commun. 6, 8652 (2014).

[89] G. Liu and B. Jacquier (Eds.). Spectroscopic Properties of Rare Earths in Optical Materials. Springer (2005).

[90] B. R. Judd, Phys. Rev. 127, 750 (1962).

[91] N. Sinclair et al., J. Lumin. 130, 1586 (2010).

[92] C. W. Thiel et al., J. Lumin. 130, 1598 (2010).

[93] Y. Sun et al., Phys. Rev. B 85, 165106 (2012).

[94] N. Sinclair et al., in preparation.

[95] D. R. Taylor and J. P. Hessler, Phys. Lett. A A50, 205 (1974).

[96] C. W. Thiel et al., Laser Physics 24, 106002 (2014).

[97] H. Krovi et al., Appl. Phys. B 122, 52 (2016).

[98] S. Guha et al., Phys. Rev. A 92, 022357 (2015).

[99] F. Jahnke (Ed.). Quantum optics with Semiconductor Nanostructures. Woodhead Publishing (2012).

[100] C. W. Thiel et al., Phys. Rev. Lett. 113, 160501 (2014).

[101] C. W. Thiel et al., Phys.l Rev. B 90, 214301 (2014).

[102] W. P. Grice, Phys. Rev. A 84, 042331 (2011).

[103] C. O'Brien et al., Phys. Rev. Lett. 113 (6), 063603 (2014).

[104] X. Fernandez-Gonzalvo et al., Phys. Rev. A 92, 062313 (2015).

[105] S. Crain et al., Appl. Phys. Lett. 105, 181115 (2014).

[106] V. Venkataraman et al., Nat. Photon. 7, 138 (2013).

[107] T. Zhong et al., Nat. Commun. 6, 8206 (2015).

[108] T. Calmano et al., Applied Physics B 100, 131 (2010).

[109] G. Kurizki et al., PNAS 112, 3866 (2015).

Appendix A

Paper 1

Physical Review Letters 113, 053603 (2014)

Spectral multiplexing for scalable quantum photonics using an atomic frequency comb quantum memory and feed-forward control

Neil Sinclair[1], Erhan Saglamyurek[1], Hassan Mallahzadeh[1], Joshua A. Slater[1], Mathew George[2], Raimund Ricken[2], Morgan P. Hedges[1], Daniel Oblak[1], Christoph Simon[1], Wolfgang Sohler[2], and Wolfgang Tittel[1]

[1]*Institute for Quantum Information Science, and Department of Physics and Astronomy, University of Calgary, 2500 University Drive NW, Calgary, Alberta T2N 1N4, Canada* [2]*Department of Physics - Applied Physics, University of Paderborn, Warburger Str. 100, 33095 Paderborn, Germany*

Abstract

Future multi-photon applications of quantum optics and quantum information science require quantum memories that simultaneously store many photon states, each encoded into a different optical mode, and enable one to select the mapping between any input and a specific retrieved mode during storage. Here we show, with the example of a quantum repeater, how to employ spectrally-multiplexed states and memories with fixed

storage times that allow such mapping between spectral modes. Furthermore, using a Ti:Tm:$LiNbO_3$ waveguide cooled to 3 Kelvin, a phase modulator, and a spectral filter, we demonstrate storage followed by the required feed-forward-controlled frequency manipulation with time-bin qubits encoded into up to 26 multiplexed spectral modes and 97% fidelity.

A.1 Introduction

Further advances towards scalable quantum optics [1, 2] and quantum information processing [3, 4] rely on joint measurements of multiple photons that encode quantum states (e.g. qubits) [3, 4, 5]. However, as photons generally arrive in a probabilistic fashion, either due to a probabilistic creation process or due to loss during transmission, such measurements are inherently inefficient. For instance, this leads to exponential scaling of the time required to establish entanglement, the very resource of quantum information processing, as a function of distance in a quantum relay [6]. This problem can be overcome by using quantum memories, which are generally realized through the reversible mapping of quantum states between light and matter [7, 8]. For efficient operation, these memories must be able to simultaneously store many photon states, each encoded into a different optical mode, and subsequently (using feed-forward) allow selecting the mapping between input and retrieved modes (e.g., different spectral or temporal modes). This enables making several photons arriving at a measurement device indistinguishable, thereby rendering joint measurements deterministic. For instance, revisiting the example of entanglement distribution, a quantum relay supplemented with quantum memories changes it to a repeater and, in principle, the scaling from exponential to polynomial [4, 9].

Interestingly, for such multimode quantum memories to be useful, it is not necessary to map any input mode onto any retrieved (output) mode, but it often suffices if a single

input mode, chosen once a photon is stored, can be mapped onto a specific output mode (e.g. characterized by the photon's spectrum and recall time) [4, 10]. This ensures that the photons partaking in a joint measurement, each recalled from a different quantum memory, are indistinguishable, as required, e.g., for a Bell-state measurement. We emphasize that it does not matter if the device used to store quantum states also allows the mode mapping, or if the mode mapping is performed after recall using appended devices – we will refer to the system allowing storage and mode mapping as *the memory*.

To date, most research assumes photons arriving at different times at the memory (i.e. temporal multiplexing), and recall on demand in terms of variable storage time [7, 8]. Here we show, with the example of a quantum repeater, that it is also possible to employ spectrally-multiplexed states and storage devices with fixed storage times, supplemented with frequency shifts based on feed-forward control. Furthermore, we report measurements using a highly broadband solid-state memory [11] that demonstrate the required mapping between input and output modes with time-bin qubits encoded into up to 26 spectral modes and a fidelity of 0.97, thereby significantly violating the classical bound of 2/3 [12].

It is worth noting that for applications requiring short storage times, such as in linear optics quantum computing, a low-loss fibre could be sufficient to delay photons until a feed-forward signal arrives. However, for applications, such as a quantum repeater, in which storage times exceed around 10 μs, fibre transmission drops below 90% and hence quantum state storage based on light-matter interaction will be necessary. Additionally, light-matter interaction affords more flexibility to perform processing tasks other than delaying [13].

Much theoretical and experimental work aiming at the development of quantum memory has been reported over the past decade [7, 8, 14], and most criteria required for such a memory to be suitable for the aforementioned applications have been independently

met. However, at most two (entangled) qubits have been stored simultaneously in a way that allowed selecting the mode mapping [15], and the scalability of the approach, which relied on encoding information into four spatial modes, to tens or hundreds of qubits and modes remains to be proven (we note related work by Lan et al. [16] that, however, is not based on memories as defined above).

Rare-earth-ion doped crystals cooled to cryogenic temperatures have demonstrated to be promising storage materials, and many benchmark results have been reported [11, 17, 18, 19, 20, 21, 22]. We emphasize that, when such crystals are used in conjunction with the atomic frequency comb (AFC) protocol, the independence of the multimode (i.e. multi-photon) capacity on optical depth constitutes an important advantage compared to other protocols [23]. However, choosing the time of recall using control lasers to perform the mode mapping in the storage device is challenging with an AFC memory [21, 23].

Drawing from the well-known temporal multiplexing approach, Fig. A.1 shows, with the example of a quantum repeater, how spectrally multimode quantum memories, including frequency shifters and filters, allow rendering photons indistinguishable without the need for a variable storage time. While a repeater that employs temporal multiplexing assumes all qubits to feature the same spectrum but to arrive at different times at the memory, our new approach assumes all qubits to arrive at the same time, but to feature distinct spectra (i.e. to be encoded into different frequency bins). The retrieval of a desired qubit at a given time and with a given spectrum can then be achieved by retrieving all qubits after the same storage time, selecting the shift of the spectra of all qubits such that the desired qubit occupies a previously agreed-upon frequency bin, and rejecting all other qubits using a filtering cavity. To quantify the performance of a quantum repeater based on spectral multiplexing, we calculate the average rate of successful distributions of entangled photon pairs over a lossy channel as a function of total distance. The results, shown in Fig. A.2, show that useful performance can already be achieved with 100

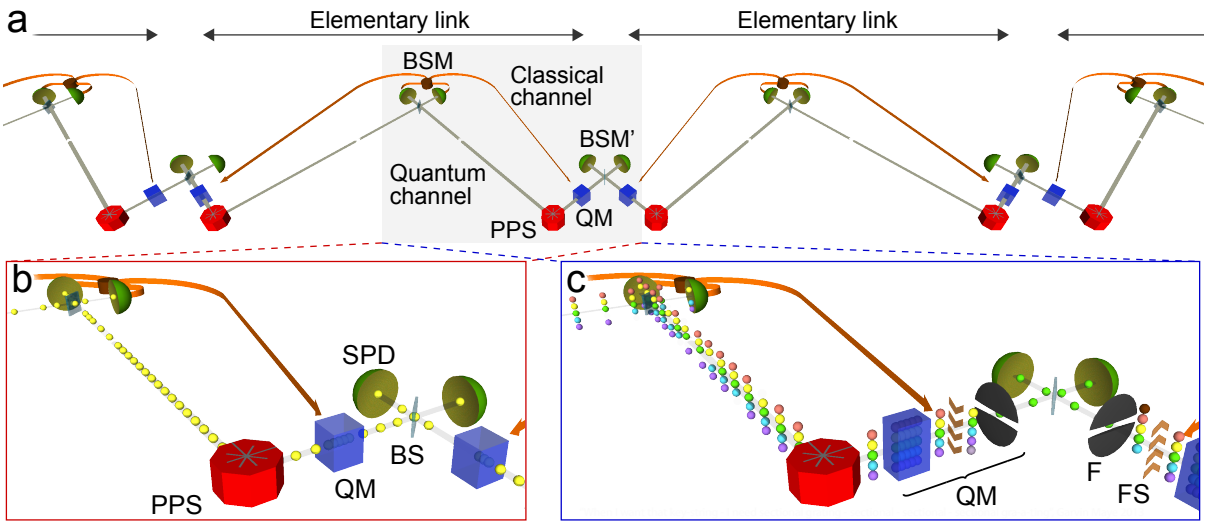

Figure A.1: Quantum repeater. **a**, Block diagram of a section of a quantum repeater that does not employ qubit multiplexing. A source generating entangled pairs of photons (PPS) is located at the end-point of each elementary link (i.e. node). One member per pair is stored in a quantum memory (QM), and the second member is sent over a 'quantum channel' to the centre of the link where it meets a member of an entangled pair generated at the other end of this link. The two photons' joint state undergoes a Bell-state measurement (BSM) – comprised of a beam splitter (BS) and two single photon detectors (SPDs), and the result is communicated over a 'classical channel' back to the end-points to herald the establishment of entangled quantum memories by means of entanglement swapping [4, 9, 24]. Entanglement is stored until the two memories that are part of an adjacent link, are also entangled. Then, photons are recalled from neighboring memories and subjected to BSM'. This results in the establishment of entanglement across the two links, and, by continuing this procedure with other links, entanglement is established between the end-points of the entire channel. **b (c)**, Operation of a repeater node assuming temporal (spectral) multiplexing. Members of entangled photon pairs, each featuring the same spectrum (temporal profile and arrival time) but separated in time (frequency), are simultaneously stored in multimode quantum memories. A heralding (feed-forward) signal, derived from a successful BSM at the centre of each elementary link, indicates which of the stored photons is to be used for the remaining step of the protocol. The heralded photons are then recalled from adjacent memories such that they arrive indistinguishably at the BSM'. For temporal multiplexing, memories that allow adjusting the recall time as well as time-resolved detection are required, while for spectral multiplexing, the memories must incorporate adjustable frequency shifts (FS) and spectral filtering (F), and the BSM must distinguish different frequency bins.

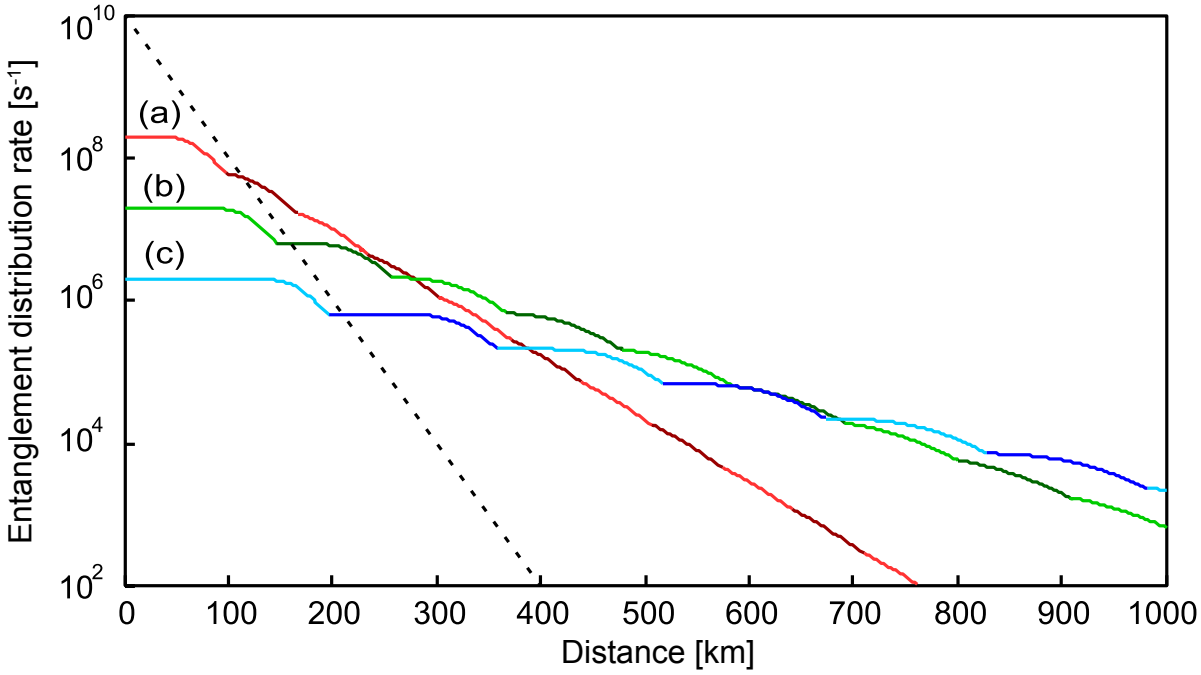

Figure A.2: Simulation of spectrally multiplexed quantum repeater performance. Optimal average entanglement distribution rate as a function of total distance. We assume loss of 0.2 dB/km, maximally entangled photon pairs emitted with 90% probability per attempt, quantum memories with 90% efficiency and total storage bandwidth of 300 GHz, and single-photon detectors with 90% efficiency and negligible dark counts. Bi–coloured curves – where a change in shading indicates the addition of an elementary link – represent **(a)** 10^2 (shown in red), **(b)** 10^3 (shown in green), and **(c)** 10^4 (shown in blue) spectral modes. The dotted line represents the direct transmission of members of entangled photon pairs produced at 10 GHz.

spectral modes, which is clearly feasible in near future. Further information regarding the derivation of these results, and comparison with the temporal multiplexing scheme are contained in the Supplemental Material.

A.2 Experiment and Results

Conjecturing similarly promising results for other multi-photon applications, we now experimentally characterize the feasibility of multimode storage and feed-forward-controlled read-out in the frequency domain. A schematic of our setup is depicted in Fig. F.2. It

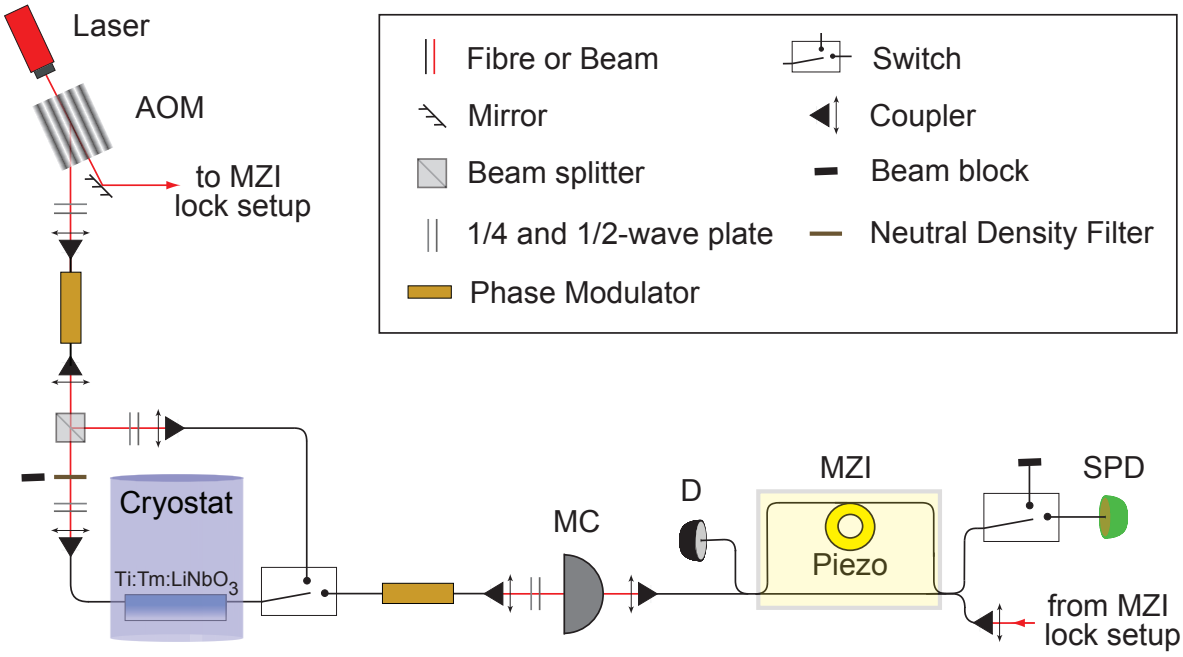

Figure A.3: Schematics of the experimental set-up. The output of a frequency-stabilized continuous-wave laser at 795.4 nm wavelength is amplitude modulated with an AOM and serrodyne chirped [26] over disjoint frequency intervals using a phase modulator (PM). During 5 ms the laser light creates a broadband multimode AFC (see Fig. A.4) in a Tm:Ti:$LiNbO_3$ waveguide located inside a 3 Kelvin cryostat and exposed to a magnetic field of 88 Gauss [11, 25]. After a 2 ms wait time, during the next 5 ms, the AOM generates, with 4 MHz repetition rate, up to 26 spectrally multiplexed pairs of 15 ns–long Gaussian-shaped pulses (pulses in the pairs are separated by 20 ns), whose relative phases and central frequencies are set using the PM. The subsequent attenuator, or beam block, reduces the mean number of photons per pulse pair to 0.5, 0.1, or zero, respectively. The resulting time-bin qubits are then sent into the waveguide, and stored for 60 ns. Frequency-selective recall is achieved by means of a second PM, combined with a monolithic cavity (MC) having 70 MHz line-width [27]. Finally, the recalled photons are detected using a Si-avalanche photodiode-based single photon detector (SPD) (allowing projections onto $|e\rangle$ and $|l\rangle$), or a phase-stabilized Mach-Zehnder interferometer (MZI) followed by a SPD (allowing projections onto $\frac{1}{\sqrt{2}}\big(|e\rangle \pm |l\rangle\big)$).

performs four tasks: First, to prepare the memory, laser light is temporally and spectrally modulated, and then sent into a Ti:Tm:$LiNbO_3$ waveguide [11, 25], thus spectrally tailoring the inhomogeneous absorption line of thulium into a series of equally-spaced absorption peaks – an AFC. For multimode storage, the preparation procedure is repeated at different detunings with respect to the original laser frequency, resulting in twenty-six, 100 MHz-wide AFC's that are, with the exception of the region around zero detuning, spectrally separated by 200 MHz gaps (see Fig. A.4). Second, our setup simultaneously generates many time-bin qubits of the form $|\psi\rangle = \alpha|e\rangle + \beta|l\rangle$, encoded into single-photon-level, phase randomized laser pulses of different intensities, in up to 26 frequency bins. Here, $|\alpha|^2 + |\beta|^2 = 1$, and $|e\rangle$ and $|l\rangle$ describe early or late emitted laser pulses, respectively. Third, the qubits are sent into the waveguide memory, where the absorption of each photon occupying a specific frequency bin leads to a collective excitation shared by the atoms forming the corresponding AFC. After a preset storage time $T_s = 1/\Delta$ (where Δ is the AFC peak spacing), the photons are emitted in their original state and spectral mode [23]. For selecting the recalled mode, the spectra of all simultaneously recalled photons are frequency shifted using another phase modulator [26], and all but the desired photons are rejected using a filter cavity with fixed resonance frequency [27]. Finally, projection measurements onto time-bin qubit states $|e\rangle$ or $|l\rangle$, or $(|e\rangle \pm |l\rangle)/\sqrt{2}$ are performed. As we describe in detail in the Supplemental Material, we post-process the measured data to assess a key figure of merit – the lower bound on the storage fidelity $\mathcal{F}_L^{(1)}$ – only from laser pulses containing exactly one photon. This procedure justifies the use of attenuated laser pulses instead of single photons to encode qubits for the purpose of our investigation. Further details about the AFC preparation, qubit generation, measurements and fidelity calculations, as well as current limitations resulting in a 1.5×10^{-4} overall memory efficiency are contained in the caption of Fig. F.2 and the Supplemental Material.

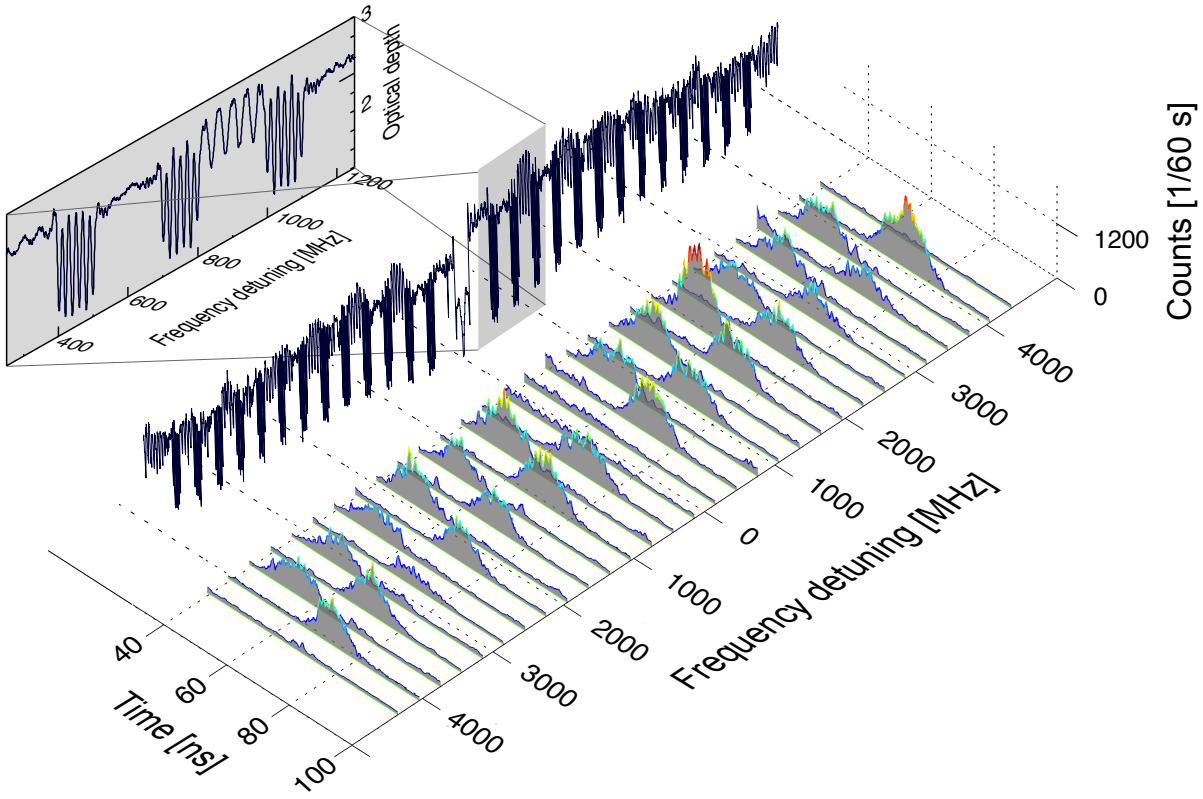

Figure A.4: Multimode storage and frequency selective recall. Histogram of arrival times of 26 simultaneously stored qubits, each containing 0.5 photons on average. Qubits are prepared in separate spectral modes and alternating temporal modes (i.e. $|e\rangle$ and $|l\rangle$), and are each recalled individually. The cavity resonance was set to 200 MHz detuning. No recall of qubits is observed in spectral modes at ± 150 and ± 4350 MHz detunings where no AFCs were prepared. The back panel and inset show the multi-binned AFC absorption profile utilized. Modulation outside of the individual combs is due to higher order effects from the phase modulation.

In the first experiment we simultaneously store 26 qubits, alternating between $|e\rangle$ and $|l\rangle$, each prepared in one of the 26 spectral bins containing AFCs. All qubits are recalled after 60 ns, and subsequently frequency shifted and spectrally filtered. Fig. A.4 shows histograms of detections as a function of time for 30 different frequency shifts, for which the cavity filtering is expected to select the recall of at most one qubit. Our results indicate that, with little cross-talk from the directly neighboring frequency bins, we can simultaneously store many qubits featuring disjoint spectra, and recall each qubit individually. We note that the total storage bandwidth of Tm:$LiNbO_3$ exceeds 300 GHz [28], which, in principle, allows expanding the current AFC to comprise more than 1000 spectral bins.

Next, to further examine the effect of cross-talk between spectral modes, we first store and retrieve a 'test' qubit prepared in $|l\rangle$ in the spectral bin having 1350 MHz detuning (with vacuum in all other spectral bins). We shift the test qubit into cavity resonance, and measure the probability to detect it in an early or a late temporal mode, which allows calculating the fidelity $\mathcal{F}_l$ of the recalled state with the input state (here and henceforth, the subscript index indicates the qubit's originally prepared state). We then increase the number of simultaneously stored qubits by creating them in neighboring spectral bins, and repeat the fidelity measurement with the test qubit. Note that all additional qubits are prepared in the orthogonal $|e\rangle$ state, such that the reduction of the fidelity of the test qubit due to cross-talk is maximized. The result, further described in the Supplemental Material, shows that cross-talk (due to the Lorentzian-shaped cavity resonance line) is restricted to qubits separated by at most two frequency bins.

Finally, we quantify the storage and recall fidelity for arbitrary qubit states stored in the AFC with multiple spectral bins shown in Fig. A.4. Supported by the previous result, we create and simultaneously store time-bin qubits prepared in five spectral bins located between 750 and 1950 MHz detuning. A test qubit in state $|\psi\rangle \in [|e\rangle, |l\rangle, \frac{1}{\sqrt{2}}(|e\rangle +$

Photon input	$\mathcal{F}_{e/l}$	$\mathcal{F}_{+/-}$
$\mu = 0.5$	$(94.67 \pm 0.43)\%$	$(94.52 \pm 0.67)\%$
$\mu = 0.1$	$(91.56 \pm 1.35)\%$	$(85.14 \pm 2.73)\%$
$n = 1$	$(94.03 \pm 1.87)\%$	$(97.76 \pm 5.54)\%$

Table A.1: Storage and recall fidelities, $\mathcal{F}_{e/l}$ and $\mathcal{F}_{+/-}$, for test qubits encoded into attenuated pulses of mean photon number μ, and lower bounds $\mathcal{F}^{(1)}_{L,e/l}$ and $\mathcal{F}^{(1)}_{L,+/-}$ on storage and recall fidelities for qubits encoded into single-photon states ($n = 1$) derived using decoy state analysis [29]. One-standard-deviation uncertainties are calculated from statistical uncertainties of photon counts.

$|l\rangle), \frac{1}{\sqrt{2}}(|e\rangle - |l\rangle)]$ is prepared in the central bin (at 1350 MHz detuning), and, for the reason already described above, the qubits in the four neighboring bins are prepared in the orthogonal state. We set the frequency shift to recall only the test qubit, and calculate the fidelity with its original state. This measurement is performed with mean photon numbers per qubit of 0.5, 0.1 and zero. Each measurement is taken over 60 s and the cavity resonance was set to a detuning of 3 GHz.

The resulting fidelities $\mathcal{F}_{e/l}$ and $\mathcal{F}_{+/-}$, averaged over each set of basis vectors (e.g. $\mathcal{F}_{e/l} = \frac{1}{2}(\mathcal{F}_e + \mathcal{F}_l)$), for mean photon numbers of 0.5 and 0.1 are displayed in Table A.1. In addition, the table shows the lower bounds on the fidelities that we would have obtained if, with no other things changed, we had performed our experiments with qubits encoded into individual photons. These bounds, denoted by $\mathcal{F}^{(1)}_{L,e/l}$ and $\mathcal{F}^{(1)}_{L,+/-}$, are derived using a decoy state method that underpins the security of quantum key distribution based on attenuated laser pulses (further explanation of this method is found in the Supplemental Material and [29]). We find that all fidelities exceed the maximum value of 2/3 achievable using a classical memory [12]. Deviations from unity fidelity are due to the limited frequency shift efficiency of the phase modulator, limited suppression of the cavity, limited visibility and stability of the Mach-Zehnder interferometer used for certain projection measurements, and remaining laser frequency and power fluctuations.

Furthermore, the measurements with mean photon number of 0.1 are impacted by system loss and detector dark counts. Finally, by averaging the single-photon fidelities over all (properly weighted) input states, we derive our key figure of merit – the lower bound on the single-photon fidelity $\mathcal{F}_L^{(1)} = \frac{1}{3}\mathcal{F}_{L,e/l}^{(1)} + \frac{2}{3}\mathcal{F}_{L,+/-}^{(1)} = 0.97 \pm 0.04$. It exceeds the classical bound by 7.5 standard deviations, proving our memory to be suitable for applications of quantum optics and quantum information science.

A.3 Conclusion

In conclusion, we have shown for the first time that it is possible to combine the simultaneous storage of multiple qubits with feed-forward controlled mapping between input and output modes using a protocol that allows scaling the number of qubits to many hundreds. This is likely to accelerate the development of quantum repeaters, linear optics quantum computing, and advanced quantum optics experiments, in particular if our frequency-based approach is combined with multiplexing using other degrees of freedom. For instance, considering as few as 10 frequency, 10 temporal and 10 spatial modes, photons in 1000 different modes can be multiplexed, which already suffices for a quantum repeater. Or, considering 500 frequency, 10 spatial [16] and 400 temporal modes [30], one could simultaneously store 10^6 qubits. Note that any multiplexed degree of freedom can be manipulated to render photons indistinguishable – in our demonstration we used frequency.

Acknowledgment

This work is supported by Alberta Innovates Technology Futures (AITF), the National Sciences and Engineering Research Council of Canada (NSERC), the US Defense Advanced Research Projects Agency (DARPA) Quiness Program under Grant No. W31P4Q-13-1-0004, the Killam Trusts, and the Carlsberg Foundation. The authors thank T.

Chanelière for help with the laser locking system, V. Kiselyov for technical support during various stages of the experiment, and A. Lvovsky for lending us the filtering cavity.

A.4 Supplemental Material

A: Performance of spectrally multiplexed quantum repeater

In the main text we briefly described an approach to quantum repeaters based on multiplexing in the spectral domain. We consider quantum memories with pre-set storage times, as discussed in detail in the main text. In this section we will first describe our architecture in more detail and then describe some of the calculations used to generate Fig. 2 in the main text: the average rate of successful entanglement creation across a lossy quantum channel.

In our architecture there exists a lossy quantum channel with length L and loss coefficient of α. We split this channel into n *elementary links*, each of length L/n. The goal of our architecture is, first, to nearly deterministically create entanglement between the ends of each elementary link, which we will refer to as *elementary-level entanglement*, and, second, create entanglement between the ends of the entire quantum channel via entanglement swapping between the elementary links. The number of elementary links n is then optimized based on the length and loss of the channel as well as the performance of other elements used in the architecture, such as detectors and quantum memories, to maximize the rate of entanglement creation. To deterministically create elementary entanglement we place a spectrally-multimode quantum memory at each end of the elementary link, as seen in Fig. 1 of the main text. Immediately beside each quantum memory we place a source that generates two-photon entanglement in many spectral modes simultaneously (i.e. a spectrally-multimode two-photon entanglement source). Note that the two-photon entangled state in each mode is independent of all other spectral modes (e.g. the source may generate the maximally-entangled $|\psi-\rangle$ Bell state in each spectral mode: $|\Psi-\rangle = |\psi-\rangle_{\omega_1}|\psi-\rangle_{\omega_2}...|\psi-\rangle_{\omega_m}$) and that each source must use the same, pre-agreed upon, set of spectral modes. One photon from each mode on

each side of the elementary link is immediately stored in the quantum memory while the second photon of each pair travels to the centre of the elementary link.

At the centre of the elementary link is a *centre station* that attempts a Bell-state measurement (BSM) on each spectral mode, using one photon from each source. In general the BSM is probabilistic due to channel loss, limited detector efficiencies, the use of linear optics for the BSM [31] and loss in other optical elements. However, as photons were emitted in many spectral modes simultaneously, the probability that at least one mode yields a successful BSM can be made arbitrarily close to 1 given a sufficiently large number of spectral modes. In essence, a successful BSM in spectral mode j heralds elementary entanglement in mode j between the quantum memories (multiple simultaneous BSM successes are ignored for simplicity). The centre station sends a classical feed-forward signal informing the quantum memories of the spectral mode in which they now share entanglement.

Finally, to establish entanglement between the end points of the entire quantum channel, neighbouring elementary links must perform entanglement swapping, involving a BSM' at the intersection of neighbouring elementary links – where the prime serves to distinguish this BSM from the one performed at the centre station. As neighbouring links likely have elementary entanglement in different spectral modes, a frequency conversion is necessary before the entanglement swapping BSM'. Then, if the intersection of all elementary links successfully performs a BSM' (again probabilistic), entanglement is created between the end points of the quantum channel.

The calculation of the average rate of entanglement creation across the quantum channel can be broken down into three parts: The first part is to calculate the probability to create elementary entanglement across all n single elementary link, denoted P(elementary). The second part is to calculate the probability to successfully create entanglement across the entire quantum channel, denoted P(success), and the third part

is to calculate the time between successive attempts, whose inverse gives the rate of entanglement creation, denoted R(success). To begin with P(elementary), we discuss the case where all sources are probabilistic single-pair entanglement sources (e.g. a source that with probability ρ emits 1 pair of maximally entangled photons and with probability $(1-\rho)$ emits vacuum. Note that if one includes multi-pair emissions typical in entanglement sources based on spontaneous parametric downconversion, four-wave mixing, etc. then one will never create maximally entangled states across the channel. In which case, one must set some kind of tolerance on how much deviation from maximal entanglement is acceptable, such as requiring a fidelity over 90%. The operating conditions of the repeater architecture could then be optimized to meet this requirement, as done in [4] or in [32] for the closely related quantum relay.

Considering a single elementary link, using only one spectral mode, the probability of a successful BSM at the centre station is given by

$$\mathrm{P}(1 \text{ mode}) = \frac{1}{2} \times \left(\eta_{d1} \times \rho \times 10^{-\alpha L/2n}\right)^2 \quad , \tag{A.1}$$

where η_{d1} is the efficiency of the centre station's detectors, α is the loss coefficient of the channel and $L/2n$ is the length that each photon must travel. The square arises as two photons must travel $L/2n$ distance each and both must be detected. Furthermore, we have assumed that the detectors are noiseless, that the BSM is carried out with linear optics (i.e. is at most 50% successful and hence the pre-factor of $1/2$, although in principle this can be made 100% with non-linear optics), and that the visibility of the two-photon measurement is perfect.

Thus, if each source instead emits m spectral modes simultaneously, the probability that all modes result in unsuccessful BSMs is given by

$$\mathrm{P}(\text{m modes, all fail}) = \left(1 - \frac{1}{2}\left(\eta_{d1}\rho 10^{-\alpha L/2n}\right)^2\right)^m . \tag{A.2}$$

In general, an extra device to distinguish the different spectral modes (e.g. wavelength-divsion-multiplexers, highly dispersive media, etc.) has to be used and will introduce extra loss. This could be included by appropriately lowering the detection efficiencies or by including another multiplicative term (within the innermost parentheses). Then, the probability that at least one spectral mode results in a successful BSM, which creates the elementary entanglement, is

$$\text{P(m modes, not all modes fail)} = 1 - \left(1 - \frac{1}{2}\left(\eta_{d1}\rho 10^{-\alpha L/2n}\right)^2\right)^m . \tag{A.3}$$

It is clear from Eq. A.3 that by choosing the number of spectral modes m sufficiently high, one can guarantee elementary entanglement with probability approaching one on every attempt. Then, the probability that all n elementary links successfully create entanglement is

$$\text{P(elementary)} = \left(1 - \left(1 - \frac{1}{2}\left(\eta_{d1}\rho 10^{-\alpha L/2n}\right)^2\right)^m\right)^n . \tag{A.4}$$

Secondly, once all elementary links have established elementary entanglement, entanglement swapping between the links is attempted. This involves recalling photons from the memories including the frequency shifting and filtering of all but one mode with total efficiency η_{mem}, and a BSM' (50% efficiency) with inefficient detectors (with detection efficiency η_{d2}). Note that η_{mem} is defined here as the probability that a photon is stored, is retrieved at the later time and is not lost during frequency shifting and filtering. If there are n elementary links there are $(n-1)$ such entanglement swappings to perform, giving

$$\text{P(m modes, n links, all links successful \& swapped)} = \left(\frac{1}{2}\eta_{mem}^2\eta_{d2}^2\right)^{(n-1)} \times \text{P(elementary)}. \tag{A.5}$$

The entanglement is only useful if it can be recalled from the memories at the ends of the quantum channel and detected, and thus the probability, P(success), of generating

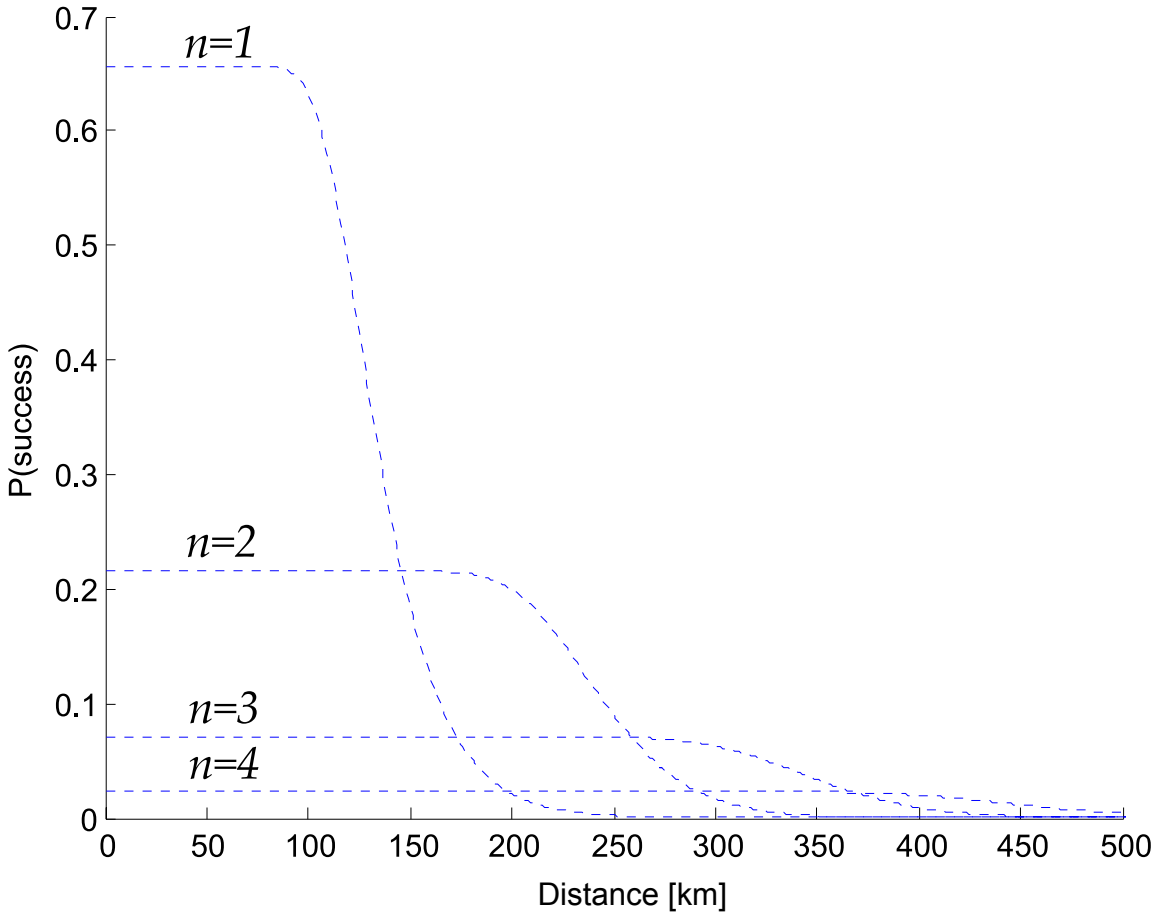

Figure A.5: The probability to create entanglement across the entire channel per attempt, P(success), as a function of total distance, for reasonable values ($m = 1000$ modes, $\eta_{mem} = \eta_{d1} = \eta_{d2} = \rho = 90\%$ and $\alpha = 0.2$ dB/km). Each curve is for a different number of elementary links $n = 1...4$.

entanglement across the entire quantum channel is given by Eq. A.5 $\times(\eta_{mem}^2\eta_{d2}^2)$ or (with minor simplification):

$$\mathrm{P(success)} = \frac{\left(\eta_{mem}\eta_{d2}\right)^{2n}}{2^{n-1}} \times \left(1-\left(1-\frac{1}{2}\eta_{d1}^2\rho^2 10^{-\alpha L/n}\right)^m\right)^n. \tag{A.6}$$

Here, P(success) has been grouped into two terms corresponding to, first, the probability to successfully swap entanglement to connect elementary links and, second, P(elementary) – the probability to create entanglement across all elementary links. It is clear that all the "loss" – or deviation from deterministic success – is contained within the the first term (connecting elementary links), while the second term is almost independent of loss, provided, again, that m is sufficiently high. This is depicted in Fig. A.5 where we plot P(success) as a function of distance for $m = 1000$ and various n. At low distance, for all n, P(success) is constant as m is high enough to keep the second term close to 1. Notice that in this flat region, for higher n, P(success) decreases. This is because using more elementary links requires more memories, detectors and BSMs, all with limited efficiency, which decreases the first term of P(success). For each n there is a distance where P(success) drops sharply, which is where the second term begins to significantly drop below 1 (i.e. m is not sufficiently large to ensure elementary entanglement). However, for larger n, this sharp decrease occurs at a larger distance. This is because for larger n (and a given total channel length L) the length of each elementary link is smaller and then P(elementary) ≈ 1. Thus, at larger distances it becomes advantageous to use more elementary links.

Lastly, we calculate the actual rate of entanglement creation R(success), which is equal to P(success) divided by the time between successive attempts. If the quantum memories are limited to storing only one qubit per spectral mode at a time, then the attempt rate would be limited by the communication time across the elementary link ($L/(nc)$, where c is the speed of light), as quantum memories cannot use their elementary

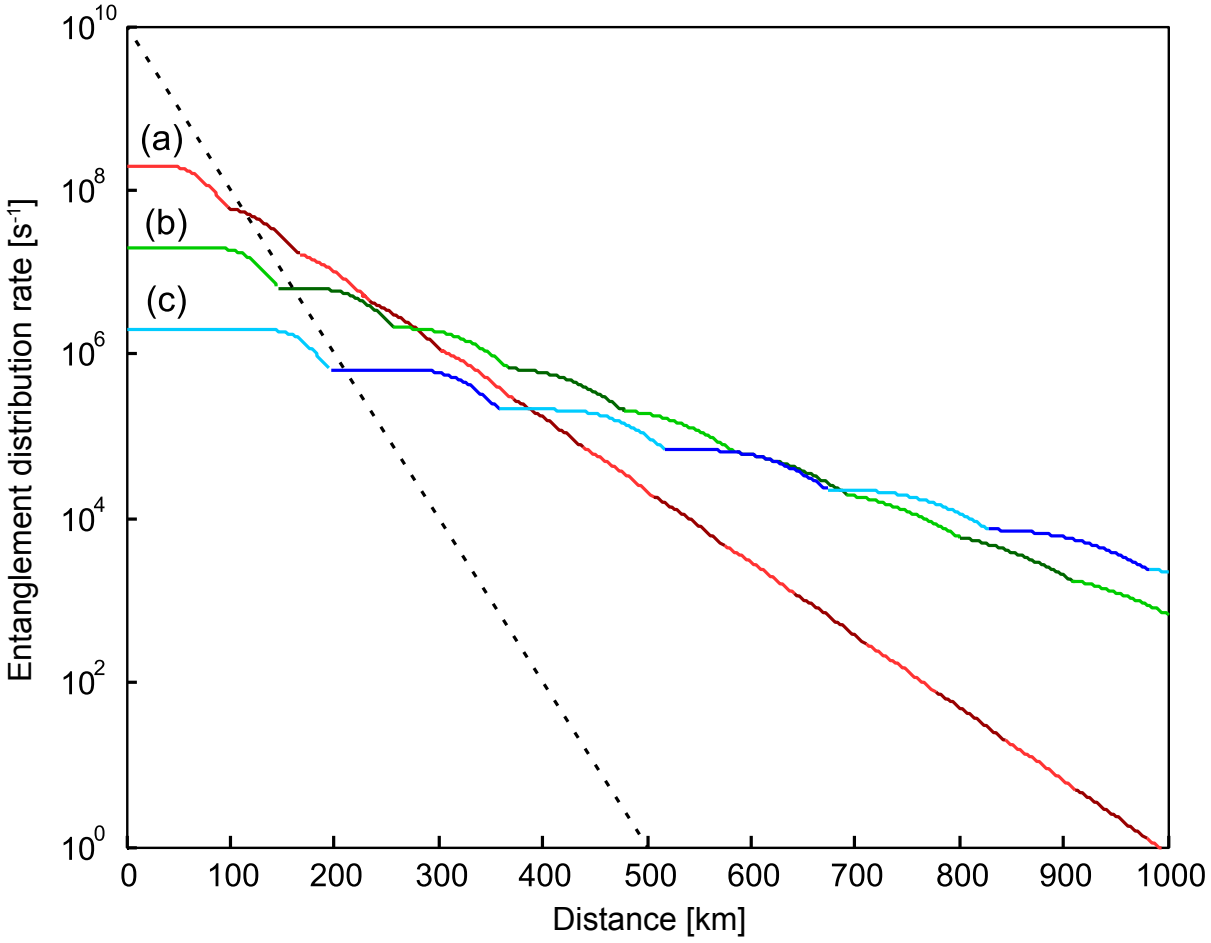

Figure A.6: R(success) as a function of total distance, for reasonable values discussed in the text. Bi-coloured curves, where a change in colour indicates that the optimal value of n has increased by one, represent (a) 10^2 (shown in red), (b) 10^3 (shown in green) and (c) 10^4 (shown in blue) spectral modes. The dotted line represents direct transmission of members of entangled photon pairs produced at 10 GHz.

entanglement until they learn the result of the BSM at the centre station. However, if the quantum memories can store many qubits in each spectral mode simultaneously (along with m spectral modes) then the attempt rate is limited by the device with the smallest operating bandwidth, assuming that all photons are Fourier-transform-limited (the spectral bandwidth of a device determines the shortest pulse duration the device can handle without loss, which determines the time between successive pulses). As optical fibre and other standard optical components already operate over many nanometers, and single-photon detectors with 10 ns recovery time have been built [33], it is reasonable to assume that quantum memories will be the bandwidth-limiting device. Assuming that quantum memories have a total bandwidth of B and, again, that m spectral modes will be used (which limits the bandwidth per mode) and allowing for a bandwidth inefficiency w as many implementations will not be able to use the entire memory bandwidth, the time between successive attempts is given by $(w \times m)/B$. Therefore,

$$\mathrm{R(success)} = \frac{B \ \times \ \left(\eta_{mem}\eta_{d2}\right)^{2n} \ \times \ \left(1 - \left(1 - \frac{1}{2}\eta_{dc}^2\rho^2 10^{-\alpha L/n}\right)^m\right)^n}{wm \times 2^{n-1}}. \tag{A.7}$$

Knowing values for all parameters we can calculate the rate of entanglement generation for any distance and any number of elementary links n. We choose the n that gives the highest rate and plot the entanglement generation rates in Fig. A.6 (identical to Fig. 2 in the main text). We have performed this optimization for $m = 100$, 1000 or 10000 spectral modes using $B = 300$ GHz (according to the zero-phonon line of a Tm:$LiNbO_3$ crystal [28]), $w = 10$, $\eta_{mem} = \eta_{d1} = \eta_{d2} = \rho = 90\%$ and $\alpha = 0.2$ dB/km. In Fig. A.6 we have also included the rate of success for direct transmission assuming a 10 GHz pulsed entanglement source. By direct transmission we specifically envisage placing a source of two-photon entanglement at one end of the quantum channel and then sending one photon from the entangled pair across the quantum channel. If the travelling photon arrives at the other end then entanglement creation has been successful. This proba-

bility is simply R(success) = R(attempt)$\times 10^{-\alpha L}$. Note that $w = 10$ is reasonable for our implementation, given that AFC with rare-earth-ion doped crystals require shelving space (in the spectral domain) for ions (roughly a factor of 2) and that time-bin qubits are composed of two temporally-separated pulses (roughly a factor of 4).

One can see that our architecture scales considerably better than direct transmission even for as little as $m = 100$ spectral modes. At shorter distances, when channel loss is minimal, one sees that the rate of success is optimized with fewer spectral modes, as this allows for a higher attempt rate (more bandwidth per spectral mode allows for shorter pulses). However, at longer distances, more spectral modes become advantageous. This is because more spectral modes allows for longer elementary links, which decreases the main source of loss – inefficient entanglement swapping between elementary links. In fact, the limited success probability for entanglement swapping between elementary links creates exponential scaling in distance for our architecture (albeit considerably better scaling than direct transmission), but this could be avoided with further advances. For instance, we assumed earlier that if elementary entanglement was established in multiple spectral modes on a single elementary link during an attempt, then only one pair was used for swapping. If every pair could be used for swapping [34] then exponential scaling could be avoided if every attempt generated many pairs of elementary entanglement per attempt, which could be achievable by increasing m.

For comparison with temporal multiplexing architecture [4], it is evident that, with ideal resources, temporal multiplexing would perform similar to spectral multiplexing. This is because given a total available bandwidth B one can subdivide it into m spectral bins and store m spectral modes of duration $t_m = m/B$ for spectral multiplexing. Conversely, one may utilize the entire bandwidth to store m pulses (temporal modes) of duration $t_1 = 1/B$ during the same time t_m for temporal multiplexing (for simplicity we have ignored the factor w, which impacts both protocols similarly). Hence, during a set

time the two approaches afford the same number of attempts to succeed at entanglement swapping at the elementary link level, and therefore feature comparable performance. Yet, this is not true any more if we take material limitations into account.

For a more realistic comparison, let us take into account two key material properties of rare-earth ion doped materials. The first is the inhomogeneous broadening of the zero-phonon line, which determines the total available bandwidth. The second is the ground level splitting, which limits the bandwidth of the individual spectral bins. Tm:$LiNbO_3$ has a particularly large inhomogeneous broadening of 300 GHz and, as shown in Fig. A.7 in the Supplemental Material, we can achieve a splitting of the Zeeman ground levels of at least 500 MHz by application of a sufficiently large magnetic field. This is more than the largest bin width of 300 MHz used in our simulations (for $m = 100$). Hence, the predicted repeater performance in the case of spectral multiplexing is not impeded by the properties of our storage material.

Realizing temporal multiplexing with recall on demand in AFC memories requires mapping of optically excited coherence onto long lived ground state coherence (often called spin-wave mapping see [35, 21, 36, 37] for recent progress). Please recall that the maximal bandwidth of a high-efficiency AFC is determined by the ground-level splitting, which is around 10 MHz in the materials used to date to implement the protocol (much less than 300 GHz, as needed for repeater performance comparable with that derived above for a spectral-multiplexing-based architecture). We point out that the value of 10 MHz is also utilized in [4] to calculate the average entanglement distribution time for a temporal multiplexing protocol with $m = 100$ modes and all other parameters as in our simulations. The simulations in [4] show that the temporally multiplexed repeater out-performs a 10 GHz direct transmission protocol at around 510 km fibre length. From Fig. A.6 in our Supplemental Material (also Fig. 2 in our main text) it is clear that our proposed architecture outperforms the temporal multiplexing scheme quite convincingly.

B: Preparation of the multimode atomic frequency comb (AFC)

Each AFC, present over the bandwidth of each spectral bin, is comprised of a periodic modulation of the optical depth composing the 795 nm, inhomogeneously broadened $^3H_6 \leftrightarrow {}^3H_4$ absorption line in Tm. It is generated by optically pumping ions to off-resonant nuclear Zeeman levels [11, 25], and from troughs in the AFC to neighbouring peaks (as we will describe below, this approach limits the efficiency of the AFC memory to approximately 17%). Optical pumping is achieved by intensity and frequency modulating laser light via an AOM and phase modulator, respectively (refer to Fig. 3 in main text). We implement frequency sweeps by driving our phase modulator with sawtooth-shaped (i.e. serrodyne) waveforms originating from a 20 GS/s arbitrary waveform generator, and simultaneously drive the AOM with a 350 MHz signal when optical pumping is desired. The memory storage time T_s is set by the AFC peak spacing $\Delta = 1/T_s$ between neighbouring teeth composing the AFC. In most experiments, the parameter Δ is set to 17 MHz, yielding 60 ns storage time. The only exception are the measurements leading to the results shown in Fig. A.7 where $\Delta = 100$ MHz, yielding $T_s = 10$ ns.

To create a multi-spectral-binned (i.e. multimode) AFC, we program the phase modulator to quickly shift the laser frequency to detunings where combs are desired and repeat the AFC preparation procedure (see Fig. 4 in the main text for the resultant absorption profile). To achieve greater contrast, and hence more efficient AFCs [23], the described preparation procedure is repeated 30 times leading to an overall optical pumping duration of 5 ms. A 2 ms wait time follows the preparation – it corresponds to 25 times the radiative lifetime of the $^3H_4$ excited level, and ensures that no luminescence masks the retrieved photons. Although a zero-phonon line of hundreds of GHz is available in Ti:Tm:$LiNbO_3$ [25, 28], our multimode AFC only takes advantage of approximately 10 GHz. This bandwidth is set by the sampling rate of our waveform generator and the operating bandwidth of our phase modulator. Referring to Fig. 4 in the main text, sig-

natures of bandwidth limitations are indicated by the generation of AFCs over intervals between desired spectral bins, which is due to higher order frequency modulations, and by reduced AFC quality at larger frequency detunings, which is due to reduced energy in the first-order modulation sideband. At the end of each multimode AFC preparation sequence we sweep the laser frequency over a 200 MHz bandwidth around zero detuning. This results in widening a spectral hole (from a linewidth of a few MHz to 200 MHz) that is created during the AFC preparation procedure. This ensures that unmodulated (i.e. zeroth order) light accompanying our multimode qubits is not temporally stretched, via interaction with the spectral hole, and produce noise counts that reduce the measured storage and retrieval fidelity of qubits.

C: Limitations to memory efficiency

The memory efficiency (i.e. the probability for a photon to be stored and recalled) is currently approximately 1.5×10^{-4}. The efficiency is determined by the transmission, or efficiency, respectively, of each element constituting our quantum memory. This includes: imperfect optical mode matching between the input and output fibres and the waveguide quantum memory, leading to a fibre-to-fibre transmission of 0.2; limited optical depth and AFC comb finesse, resulting in a probability for an incoming photon to be absorbed and re-emitted of 0.01; 50% insertion loss into our phase modulator; average efficiency of serrodyne shifting of 0.6; imperfect mode matching into and out of the filtering cavity, resulting in additional 75% loss.

To increase the total system efficiency, as required for a practical quantum memory, the following improvements can be made. First, better optical mode matching at both fibre-to-waveguide interfaces can raise fibre-to-fibre coupling in principle from 20% up to 100%. Alternatively, using bulk rare-earth-ion doped crystals and fibres with gradient-index lenses, transmission can also be raised to near unity. Second, the inser-

tion loss of our phase modulator can be overcome by integrating it with our waveguide Ti:Tm:$LiNbO_3$ crystal. Alternatively, the frequency of the recalled photons can be shifted by means of sum-frequency generation [38] using a pump beam of variable frequency. This can in principle be done with 100% conversion efficiency [39]. Third, higher-bandwidth modulators and driving electronics would allow employing less distorted serrodyne waveforms, resulting in more efficient frequency chirps. Fourth, the filtering cavity needs to be optimized for the particular application (we used an already existing cavity). Finally, in regards to the AFC itself, the quantum memory protocol theoretically allows for 100% efficiency [23]. Improvements from our current 1% rely on increased comb contrast and comb finesse $F = \Delta/\gamma$ (where Δ is the teeth spacing and γ is the linewidth of each tooth [23]), and the preparation of a spatio-spectral grating [40] or embedding of the rare-earth-ion-doped crystal into an impedance-matched cavity [41, 42, 20, 37]. We note that the possibility to increase the finesse, as well as to achieve longer storage times, relies on minimizing the parameters Δ and γ. Since both are limited by the homogeneous linewidth of Tm, this can be achieved by, for example, reduced operating temperatures [28].

D: Creating high finesse AFCs

The AFC shown in Fig. 4 of the main text is generated by optically pumping atomic population from troughs (i.e. the regions of transparency between teeth) into adjacent teeth [11, 22]. Towards this end, we apply a magnetic field along the C_3-axis of Tm:$LiNbO_3$. The ground and excited state of the ${}^3H_6 \leftrightarrow {}^3H_4$ transition in Tm then split into two pairs of nuclear Zeeman levels [25, 28], which are tuned such that the frequency difference between pairs is $\Delta/2$. While this approach maximizes the probability for a photon to be absorbed (all atoms continue to contribute to the absorption), it also results in the creation of an AFC with finesse of two. Assuming the use of an impedance-matched

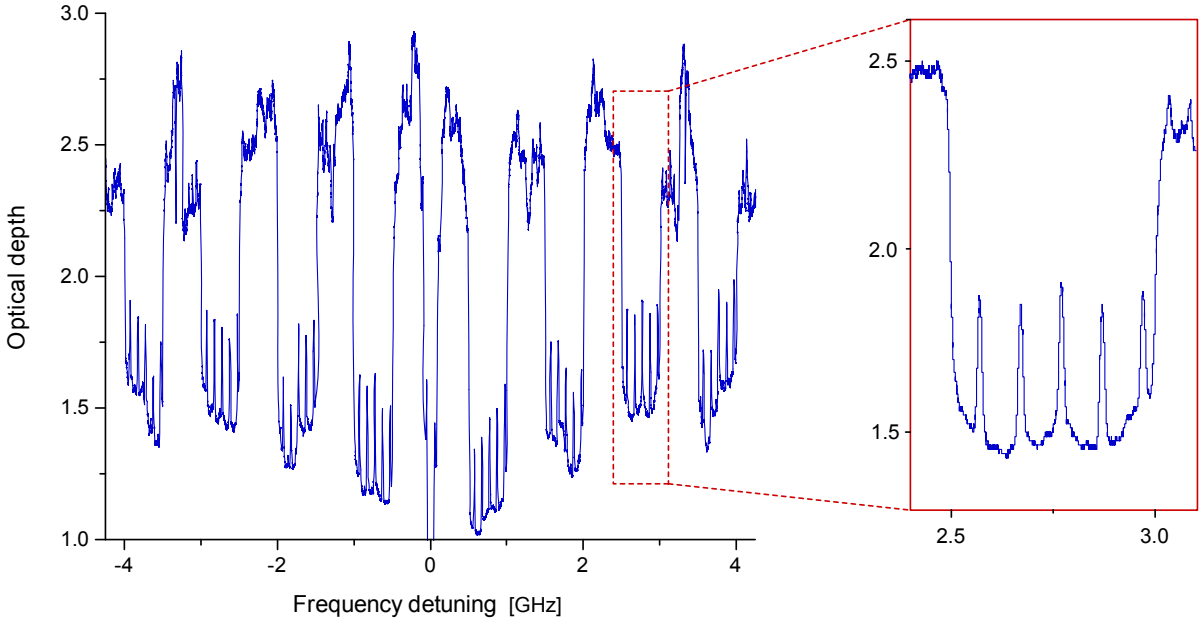

Figure A.7: Multimode AFC of finesse >2. Eight 500 MHz-wide AFCs, each having finesse of eight, prepared over a total bandwidth of 9 GHz. The optical depth at the centre of each comb tooth is approximately 0.35 – it is limited by our preparation method, Zeeman level lifetimes, and decay mechanisms present in our crystal. The reduced comb depths that are seen at larger detunings are due to reduced efficiency of the phase modulator. The magnetic field is set to 0.2 Tesla. The inset shows the AFC at the spectral bin between 2.5 and 3 GHz detuning.

cavity [41, 42, 20], the memory efficiency η – in the limit of the AFC optical depth to finesse ratio being much lower than one – is given by

$$\eta = e^{-\frac{7}{F^2}} \quad , \tag{A.8}$$

which limits the efficiency for an $F = 2$ AFC to 17%. Note that this equation assumes each AFC tooth has a Gaussian shape[41], and ignores decay between nuclear Zeeman levels (causing loss). The latter can be approximated when operating at sufficiently low temperatures [28].

Since improvements in efficiency rely on increased comb finesse F, we create and measure a multimode AFC having $F = 8$ in a separate experiment (see Fig. A.7). Towards this end, we increase the magnetic field to 0.2 Tesla, and hence increase the difference in the aforementioned ground and excited-state Zeeman splitting to more than the separation between troughs and neighboring peaks. This allows optical pumping of Tm ions out of the bandwidth occupied by an AFC, and potentially a larger memory efficiency. However, as briefly described above, this also results in a reduction of effective optical depth. Yet, if an impedance-matched cavity is used, according to Eq. A.8, this results in an efficiency of $\eta_{F=8} = 90\%$.

E: Generation of qubits in many spectral modes

Multimode time-bin qubits are generated by intensity and frequency modulating laser light using the aforementioned AOM and phase modulator. Each qubit consists of one (early or late), or two (early and late), 15 ns-long Gaussian-shaped pulses, generated using the AOM and separated by 20 ns, with each pulse having a frequency bandwidth matching that of an AFC (i.e. a spectral bin). The fibre frequency of each qubit is defined by driving the phase modulator with a sinusoidal signal, whose frequency (more precisely: the positive-detuned first order sideband) defines that of the spectral mode

to be occupied by the qubit. Furthermore, the sinusoidal signal's phase can be changed in between the generation of the first and second temporal mode, which allows creating various qubit states. Multimode qubit generation is accomplished by simultaneously driving the phase modulator with many independent sinusoidal signals. To generate the qubits shown in Fig. 4 of the main text, each sinusoidal signal was used to generating two qubits in spectral bins with with opposite-signed detunings.

F: Measurement of fidelity

The fidelity $\mathcal{F}$ quantifies how close a recalled quantum state is with respect to the originally created state. In our experiment, we employ time-bin qubits in states $|\psi\rangle \in [|e\rangle, |l\rangle, |+\rangle, |-\rangle]$, where $|\pm\rangle \equiv \frac{1}{\sqrt{2}}(|e\rangle \pm |l\rangle)$. Because we employ the decoy state analysis - described in the next section - it is possible to speak of qubit states encoded into the attenuated laser pulses that we use in our experiments. The average fidelity is quantified by $\mathcal{F} = \frac{1}{3}\mathcal{F}_{e/l} + \frac{2}{3}\mathcal{F}_{+/-}$ where, for example, $\mathcal{F}_{e/l} = \frac{1}{2}(\mathcal{F}_e + \mathcal{F}_l)$ and $\mathcal{F}_{e(l)}$ is the fidelity of an $|e\rangle$ ($|l\rangle$) state. The parameter $\mathcal{F}_l$ is calculated as $\mathcal{F}_l = C_{l|l}/(C_{e|l} + C_{l|l})$ where, for example, $C_{e|l}$ denotes the number of early detection events given $|l\rangle$ was originally encoded. The parameters $\mathcal{F}_e$, $\mathcal{F}_+$, and $\mathcal{F}_-$ are calculated in a similar way. The fidelity of time-bin qubits prepared in $|e\rangle$ or $|l\rangle$ are measured by recording photon arrival times using single photon detectors based on Si-avalanche photodiodes. Measuring qubits prepared in $|+\rangle$ or $|-\rangle$ requires detecting photons that have passed through an interferometer. This measurement as well as steps to stabilize and phase-align the interferometer are discussed next.

First, preceding each measurement, the phase of a fibre-based Mach-Zehnder interferometer having 4 m path-length difference (corresponding to 20 ns travel-time difference) and 98% intrinsic visibility is aligned to allow projection measurements onto $\frac{1}{\sqrt{2}}(|e\rangle + |l\rangle)$. Specifically, qubits prepared in $\frac{1}{\sqrt{2}}(|e\rangle + |l\rangle)$, each having mean photon number of 20, are

sent into the interferometer and the resultant interference signal at one particular output of the interferometer is maximized by stretching the fibre in one arm of the interferometer using a piezo actuator. To keep the phase stable, we then send light from our continuous-wave laser into the interferometer, detect the interference signal at the output of the interferometer using a linear photodetector (shown as 'D' in Fig. 3 of the main text), and keep the signal constant using feedback to the piezo actuator. This feedback is applied during each AFC preparation sequence, i.e. for 2 ms every 12 ms, which is sufficient to avoid thermal drifts. The interferometer stabilization setup is indicated by "to (from) MZI lock setup" in Fig. 3 of the main text.

After these steps, the measurement sequence begins by reducing the mean photon number per qubit to the single-photon level (either 0.5, 0.1, or zero photons per qubit), creating and storing photons in the desired quantum states (either $|+\rangle$ or $|-\rangle$), recalling photons from the AFC memory, and subsequently projecting them onto $|+\rangle$ and $|-\rangle$. The latter corresponds to detections in the interferometer output mentioned above, or detections in this output after having introduced an additional π phase shift using the interferometer's piezo actuator.

Finally, we note that frequency shifting of time-bin qubits by an amount $\Delta\nu$ comes along with a modification of the phase φ that determines the superposition of early and late temporal modes: $\Delta\varphi = 2\pi\Delta\nu\Delta t$, where Δt denotes the difference between early and late. We use the phase modulator that preceds the filtering cavity to both frequency shift and correct any phase shifts introduced when recalling qubits.

G: Bounding the single-photon fidelity using decoy state analysis

Decoy state analysis allows implementing quantum key distribution protocols using phase-randomized attenuated laser pulses without compromising the protocol's security due to photon number splitting attacks [43, 44]. It ensures that the final key stems only from

attenuated laser pulses containing one photon. The application of this analysis can be further generalized to allow any experiment performed with weak coherent states, such as attenuated laser pulses, to mimic an experiment using a much more elaborate setup that incorporates single photon (Fock) states. For the purpose of proving the quantum nature of e.g. memories, as in our experiment, the decoy state analysis provides an avenue for simpler experimental demonstrations of complex protocols. Here we provide a brief outline of how we employ the decoy state analysis to our experiment. It follows the original work by Ma *et al.* [29].

In order to show the quantum nature of our spectrally multimode memory, we must verify that the fidelity of the recalled state with the input state is higher than the classical bound of 2/3 [12]. However, this bound is only valid when using genuine qubits, i.e. for quantum states encoded into single photons. When using attenuated laser pulses, the classical bound has to be increased to account for the statistical distribution of the number of photons in a pulse and is also impacted by the memory efficiency [45, 46]. To be able to apply the 2/3 classical bound, we use a decoy state method to find a lower bound for the fidelity for the single photon component of the attenuated laser pulse. The derivation assumes a Poissonian photon number distribution in the light such as in the attenuated laser pulses at our memory's input. Furthermore, the pulses need to be phase randomized, which results in a states described by

$$\rho = \sum_{n=0}^{\infty} P(n)|n\rangle\langle n| \quad , \tag{A.9}$$

where $P(n)$ is the Poissonian distribution and $|n\rangle\langle n|$ denotes an n-photon Fock state.

As a first step we define the error rate

$$E_{\psi} = C_{\psi_{\perp}|\psi}/(C_{\psi_{\perp}|\psi} + C_{\psi|\psi}) \quad , \tag{A.10}$$

where, as in the preceding section, $C_{\psi_{\perp}|\psi}$ denotes the number of detection events corresponding to the state $|\psi_{\perp}\rangle$ given the state $|\psi\rangle$ was originally encoded. Since $|\psi_{\perp}\rangle$

corresponds to a state orthogonal to $|\psi\rangle$, a count of this type constitutes an error. Comparing to the expression for the fidelity it is furthermore clear that $\mathcal{F} = 1 - E$.

Using Eq. (25) from [29] the error rate $E^{(1)}$ for the single photon component of the coherent pulses is upper bounded by $E_U^{(1)}$, which is given by

$$\begin{aligned} E^{(1)} \leq E_U^{(1)} &= \frac{E^{(\mu_{d1})}Q^{(\mu_{d1})}e^{\mu_{d1}} - E^{(\mu_{d2})}Q^{(\mu_{d2})}e^{\mu_{d2}}}{(\mu_{d1} - \mu_{d2})Y_L^{(1)}} \\ &= \frac{E^{(\mu_{d1})}Q^{(\mu_{d1})}e^{\mu_{d1}} - E^{(0)}Y^{(0)}}{\mu_{d1}Y_L^{(1)}}, \end{aligned} \tag{A.11}$$

where $Y^{(0)}$ and $Y_L^{(1)}$ are the zero-photon yield and the lower bound for the single photon yield (defined below), respectively, $\mu_{d1} = 0.1$ and $\mu_{d2} = 0$ are mean photon numbers for the two *decoy states* used in our experiment, and $E^{(\mu_{d1})}$ and $E^{(\mu_{d2})} = E^{(0)}$ are the corresponding error rates, which can be estimated from measurements using Eq. (A.10). (The second line of Eq. (A.11) specifically assumes that $\mu_{d2} = 0$, i.e. the second decoy state is a vacuum state.) The gain $Q^{(\mu)}$ is the probability that a detector registers a count and depends on the mean photon number μ at the (memory) input and the loss up until the detector including the detector's quantum efficiency. Hence the gain can be directly calculated from the total number of counts accrued and the repetition rate of the pulses.

For phase randomized coherent states with a Poissonian photon number distribution the gain can be expressed as

$$Q^{(\mu)} = \sum_{n=0}^{\infty} Y^{(n)} \frac{\mu^n}{n!} e^{-\mu} \quad , \tag{A.12}$$

where the yield of an n-photon state $Y^{(n)}$ denotes the conditional probability of a detection given that an n-photon state was sent. The yields can generally not be directly measured without sources of photon number (Fock) states. An exception is the yield of the vacuum state, for which $Y^{(0)} = Q^{(0)}$. This fact is used to simplify Eq. (A.13) and in the second line of Eq. (A.11). Instead one can derive a lower bound $Y_L^{(1)}$ for the single

photon yield (used in Eq. (A.11)), which for the specific case of $\mu_{d2} = 0$ is given by [47]

$$Y^{(1)} \geq Y_L^{(1)} = \frac{\mu_s}{\mu_s \mu_{d1} - \mu_{d1}^2} \left(Q^{(\mu_{d1})} e^{\mu_{d1}} - \frac{\mu_{d1}^2}{\mu_s^2} Q^{(\mu_s)} e^{\mu_s} - \frac{\mu_s^2 - \mu_{d1}^2}{\mu_s^2} Y^{(0)} \right) \tag{A.13}$$

where $\mu_s = 0.5$ is the mean photon number of the *signal state*. The right-hand sides of equations (A.11) and (A.13) now contain directly measurable values and thus allow us to calculate the upper bound on the error rate $E_U^{(1)}$. By means of Eq. (A.10) we can compute the lower bound on the fidelity

$$\mathcal{F}^{(1)} = 1 - E^{(1)} \geq 1 - E_U^{(1)} \equiv \mathcal{F}_L^{(1)} \ , \tag{A.14}$$

which thus allows us to calculate the values in Table I in the main text.

This covers the essence of the decoy state analysis. Using it we derive a bound on the fidelity that we would have achieved if – all other things the same – we had utilized true single photons to encode qubits at the memory input.

H: Measurement of cross-talk between spectral modes

To examine the effect of cross-talk between spectral modes, we first store and retrieve a 'test' qubit prepared in $|l\rangle$ in the spectral bin having 1350 MHz detuning (refer to Fig. 4 of the main text). We then shift the test qubit into cavity resonance having 2.85 GHz detuning, measure the probability to project it onto $|l\rangle$ and calculate $\mathcal{F}_l$. We then increase the number of simultaneously stored qubits by creating them in neighbouring spectral bins, and repeat the fidelity measurement with the test qubit. Note that all additional qubits are prepared in the orthogonal $|e\rangle$ state, such that the reduction of the fidelity of the test qubit due to cross-talk is maximized. The results are shown in Figure A.8. We find that while there is a small amount of cross-talk between neighbouring modes, it is only significant when considering qubits separated by at most two spectral bins. Improvements in the fidelity can be achieved, for example, by increasing the separation between spectral bins.

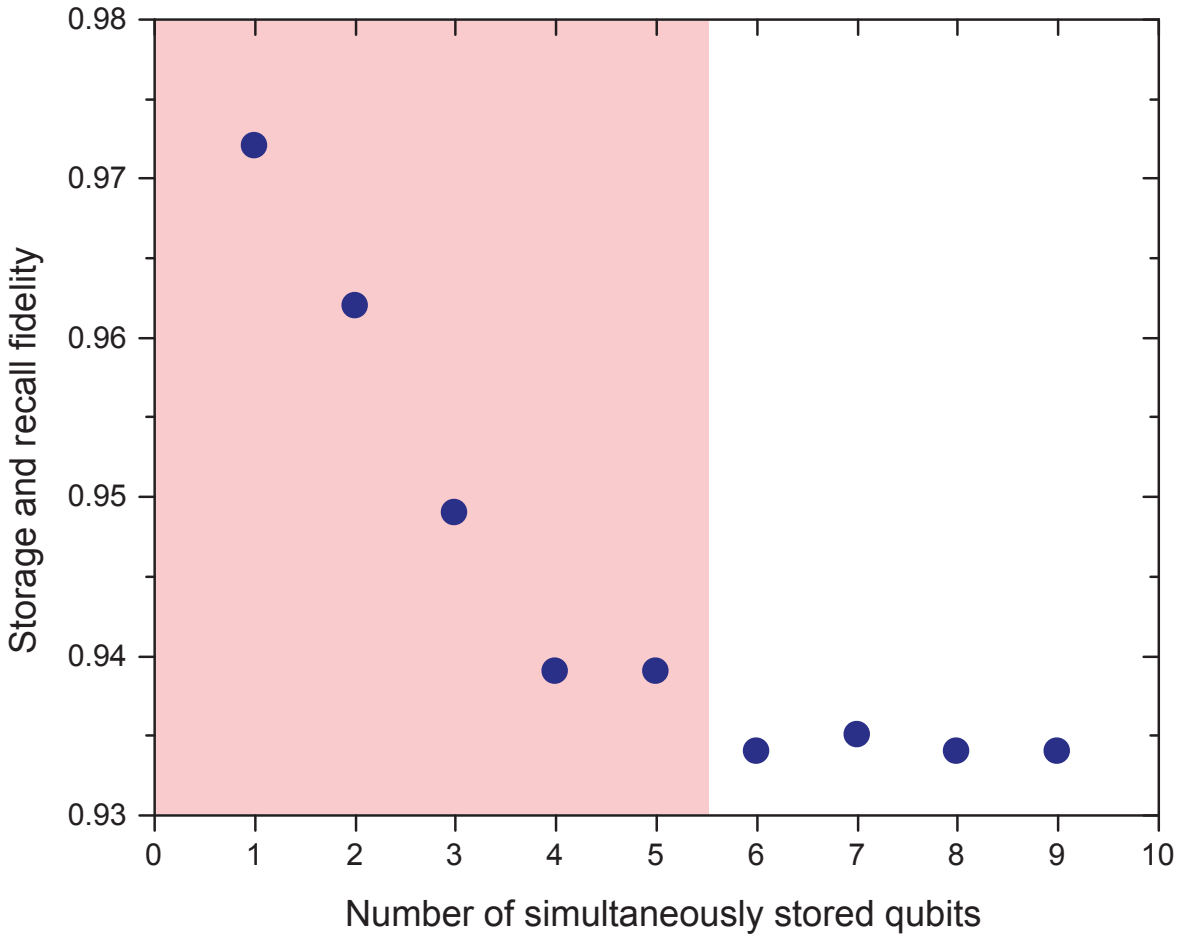

Figure A.8: Measurement of cross-talk. Dependence of storage and recall fidelity of the test qubit on the number of simultaneously stored qubits in neighboring spectral bins. The test qubit in $|l\rangle$ occupied the spectral bin having 1350 MHz detuning, while orthogonal qubits were added one-by-one to neighboring spectral bins in the following order: 1650 MHz, 1050 MHz, 1950 MHz, 750 MHz, etc. The cavity resonance was set to 2.85 GHz detuning. We find that the fidelity is constant when storing more than 5 modes simultaneously (shown in the white region of the plot). Hence, crosstalk (due to the Lorenzian linewidth of the cavity) is limited to coming from the nearest and second-nearest neighbour (shown in the shaded region of the plot). A further reduction in fidelity is due to limited frequency shift efficiency of our phase modulator, and is independent of the number of qubits simultaneously stored. Each projection measurement was taken over 60 s, the mean photon number per qubit was 0.6, and uncertainty (one standard deviation) was calculated from error propagation using statistical uncertainties of photon counts (not shown as it is smaller than the symbol size).

Bibliography

[1] Focus Issue: December 2009. Nature Photonics **3(12)**, 669 (2009).

[2] M. Scully and M. Zubairy, Quantum Optics, Cambridge University Press (1997).

[3] P. Kok , W. J. Munro, K. Nemoto, T. C. Ralph, J. P. Dowling, and G. J. Milburn, Rev. Mod. Phys. **79**, 135 (2007).

[4] N. Sangouard, C. Simon, H. de Riedmatten, and N. Gisin, Rev. Mod. Phys. **83**, 33-80 (2011).

[5] J. Nunn, N. K. Langford, W. S. Kolthammer, T. F. M. Champion, M. R. Sprague, P. S. Michelberger, X.-M. Jin, D. G. England, and I. A. Walmsley, Phys. Rev. Lett **110**, 133601 (2013).

[6] D. Collins, N. Gisin, and H. de Riedmatten, J. Mod. Opt. **52**, 735 (2005).

[7] A. I. Lvovsky, B. C. Sanders, and W. Tittel, Nat. Photon. **3**, 706 (2009).

[8] F. Bussières, N. Sangouard, M. Afzelius, H. de Riedmatten, C. Simon, and W. Tittel, J. of Mod. Opt. **60** 1519 (2013)

[9] H.-J. Briegel, W. Dür, J. I. Cirac, and P. Zoller, Phys. Rev. Lett. **81**, 5932 (1998).

[10] C. Simon, H. de Riedmatten, M. Afzelius, N. Sangouard, H. Zbinden, and N. Gisin, Phys. Rev. Lett. **98**, 190503 (2007).

[11] E. Saglamyurek, N. Sinclair, J. Jin, J. A. Slater, D. Oblak, F. Bussières, M. George, R. Ricken, W. Sohler, and W. Tittel, Nature **469**, 512 (2011).

[12] S. Massar and S. Popescu, Phys. Rev. Lett. **74**, 1259 (1995).

[13] E. Saglamyurek, N. Sinclair, J. A. Slater, K. Heshami, D. Oblak, W. Tittel, arXiv:1402.0481 (accepted in New J. of Phys.).

[14] C. Simon *et al.*, Euro. Phys. J. D **58(1)**, 1 (2010).

[15] H. N. Dai *et al.*, Phys. Rev. Lett. **108**, 210501 (2012).

[16] S.-Y. Lan, A. G. Radnaev, O. A. Collins, D. N. Matsukevich, T. A. B. Kennedy, and A. Kuzmich, Opt. Express **17** (16), 13639 (2009).

[17] C. Clausen, I. Usmani, F. Bussières, N. Sangouard, M. Afzelius, H. de Riedmatten, and N. Gisin, Nature **469**, 508 (2011).

[18] M. P. Hedges, J.J. Longdell, Y. Li, and M. J. Sellars, Nature **465**, 1052 (2010).

[19] I. Usmani, M. Afzelius, H. de Riedmatten, and N. Gisin, Nat. Comm. **1**, 12 (2010).

[20] M. Sabooni, Q. Li, S. Kröll, and L. Rippe, Phys. Rev. Lett. **110**, 133604 (2013).

[21] N. Timoney, I. Usmani, P. Jobez, M. Afzelius, and N. Gisin, Phys. Rev. A, **88** 022324 (2013).

[22] J. Jin, J. A. Slater, E. Saglamyurek, N. Sinclair, M. George, R. Ricken, D. Oblak, W. Sohler, and W. Tittel, Nat. Comm. **4**, 2386 (2013).

[23] M. Afzelius, C. Simon, H. de Riedmatten, and N. Gisin, Phys. Rev. A **79**, 052329 (2009).

[24] C. H. Bennett, G. Brassard, C. Crépeau, R. Jozsa, A. Peres, and W. K. Wootters, Phys. Rev. Lett. **70**, 1895 (1993).

[25] N. Sinclair, E. Saglamyurek, M. George, R. Ricken, C. La Mela, W. Sohler, and W. Tittel, J. Lumin. **130**, 1586 (2010).

[26] L. M. Johnson, and C. H. Cox, J. Light. Techn. **6**, 109 (1988).

[27] P. Palittapongarnpim, A. MacRae, and A. I. Lvovsky, Rev. Sci. Inst. **83**, 066101 (2012).

[28] Y. Sun, C. W. Thiel, and R. L. Cone, Phys. Rev. B **85**, 165106 (2012).

[29] X. Ma, B. Qi, Y. Zhao, and H.-K. Lo, Phys. Rev. A **72**, 012326 (2005).

[30] M. Bonarota, J. L. Le Gouët, and T. Chaneliere, New J. Phys. **13**, 013013 (2011).

[31] N. Lütkenhaus, J. Calsamiglia, and K.-A. Suominen, Phys. Rev. A **59**, 3295 (1999).

[32] A. Khalique, W. Tittel, and B. C. Sanders, Phys. Rev. A **88**, 022336 (2013).

[33] N. Walenta, T. Lunghi, O. Guinnard, R. Houlmann, H. Zbinden, and N. Gisin, J. Appl. Phys. **112**, 063106 (2012).

[34] O. A. Collins, S. D. Jenkins, A. Kuzmich, and T. A. B. Kennedy, Phys. Rev. Lett. **98**, 060502 (2007).

[35] M. Afzelius, I. Usmani, A. Amari, B. Lauritzen, A. Walther, C. Simon, N. Sangouard, J. Minář, H. de Riedmatten, N. Gisin, and S. Kröll, Phys. Rev. Lett., **104** 040503 (2010).

[36] M. Gündoğan, M. Mazzera, P. M. Ledingham, M. Cristiani, and H. de Riedmatten, New J. of Phys. **15**, 045012 (2013)

[37] P. Jobez, I. Usmani, N. Timoney, C. Laplane, N. Gisin, and M. Afzelius, ArXiv:1404.3489 (2014).

[38] S. Tanzilli, W. Tittel, M. Halder, O. Alibart, P. Baldi, N. Gisin, and H. Zbinden, Nature **437**, 116 (2005).

[39] A. P. VanDevender and P. G. Kwiat, J. Opt. Soc. Am. B **24** (2), 295 (2007).

[40] M. Tian, D. Vega, and J. Dilles, Phys. Rev. A **87**, 042338 (2013).

[41] M. Afzelius and C. Simon, Phys. Rev. A **82**, 022310 (2010).

[42] S. A. Moiseev, S. N. Andrianov, and F. F. Gubaidullin, Phys. Rev. A **82**, 022311 (2010).

[43] M. Dusek, O. Haderka, and M. Hendrych, Opt. Commun. **169** 103 (1999).

[44] G. Brassard, N. Lütkenhaus, T. Mor, and B. C. Sanders, Phys. Rev. Lett. **85** 1330 (2000).

[45] H. P. Specht, *et al.*,Nature **473**, 190 (2011)

[46] M. Gündoğan, P. M. Ledingham, A. Almasi, M. Cristiani, H. de Riedmatten, Phys. Rev. Lett. **108**, 190504 (2012)

[47] I. Lucio-Martinez, P. Chan, X. Mo, S. Hosier, and W. Tittel, New J. of Phys. **11** 095001 (2009)

Appendix B

Paper 2

Physical Review Letters 108, 083602 (2012)

Conditional detection of pure quantum states of light after storage in a waveguide

Erhan Saglamyurek[1], Neil Sinclair[1], Jeongwan Jin[1], Joshua A. Slater[1], Daniel Oblak[1], Félix Bussières[1], Mathew George[2], Raimund Ricken[2], Wolfgang Sohler[2], and Wolfgang Tittel[1]

[1]*Institute for Quantum Information Science, and Department of Physics and Astronomy, University of Calgary, 2500 University Drive NW, Calgary, Alberta T2N 1N4, Canada* [2]*Department of Physics - Applied Physics, University of Paderborn, Warburger Str. 100, 33095 Paderborn, Germany*

Abstract

Conditional detection is an important tool to extract weak signals from a noisy background and is closely linked to heralding, which is an essential component of protocols for long distance quantum communication and distributed quantum information processing in quantum networks.Here we demonstrate the conditional detection of time-bin

qubits after storage in and retrieval from a photon-echo based waveguide quantum memory. Each qubit is encoded into one member of a photon-pair produced via spontaneous parametric down conversion, and the conditioning is achieved by the detection of the other member of the pair. Performing projection measurements with the stored and retrieved photons onto different bases we obtain an average storage fidelity of 0.885 ± 0.020, which exceeds the relevant classical bounds and shows the suitability of our integrated light-matter interface for future applications of quantum information processing.

B.1 Introduction

Quantum memories are key elements for future applications of quantum information science such as long-distance quantum communication via quantum repeaters [1, 2] and, more generally, distributed quantum information processing in quantum networks [3]. They enable reversible mapping of arbitrary quantum states between travelling and stationary carriers (i.e. light and matter). This reduces the impact of loss on the time required to establish entanglement between distant locations [1], and allows the implementation of local quantum computers based on linear optics [4]. However, towards these ends, the successful transfer of a quantum state into the memory must be announced by a heralding signal. When using an individual absorber, such a signal can be derived through the detection of a change of atomic level population [5]. In atomic ensembles, this approach is infeasible. Instead, storage is derived from the detection of a second photon that either indicates the absorption [6], or the presence of the first at the input of the memory [7] (the first approach relies on spontaneous Raman scattering, the second on using pairs of photons). Furthermore, quantum memories must allow on-demand read-out after second-long storage with high efficiency [7, 8], and, for viable quantum technology, should be robust and simple to operate (e.g. be based on integrated optics).

A lot of progress towards these (and other) figures of merit has been reported over the past few years, including work that explores electromagnetically induced transparency (EIT), as well as photon-echo and cavity QED-based approaches (see [7, 8, 2, 10, 12, 11, 5, 9, 13, 14] for reviews and latest achievements). Yet, strictly, most of these experiments did not report true heralding – either heralding was not actually implemented, or the 'heralding' signal was generated only after the stored photon left the memory, or the signal could, due to technical issues, only be derived once the stored photon was detected. Nevertheless, experiments that employ photon pairs [15, 12, 11, 13] do gain from conditioning the detection of the stored photon on that of the auxiliary photon (i.e. *a posteriori* 'heralding'): by reducing the effects of loss and detector noise conditioning generally increases the fidelity between the quantum state of the original and the retrieved photon.

Supplementing the experiments on storage of entangled photons [11, 15, 12, 13], we now report another step towards the goal of building universal, viable, and heralded quantum memory devices – the storage of photons in pure quantum states in a solid state waveguide, their retrieval, and their conditional detection by means of temporal correlations with auxiliary photons. We point out that the step to true heralding is minor and of purely technical nature; it simply requires using different, existing, single-photon detectors (see, e.g., [16, 17]).

B.2 Experiment

Our experimental setup consists of two main blocks, see Fig. F.2: A spontaneous parametric down-conversion (SPDC) photon-pair source, and a Ti:Tm:$LiNbO_3$ single mode waveguide fabricated by indiffusion processes [18]. When cooled to 3 K, and using a photon-echo quantum memory protocol [19, 7, 8], the Tm-doped waveguide allows stor-

age and retrieval of quantum states encoded into one member of each photon pair, while the detection of the other member provides the conditioning signal.

In the photon-pair source a mode-locked pump laser generates 6 ps long pulses at a rate of 80 MHz and 1047.328 nm central wavelength. They are subsequently frequency-doubled (FD) in a periodically poled $LiNbO_3$ (PPLN) crystal, yielding pulses with 523.664 nm central wavelength, 16 ps duration, and 90 mW average power. The FD pulses are sent to a second PPLN crystal that, via SPDC, produces pairs of photons centred at 795.506 nm and 1532.426 nm. Frequency filtering the 795 nm photons with a 6 GHz-bandwidth Fabry-Perot filter (FPF) and the 1532 nm photons with a 9 GHz-bandwidth fiber-Bragg grating (FBG) we obtain frequency uncorrelated pairs. Each 795 nm photon travels through an imbalanced Mach-Zehnder interferometer with 42 cm path-length difference, corresponding to 1.4 ns relative delay. Thus, each photon emerges in a superposition of two temporal modes (early and late), i.e., in a time-bin qubit state [20]. They are then directed into the quantum memory, stored, retrieved, and finally detected by a Si avalanche-photo-diode (APD)-based single-photon detector.

All 1532 nm photons are sent through 30 m standard telecommunication fiber to an InGaAs APD-based single-photon detector. As is typically done, the detector is gated to reduce noise. The gate signal could in principle be the SYNC signal derived from each pulse emitted by the pump laser. However, as its repetition rate of 80 MHz by far exceeds the maximum gate frequency of our detector, around 1 MHz, we first AND the SYNC pulses with pulses generated by each Si-APD detection, and then use this low-rate signal to gate the InGaAs-APD. Provided the latter is ready for photon detection (i.e. not deadtime-blocked due to a previous detection), this signal also starts a time-to-digital converter (TDC), which then records the time-difference between the detection events produced by the Si-APD and the InGaAs-APD. This data is used to obtain statistics for single detections of the retrieved 795 nm photons, as well as for

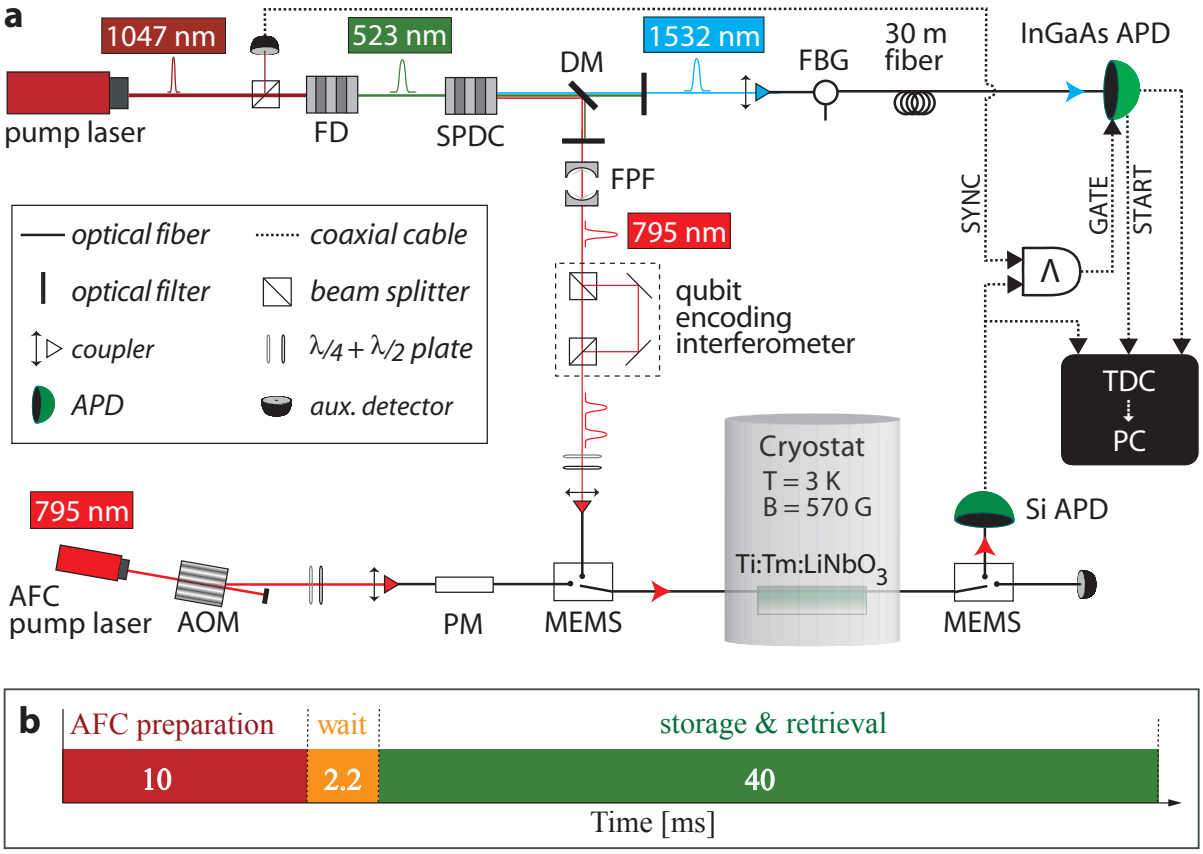

Figure B.1: **a.** Photon pair source and quantum memory setup (see text for details). Wave-plates align light polarization along the $LiNbO_3$'s C_3-axis. The waveguide is held at 3 K, and a 570 G magnetic field is applied along the crystal's C_3-axis (see Fig. 2a). **b.** Timing sequence containing three repeated phases: 10 ms *AFC preparation* for optical pumping, 2.2 ms *wait* to allow excited population to decay, and 40 ms *storage and retrieval*, during which 795 nm photons are successively stored for $t_{st} = 6$ ns and then recalled.

detections conditioned on the existence of 1532 nm photons. We emphasize that if an InGaAs APD supporting 80 MHz gate rate had been available [16, 17], then 1532 nm photons could have been detected without the need for *a priori* detection of a 795 nm photon. This simple modification of our setup would have turned the conditional detection of 795 nm photons into detections that are heralded by clicks of the InGaAs APD.

The other main block of our setup is a Ti:Tm:$LiNbO_3$ waveguide that allows storage and retrieval of the 795 nm photons via the atomic frequency comb (AFC) quantum memory protocol [19]. This approach to quantum state storage requires the spectral absorption of an atomic ensemble to be constituted of a series of equally spaced lines with frequency spacing Δ_ν. The interaction between such an AFC and a photon with wavevector k leads to the absorption of the photon and generates a collective excitation in the atomic medium that is described by

$$|\Psi\rangle = \frac{1}{\sqrt{N!}} \sum_{j=1}^{N} c_j e^{i2\pi m_j \Delta_\nu t} e^{-ikz_j} \, |g_1, \cdots e_j, \cdots g_N\rangle \, . \tag{B.1}$$

Here, $|g_j\rangle$ ($|e_j\rangle$) denotes the ground (excited) state of atom j, $m_j\Delta_\nu$ is the detuning of the atom's transition frequency from the photon carrier frequency, z_j its position measured along the propagation direction of the light, and the factor c_j depends on the atom's resonance frequency and position. Due to the presence of different atomic transition frequencies, the excited collective coherence dephases rapidly. However, the particular shape of the absorption line results in the recovery of the collective coherence after storage time $t_{st} = 1/\Delta_\nu$. This can easily be seen from Eq. (B.1): for $t = 1/\Delta_\nu$ all frequency dependent phase factors are zero (mod 2π). This leads to re-emission of the photon into the original mode and quantum state with maximally 54% efficiency for an optimally implemented AFC. Modifications to the procedure enable recall on demand and up to 100% efficiency [19].

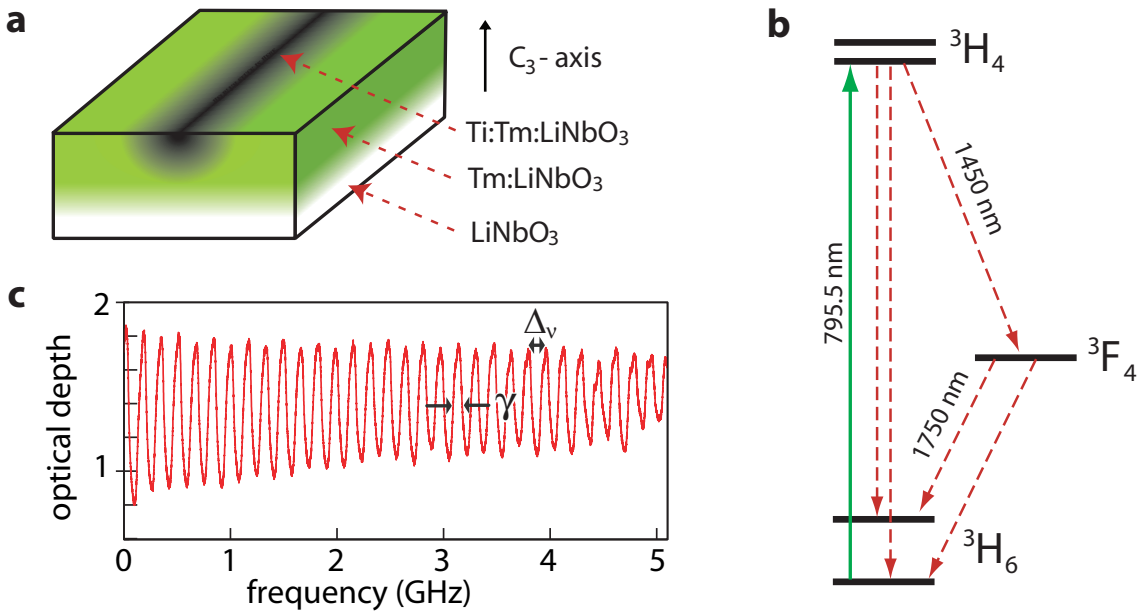

Figure B.2: **a.** Waveguide geometry: The sample surface is first doped by indiffusing a $\approx$ 20 nm thick Tm layer yielding a concentration profile of $\approx$ 6 μm depth with $\approx 10^{20}$ ions per cm^3 surface concentration. Subsequently a 3 μm wide channel waveguide is fabricated by indiffusion of a 40 nm thick vacuum-deposited Ti stripe. AFC preparation light and single photons are coupled in and out of the waveguide with 10% total efficiency by butt-coupling single mode fibers. **b.** Simplified energy level diagram of Tm ions: The optical coherence time of the ^{3}H$_6$-^{3}H$_4$ transition at 3 K is 1.6 μs, and the radiative lifetimes of the ^{3}H$_4$ and ^{3}F$_4$ levels are 82 μs and 2.4 ms, respectively. A 570 G magnetic field splits the ground and excited levels into Zeeman sub-levels. The ground Zeeman level splitting is $\sim$ 83 MHz, and the lifetime of the upper ground level exceeds one second. **c.** 5 GHz-bandwidth AFC: The tooth separation is Δ_ν = 167 MHz, corresponding to 6 ns storage time. The line-width of the teeth is γ = 83 MHz.

Suitable media in which to implement the AFC protocol are cryogenically cooled rare-earth ion doped crystals [7, 21]. They feature inhomogeneously broadened absorption profiles, often posses long-lived atomic sub-levels that can serve as shelving levels for tailoring the AFC through persistent spectral hole burning, and generally have long coherence times on optical and spin transitions. We use the $^3H_6$-$^3H_4$ transition of Tm ions in a single-mode channel waveguide fabricated by Ti indiffusion into the Tm doped surface of a Z-cut $LiNbO_3$ crystal, see Fig. B.2a [18]. To tailor the desired AFC into the inhomogeneously broadened absorption profile, Tm ions with transition frequencies within the comb's troughs are optically pumped via the excited level into long-lived nuclear Zeeman levels, see Fig. B.2b [18, 22]. To achieve frequency selective optical pumping we employed a linear side-band chirp technique [23, 11] that allowed us to create a 5 GHz broad grating (matching the spectral width of the 795 nm photons) with tooth spacing of 167 MHz, see Fig. B.2c. This corresponds to a storage time of 6 ns. After each 10 ms-long AFC preparation a 2.2 ms-long wait time allows atoms excited by the optical pumping to decay before the photon storage (see Fig. F.2b for the timing per experimental cycle). A set of micro electro-mechanical switches (MEMS) then open the channel for qubits to enter the memory, and, after recall, direct them towards the Si-APD. We assessed our memory's retrieval efficiency to be 2%. Taking the 10 dB fibre-to-fibre coupling loss in and out of the waveguide into account, this yields an overall system efficiency of 0.2%.

An interesting and useful aspect of photon-echo quantum memory protocols is that they provide a robust tool to manipulate time-bin qubits [24, 25, 26, 27]. For example, using the AFC approach, any projection measurement on time-bin qubit states can be performed by superimposing two combs (double AFC) with appropriately chosen relative center frequencies and amplitudes [25]. This leads to two re-emission times that can be set to differ by the temporal mode separation of the qubit to be analyzed (1.4 ns for our

experiments). Hence, as a previously absorbed photon is re-emitted by the superimposed combs, early and late temporal modes interfere, allowing the qubit state to be analyzed in the same way as is typically done with an imbalanced Mach-Zehnder interferometer [25]. Double AFC recall will, however, lead to a reduction of the recall efficiency (compared to single recall).

B.3 Measurements and Results

To demonstrate faithful storage and retrieval of quantum states from the memory, we performed projection measurements with various time-bin qubits onto different bases using single (standard) and double AFC schemes as explained before. In all our measurements the average photon number per qubit was 0.1 at the output of the qubit-preparation interferometer. First we generated qubit states that occupy only early $|e\rangle$ or late $|l\rangle$ temporal modes by blocking either the long or short arm of the qubit-encoding interferometer, respectively, and then stored these states in the memory for 6 ns. Fig. B.3 (left) shows single detections (no conditioning) of the retrieved photons as a function of the time difference with respect to the START signal. The dark counts from the Si-APD reduce the signal to noise ratio (SNR) to ~ 5. For an input state $|e\rangle$, we compute the fidelity as $\mathcal{F}_e = C_{e|e}/(C_{e|e} + C_{l|e})$, where, e.g., $C_{l|e}$ denotes the number of detected counts in the late time-bin given $|e\rangle$ was encoded in the qubit at the input. Similarly, we can find $\mathcal{F}_l$, enabling us to calculate the mean fidelity: $\mathcal{F}_{el} = (\mathcal{F}_e + \mathcal{F}_l)/2 = 0.8514 \pm 0.0004$. On the other hand, conditioning the detections of the retrieved photons on the detection of 1532 nm photons leads to a substantial increase of the SNR to ~ 22, as shown in Fig. B.3 (right). This yields a mean fidelity of $\mathcal{F}^*_{el} = 0.954 \pm 0.015$.

Next, qubit states in an equal superposition of early and late temporal modes $\frac{1}{\sqrt{2}}(|e\rangle +$

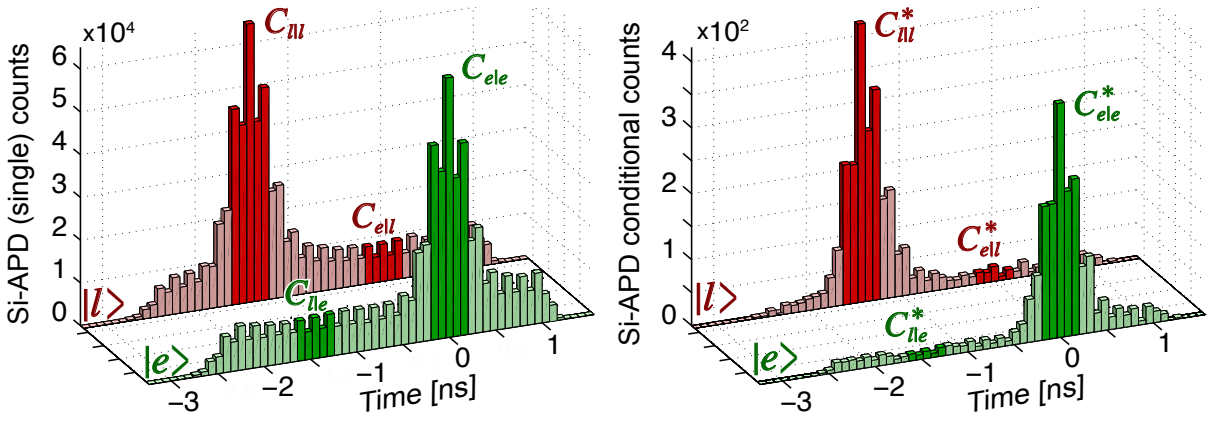

Figure B.3: Storage of early and late time-bin qubit states in the AFC memory. The left-hand figure depicts the histograms from 180 min of single detections of the retrieved 795 nm photons prepared in early (red) and late (green) qubit states with the highlighted regions marking the relevant detection windows. The right-hand figure shows the detections conditioned on 1532 nm photons for the same states. Without conditioning the fidelities are $\mathcal{F}_e = 0.8652 \pm 0.0006$ and $\mathcal{F}_l = 0.8376 \pm 0.0004$ for the storage of early and late time-bin states, respectively. Correspondingly, with conditioning, the fidelities are $\mathcal{F}^*_e = 0.9505 \pm 0.0058$ and $\mathcal{F}^*_l = 0.9573 \pm 0.0033$.

$e^{i\phi}|l\rangle$) were produced with ϕ set to zero. Storage and projection measurements were performed using the double AFC scheme with the relative phase of the two combs (measured w.r.t. the phase introduced by the qubit-preparation interferometer) varied by $\pi/2$ increments. The results for single and conditional detections are given in Fig. B.4. The histograms show the detection statistics for zero and π double AFC phase settings, from which we extract a SNR slightly above 1 for the single, and above 6 for the conditional detection. In the lower part of Fig. B.4 we show the normalized counts for each projection setting for the single and conditional detections. Fitting sinusoidal curves to these we derive visibilities $\mathcal{V}$, which, in turn, yield a fidelity $\mathcal{F} = (1 + \mathcal{V})/2$ for single detections of $\mathcal{F}_\phi = 0.682 \pm 0.020$. For conditional detections we find a significantly larger value of $\mathcal{F}^*_\phi = 0.851 \pm 0.030$. These figures allow establishing an average, single detection fidelity: $\overline{\mathcal{F}} \equiv (\mathcal{F}_{el} + 2\mathcal{F}_\phi)/3 = 0.738 \pm 0.029$. This violates the quantum classical bound [28] of ~ 0.667, thus verifying that our memory outperforms any classical storage

protocol. However, it is below the bound of ~ 0.833 for an optimal universal quantum cloner [29]. Harnessing the conditional detection we find $\overline{\mathcal{F}^*} = 0.885 \pm 0.020$. This beats the quantum-classical bound by 10 standard deviations and also violates the optimal universal quantum cloner bound by 2.5 standard deviations.

B.4 Conclusion

To conclude, we have demonstrated storage, retrieval, and conditional detection of different time-bin qubit states using a solid-state Ti:Tm:LiNbO3 waveguide quantum memory with average fidelity $\overline{\mathcal{F}^*} = 0.885 \pm 0.020$, which exceeds the relevant classical bounds. Operating the memory in a heralded fashion is readily achievable with high-rate APDs that have recently become commercially available. Despite our memory device's current limitations, namely efficiency, storage time, and preset recall time, the high fidelity and the wide spectral acceptance makes our approach promising for future quantum communication schemes and quantum networks. The $LiNbO_3$ host crystal and the waveguide structure have potential advantages in quantum memory applications such as fast electric field control of collective atomic phase evolution and, due to the resemblance with building blocks of classical integrated optical devices [30], it holds promise for simple integration with existing information technology. Furthermore, the ability to perform projection measurements using a photon-echo memory provides a simple and robust tool that might find use in other applications of quantum information processing.

Acknowledgment

We thank C. La Mela and T. Chanelière for helping in the initial stages of this work, V. Kiselyov for technical support, and NSERC, GDC, iCORE (now part of AITF), QuantumWorks, CFI and AET for financial support. D.O. thanks the Carlsberg Foundation and F.B. thanks FQRNT for support.

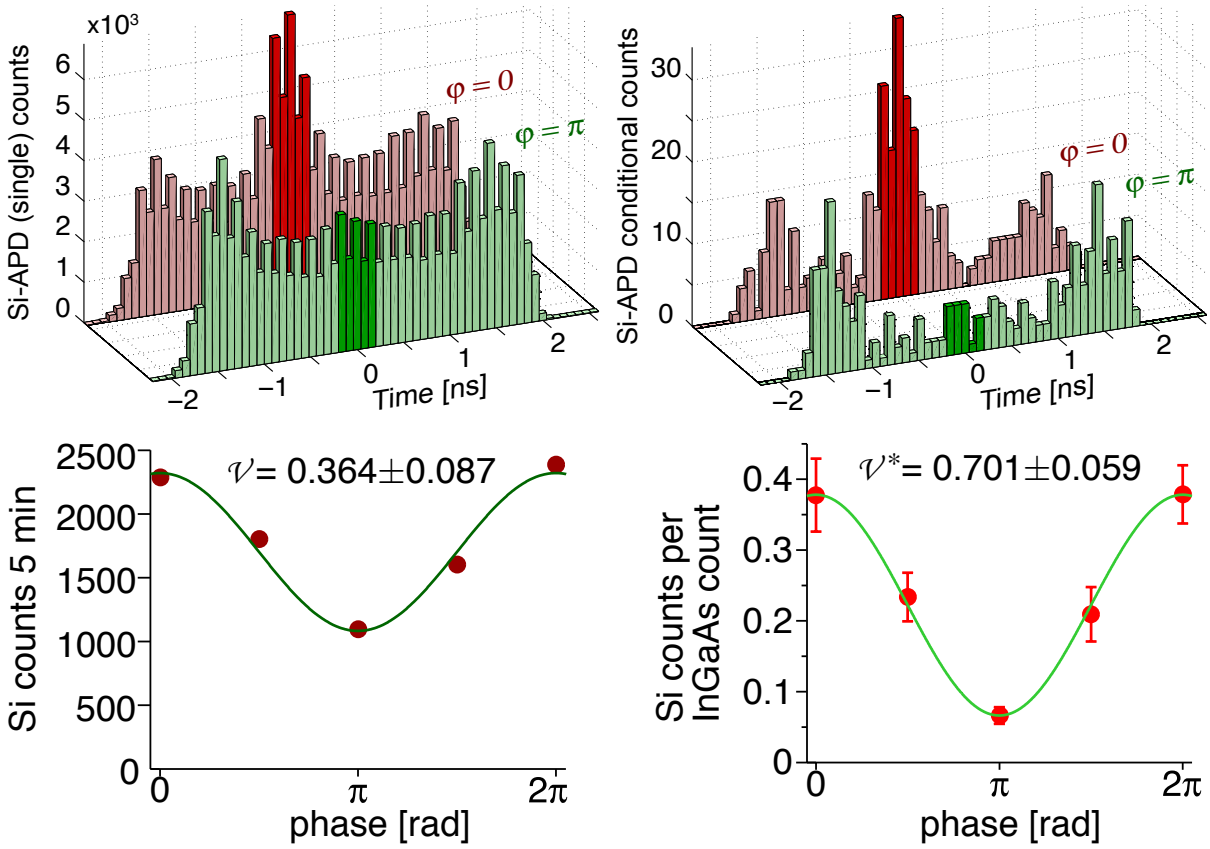

Figure B.4: Retrieval of qubits created in a superposition of early and late temporal modes. The top left figure presents histograms of single detections of the retrieved 795 nm photons with AFC phase settings of zero (red) and π (green), collected during 80 min. The top right figure shows the same histograms for conditional detections. The highlighted regions mark detection windows used to derive projection probabilities required to calculate fidelities. The lower curves show single and coincidence counts obtained for all phase settings for single detections (left) and conditional detections (right), yielding visibilities of 0.364 ± 0.087 and 0.701 ± 0.059, respectively.

Bibliography

[1] H.-J. Briegel *et al.*, Phys. Rev. Lett. **81**, 5932 (1998).

[2] N. Sangouard *et al.*, Rev. Mod. Phys. **83**(1), 33 (2011).

[3] J. Kimble, Nature **453**, 1023 (2008).

[4] P. Kok *et al.*, Rev. Mod. Phys. **79**, 135 (2007).

[5] H. P. Specht *et al.*, Nature **473**, 190 (2011).

[6] H. Tanji *et al.*, Phys. Rev. Lett. **103**, 043601 (2009).

[7] W. Tittel *et al.*, Laser & Phot. Rev. **4**, 244 (2010).

[8] A. I. Lvovsky, B.C. Sanders and W. Tittel, Nature Photonics **3**, 706 (2009).

[9] M. Hosseini *et al.*, Nature Physics **7**, 794 (2011).

[10] M. Hedges *et al.*, Nature **465**, 1052 (2010).

[11] E. Saglamyurek, et al., Nature **469**), 512 (2011)

[12] C. Clausen, et al., Nature **469**, 508 (2011)

[13] H. Zhang *et al.*, Nat. Photon. **5**, 628 (2011).

[14] K. F. Reim *et al.*, Phys. Rev. Lett. **107**, 053603 (2011).

[15] K. Akiba *et al.*, New J. Phys. **11**, 013049 (2009).

[16] M. D. Eisaman, et al., **82**(7), 071101 (2011)

[17] ID-Quantique SA, Physics today, **64**, 59 (2011).

[18] N. Sinclair *et al.*, J. Lumin. **130**, 1586 (2010).

[19] M. Afzelius *et al.*, Phys. Rev. A **79**, 052329 (2009).

[20] W. Tittel and G. Weihs, Quant. Inf. Comp., **1**(2), 3 (2001)

[21] C. Thiel, T. Böttger and R. Cone, J. Lumin. **131**, 353 (2011).

[22] C. W. Thiel *et al.*, J. Lumin. **130**, 1598 (2010).

[23] R. R. Reibel *et al.*, J. Lumin. **107**, 103 (2004).

[24] S. A. Moiseev and B. S. Ham, Phys. Rev. A **70**, 063809 (2004).

[25] H. de Riedmatten *et al.*, Nature **456**, 773 (2008).

[26] M. Hosseini *et al.*, Nature **461**, 241 (2009).

[27] S. A. Moiseev and W. Tittel, Phys. Rev. A **82**, 012309 (2010).

[28] S. Massar and S. Popescu, Phys. Rev. Lett. **74**, 1259 (1995).

[29] V. Bužek and M. Hillery, Phys. Rev. A **54**, 1844 (1996).

[30] W. Sohler *et al.*, Opt. Photon. News **19**, 24 (2008).

Appendix C

Paper 3

Nature 469, 512 (2011)

Broadband Waveguide Quantum Memory for Entangled Photons

Erhan Saglamyurek[1], Neil Sinclair[1], Jeongwan Jin[1], Joshua A. Slater[1], Daniel Oblak[1], Félix Bussières[1], Mathew George[2], Raimund Ricken[2], Wolfgang Sohler[2], and Wolfgang Tittel[1]

[1]*Institute for Quantum Information Science, and Department of Physics and Astronomy, University of Calgary, 2500 University Drive NW, Calgary, Alberta T2N 1N4, Canada* [2]*Department of Physics - Applied Physics, University of Paderborn, Warburger Str. 100, 33095 Paderborn, Germany*

Abstract

The reversible transfer of quantum states of light into and out of matter constitutes an important building block for future applications of quantum communication: it will allow the synchronization of quantum information [1], and the construction of quantum repeaters [2] and quantum networks [3]. Much effort has been devoted to the development of such quantum memories [1], the key property of which is the preservation of entanglement during storage. Here we report the reversible transfer of photon–photon entanglement into entanglement between a photon and a collective atomic excitation in a solid–state device. Towards this end, we employ a thulium-doped lithium niobate waveguide in conjunction with a photon-echo quantum memory protocol [4], and increase the

spectral acceptance from the current maximum [5] of 100 Megahertz to 5 Gigahertz. We assess the entanglement-preserving nature of our storage device through Bell inequality violations [6] and by comparing the amount of entanglement contained in the detected photon pairs before and after the reversible transfer. These measurements show, within statistical error, a perfect mapping process. Our broadband quantum memory complements the family of robust, integrated lithium niobate devices [7]. It simplifies frequency-matching of light with matter interfaces in advanced applications of quantum communication, bringing fully quantum-enabled networks a step closer.

C.1 Introduction

Quantum communication is founded on the encoding of information, generally referred to as quantum information, into quantum states of light [6]. The resulting applications of quantum physics at its fundamental level offer cryptographic security through quantum key distribution without relying on unproved mathematical assumptions [8] and allow for the disembodied transfer of quantum states between distant places by means of quantum teleportation [6]. Reversible mapping of quantum states between light and matter is central to advanced applications of quantum communication such as quantum repeaters [2] and quantum networks [3], in which matter constitutes nodes that hold quantum information until needed, and thereby synchronize the information flow through the communication channel or network. Furthermore, such a quantum interface allows the generation of light–matter entanglement through the mapping of one of two entangled photons into matter. To determine whether and how different physical systems can be entangled, and to localize the fundamental or technological boundaries where this fascinating quantum link breaks down, are central goals in quantum physics and have received much attention over the past decades [6].

The reversible light–matter interface can be realized through the direct transfer of quantum states from light onto matter and back, or through the generation of light–matter entanglement followed by teleportation of quantum information from an externally provided photon into matter, and eventually back. Experimental capabilities have advanced rapidly over the past years and quantum state transfer between light and atomic vapour [9, 10, 11, 12, 13], solid–state ensembles [4, 14], or single absorbers [15], as well as the generation of light–matter entanglement through the absorption of photons [16, 17, 18], or the emission of photons from atomic ensembles [19, 20, 21] or single emitters [22, 23] have all been reported.

For quantum memory to become practical, it is important to reduce the complexity of experimental implementations, and the recent addition of rare-earth-ion-doped crystals [4, 14] to the set of storage materials has been a valuable step towards this goal. The promise of such crystals is further enhanced through potentially long storage times– up to several seconds in $Pr:Y_2SiO_5$ [24]. In addition, given the large inhomogeneous broadening of optical zero-phonon lines, up to 100 Gigahertz (GHz), rare-earth-ion-doped crystals in principle offer storage of photons with less than 100-picosecond duration when being used in conjunction with a suitable quantum memory protocol [4]. Yet, the reversible state transfer between light and solid–state devices has so far not been shown to preserve entanglement. This is largely due to the limited spectral bandwidth of current implementations, 100 Megahertz (MHz) at most [5], which is orders of magnitude smaller than that of entangled photon pairs generated in the widely used process of spontaneous parametric down-conversion [6]. In this work, we approach the problem from both ends: we increase the acceptance bandwidth of our storage device to 5 GHz and narrow the bandwidths of our entangled photons to similar values. Furthermore, by using a wave-guiding storage medium, we move fundamental quantum memory research

further towards application.

C.2 Experiment

The layout of our experiment is depicted in Fig. C.1. Short pulses of 523-nm wavelength light travel through an unbalanced interferometer. For sufficiently small pulse energies, subsequent spontaneous parametric down-conversion yields, to a good approximation, individual pairs of photons, centred at wavelengths around 795 nm and 1,532 nm, in the time-bin entangled qubit state [25]:

$$|\phi^+\rangle = \frac{1}{\sqrt{2}} \left(|e, e\rangle + |l, l\rangle \right) \tag{C.1}$$

Here, $|e\rangle$ and $|l\rangle$ denote early and late temporal modes and replace the usual spin-down and spin-up notation for spin-half particles. More specifically, $|i, j\rangle$ denotes a quantum state in which the 795-nm photon has been created in the temporal mode i, and the 1,532-nm photon has been created in the temporal mode j. We point out that, owing to the spectral filtering, our source generates frequency-uncorrelated entangled photons at wavelengths that match the low-loss windows of free-space and standard telecommunication fibre. It can thus be readily used in real-world applications of quantum communication that involve quantum teleportation and entanglement swapping.

The 1,532-nm photon is directed to a qubit analyser. It consists of either a fibre delay line followed by a single-photon detector that monitors the photon's arrival time, or a fibre-optical interferometer that is unbalanced in the same way as the pump interferometer, followed by single-photon detectors. The role of the delay line is to perform projection measurements of the photon's state onto early and late qubit states. Alternatively, the interferometer enables projections onto equal superpositions of early and late modes [25]. Using the language of spin-half systems, this corresponds to projections onto σ_z and, for

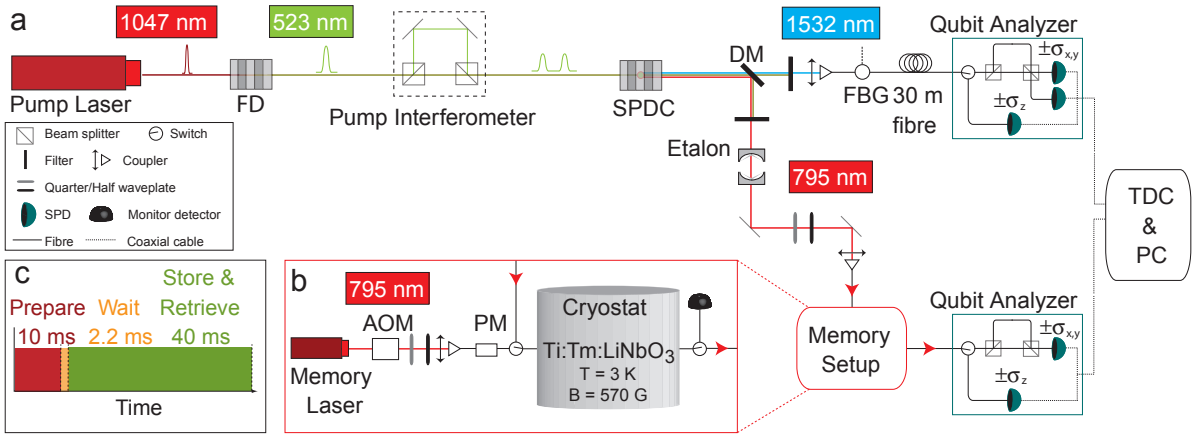

Figure C.1: **Schematics of the experimental set-up: a**. Generating and measuring entanglement. Six-picosecond-long pump laser pulses (1,047.328 nm wavelength, 80 MHz repetition rate) are frequency doubled (FD) in a periodically poled lithium niobate (PPLN) crystal. Each resulting 16-ps-long pulse (523.664-nm wavelength, 90 mW average power) is coherently split into two by the unbalanced pump interferometer, featuring a 1.4-ns travel-time difference. Spontaneous parametric down-conversion (SPDC) in a second PPLN crystal followed by frequency filtering using an etalon and a fibre Bragg grating (FBG) (bandwidths of 6 GHz and 9 GHz, respectively), yields maximally entangled pairs of photons centred at 795.506-nm and 1,532.426-nm wavelength (DM, dichroic mirror). The 1,532-nm photon travels through a 30-m telecommunication fibre, and the 795-nm photon is either stored in the memory or sent through a fibre delay line (not pictured). To characterize the bi-photon state, we use qubit analysers consisting of delay lines or unbalanced interferometers connected to single-photon detectors. Detection events are collected with a time-to-digital converter (TDC) connected to a personal computer (PC). All interferometers are phase-locked to stable reference lasers (not shown). **b**. Memory set-up. The 795.506-nm continuous-wave memory laser beam is intensity- and phase/frequency-modulated using an acousto-optic modulator (AOM) and a phase modulator (PM). The waveguide is cooled to 3 K and exposed to a 570-G magnetic field aligned with the crystal's C_3-axis. Waveplates allow adjusting the polarization of the beam to the waveguide's transverse magnetic (TM) mode, and optical switches combine and separate the optical pump beam and the 795-nm photons. **c**. Timing sequence. We use three continuously repeated phases: the 10 ms "prepare" phase for optical pumping, the 2.2-ms "wait" phase, which ensures stored photons are not polluted by fluorescence from the excited state, and the 40-ms "store and retrieve" phase, during which many 795-nm photons are successively stored in the waveguide and recalled after 7 ns.

appropriately chosen phases, σ_x and σ_y, respectively.

The 795-nm photon is transmitted to the quantum memory where its state –specifically that it is entangled with the 1,532-nm photon– is mapped onto a collective excitation of millions of thulium ions. Some time later, the state is mapped back onto a photon that exits the memory through a fibre in well-defined spatio-temporal modes and is probed by a second qubit analyser.

To reversibly map the 795-nm photon onto matter, we use a photon-echo quantum memory protocol based on atomic frequency combs (AFC) [4]. It is rooted in the interaction of light with an ensemble of atomic absorbers (so far rare-earth-ion-doped crystals cooled to cryogenic temperatures) with an inhomogeneously broadened absorption line that has been tailored into a series of equally spaced absorption peaks (see Fig. C.2). The absorption of a single photon leads to a collective excitation shared by many atoms. Owing to the particular shape of the tailored absorption line, the excited collective coherence rapidly dephases and repeatedly recovers after multiples of the storage time T_s. This results in the re-emission of a photon in the state encoded into the original photon.

In our implementation the moment of photon re-emission is predetermined by the spacing of the teeth in the comb, $T_s = 1/\Delta$, and the storage process can be described as arising from the linear response of an optical filter made by spectral hole burning. Yet, read-out on demand can be achieved by temporarily mapping the optically excited coherence onto ground-state coherence where the comb spacing is smaller or the comb structure is washed out [4], or by combining the AFC protocol with controlled reversible inhomogeneous broadening of each absorption line, similar to the storage mechanism used in another photon-echo quantum memory protocol [1].

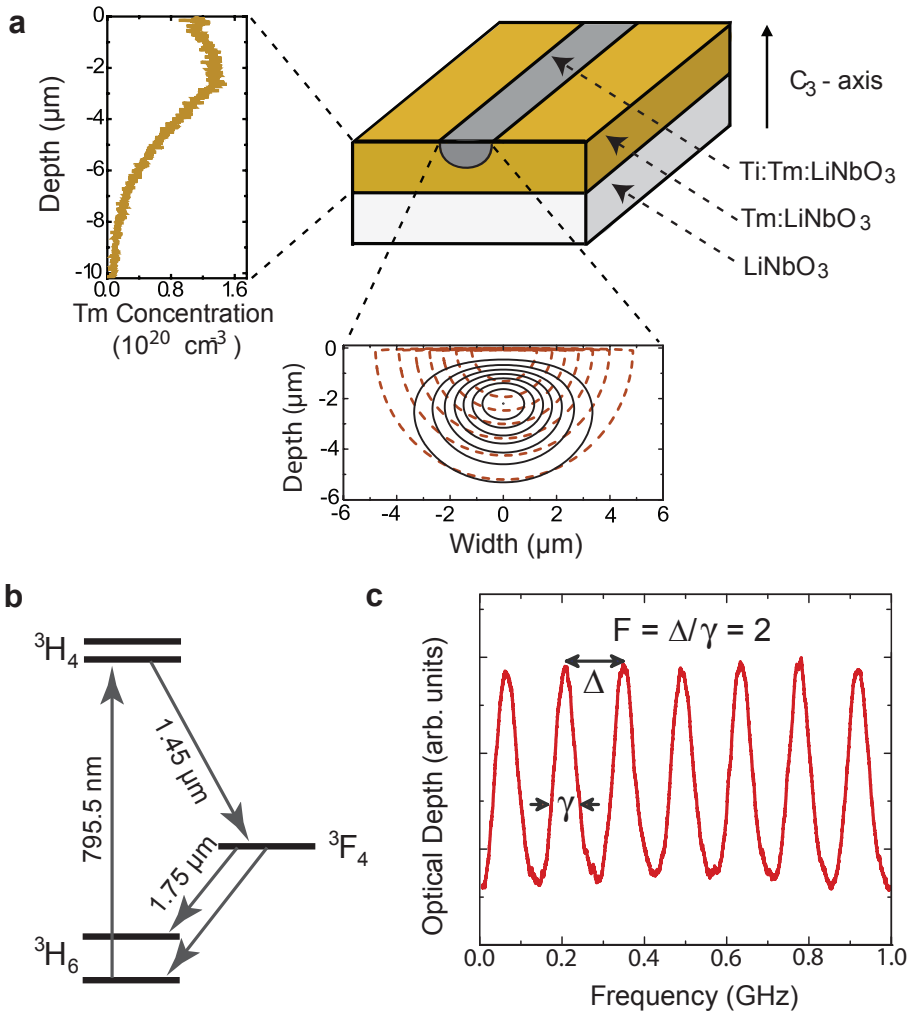

Figure C.2: **The storage medium: a**. Waveguide geometry. The measured thulium (Tm) concentration profile is given on the left and the calculated intensity distribution of the fundamental TM-mode at the 795-nm wavelength is shown below. Iso-intensity lines are plotted corresponding to 90%, 87.5%, 75% and so on of the maximum intensity. **b**. Simplified energy level diagram of thulium ions. The optical coherence time of the $^3H_6 \leftrightarrow ^3H_4$ transition at 3 K is 1.6 μs, the radiative lifetimes of the $^3H_4$ and $^3F_4$ levels are 82 μs and 2.4 ms, respectively, and the branching ratio from the $^3H_4$ to the $^3F_4$ level is 44%. Upon application of a magnetic field of 570 G, the ground and excited levels split into magnetic sublevels with lifetimes exceeding one second [27].**c**. Atomic frequency comb. The bandwidth of our AFC is 5 GHz (shown here is a 1-GHz broad section). The separation between the teeth is $\Delta \approx 143$ MHz, resulting in 7 ns storage time. The line width of the peaks is $\gamma \approx 75$ MHz, yielding a finesse $F = 2$, as expected for the sinus-type comb.

Our storage device, a Ti:Tm:$LiNbO_3$ optical waveguide cooled to 3 K, is detailed in Fig. C.2. It was previously characterized to establish its suitability as a photon-echo quantum memory material [26]. It combines interesting properties from the specific rare-earth element (795-nm storage wavelength), the host crystal (allowing for controlled dephasing and rephasing by means of electric fields), and from the wave-guiding structure (ease-of-use). Lithium niobate waveguides have also been doped with neodymium, praseodymium and erbium [7], and we conjecture that other rare-earth ions could also be used. This could extend the properties of $LiNbO_3$ and allow an integrated approach to other storage wavelengths, ions with different level structures, and so on.

To generate the AFC, we use a sideband-chirping technique (see Supplementary Information) to transfer atomic population between magnetic sublevels and create troughs and peaks in the inhomogeneously broadened absorption line. They form a 5-GHz-wide comb with tooth spacing of 143 MHz, setting the storage time to 7 ns. The system efficiency in our implementation is currently about 0.2%. This is in part due to the 90% fibre-to-waveguide input and output coupling loss, which we attribute to imperfect mode overlap. In addition, owing to the specific level structure of thulium under current experimental conditions, the finesse of the comb in the broadband approach is two, which limits the memory efficiency to about 10%. However, imperfections in the creation of the comb decrease this efficiency to around 2%. The system efficiency can be increased by improving the spectral tailoring of the AFC, and triggering photon re-emission in the backward direction. By also optimizing the mode overlap, we anticipate that it could reach approximately 15%. Furthermore, if the two long-lived atomic levels between which population is transferred during the optical pumping procedure (in our case the two magnetic ground states; see Fig. C.2) are spaced by more than the storage bandwidth, the

memory efficiency can theoretically reach unity (see Supplementary Information).

C.3 Measurements and Results

To assess the quantum nature of our light–matter interface, we first make projection measurements with the 795 nm photons and the 1532 nm photons onto time-bin qubit states characterized by Bloch vectors aligned along $\boldsymbol{a}$, $\boldsymbol{b}$, respectively, where $\boldsymbol{a}, \boldsymbol{b} \in [\pm\sigma_x, \pm\sigma_y, \pm\sigma_z]$ (see Fig. C.3). Experimentally, this is done by means of suitably adjusted qubit analyzers, and by counting the number $C(\boldsymbol{a}, \boldsymbol{b})$ of detected photon pairs. From two such spin-measurements, we calculate the normalized *joint-detection probability*

$$P(\boldsymbol{a}, \boldsymbol{b}) = \frac{C(\boldsymbol{a}, \boldsymbol{b})}{C(\boldsymbol{a}, \boldsymbol{b}) + C(\boldsymbol{a}, -\boldsymbol{b})} \tag{C.2}$$

The measurement and the results with the fibre delay line, as well as the memory, are detailed in Fig. C.3 and the Supplementary Information. From this data, we reconstruct the bi-photon states before and after storage in terms of their density matrices ρ_{in} and ρ_{out}, depicted in Fig. C.3, using a maximum likelihood estimation [27]. This, in turn, allows us to examine the entanglement of formation [28], a measure that indicates entanglement if it exceeds zero; it is upper-bounded by one. The results, listed in Table C.1, clearly show the presence of entanglement in ρ_{in} and ρ_{out} and, within experimental uncertainty, establish that the storage process preserves entanglement without measurable degradation. Furthermore, we note that the fidelity $\mathcal{F}$ between ρ_{in} and ρ_{out} is close to one, and hence the unitary transformation introduced by the storage process is almost the identity transformation.

In addition, as a second entanglement measure, we perform tests of the Clauser–Horne–Shimony–Holt (CHSH) Bell inequality [6]. This test indicates non-local correlations and thus the possibility of using the bi-photons for entanglement-based quantum key

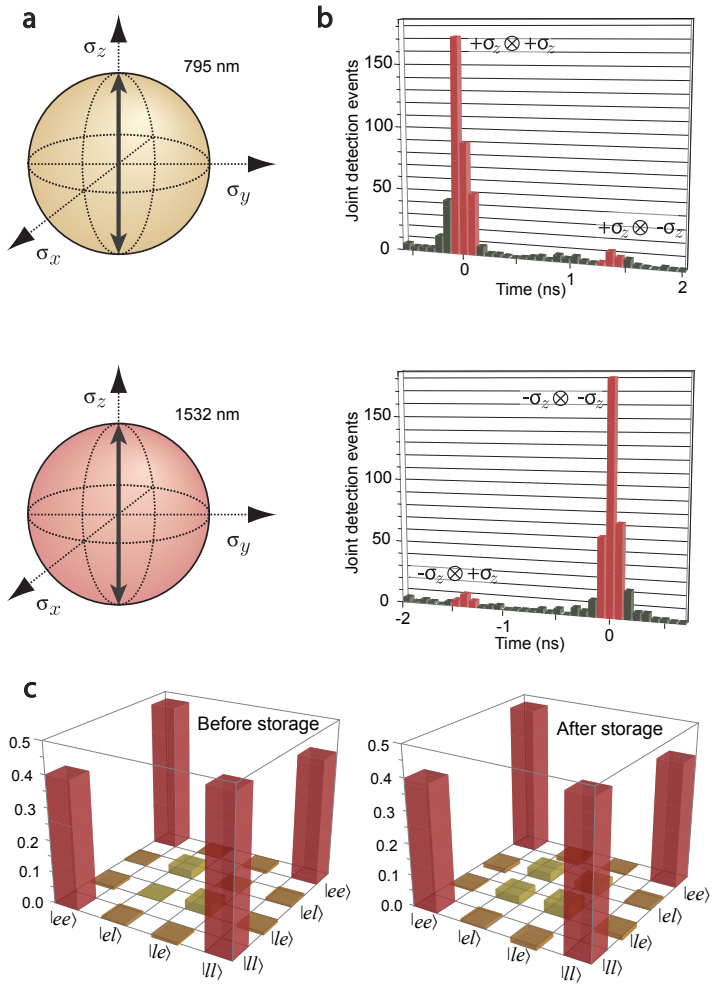

Figure C.3: **Measurement of density matrices: a**. Visualization of projection measurements. The measurement settings for the 795-nm (or 1,532-nm) qubit analyser are depicted on the upper (or lower) Bloch sphere. The example shows joint settings that enable calculating normalized probabilities for projections onto $\sigma_z \otimes \sigma_z$ $\sigma_z \otimes -\sigma_z$. **b**. Results for joint projection measurement after storage. The top (bottom) histogram displays joint detection events for the projection onto $\sigma_z \otimes \sigma_z$ and $\sigma_z \otimes -\sigma_z$($-\sigma_z \otimes \sigma_z$ and $-\sigma_z \otimes -\sigma_z$) as a function of the time difference between detections of the 795-nm and the 1,532-nm photons. The desired events are those within the red-highlighted time windows. This allows us to calculate the joint-detection probabilities for projections onto $\sigma_z \otimes \sigma_z$ and $\sigma_z \otimes -\sigma_z$ (for results with other joint settings see the Supplementary Information). **c**. Density matrices. Density matrices were calculated using a maximum-likelihood estimation for the bi-photon states before and after storage. Only the real parts are shown-the absolute values of all imaginary components are below 0.04.

	Entanglement of formation (%)	**Purity (%)**	**Fidelity with $\|\phi^+\rangle$**	**Input/output fidelity (%)**	**Expected S_{th}**	**Measured S**
ρ_{in}	64.4 ±4.2	75.7 ± 2.4	86.2±1.5		2.235 ±0.085	2.379 ±0.034
ρ_{out}	65 ±11	76.3±5.9	86.6 ±3.9	95.4 ±2.9	2.2 ±0.22	2.25 ±0.060.22

Table C.1: **Entanglement measures, purities and fidelities:** Entanglement of formation (normalized with respect to the entanglement of formation of $|\phi^+\rangle$, purity P=tr(ρ^2)), fidelity with $|\phi^+\rangle$, input–output fidelity $\mathcal{F} = \left(\mathrm{tr}\sqrt{\sqrt{\rho_{out}}\rho_{in}\sqrt{\rho_{out}}}\right)^2$ (referring to the fidelity of ρ_{out} with respect to ρ_{in}), and expected and experimentally obtained S values for tests of the CHSH Bell inequality (measured for $\boldsymbol{a} = \sigma_x$, $\boldsymbol{a'} = \sigma_y$, $\boldsymbol{b} = \sigma_x + \sigma_y$ and $\boldsymbol{b'} = \sigma_x - \sigma_y$). The correlation coefficients used to compute S and the calculation of S_{th} are detailed in the Supplementary Information. We note that the original state (and hence the recalled state) has limited purity and fidelity with $|\phi^+\rangle$. This is due to the probabilistic nature of our spontaneous parametric down-conversion source, which features a non-negligible probability of generating more than two photons simultaneously [26]. Uncertainties indicate one-sigma standard deviations and are estimated from Poissonian detection statistics and using a Monte Carlo simulation

distribution [8] if the sum:

$$S = |E(\boldsymbol{a},\boldsymbol{b}) + E(\boldsymbol{a'},\boldsymbol{b}) + E(\boldsymbol{a},\boldsymbol{b'}) - E(\boldsymbol{a'},\boldsymbol{b'})| \tag{C.3}$$

of four correlation coefficients

$$E(\boldsymbol{a},\boldsymbol{b}) = \frac{C(\boldsymbol{a},\boldsymbol{b}) - C(\boldsymbol{a},-\boldsymbol{b}) - C(-\boldsymbol{a},\boldsymbol{b}) + C(-\boldsymbol{a},-\boldsymbol{b})}{C(\boldsymbol{a},\boldsymbol{b}) + C(\boldsymbol{a},-\boldsymbol{b}) + C(-\boldsymbol{a},\boldsymbol{b}) + C(-\boldsymbol{a},-\boldsymbol{b})} \tag{C.4}$$

with appropriately chosen settings $\boldsymbol{a}$, $\boldsymbol{a'}$ and $\boldsymbol{b}$, $\boldsymbol{b'}$ exceeds the classical bound of two; quantum mechanically it is upper-bounded by $2\sqrt{2}$. As detailed in Table C.1, we find $S_{in} = 2.379 \pm 0.034 > 2$ before the memory and, crucially, $S_{out} = 2.25 \pm 0.06 > 2$, which is in agreement with the value $S_{th} = 2.2 \pm 0.22$ predicted from the reconstructed density matrix ρ_{out}. This validates the suitability of our set-up for quantum communication.

C.4 Discussion and Conclusion

Our investigation provides an example of entanglement being transferred between physical systems of different nature, thereby adding evidence that this fundamental quantum

property is not as fragile as is often believed. Furthermore, our broadband integrated approach permits the linkage of a promising quantum storage device with extensively used, high-performance sources of photons in bi- and multi-partite entangled states [6]. Although the storage efficiency and the storage time need to be significantly increased, and the moment of recall was pre-set, this study opens the way to new investigations of fundamental and applied aspects of quantum physics. Having increased the storage bandwidth also significantly facilitates the building of future quantum networks, because mutual frequency matching of photons and distant quantum memories will be simple. In addition, a large storage bandwidth –that is, the possibility to encode quantum information into short optical pulses– allows us to increase the number of temporal modes that can be stored during a given time. This enhances the flow of quantum information through a network and decreases the time needed to establish entanglement over a large distance using a quantum repeater [1, 2].

We note that, parallel to this work, Clausen et al. have demonstrated the storage of an entangled photon using a neodymium-doped crystal [29].

Acknowledgment

This work is supported by NSERC, QuantumWorks, General Dynamics Canada, iCORE (now part of Alberta Innovates), CFI, AAET and FQRNT. We thank C. La Mela, T. Chanelière, T. Stuart, V. Kiselyov and C. Dascollas for help during various stages of the experiment, C. Simon, K. Rupavatharam and N. Gisin for discussions, and A. Lvovsky for lending us a single-photon detector.

Author Contributions

The Ti:Tm:$LiNbO_3$ waveguide was fabricated and characterized at room temperature by M.G., R.R. and W.S. The photon-pair source was built by J.J., J.A.S. and F.B., the AFC memory set-up was developed by E.S. and N.S., and the complete experiment was conceived and directed by W.T. The measurements and the analysis were done by E.S., N.S., J.J., J.A.S., D.O. and W.T., and W.T., E.S., N.S., J.J., J.A.S. and D.O. wrote the paper. E.S., N.S., J.J. and J.A.S. contributed equally to this work.

C.5 Supplementary Information

Preparation of the Atomic Frequency Comb (AFC)

The AFC amounts to a periodic modulation in frequency of the optical density of the inhomogeneously broadened $^3H_6 \leftrightarrow ^3H_4$ thulium absorption line. It can be generated by optically pumping atoms to off-resonant shelving levels - in our case nuclear Zeeman levels [30]. To that end, we modulate the intensity of the 795 nm memory laser while scanning its frequency [31] . The frequency sweep is implemented using a lithium niobate phase modulator driven by a 20 GS/s arbitrary waveform generator. To avoid overlap of first and higher order modulation, the sweep extends from 5 GHz to 10 GHz, thus efficiently preparing a 5 GHz-bandwidth AFC memory. The laser intensity modulation is achieved by beating two frequency components, generated in an acousto-optic modulator (AOM) placed before the phase-modulator.

The memory storage time T_s is set by the frequency spacing between the teeth of the AFC, and is determined by $T_s = \delta/\alpha$, where $\delta = 0.35$ MHz is the difference between the two frequency components and $\alpha = 50 \times 10^{12}$ MHz/s is the sweep rate. This yields 142.85 MHz spacing between the AFC teeth, which translates into 7 ns memory storage time. For a high contrast AFC, the chirp cycle is repeated 100 times leading to a 10 ms overall optical pumping duration. The 2.2 ms wait time following the preparation corresponds to 27 times the radiative lifetime of the $^3H_4$ excited level, and ensures no fluorescence masks the retrieved photons.

The optical pumping involves population transfer between ground-state sublevels. As the comb structure extends over all these levels, we carefully chose the magnetic field to make sure that those ions that initially absorb at frequencies where we desire a trough

are transferred to frequencies where we desire a peak.

The Ti:Tm:$LiNbO_3$ waveguide

To fabricate the Ti:Tm:$LiNbO_3$ waveguide, a commercially available 0.5 mm thick Z-cut wafer of undoped, optical grade congruent lithium niobate (CLN) was cut into samples of 12 mm x 30 mm size. Tm doping was achieved by indiffusing a vacuum-deposited (electron-beam evaporated) Tm layer of 19.6 nm thickness. The diffusion was performed at 1130 °C during 150 h in an argon-atmosphere followed by a post treatment in oxygen (1 h) to get a full re-oxidization of the crystal. Tm occupies regular Li-sites when incorporated in CLN by diffusion [32]. The Tm indiffusion leads to a 1/e penetration depth of about 6.5 μm. The maximum Tm concentration of about 1.35×10^{20} cm^{-3} corresponds to a concentration of 0.74 mole %, which is considerably below the solid solubility of Tm in CLN [33]. Subsequently, the waveguide was formed by the well-known Ti–indiffusion technique. At first, a 40 nm thick titanium layer was electron-beam deposited on the Tm-doped surface of the CLN substrate. From this layer, 3.0 μm wide Ti stripes were defined by photo-lithography and chemical etching and subsequently in-diffused at 1060°C for 5 h to form 30 mm long optical strip waveguides. In the wavelength range around 795 nm, the waveguides are single mode for TE- and TM-polarization. To finish the fabrication, the waveguide was cut to 15.7 mm and end faces were carefully polished normal to the waveguide axis.

Limitation to efficiency

While the current system efficiency (characterizing the probability for a photon that enters the cryostat to leave it after recall) of around 0.2% is sufficient to show the

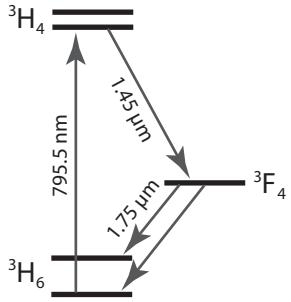

Figure C.4: Simplified level diagram for Tm:$LiNbO_3$.

entanglement-preserving nature of the storage process, it is clear that this number has to be improved to make the memory more practical and to allow for more involved fundamental measurements.

First, we note that better optical mode matching between the fibre and the $LiNbO_3$ waveguide can be expected to improve the fibre-to-fibre transmission from 10% to 50%.

Second, assuming storage in optical coherence and Gaussian-shaped teeth, the efficiency of the first recall in the forward direction is given by

$$\epsilon = (d_1/F)^2 e^{-d_1/F} e^{-7/F^2} e^{-d_0} \tag{C.5}$$

where $F = \Delta/\gamma$ denotes the finesse of the comb, and d_1/F and d_0 are the reversible and irreversible optical depth [34] (see supplementary figure C.4). As discussed above, our comb structure extends over all ground state levels. This fixes the fidelity of the comb to two, as ions can only be "shuffled around" but not removed from the spectral region covered by the SPDC photons. This impacts on the memory efficiency and sets, according to Eq. C.5, an upper bound of $\approx 10\%$. Yet, we note that the memory efficiency can be increased when applying a phase-matching operation that results in backward emission of the stored photon. Further improvement is expected when changing the teeth

shape from Gaussian to square [35]. All options combined, it seems possible to achieve a system efficiency of around 15%, which is 75 times larger than in the current implementation. We point out that the limitation due to the comb finesse is not necessarily a consequence of generating broadband combs, but of the small Zeeman splitting of the thulium ground state levels relative to the storage bandwidth. Provided the splitting between the long-lived atomic levels involved in the optical pumping procedure exceeds the storage bandwidth, the finesse can be increased beyond two, and memory efficiencies up to 100% are possible. This may be possible when using the $^3F_4$ level as shelving level, or for other RE impurities featuring greater sensitivity to magnetic fields [36].

Longer storage time and on-demand readout

Currently, the maximum storage time of our memory is approximately 300 ns. This value is determined by the minimum tooth spacing of the AFC, which is limited by spectral diffusion [30] . However, spectroscopic investigation of a Tm:$LiNbO_3$ bulk crystal shows that spectral diffusion decreases when lowering the temperature, similar to the observed improvement of the optical coherence time [30]. This implies the possibility to extend the storage time.

In addition, it may be possible to further improve the storage time and achieve on-demand recall by temporarily transferring the optical excited coherence between the $^3H_6$ and $^3H_4$ levels to coherence between the $^3H_6$ and $^3F_4$ electronic levels, similar to storage of coherence in spin-waves [37]. However, the coherence properties and the suitability of the $^3F_4$ state for such a transfer remains to be investigated. Furthermore, combining the AFC protocol with a quantum memory approach based on controlled reversible inhomogeneous broadening (CRIB) [36] allows one to inhibit the pre-set rephasing of coherence by adding

additional, controlled inhomogeneous broadening of each line in the AFC. Rephasing would occur only after reversing, i.e. undoing, the additionally introduced dephasing, and readout would be possible after any multiple of the AFC recall time determined by the tooth spacing.

The measurement

First, we stabilize the pump interferometer and the 1532 nm interferometer to arbitrarily chosen phase values. We define the phase introduced by the pump interferometer to be zero, i.e. we absorb it into the definition of the "early" and "late" qubit states, leading to the maximally entangled state

$$|\phi^+\rangle = \frac{1}{\sqrt{2}}\left(|e,e\rangle + |l,l\rangle\right) \tag{C.6}$$

Furthermore, we define the measurement performed by the 1532 nm qubit analyzer to be $+\sigma_x$. Next, we change the phase of the 795 nm interferometer and maximize the normalized *joint detection probability*

$$P(\boldsymbol{a},\boldsymbol{b}) = \frac{C(\boldsymbol{a},\boldsymbol{b})}{C(\boldsymbol{a},\boldsymbol{b}) + C(\boldsymbol{a},-\boldsymbol{b})} \tag{C.7}$$

with a fibre delay line in place of the memory. We define this setting to correspond to a projection onto $+\sigma_x$, and we measure $P_{in}(\sigma_x \otimes \sigma_x)$ over 5 minutes. This measurement (without the memory) is taken as being on the state ρ_{in}, i.e. the bi-photon state before storage. Next, we add the memory and similarly measure $P_{out}(\sigma_x \otimes \sigma_x)$ over approximately 5 hours. When necessary to change the setting of either qubit analyzer to σ_y, we increase the phase difference introduced by the respective interferometer by $\pi/2$. For projection measurements onto σ_z, we use the delay line in the qubit analyzer. Each joint projection measurement is done with and without memory; the results, given in

	$\sigma_x \otimes \sigma_x$	$\sigma_x \otimes \sigma_y$	$\sigma_x \otimes \sigma_z$	$\sigma_x \otimes -\sigma_z$	$\sigma_y \otimes \sigma_x$	$\sigma_y \otimes \sigma_y$	$\sigma_y \otimes \sigma_z$	$\sigma_y \otimes -\sigma_z$
P_{in} [%]	90±2	49±1	49±1	51±1	52±1	10±2	51±1	49±1
P_{out} [%]	89±6	49±8	48±4	52±4	49±6	14±5	49±4	51±4
	$\sigma_z \otimes \sigma_x$	$\sigma_z \otimes \sigma_y$	$\sigma_z \otimes \sigma_z$	$\sigma_z \otimes -\sigma_z$	$-\sigma_z \otimes \sigma_x$	$-\sigma_z \otimes \sigma_y$	$-\sigma_z \otimes \sigma_z$	$-\sigma_z \otimes -\sigma_z$
P_{in} [%]	46±1	46±1	94.2±0.1	5.8±0.1	46±1	45±1	7.6±0.2	93.0±0.2
P_{out} [%]	51±6	56±6	94±1	6±1	48±5	52±5	6±1	94±1

Table C.2: **Joint-detection probabilities for density matrix reconstruction:** Measured joint-detection probabilities for all projection measurements required to calculate the density matrices for the bi-photon state emitted from the source (P_{in}), and after storage and recall of the 795 nm photon (P_{out}). Uncertainties indicate one-sigma standard deviations based on Poissonian detection statistics.

supplementary table C.2, allow calculating the density matrices ρ_{in} and ρ_{out} describing the photon pair states before and after storage, respectively [27].

To measure the correlation coefficients

$$E(\boldsymbol{a},\boldsymbol{b}) = \frac{C(\boldsymbol{a},\boldsymbol{b}) - C(\boldsymbol{a},-\boldsymbol{b}) - C(-\boldsymbol{a},\boldsymbol{b}) + C(-\boldsymbol{a},-\boldsymbol{b})}{C(\boldsymbol{a},\boldsymbol{b}) + C(\boldsymbol{a},-\boldsymbol{b}) + C(-\boldsymbol{a},\boldsymbol{b}) + C(-\boldsymbol{a},-\boldsymbol{b})} \tag{C.8}$$

required for testing the Clauser-Horne-Shimony-Holt (CHSH) Bell inequality [38]. we chose, $\boldsymbol{a} = \sigma_x$, $\boldsymbol{a'} = \sigma_y$, $\boldsymbol{b} = \sigma_x + \sigma_y$, and $\boldsymbol{b'} = \sigma_x - \sigma_y$. Projections onto $\sigma_x \pm \sigma_y$ require changing phase differences by $\pm\pi/4$ as compared to those defining projections onto σ_x. For this measurement we added a detector to the second output of the interferometer in the 795 nm qubit analyzer so that C(**a**,**b**), C(**-a**,**b**), C(**a**,**-b**) and C(**-a**,**-b**) could be measured simultaneously. Measurements without memory are done over 15 min, those with memory over 12-15 hours. The resulting correlation coefficients are detailed in supplementary table C.3. From these we calculate $S_{in} = 2.379 \pm 0.034 > 2$ before storage and $S_{out} = 2.25 \pm 0.06 > 2$ after storage. Both are approximately equal, larger than 2, and hence violate the CHSH Bell inequality, proving again the presence of entanglement

	$\sigma_y \otimes (\sigma_x + \sigma_y)$	$\sigma_y \otimes (\sigma_x - \sigma_y)$	$\sigma_x \otimes (\sigma_x + \sigma_y)$	$\sigma_x \otimes (\sigma_x - \sigma_y)$
E_{in} [%]	59.7±1.7	-55.4±1.9	52.0±1.5	70.8±1.8
E_{out} [%]	54±3	-64±4	53±3	53±3

Table C.3: **Correlation coefficients for Bell-inequality tests:** Measured correlation coefficients (see Eq. C.8) required to test the CHSH Bell inequality. Uncertainties indicate one-sigma standard deviations based on Poissonian detection statistics.

and, beyond that, the suitability of the bi-photon states for quantum key distribution [8] . Moreover, the measured S–values are in good agreement with the respective theoretical values of $S_{th} = 2.235 \pm 0.085$ and $S_{th} = 2.2 \pm 0.22$ calculated using the measured density matrix with uncertainties estimated from Monte-Carlo simulations.

Calculation of purity, entanglement measures [28] and fidelities

Assuming an arbitrary two-qubit input state ρ, the *concurrence* is defined as $C(\rho) = \max\{0, \lambda_1 - \lambda_2 - \lambda_3 - \lambda_4\}$, where the λ_i's are, in decreasing order, the square roots of the eigenvalues of the matrix $\rho(\sigma_y \otimes \sigma_y)\rho^*(\sigma_y \otimes \sigma_y)$ and ρ^* is the element wise complex conjugate of ρ. The *entanglement of formation* is then calculated as

$$E_F(\rho) = H\left(0.5 + 0.5\sqrt{1 - C^2(\rho)}\right) \tag{C.9}$$

where $H(x) = -x\log_2 x - (1-x)\log_2(1-x)$. Finally, fidelity between ρ and σ is

$$F(\rho, \sigma) = \left(tr\sqrt{\sqrt{\rho}\sigma\sqrt{\rho}}\right)^2 \tag{C.10}$$

and the *purity* of a state ρ is

$$P = \mathrm{tr}(\rho^2) \tag{C.11}$$

Bibliography

[1] Lvovsky, A. I., Sanders, B. C., &. Tittel, W. Optical quantum memory. Nature Photon. 3, 706–714 (2009)

[2] Sangouard, N., Simon, C., de Riedmatten, H. & Gisin, N. Quantum repeaters based on atomic ensembles and linear optics. Preprint at http://arxiv.org/abs/ 0906.2699 (2009)

[3] Kimble, H. J. The quantum Internet. Nature 453, 1023–1030 (2008)

[4] de Riedmatten, H., Afzelius, M., Staudt, M. U., Simon, C. & Gisin, N. A solid–state light–matter interface at the single-photon level. Nature 456, 773–777 (2008)

[5] Usmani, I., Afzelius, M., de Riedmatten, H. & Gisin, N. Mapping multiple photonic qubits into and out of one solid–state atomic ensemble. Nature Commun. 1, 1–7 (2010)

[6] Pan, J.-W., Chen, Z.-B., Zukowski, M., Weinfurter, H. & Zeilinger, A. Multi-photon entanglement and interferometry. Preprint at http://arxiv.org/abs/0805.2853 (2008)

[7] Sohler, W. et al. Integrated optical devices in lithium niobate. Opt. Photon. News 24–31 (2008)

[8] Gisin, N., Ribordy, G., Tittel, W. & Zbinden, H. Quantum cryptography. Rev. Mod. Phys. 74, 145–195 (2002)

[9] Julsgaard, B., Sherson, J. & Cirac, J. I. J. Fiurasek, J. & Polzik, E. S. Experimental demonstration of quantum memory for light. Nature 432, 482–486 (2004)

[10] Chaneliere, T. et al. Storage and retrieval of single photons transmitted between remote quantum memories. Nature 438, 833–836 (2005)

[11] Eisaman, M. D. et al. Electromagnetically induced transparency with tunable single-photon pulses. Nature 438, 837–841 (2005)

[12] Honda, K. et al. Storage and retrieval of a squeezed vacuum. Phys. Rev. Lett. 100, 093601 (2008)

[13] Appel, J., Figueroa, E., Korystov, D., Lobino, M. & Lvovsky, A. Quantum memory for squeezed light. Phys. Rev. Lett. 100, 093602 (2008)

[14] Hedges, M. P., Longdell, J. J., Li, Y. & Sellars, M. J. Efficient quantum memory for light. Nature 465, 1052–1056 (2010)

[15] Boozer, A. D. et al. Reversible state transfer between light and a single trapped atom. Phys. Rev. Lett. 98, 193601 (2007).

[16] Choi, K. S. Deng, H. Laurat, J. & Kimble, H. J. Mapping photonic entanglement into and out of a quantum memory. Nature 452, 67–71 (2008)

[17] Akiba, K., Kashiwagi, K. Arikawa, M. & Kozuma, M. Storage and retrieval of nonclassical photon pairs and conditional single photons generated by the parametric down-conversion process. N. J. Phys. 11, 013049 (2009)

[18] Jin, X.-M. et al. Quantum interface between frequency-uncorrelated down converted entanglement and atomic-ensemble quantum memory. Preprint at http://arxiv.org/abs/1004.4691 (2011)

[19] Chou, C. W. et al. Measurement-induced entanglement for excitation stored in remote atomic ensembles. Nature 438, 828–832 (2005)

[20] Matsukevich, D. N. et al. Entanglement of a photon and a collective atomic excitation. Phys. Rev. Lett. 95, 040405 (2005)

[21] Yuan, Z.-S. et al. Experimental demonstration of a BDCZ quantum repeater node. Nature 454, 1098–1101 (2008)

[22] Blinov, B. B., Moehring, D. L., Duan, L.M. & Monroe, C. Observation of entanglement between a single trapped atom and a single photon. Nature 428, 153–157 (2004)

[23] Togan, E. et al. Quantum entanglement between an optical photon and a solid state spin qubit. Nature 466, 730–734 (2010)

[24] Longdell, J., Fraval, E., Sellars, M. & Manson, N. Stopped light with storage times greater than one second using electromagnetically induced transparency in a solid. Phys. Rev. Lett. 95, 063601 (2005)

[25] Marcikic, I. et al. Time-bin entangled qubits for quantum communication created by femtosecond pulses. Phys. Rev. A 66, 062308 (2002)

[26] Sinclair, N. et al. Spectroscopic investigations of a Ti:Tm:$LiNbO_3$ waveguide for photon-echo quantum memory. J. Lumin. 130, 1586–1593 (2010)

[27] Altepeter, J. B., Jeffrey, E. R., &. Kwiat, P. G. Photonic state tomography. Adv. At. Mol. Opt. Phys. 52, 105–159 (2005)

[28] Plenio, M. B. & Virmani, S. An introduction to entanglement measures. Quant. Inf. Comput. 7, 1–51 (2007)

[29] Clausen, C. et al. Quantum storage of photonic entanglement in a crystal. Nature doi:10.1038/nature09662 (this issue).

[30] Thiel, C.W., Sun, Y., Bottger, T., Babbitt, W.R. and Cone, R.L. Optical decoherence and persistent spectral hole burning in Tm^{3+}:$LiNbO_3$. J. Lumin, 130 (9), 1603-1609 (2010).

[31] Reibel R.R., Barber, Z.W., Fischer, J.A., Tian, M. and Babbitt, W.R. Broadband demonstrations of true-time delay using linear sideband chirped programming and optical coherent transients. J. Lumin. 107, 103-113 (2004)

[32] Novikov, D. V. et al. Plane wave GID topography of defects in lithium niobate after diffusion doping, Nuclear Instruments and Methods in Physics Research B 97, 342-345 (1995)

[33] Quintanilla, M., Cantelar, E., Sanz-Garca, J.A. Cusso, F. Growth and optical characterization of Tm^{3+}-doped $LiNbO_3$. Optical Materials 30, 1098-1102 (2008)

[34] Afzelius, M., Simon, C., de Riedmatten, H. and Gisin, N. Multimode quantum memory based on atomic frequency combs. Phys. Rev. A 79, 052329 (2009)

[35] Bonarota, M., Ruggiero, J., Le Gouet, J.-L. and Chaneliere, T. Efficiency optimization for Atomic Frequency Comb storage. Preprint at http://arxiv.org/abs/0911.4359 (2009)

[36] Tittel, W. et al. Photon-echo quantum memory in solid state systems. Laser and Photon. Rev. 4, (2), 244-267 (2010)

[37] Afzelius, M. et al. Demonstration of Atomic Frequency Comb Memory for Light with Spin-Wave Storage. Phys. Rev. Lett. 104, 040503 (2010)

[38] Clauser, J.F., Horne, M.A., Shimony, A. and Holt, R.A. Proposed experiment to test local hidden-variable theories. Phys. Rev. Lett. 23, 880-884 (1969)

Appendix D

Paper 4

Nature Communications 4, 2386 (2013)

Two-photon interference of weak coherent laser pulses recalled from separate solid-state quantum memories

Jeongwan Jin[1], Joshua A. Slater[1], Erhan Saglamyurek[1], Neil Sinclair[1], Mathew George[2], Raimund Ricken[2], Daniel Oblak[1], Wolfgang Sohler[2], and Wolfgang Tittel[1]

[1]*Institute for Quantum Information Science, and Department of Physics and Astronomy, University of Calgary, 2500 University Drive NW, Calgary, Alberta T2N 1N4, Canada* [2]*Department of Physics - Applied Physics, University of Paderborn, Warburger Str. 100, 33095 Paderborn, Germany*

Abstract

Quantum memories for light, which allow the reversible transfer of quantum states between light and matter, are central to the development of quantum repeaters [1], quantum networks [2], and linear optics quantum computing [3]. Significant progress has been reported in recent years, including the faithful transfer of quantum information from photons in pure and entangled qubit states [4, 5, 6, 7, 8, 9, 10]. However, none of these demonstrations confirm that photons stored in and recalled from quantum memories remain suitable for two-photon interference measurements, such as C-NOT gates and Bell-state measurements, which constitute another key ingredient for all aforementioned applications of quantum information processing. Using pairs of weak laser pulses,

each containing less than one photon on average, we demonstrate two-photon interference as well as a Bell-state measurement after either none, one, or both pulses have been reversibly mapped to separate thulium-doped titanium-indiffused lithium niobate (Ti:Tm:$LiNbO_3$) waveguides. As the interference is always near the theoretical maximum, we conclude that our solid-state quantum memories, in addition to faithfully mapping quantum information, also preserves the entire photonic wavefunction. Hence, we demonstrate that our memories are generally suitable for use in advanced applications of quantum information processing that require two-photon interference.

D.1 Introduction

When two indistinguishable single photons impinge on a 50/50 beam-splitter (BS) from different input ports, they bunch and leave together by the same output port. This so-called Hong-Ou-Mandel (HOM) effect [11] is due to destructive interference between the probability amplitudes associated with both input photons being transmitted or both reflected, see Fig. 1. Since no such interference occurs for distinguishable input photons, the interference visibility V provides a convenient way to verify that two photons are indistinguishable in all degrees of freedom, i.e. spatial, temporal, spectral, and polarization modes. The visibility is defined as

$$V = (\mathcal{R}_{\max} - \mathcal{R}_{\min})/\mathcal{R}_{\max}, \tag{D.1}$$

where $\mathcal{R}_{\min}$ and $\mathcal{R}_{\max}$ denote the rate with which photons are detected in the two output ports in coincidence if the incoming photons are indistinguishable and distinguishable, respectively. Consequently, the HOM effect has been employed to characterize the indistinguishability of photons emitted from a variety of sources, including parametric down-conversion crystals [12], trapped neutral atoms [13, 9], trapped ions [14], quantum dots [15, 16, 17], organic molecules [18], nitrogen-vacancy centres in diamond [19, 20],

and atomic vapours [21, 22, 23, 24, 25]. Furthermore, two-photon interference is at the heart of linear optics Bell-state measurements [26], and, as such, has already enabled experimental quantum dense coding [27], quantum teleportation [28], and entanglement swapping [29]. However, to date, the possibility to perform Bell-state measurements with photons that have previously been stored in a quantum memory, as required for advanced applications of quantum information processing, has not yet been established. For these measurements to succeed, photons need to remain indistinguishable in all degrees of freedom, which is more restrictive than the faithful recall of encoded quantum information. Indeed, taking into account that photons may or may not have been stored before the measurement, this criterion amounts to the requirement that a quantum memory preserves a photon's wavefunction during storage. Similar to the case of photon sources, the criterion of indistinguishability is best assessed using HOM interference, provided single-photon detectors are employed.

D.2 Experiment

Our experimental setup is depicted in Fig. D.2. We employ solid-state quantum memories, more precisely thulium-doped lithium-niobate waveguides in conjunction with the atomic frequency comb (AFC) quantum memory protocol [30], which have shown great promise for advanced applications of quantum information processing [5, 6, 7]. We then interfere various combinations of recalled and non-stored (i.e. directly transmitted) pulses on a 50/50 BS (HOM-BS). When using single photon Fock states at the memory inputs, the HOM visibility given in (D.1) theoretically reaches 100% as illustrated in Fig. D.1. However, with phase incoherent laser pulses obeying Poissonian photon-number statistics, as in our demonstration, the maximally achievable visibility is 50% [31], irrespective of the mean photon number (see Supplementary Information). Nevertheless, attenuated

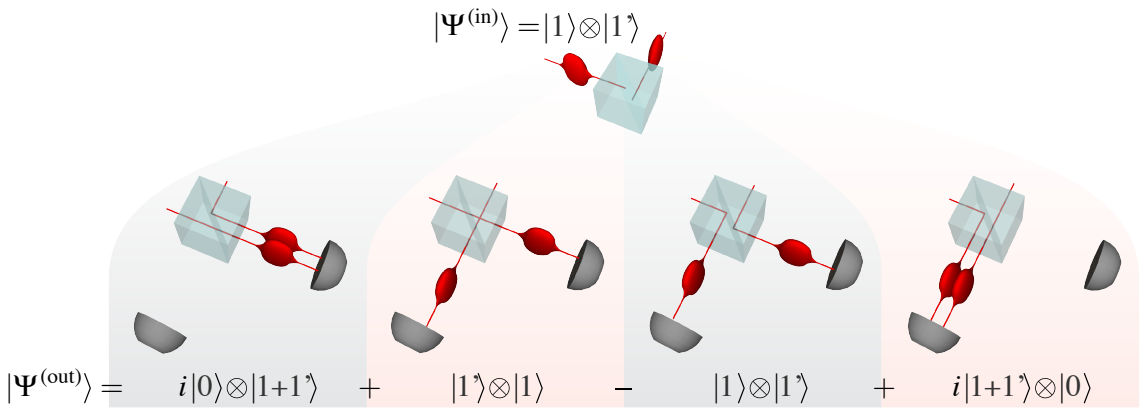

Figure D.1: Illustration of HOM-interference in the case of single photons at BS input $|\psi^{(in)}\rangle = |1, 1'\rangle$, where the prime on the latter input indicates the possibility to distinguish that input photon from the other in some degree of freedom e.g. by being polarized orthogonally. The four possible paths of the photons are illustrated, together with their corresponding output states. If the input photons are indistinguishable with respect to all degrees of freedom we can ignore the primes in the output states and the paths shown in the two central pictures are identical and, due to the different signs, thus cancel. This leaves in the output state $|\psi^{(out)}\rangle$ only the possibilities in which photons bunch. For distinguishable photons, e.g. having orthogonal polarizations, all paths are distinguishable and all terms remain in $|\psi^{(out)}\rangle$.

laser pulses are perfectly suitable for assessing the effect of our quantum memories on the photonic wavefunction. Any reduction of indistinguishability due to storage causes a reduction of visibility, albeit from maximally 50%. This approach extends the characterization of quantum memories using attenuated laser pulses [32] from assessing the preservation of quantum information during storage to assessing the preservation of the entire wavefunction, and from first- to second-order interference.

D.3 Measurements and Results

We first deactivate both quantum memories (see Supplementary Information), to examine the interference between directly transmitted pulses, and thereby establish a reference visibility for our experimental setup. We set the mean photon number per pulse before the memories to 0.6, i.e. to the single-photon level. Using the wave plates, we rotate the

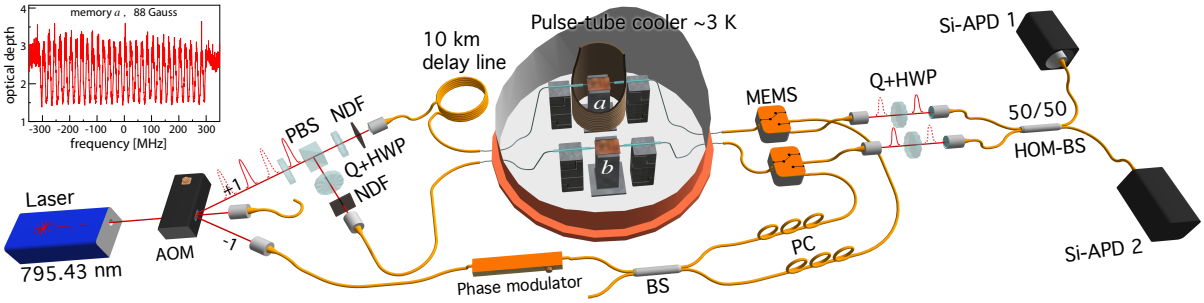

Figure D.2: Experimental setup. Light from a 795.43 nm wavelength CW laser passes through an acousto-optic modulator (AOM) driven by a sinusoidally varying signal. The first negative refraction order is fibre coupled into a phase modulator and, via a beam-splitter (BS), two polarization controllers (PCs) and two micro-electromechanical switches (MEMS), injected from the back into two Ti:Tm:$LiNbO_3$ waveguides (labelled a and b) cooled to 3 K [[33]]. Waveguide a is placed inside a superconducting solenoid. Using a linear frequency-chirping technique [34] we tailor AFCs with 600 MHz bandwidth and a few tens of MHz peak spacing, depending on the experiment, into the inhomogeneously broadened absorption spectrum of the thulium ions, as shown for crystal a in the inset. After 3 ms memory preparation time and 2 ms wait time we store and recall probe pulses during 3 ms. The 8 ns long probe pulses with $\approx$ 50 MHz Fourier-limited bandwidth are derived from the first positive diffraction order of the AOM output at a repetition rate of 2.5-3 MHz. Each pulse is divided into two spatial modes by a half-wave plate (HWP) followed by a polarizing beam-splitter (PBS). All pulses are attenuated by neutral-density filters (NDFs) and coupled into optical fibres and injected from the front into the Ti:Tm:$LiNbO_3$ waveguides. After exiting the memories (i.e. either after storage, or after transmission), the pulses pass quarter- and half-wave plates used to control their polarizations at the 50/50 BS (HOM-BS) where the two-photon interference occurs. Note that, to avoid first-order interference, pulses passing through memory a propagate through a 10 km fibre to delay them w.r.t. the pulses passing through memory b by more than the laser coherence length. Finally, they are detected by two single-photon detectors (actively quenched silicon avalanche photodiodes, Si-APDs) placed at the outputs of the beam-splitter, and coincidence detection events are analyzed with a time-to-digital convertor (TDC) and a computer.

polarizations of the pulses at the two HOM-BS inputs to be parallel (indistinguishable) or orthogonal (distinguishable). Employing (D.1) we find a visibility of $(47.9 \pm 3.1)\%$.

Subsequently, we activate memory a while keeping memory b off, and adjust the timing of the pulse preparation so as to interfere a recalled pulse from the active memory with a directly transmitted pulse from the inactive memory (see Supplementary Information). Pulses are stored for 30 ns in memory a, and the mean photon number per pulse at the quantum memory input is 0.6. Taking the limited storage efficiency of $\approx 1.5\%$ and coupling loss into account, this results in 3.4×10^{-4} photons per pulse at the HOM-BS inputs. As before, changing the pulse polarizations from mutually parallel to orthogonal, we find $V = (47.7 \pm 5.4)\%$, which equals our reference value within the measurement uncertainties.

As the final step, we activate both memories to test the feasibility of two-photon interference in a quantum-repeater scenario. We note that in a real-world implementation, memories belonging to different network nodes are not necessarily identical in terms of material properties and environment. This is captured by our setup where the two Ti:Tm:$LiNbO_3$ waveguides feature different optical depths and experience different magnetic fields (see Fig. D.2 and Supplementary Information). To balance the ensuing difference in memory efficiency we set the mean photon number per pulse before the less efficient and more efficient memories to 4.6 and 0.6, respectively, so that, as before, the mean photon numbers are 3.4×10^{-4} at both HOM-BS inputs. With the storage time of both memories set to 30 ns, we get $V = (47.2 \pm 3.4)\%$, in excellent agreement with the values from the previous measurements. The consistently high visibilities, compiled in the first column of Table D.1, hence confirm that our storage devices do not introduce any degradation of photon indistinguishability during the reversible mapping process, and that two-photon interference is feasible with photons recalled from separate quantum memories, even if the memories are different.

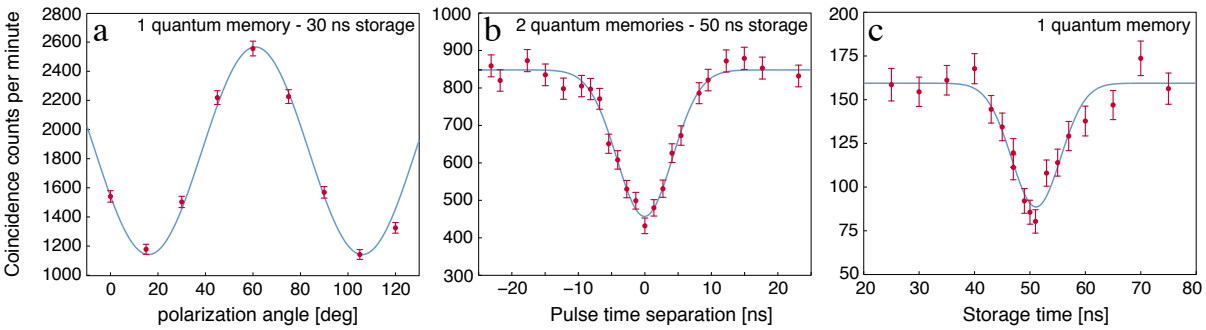

Figure D.3: HOM interference plot examples for one or two active memory configurations (as labelled). a) Varying mutual polarization difference. b) Varying temporal overlap by changing timing of pulse generation. c) Varying temporal overlap by changing storage time. The acquisition time per data point is 60 s in a,b and 120 s in c.

We now investigate in greater detail the change in coincidence count rates as photons gradually change from being mutually indistinguishable to completely distinguishable w.r.t. each degree of freedom accessible for change in single-mode fibres, i.e. polarization, temporal, and spectral modes (see Supplementary Information). To acquire data more efficiently we increase the mean number of photons per pulse at the memory input to between 10 and 50 (referred to as few-photon-level measurements). However, the mean photon number at the HOM-BS remains below one. Example data plots are shown in Fig. D.3, while the complete set of plots is supplied in the Supplementary Information Figs. D.6-D.8.

In Fig. D.3a we show the coincidence counts rates as a function of the polarization of the recalled pulse for the case of one active memory. The visibilities for all configurations (i.e. zero, one, or two active memories) extracted from fits to the experimental data are listed in column 2 of Table D.1. They are – as in the case of single-photon-level inputs – equal to within the experimental uncertainty.

Next, in Fig. D.3b, we depict the coincidence count rates as a function of the temporal overlap (adjusted by the timing of the pulse generation) for the two-memory configuration. Column 3 of Table D.1 shows the visibilities extracted from Gaussian fits

to the data, reflecting the temporal profiles of the probe pulses, for all configurations. Within experimental uncertainty, they are equal to each other. Alternatively, in the single-memory configuration, we also change the temporal mode overlap by adjusting the storage time of the pulse mapped to the quantum memory. Again the measured visibility of $V = (44.4 \pm 6.9)\%$ (see Fig. D.3c) is close to the theoretical maximum.

Finally, we vary the frequency difference between the two pulses (see Supplementary Information) to witness two-photon interference w.r.t. spectral distinguishability. For this measurement, we consider only the configurations in which neither, or a just single memory is active. In both cases the visibilities, listed in the last column of Table D.1, are around 43%. While this is below the visibilities found previously, for reasons discussed in the Supplementary Information, the key observation is that the quantum memory does not affect the visibility.

Table D.1: Experimental two-photon interference visibilities (%) for different degrees of freedom

Storage configuration	Single-photon level	Few-photon level		
	Polarization	Polarization	Temporal	Spectral
No-storage	47.9 ± 3.1	51.0 ± 5.6	42.4 ± 2.3	43.7 ± 1.7
Single-storage	47.7 ± 5.4	55.5 ± 4.1	47.6 ± 3.0	42.4 ± 3.5
Double-storage	47.2 ± 3.4	53.1 ± 5.3	46.1 ± 3.2	N. A.

As stated in the introduction, Bell-state measurements (BSM) with photonic qubits recalled from separate quantum memories are key ingredients for advanced applications of quantum communication. To demonstrate this important element, we consider the asymmetric (and arguably least favourable) case in which only one of the qubits is stored and recalled. Appropriately driving the AOM in Fig. D.2, we prepare the states $|\Psi_1\rangle$ and $|\Psi_2\rangle$, which describe time-bin qubits [35] of the form $|e\rangle$, $|l\rangle$, $\frac{1}{\sqrt{2}}(|e\rangle + |l\rangle)$, or $\frac{1}{\sqrt{2}}(|e\rangle - |l\rangle)$, where e and l, respectively, label photons in early or late temporal modes, which

are separated by 25 ns. The qubits are directed to the memories of which only one is activated. The mean photon number of the qubit that is stored is set to 0.6, yielding a mean photon number of both qubits at the HOM-BS input of 6.7×10^{-4}. We ensure to overlap pulses encoding the states $|\Psi_1\rangle$ and $|\Psi_2\rangle$ at the HOM-BS and count coincidence detections that correspond to a projection onto the $|\psi^-\rangle = \frac{1}{\sqrt{2}}(|e\rangle|l\rangle - |l\rangle|e\rangle)$ Bell state. This projection occurs if the two detectors click with 25 ns time difference [35]. Because $|\psi^-\rangle$ is antisymmetric w.r.t. any basis, the count rate is expected to reach a minimum value $\mathcal{R}_{\|}$ if the two input pulses are prepared in equal states, and a maximum value $\mathcal{R}_{\perp}$ if prepared in orthogonal states. Accordingly, we define an error rate that quantifies the deviation of the minimum count rate from its ideal value of zero:

$$e \equiv \frac{\mathcal{R}^{\|}}{\mathcal{R}^{\|} + \mathcal{R}^{\perp}} \,. \tag{D.2}$$

First, choosing to encode $|\Psi_1\rangle$ and $|\Psi_2\rangle$ in states $|e\rangle$ and $|l\rangle$ we obtain the error rate $e_{e/l}^{(\mathrm{exp})} = 0.039 \pm 0.037$, which is near the theoretical value of $e_{e/l}^{(\mathrm{QM})} = 0$ (see the Supplementary Information for derivations of the theoretical values and bounds). In addition it clearly violates the lower bound $e_{e/l}^{(\mathrm{CM})} = 0.33$ that can be obtained for a Bell-state measurement on two qubits of which one is recalled from a classical memory (CM). Note that values for $e_{e/l}^{(\mathrm{QM})}$ and $e_{e/l}^{(\mathrm{CM})}$ are independent of whether $|e\rangle$ and $|l\rangle$ qubits are encoded into single photons or attenuated laser pulses. Next, using instead the states $|+\rangle \equiv \frac{1}{\sqrt{2}}(|e\rangle + |l\rangle)$, and $|-\rangle \equiv \frac{1}{\sqrt{2}}(|e\rangle - |l\rangle)$ we measure $e_{+/-}^{(\mathrm{exp})} = 0.287 \pm 0.020$, which again only slightly exceeds the lowest possible value for attenuated laser pulses of $e_{+/-}^{(\mathrm{att,QM})} = 0.25$. The crucial observation is once more that $e_{+/-}^{(\mathrm{exp})}$ violates both the lower bound for qubits encoded into single photons $e_{+/-}^{(\mathrm{sing,CM})} = 0.33$ and attenuated laser pulses $e_{+/-}^{(\mathrm{att,CM})} = 0.417$ that are recalled from a classical memory.

D.4 Conclusion

Our demonstrations show that solid-state AFC quantum memories are suitable for two-photon interference experiments, even in the general case of storing the two photons an unequal number of times. With improved system efficiency [36] and multi-mode storage supplemented by read-out on demand[37, 38, 39], such memories can be used as synchronization devices in multi-photon experiments, which will allow increasing the number of photons that can be harnessed simultaneously for quantum information processing beyond the current limit of eight [40]. A subsequent goal is to develop workable quantum repeaters or, more generally, quantum networks, for which longer storage times are additionally needed. Depending on the required value, which may range from hundred micro-seconds [41] to seconds [1, 42], this may be achieved by storing quantum information in optical coherence, or it may require mapping of optical coherence onto spin states [30].

Acknowledgment

We thank Vladimir Kiselov for technical support and NSERC and AITF for financial support. J.A.S. thanks the Killam Trusts and D.O. thanks the Carlsberg Foundation for financial support.

Author Contributions

M.G., R.R. and W.S. fabricated the Ti:Tm:LiNbO3 waveguide and characterized it at room temperature. J.J., J.A.S., E.S., N.S., D.O. and W.T. all made significant contributions to the development of the experiment, measurement and analysis of the data, and preparation of the manuscript.

D.5 Supplementary Information

Memory operation and properties

A quantum memory is said to be activated when we configure the MEMS to allow the optical pumping light to reach the waveguide during the preparation stage and thus tailor an AFC in the inhomogeneously broadend absorption spectrum of thulium ions (see Fig. D.2). If the optical pumping is blocked, the memory is said to be deactivated and light entering the waveguide merely experiences constant attenuation over its entire spectrum. If a memory is activated, an incident photon is mapped onto a collective excitation of thulium ions in the prepared AFC and subsequently re-emitted at a time given by the inverse of the comb tooth spacing [30], i.e., $t = 1/\Delta$ (see Fig. D.2). In all cases, we adjust the mean photon number at the memory inputs so that mean photon numbers are equal at the HOM-BS inputs. This is required for achieving maximum visibility with attenuated laser pulses (further details later in Supplementary Information).

The two Ti:Tm:$LiNbO_3$ waveguides are fabricated identically but differ in terms of overall length, yielding optical depths of 2.5 for memory a and 3.2 for memory b. As shown in Figure 1, memory a is placed at the centre of a solenoid in a uniform magnetic field, while memory b is placed outside the solenoid and thus experiences only a much weaker stray field. Therefore it is not possible to achieve the optimal efficiency for both memories at the same time (further details later in Supplementary Information).

Changing degrees of freedom

a) The polarization degree is easily adjusted using the free-space half- and quarter-wave plate set at each HOM-BS input. For our measurements we rotate the half-wave plate in steps of either 45 or 7.5 degrees. **b)** The temporal separation δt between a pulse arriving at one of the HOM-BS inputs and the next pulse in the train arriving at the other input

can be expressed as $\delta t = \{nl/c\} \bmod \delta t_r$, where n is the refractive index of the fibres, $l \approx 10$ km is the path-length difference for pulses interacting with memory a and b, and δt_r is the repetition period of the pulse train from the AOM, which is set in the range of 350-400 ns. As we can change δt_r with 10 ps precision, we can tune δt on the ns scale. **c)** For the storage time scan, the recall efficiency decreases with storage time due to decoherence. Hence, we balance the mean photon number per pulse for stored and transmitted pulses for each storage time. **d)** Finally, to change the spectral overlap of the pulses input to the HOM-BS we can utilize that these pulses were generated at different times in the AOM and thus we can chose their carrier frequencies independently. We interchangeably drive the AOM by frequencies ν_a and ν_b and thus create two interlaced trains of pulses with different frequencies. Adjusting the pulse timing we can ensure that the pulses overlapped at the HOM-BS belong to different trains and thus have a spectral overlap given by $\delta\nu = \nu_a - \nu_b$. Due to the limited bandwidth of the AOM we are only able to scan $\delta\nu$ by 100 MHz, which, when compared to the 50 MHz pulse bandwidth, is not quite sufficient to make the pulses completely distinguishable. To achieve complete distinguishability, we supplement with a measurement using orthogonal polarizations at the inputs (further details later in Supplementary Information).

Preparing states for Bell-state measurement

For the Bell-state projection measurement we interchangeably prepare the time-bin qubits in either $|e\rangle$ or $|l\rangle$, or in $\frac{1}{\sqrt{2}}(|e\rangle + |l\rangle)$ and $\frac{1}{\sqrt{2}}(|e\rangle - |l\rangle)$ by setting the relative phase and intensity of the AOM drive signal. Adjusting the timing of the pulse preparation we ensure that qubits in different states overlap at the HOM-BS.

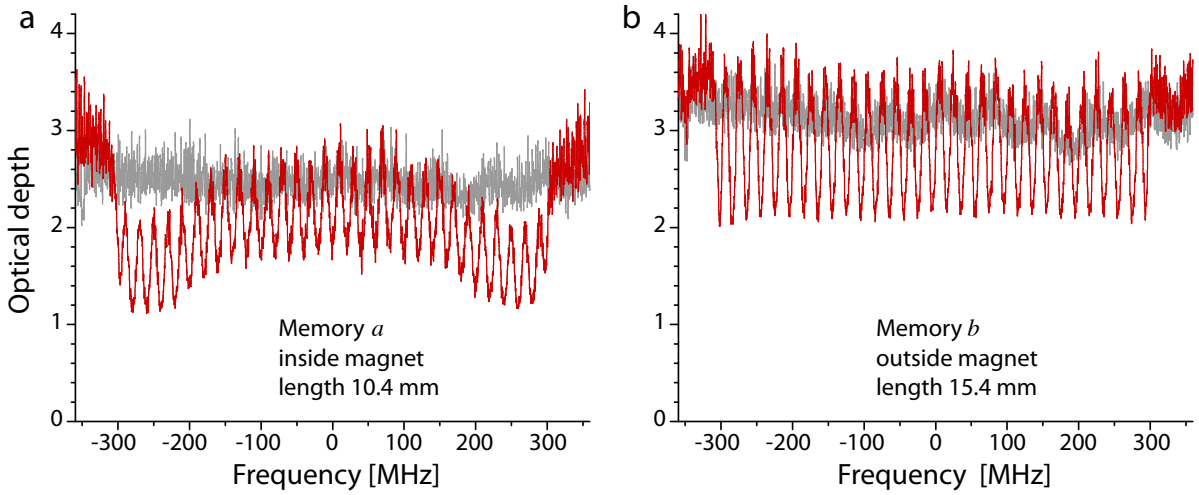

Figure D.4: Measured optical depths of our two Ti:Tm:$LiNbO_3$ waveguides as a function of frequency shift of the probing light imparted by the phase-modulator. Light grey traces show optical depths when the memories are inactive, i.e. no AFC is prepared. Dark red traces show the prepared AFCs at a magnetic field of 900 Gauss at the centre of the solenoid.

Properties of waveguide $LiNbO_3$ crystal and AFC

In the experimental configuration in which the HOM-interference occurs between two pulses recalled from separate quantum memories we pointed, in the main text, to the different properties of the two memory devices. In this section we wish to elaborate on the differences between the two memories based on their physical dissimilarity and measured optical depth as a function of frequency. Memory waveguide a is 10.4 mm long and crystal b is 15.4 mm long. The optical depths at 795.43 nm are around 2.5 and 3.2 for waveguide a and b, respectively, as shown by the light-grey curves in Fig. D.4 a,b, corresponding to the case in which the memories are not activated.

In order to spectrally tailor an AFC in Tm:$LiNbO_3$, a magnetic field must be applied along the crystal's c-axis so as to split the ground and excited level multiplets into their two nuclear Zeeman sublevels [33]. However, as one crystal is located at the centre of the setup's solenoid and the other outside the solenoid (see Fig. D.2) it is not possible to apply the same B-field at the two crystals. Thus when we activate both memories we generally

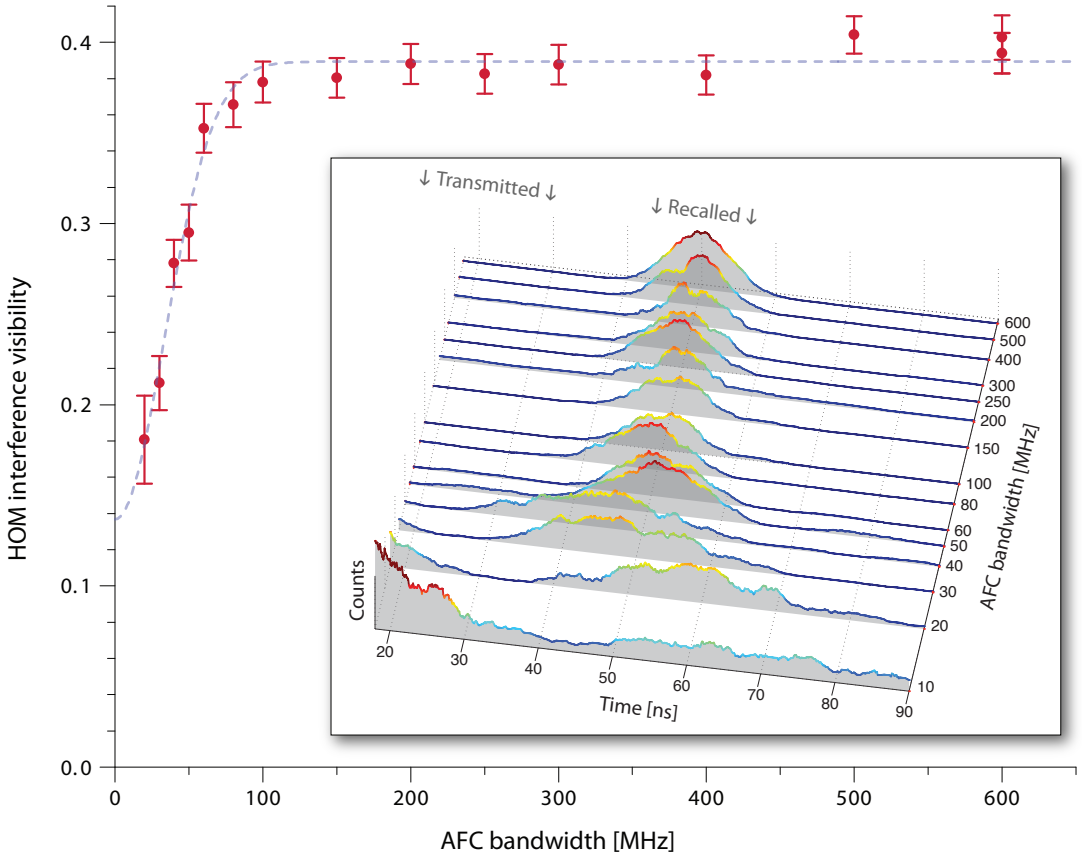

Figure D.5: HOM interference visibility if HOM-BS input pulses are recalled from AFCs with varying bandwidths. Insert: Histograms of recalled pulse detection times for different AFC bandwidths clearly showing broadening of recalled (and transmitted) pulses for bandwidths below 100 ns.

apply a magnetic field, which provides a reasonable balance in recall efficiencies but is not optimal for either memory. This circumstance is reflected by the different shapes of optical-depth profiles of the AFCs shown in red in Fig. D.4a,b.

Two-photon interference in imperfectly prepared memories

In all our demonstrations of the HOM interference we consistently observe that the HOM visibility is close to the theoretical maximum for coherent states. Yet, it is important to realize that an improperly configured AFC quantum memory does alter a stored photon's wavefunction, resulting in imperfect HOM interference with a non-stored photon.

To support this claim we activate only memory a, whose performance we change by varying the bandwidth of the AFC, and interfere the recalled pulses with pulses directly transmitted through the deactivated memory b. As the AFC bandwidth decreases below that of the probe pulses, the AFC effectively acts as a bandpass filter for the stored photons and we thus expect the recalled pulses to be temporally broadened w.r.t. the original pulse. This is observed in the insert of Fig. D.5, which shows smoothed histograms of photon detection events as a function time. It is worth noting that the small bandwidth AFC also acts as a bandpass filter for the transmitted pulse by virtue of the different effective optical depths inside and outside the AFC. Thus the broadened transmitted pulse starts to overlap with the echo for the narrow AFC bandwidth traces, as is also observed in the insert of Fig. D.5.

Another consequence of reducing the AFC bandwidth is that the overall efficiency of the quantum memory decreases, which causes an imbalance between the mean photon numbers at the HOM-BS inputs and thus reduces HOM interference visibility. We circumvent the change to the echo efficiency by adapting the mean photon number at the memory input so as to keep the mean photon number of the recalled pulse constant. With this remedial procedure, we assess the HOM visibility by changing the HOM-BS

inputs from parallel to orthogonal polarizations for a series of different AFC bandwidths. The HOM visibility in Fig. D.5 is steady for bandwidths from around 100 MHz and up. However, below 100 MHz the visibility begins to drop significantly. The dashed line is a fit of the visibilities to a Gaussian function with full-width at half-maximum (FWHM) of $79 \pm 4\ MHz$. Note, that the reason for the visibility being limited to around 40% is solely that, for this measurement, we do not go through the usual careful optimization steps.

With these measurements we have illustrated how a quantum memory could alter the photonic wavefunction resulting in a reduced HOM interference visibility. A combination of spectral and temporal distortion of the photonic wavefunction is indeed a common type of perturbation by quantum memories. [43, 44] It is particularly worth noting that the gradient-echo memory (GEM) quantum memory protocol, though similar to the AFC protocol, imparts a frequency chirp to the recalled pulse [45]. If not corrected, this feature constitutes a perturbation of the wavefunction of the recalled pulse, which may render it unsuitable for applications relying on two-photon interference.

Analytical model of second-order interference in coincidence measurements

In the following theoretical treatment we will derive expressions for the coincidence and single-detector counts in terms of probabilities. By multiplying these probabilities with the average experimental repetition rate we can easily calculate the predicted experimental count rates. To a large extent though, we will mainly be interested in relative probabilities or count rates between different settings of the degrees of freedom of pulses.

It is reasonably straightforward to derive the rates of detection of photons at the outputs of a BS (note that in this Supplementary Information, the HOM-BS of the main text will be referred to as just BS) In our case coherent states $|\alpha\rangle$ and $|\beta\rangle$, characterized by mean photon numbers $\langle \hat{a}^\dagger \hat{a} \rangle = |\alpha|^2$ and $\langle \hat{b}^\dagger \hat{b} \rangle = |\beta|^2$, occupy the two spatial input

modes of the BS. In the Fock-basis the coherent state can be represented as

$$|\alpha\rangle = \sum_{n=0}^{\infty} e^{-\frac{|\alpha|^2}{2}} \frac{\alpha^n}{\sqrt{n!}} |n\rangle = \sum_{n=0}^{\infty} e^{-\frac{|\alpha|^2}{2}} \frac{\alpha^n}{n!} (\hat{a}^\dagger)^n |0\rangle, \tag{D.3}$$

and similarly for $|\beta\rangle$.

To account for the cases of photons being distinguishable and indistinguishable at the BS we must allow for an additional degree of freedom in each of the spatial modes, e.g. polarization, frequency, or time. Thus we write the input state at one of the BS inputs as $|\alpha_1,\, \alpha_2\rangle \equiv |\alpha_1\rangle \otimes |\alpha_2\rangle$, where α_1 and α_2 are the coherent state amplitudes in the two orthogonal modes of the auxiliary degree of freedom within the same spatial mode. We treat the coherent state at the other BS input in a similar way.

For the case in which the fields at the inputs of the BS are distinguishable with respect to the auxiliary degree of freedom, the inputs to the BS are described as being in the state $|\alpha,\, 0\rangle|0,\, \beta\rangle \equiv |\alpha,\, 0\rangle \otimes |0,\, \beta\rangle$, whereas in the case of them being indistinguishable (up to a difference in the mean photon number) the input fields are written as $|\alpha,\, 0\rangle|\beta,\, 0\rangle$.

The BS is characterized by its reflection amplitude r and transmission amplitude $t = \sqrt{1 - |r|^2}$, which cause the input creation operators to transform as $\hat{a}^\dagger \to t\hat{c}^\dagger + ir\hat{d}^\dagger$ and $\hat{b}^\dagger \to ir\hat{c}^\dagger + t\hat{d}^\dagger$. With this in hand, we can compute the state in the BS outputs for any combination of Fock states at the inputs. When the two input states are indistinguishable, i.e. in the same auxiliary degree of freedom, we get [46]

$$|n, 0\rangle|m, 0\rangle \to \sum_{j=0}^{n} \sum_{k=0}^{m} K_{\|}(n, m, j, k)\, |j + k,\, 0\rangle|n + m - j - k,\, 0\rangle \tag{D.4}$$

$$K_{\|}(n, m, j, k) = t^{m-k+j} (ir)^{n-j+k} \sqrt{\binom{n}{j}\binom{m}{k}\binom{j+k}{j}\binom{n+m-j-k}{n-j}},$$

where the binomial coefficient $\binom{x}{y} = \frac{x!}{y!(x-y)!}$. For distinguishable input fields the output

state is slightly simpler

$$|n,0\rangle|0,m\rangle \rightarrow \sum_{j=0}^{n}\sum_{k=0}^{m} K_{\perp}(n,m,j,k)\,|j,\,k\rangle|n-j,\,m-k\rangle \tag{D.5}$$

$$K_{\perp}(n,m,j,k) = \sum_{j=0}^{n}\sum_{k=0}^{m} t^{m-k+j}(ir)^{n-j+k}\sqrt{\binom{j}{k}\binom{n-j}{m-k}}.$$

The above calculated output modes impinge on the single photon detectors (SPDs). These may be characterized by the probability of detecting an incident single photon. From this single photon detection probability η it is also possible to deduce the probability of detecting a pulse consisting of multiple photons, keeping in mind that, irrespective of the number of photons, only a single detection event can be generated. We write $p_1(n)$ for the probability for generating one detector event given n incident photons, and it is useful to note that it relates to the probability $p_0(n)$ of detecting nothing as $p_1(n) = 1 - p_0(n)$. The probability for not detecting n photons is, on the other hand, easily computed as $p_0(n) = (1-\eta)^n$. Since the two detectors at the BS outputs are independent, the probability $p_{11}(n,m)$ of generating a coincidence event, i.e. having simultaneous detection events in each of the detectors, given n and m photons in one and the other output is simply $p_{11}(n,m) = p_1(n)p_1(m)$. Thus the probability for a coincidence detection becomes

$$p_{11}(n,m) = \left[1-(1-\eta_1)^n\right]\left[1-(1-\eta_2)^m\right]\,, \tag{D.6}$$

where η_1 and η_2 are the single photon detection probabilities for detector 1 and 2, respectively. Expressing the coincidence detection probability in terms of Fock states at the BS input we have

$$\begin{aligned} P_{11}^{\parallel}(n,m) &= \sum_{j=0}^{n}\sum_{k=0}^{m} |K_{\parallel}(n,m,j,k)|^2\; p_{11}(j+k,\,n+m-j-k) \\ &= \sum_{j=0}^{n}\sum_{k=0}^{m} |K_{\parallel}(n,m,j,k)|^2\; \left[1-(1-\eta_1)^{j+k}\right]\left[1-(1-\eta_2)^{n+m-j-k}\right]\,, \end{aligned} \tag{D.7}$$

where $K_{\|}(n,m,j,k)$ should be substituted with the factor from (D.4). For distinguishable inputs we find a similar expression for $P_{11}^{\perp}(n,m)$ using the factor $K_{\perp}(n,m,j,k)$ from (D.5). It is assumed that the detector at a given spatial output mode is equally sensitive to photons in both auxiliary modes, i.e. it detects the states $|k,\, j\rangle$ and $|j,\, k\rangle$ with equal probability.

We are now in the position to formulate an expression for the different detection probabilities given a particular set of coherent input fields. The probability to generate a detection event in both detectors, given coherent input fields of amplitudes α and β, is

$$\mathcal{P}_{11}^{\|(\perp)}(\alpha,\beta) = \sum_{n=0}^{\infty}\sum_{m=0}^{\infty} e^{-|\alpha|^2-|\beta|^2}\frac{(\alpha^n\beta^m)^2}{n!\,m!}P_{11}^{\|(\perp)}(n,m)\,. \tag{D.8}$$

(Note that to distinguish the probability in (D.7), which is applicable to Fock states, from that in(D.8), which applies to coherent state inputs, we use P to denote the former and $\mathcal{P}$ for the latter.) This allows us to derive the visibility of the HOM interference on the two detectors as

$$\mathcal{V}_{11}(\alpha,\beta,\eta_1,\eta_2,r) = \frac{\mathcal{P}_{11}^{\perp}(\alpha,\beta)-\mathcal{P}_{11}^{\|}(\alpha,\beta)}{\mathcal{P}_{11}^{\perp}(\alpha,\beta)}\,, \tag{D.9}$$

where we have spelled out the parameters that affect the value of the visibility. The quantity $\mathcal{V}_{11}$ is referred to as the *HOM visibility*.

Simplified model for HOM visibility

To gain some intuitive understanding of the way the HOM visibility is affected by the experimental parameters we resort to a couple of approximations. Firstly, we assume equal mean photon numbers at the inputs of the beam-splitter, $|\alpha|^2 = |\beta|^2 \equiv \mu$, the BS ratio to be 50:50 (i.e. $r = t = 1/\sqrt{2}$), and the detectors to have equal single photon detection probability $\eta_1 = \eta_2 \equiv \eta$. Secondly, since we normally work at very low mean photon numbers $\mu < 1$ only the first couple of terms of (D.3) need to be included.

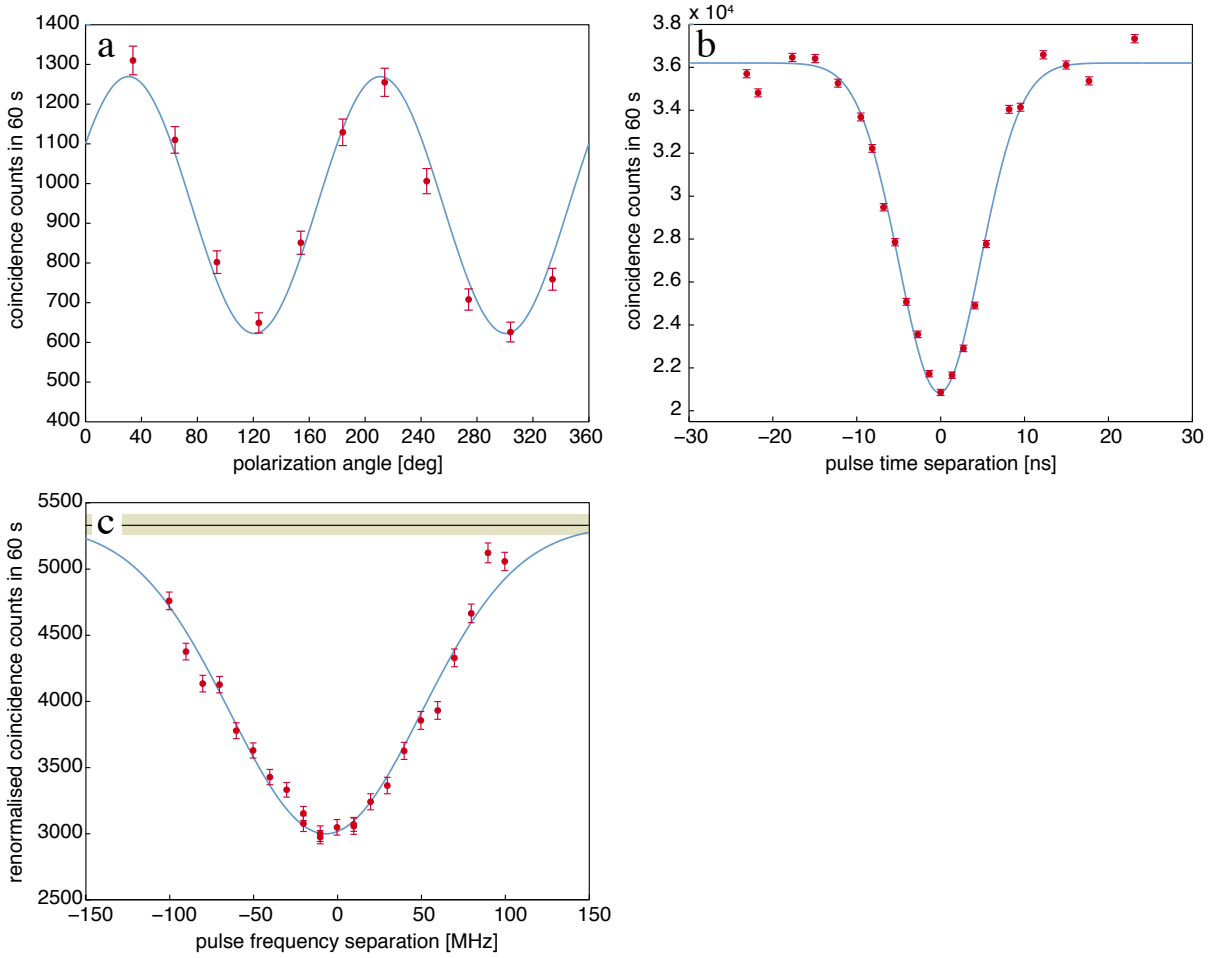

Figure D.6: HOM interference manifested in coincidence counts between BS outputs with inactive memories. a) Changing the polarization angle between the pulses yields a HOM visibility of $\mathcal{V} = 50.96 \pm 5.56\%$. b) Varying the temporal overlap of the pulses produces $\mathcal{V} = 42.43 \pm 2.27\%$. c) Altering the frequency overlap of the pulse spectra results in $\mathcal{V} = 43.72 \pm 1.70\%$.

Specifically, we Taylor expand $e^{-\mu/2}$ and keep only terms in the sum up to 2^{nd} order in μ. Thus, for the coincidence detection events we get the probabilities

$$\mathcal{P}_{11}^{\parallel} = \eta^2 \frac{\mu^2}{2} \tag{D.10}$$

$$\mathcal{P}_{11}^{\perp} = \eta^2 \mu^2 \,, \tag{D.11}$$

which results in a HOM visibility of

$$\mathcal{V}_{11} = \frac{1}{2} \,. \tag{D.12}$$

A key point is that the HOM visibility of 50% is independent of the mean photon number μ. This observation can be explained by noting that in this low order treatment the coincidences in the case of indistinguishable input modes stem mostly from events in which two photons are present at the same input, which occurs with probability $p_0 p_2 + p_2 p_0$. For distinguishable input modes the coincidences stem from all events that contain two photons at the input, i.e. $p_1 p_1 + p_0 p_2 + p_2 p_0$. Since, according to (D.3), for coherent input states, all of these probabilities scale in the same way with the mean photon number, their ratio, and thus the visibility of (D.9), is constant for all mean photon numbers.

Compilation of experimental results for HOM interference at the few-photon level

Here we show the plots of coincidence count rates on which the few-photon values in Table D.1 of the main text are based. We restate that coincidence count rates are proportional to coincidence probabilities by a factor that is given by the average experimental repetition rate. Moreover, when calculating the HOM visibility, only the relative probabilities or count rates in a measurement are important. In the experiments we change the mutual polarization, time separation, or frequency difference of the pulses at the BS (in the main text referred to as HOM-BS) input as explained in the earlier in the Supplementary Information.

Deactivated memories: We present the data in order of the number of activated memories starting with none, i.e. pulses merely pass through attenuated to the BS. In Fig. D.6a) we show the coincidence counts as we vary the polarization difference of the pulses at the two inputs of the BS. Fitting the data to a sine function we obtain a visibility of $\mathcal{V} = 50.96 \pm 5.56\%$. In Fig. D.6b) we display the coincidence counts as we step the temporal separation of the pulses at the two inputs of the BS. The count rates for these measurements are generally higher than all the other count rates presented. This is because this data was acquired by looking at coincidences between the transmitted part of the probe pulses in the configuration of two active quantum memories (shown in Fig. D.8b)). Hence, the balancing of the mean photon number in the transmitted pulses done less meticulously, which is the most likely reason for the observed lower visibility of $\mathcal{V} = 42.43 \pm 2.27\%$ in this case.

Fig. D.6c) shows the coincidence count rates as function of the frequency difference of the two pulses at the BS inputs. The horizontal line and surrounding shaded band shown in Fig. D.6c) – as well as in Fig. D.7c) – give the coincidence counts for completely distinguishable input photons as obtained by making the polarizations orthogonal. As noted earlier in the Supplementary Information, it is necessary to resort to the polarization degree of freedom in order to make the pulses completely distinguishable. The visibility from the fit is noticeably lower than that obtained when we change the other degrees of freedom. There are two main reasons for this. The first is that, in order to generate pulses with different frequencies, we drive the AOM at the limits of its bandwidth. This, in turn, necessitates setting the RF drive signal amplitude high whereby the frequency purity of the signal is contaminated by higher-order harmonics. Although it is not expected to change the maximal interference value occurring when the pulses are generated with the same modulation frequency, it will alter the shape of the interference as a function of the pulse frequency difference. Hence, the fitted Gaussian curve, assuming a Fourier limited

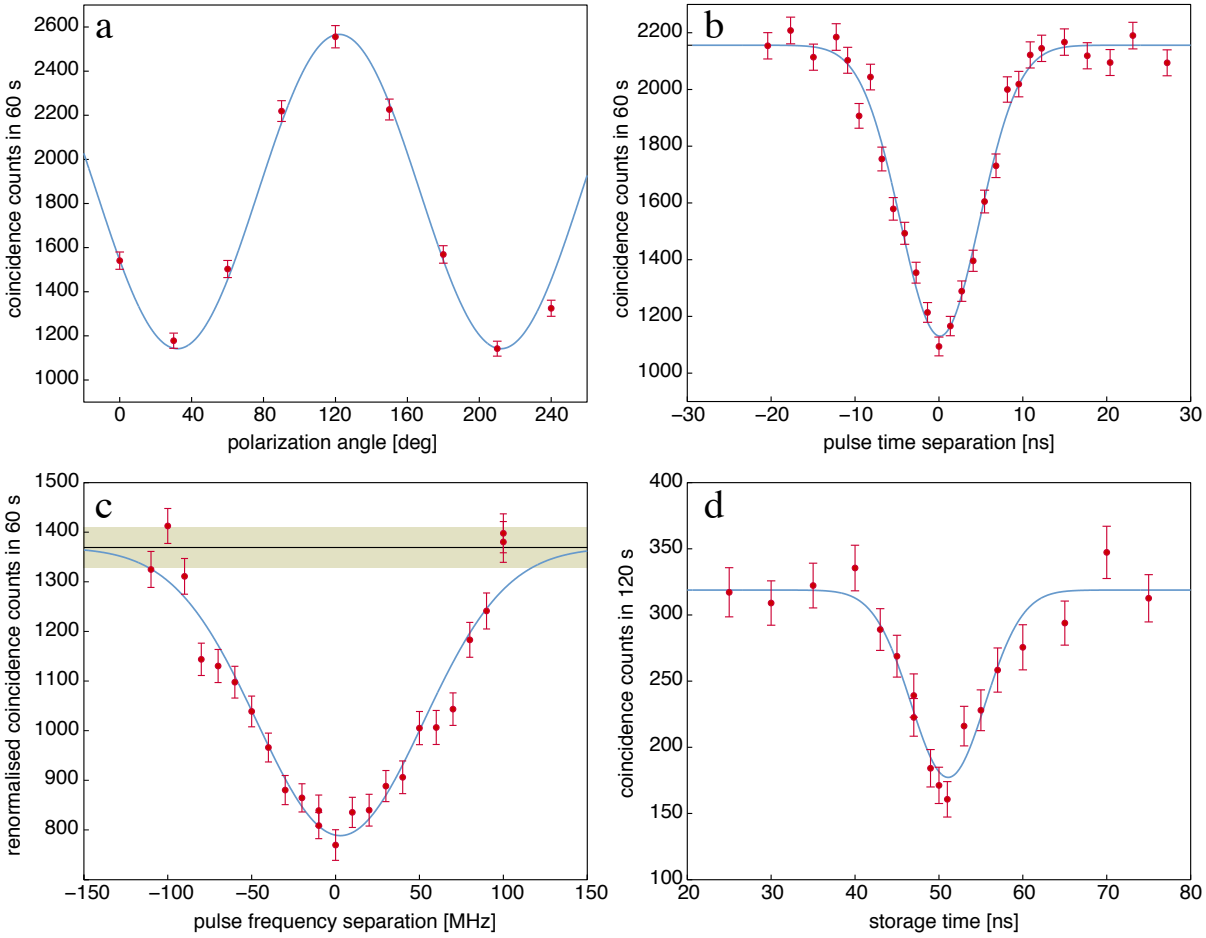

Figure D.7: HOM interference manifested in coincidence counts between BS outputs with one active memory. a) Changing the polarization angle between the pulses yields a HOM visibility of $\mathcal{V} = 55.51 \pm 4.09\%$. b) Varying the temporal overlap of the pulses produces $\mathcal{V} = 47.57 \pm 2.96\%$. c) Altering the frequency overlap of the pulse spectra results in $\mathcal{V} = 42.40 \pm 3.51\%$. d) Varying the storage time of the quantum memory and thus the temporal overlap of the pulses yields $\mathcal{V} = 44.4 \pm 6.9\%$.

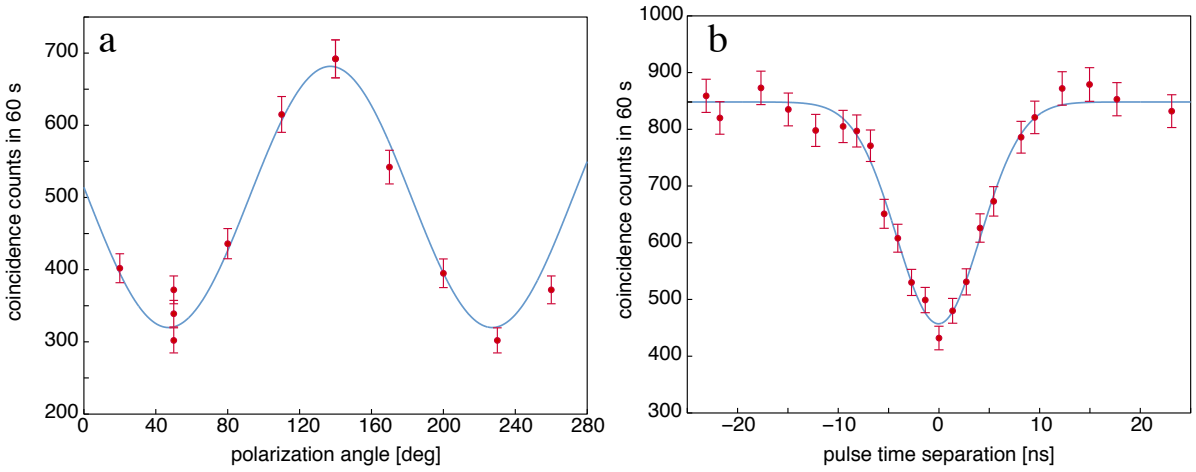

Figure D.8: HOM interference manifested in coincidence counts between BS outputs with two active memories. a) Changing the polarization angle between the pulses yields a HOM visibility of $\mathcal{V} = (53.1 \pm 5.3)\%$. b) Varying the temporal overlap of the pulses produces $\mathcal{V} = (46.1 \pm 3.2)\%$.

pulse, may not correctly reproduce the actual frequency dependence of the interference. Indeed, the minimum coincidence rates consistently fall below the fitted curve. A second factor reducing the observed visibility is related to the need to adjust the AOM drive amplitude to balance the bandwidth limitation. The limited accuracy with which we are able to estimate the appropriate RF amplitude results in significant scattering of the coincidence counts due to variations in input pulse intensities. To amend this we have found that it is necessary to normalize the points to the count rates on the individual detectors, as indicated on the y-axis of plot Fig. D.7c. Unfortunately, the manifestation of the HOM interference in the single-detector count rates – which will be elaborated later in the Supplementary Information – means that such a normalization procedure tends to reduce the visibility in the coincidence counts.

One active memory: Next in line are the plots for the case in which only memory a is activated, while the other is left inactive. In Fig. D.7 we present the coincidence count rates when changing the same degrees of freedom as in case of both memories being

inactive. Additionally, in Fig. D.7d, we plot the coincidence count rates when changing the storage time in the quantum memory.

Two active memories: Lastly, we present the plots for the case in which both memories are activated. Due to limitations in our current setup it is not possible to simultaneously generate two quantum memories with different storage times, and therefore we do not acquire a storage time scan when both memories are active. Furthermore, we skip the characterization with respect to the spectral degree of freedom. The coincidence count data for the remaining two degrees of freedom are plotted in Fig. D.8, which also includes the appropriate fits.

Manifestation of HOM interference in single detector counts

We also evaluate the effect of the two-photon interference on the counts registered by a single detector. This is easily done by amending the detection probability to the case of one detection event in one detector and any number of events x (i.e. $x = 0, 1$) in the other detector. We arrive at

$$p_{1x}(n, m) = 1 - (1 - \eta_1)^n \,. \tag{D.13}$$

This expression can be inserted into (D.7) to calculate $P_{1x}^{\|(\perp)}(n, m)$, which, through (D.8), gives us $\mathcal{P}_{1x}^{\|(\perp)}(\alpha, \beta)$, and from which the *single-detector visibility* $\mathcal{V}_{1\mathrm{x}}$ is defined analogous to (D.9).

We can formulate a simplified expression by using the same approximations as in the case of coincidence detections:

$$\mathcal{P}_{1x}^{\|} = \eta\mu + \eta\left(2 - \frac{3\eta}{4}\right)\mu^2 \tag{D.14}$$

$$\mathcal{P}_{1x}^{\perp} = \eta\mu + \eta\left(2 - \frac{\eta}{2}\right)\mu^2 \,, \tag{D.15}$$

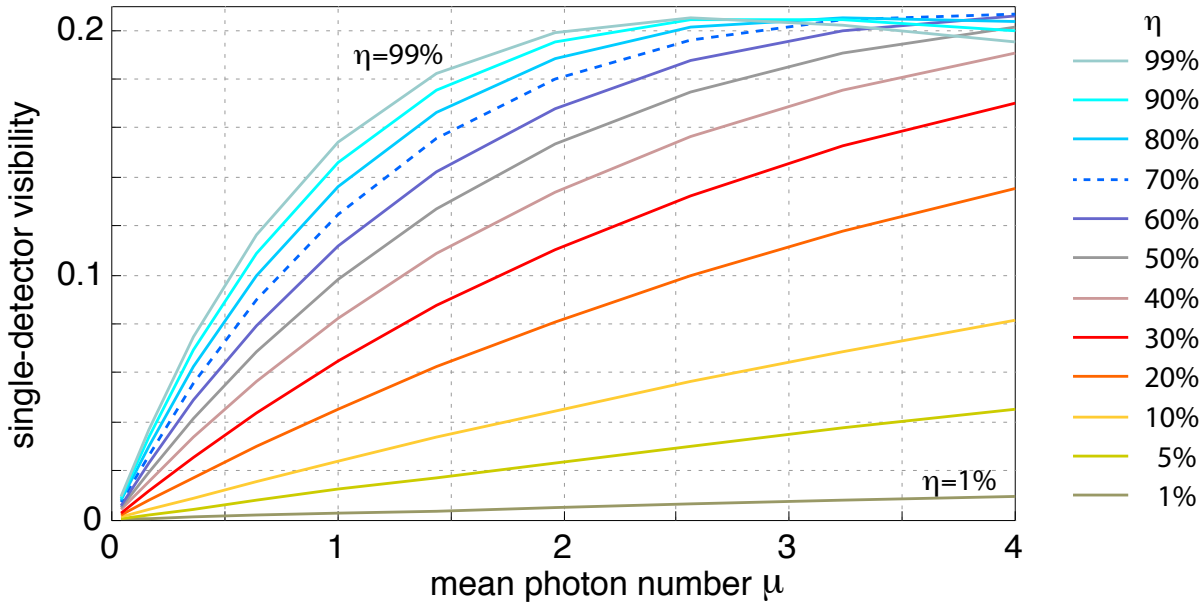

Figure D.9: Plots of single-detector visibility as a function of the mean photon number for detectors with a range of single photon detection probabilities η. The $\eta = 70\%$ trace, highlighted with a dashed line, corresponds approximately to our detectors, which have $65\% \leq \eta \leq 75\%$.

from which we get the single-detector visibility

$$\mathcal{V}_{1x} = \frac{\eta\mu}{4 + 2(4-\eta)\mu}\,. \tag{D.16}$$

In the limit of low detector efficiency, $\mathcal{V}_{1x} \approx 0$, since, in that case, the probability of detecting two photons impinging on the detector is simply twice that of detecting one. This nulls the limitation that only a single detection event can be generated per pulse. Furthermore, the single-detector visibility also goes to zero for very low mean photon numbers. In this case it is very unlikely to have two photons either at the *same* or at *different* input ports of the BS, hence most of the single detector counts stem from single photons from either one or the other input of the BS. It is interesting to note that if η is known for a detector, then, from observing the single-detector visibility (see (D.16)), it is in principle possible to estimate the mean photon number per pulse μ.

Another important consequence of the manifestation of two-photon interference in the single-detector counts is that the single-detector counts cannot generally be used to

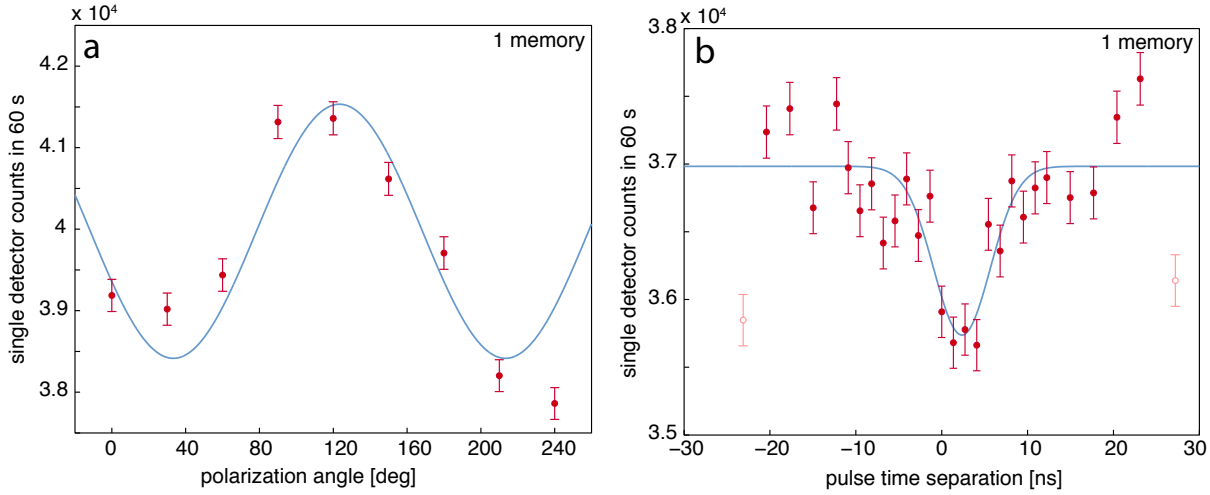

Figure D.10: HOM interference manifested in single-detector counts in the case of one active quantum memory when changing a) polarization and b) time difference between pulses at BS input. For the polarization scan in a) we find $\mathcal{V}_{1x} = (7.51 \pm 3.80)\%$ and for the time scan in b) we get $\mathcal{V}_{1x} = (7.75 \pm 3.25)\%$. For this measurement we only recorded the single-detector counts from Si-APD 1.

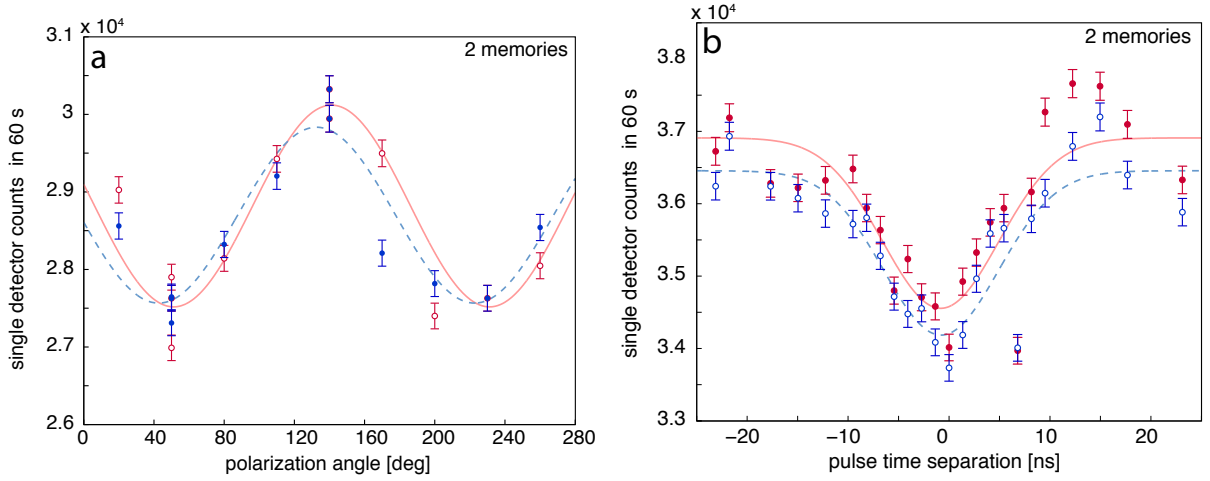

Figure D.11: HOM interference manifested in single-detector counts in the case of two active quantum memories when changing a) polarization and b) time difference between pulses at BS input. For the polarization scan in a) we find $\mathcal{V}_{1x} = (8.64 \pm 2.50)\%$ and $\mathcal{V}_{1x} = (7.60 \pm 2.36)\%$ for Si-APD 1 and 2, respectively. For the time scan in b) we measure $\mathcal{V}_{1x} = (6.38 \pm 2.01)\%$ and $\mathcal{V}_{1x} = (6.23 \pm 1.61)\%$ for Si-APD 1 and 2, respectively.

normalize the coincidence counts w.r.t. fluctuations in the input pulse intensities. Only for detectors with low detection efficiency or very low mean photon numbers, in which case $\mathcal{V}_{1x} \approx 0$, is this normalization possible.

Experimental results on HOM interference manifested in single-detector counts

First, in Figure D.10, we present the single-detector counts corresponding to the coincidence counts depicted in Figure D.7a,b. In the case where we vary the polarization and time separation we see a clear change in the single-detector counts, which, moreover, is evidently correlated with the change in coincidence counts. The count variation due to the two-photon interference is somewhat masked by the single-detector count scatter, which is due to intensity fluctuations mainly in the light going through the 10 km delay line. We fit the data in Figures D.10a and b with a sine and Gaussian function, respectively. For the former we find a mean photon number of $\mu = 0.52$ while from the latter we estimate $\mu = 0.54$. From the number of single-detector counts there is some evidence to conclude that the light intensity is about 15% higher. To this should be added about 25% uncertainty for the intensity at the BS w.r.t. the intensity at the detector due to variation in the loss in the fibre mating sleeves. Finally, the scatter of the counts makes the fits themselves rather uncertain. Nevertheless, the mere fact that the two-photon interference is manifested in the single-detector counts validates the order of magnitude of the mean photon number, as depicted in Fig. D.9.

Figure D.11 depicts the single-detector counts corresponding to the coincidence counts depicted in Figure D.8a,b. Again, from fitting the appropriate functions to the polarization and time data yields visibilities around 7%, corresponding to mean photon numbers of around $\mu = 0.5$.

Bell-state measurement

In this section we derive an analytical expression for the coincidence count rates corresponding to projections onto the $|\psi^-\rangle$ Bell-state for time-bin qubits detected by the two detectors at the output of the HOM-BS. To that end, we will introduce a number of approximations as we did previously in order to calculate the HOM interference in the coincidence counts. In the limit of low mean photon numbers, two coherent states impinging onto the two inputs of a 50:50 BS can be represented in terms of Fock states as

$$\begin{aligned} |\psi\rangle_{ab} &= \sqrt{p(1,1)}|11\rangle_{a,b} + \sqrt{p(2,0)}|20\rangle_{a,b} + \sqrt{p(0,2)}|02\rangle_{a,b} \\ &= \left(\sqrt{p(1,1)}(\hat{a}^\dagger \otimes \hat{b}^\dagger) + \frac{1}{\sqrt{2!}}\left[\sqrt{p(2,0)}((\hat{a}^\dagger)^2 \otimes I) + \sqrt{p(0,2)}(I \otimes (\hat{b}^\dagger)^2)\right]\right)|00\rangle_{a,b} \quad , \end{aligned} \tag{D.17}$$

where the subscripts on the state vector refer to the order of listing the input modes, i.e. $|00\rangle_{a,b} \equiv |0\rangle_a \otimes |0\rangle_b$. The factors written as $p(n,m)$ denote the probability of having n and m photons in mode a and b, and are given by $p(n,m) = |({}_a\langle n| \otimes_b \langle m|)(|\alpha\rangle_a \otimes |\beta\rangle_b)|^2 = \frac{e^{-(|\alpha|^2+|\beta|^2)}}{n!m!}(|\alpha|^2)^n(|\beta|^2)^m$. Stemming from the low mean photon number assumption, we do not include terms with more than two photons. Assuming that our detectors are noiseless, terms with a total of one or no photons are also left out as they cannot generate any coincidence counts.

For a time-bin qubit, the Fock state is created in a superposition of two temporal modes, i.e., an *early* (e) and a *late* (l) mode, by the creation operators for the spatial input mode $x^\dagger$ ($x^\dagger = a^\dagger, b^\dagger$) of the beam-splitter, as

$$(\hat{x}^\dagger)^n|0\rangle_x \rightarrow \left[\cos\left(\frac{\theta_x}{2}\right)\,\hat{x}_e^\dagger \otimes I + e^{i\phi_x}\sin\left(\frac{\theta_x}{2}\right)\,I \otimes \hat{x}_l^\dagger\right]^n |00\rangle_{xe,xl} \quad , \tag{D.18}$$

where $\cos\left(\frac{\theta_x}{2}\right)$ and $\sin\left(\frac{\theta_x}{2}\right)$ are the amplitudes of, and ϕ_x is the relative phase between, the two temporal modes composing the time-bin qubit. The subsript xe refers to the early time-bin of the spatial mode x and similarly for xl. Note, that we sometimes simplify the

notation for the time-bin qubit states as $|e\rangle_x \equiv |10\rangle_{xe,xl} = (\hat{x}_e^\dagger \otimes I)|00\rangle_{xe,xl}$. If we insert the expression in (D.18) in place of the $\hat{a}$ and $\hat{b}$ operators in (D.17) we get the expression for the wavefunction $|\psi(\theta_a, \phi_a, \theta_b, \phi_b)\rangle_{ab}$ for time-bin qubits at the HOM-BS inputs. We split this expression into the various contributions given in (D.17)

$$
\begin{aligned}
(\hat{a}^\dagger \otimes \hat{b}^\dagger)|00\rangle_{ab} \rightarrow \frac{1}{2}\Bigg[& \left(ie^{i\phi_b} \cos\!\left(\frac{\theta_a}{2}\right) \sin\!\left(\frac{\theta_b}{2}\right) + ie^{i\phi_a} \sin\!\left(\frac{\theta_a}{2}\right) \cos\!\left(\frac{\theta_b}{2}\right) \right) \left(\hat{c}_e^\dagger \hat{c}_l^\dagger + \hat{d}_e^\dagger \hat{d}_l^\dagger \right) \\
& + \left(e^{i\phi_b} \cos\!\left(\frac{\theta_a}{2}\right) \sin\!\left(\frac{\theta_b}{2}\right) - e^{i\phi_a} \sin\!\left(\frac{\theta_a}{2}\right) \cos\!\left(\frac{\theta_b}{2}\right) \right) \left(\hat{c}_e^\dagger \hat{d}_l^\dagger - \hat{c}_e^\dagger \hat{d}_l^\dagger \right) \\
& + ie^{i(\phi_a+\phi_b)} \sin\!\left(\frac{\theta_a}{2}\right) \sin\!\left(\frac{\theta_b}{2}\right) \left((\hat{c}_l^\dagger)^2 + (\hat{d}_l^\dagger)^2 \right) \\
& + i \cos\!\left(\frac{\theta_a}{2}\right) \cos\!\left(\frac{\theta_b}{2}\right) \left((\hat{c}_e^\dagger)^2 + (\hat{d}_e^\dagger)^2 \right) \Bigg] |0000\rangle_{ce,cl,de,dl}
\end{aligned} \tag{D.19a}
$$

$$
\begin{aligned}
((\hat{a}^\dagger)^2 \otimes I)|00\rangle_{ab} \rightarrow \frac{1}{2}\Bigg[& 2e^{i\phi_a} \cos\!\left(\frac{\theta_a}{2}\right) \sin\!\left(\frac{\theta_a}{2}\right) \left(\hat{c}_e^\dagger \hat{c}_l^\dagger - \hat{d}_e^\dagger \hat{d}_l^\dagger \right) \\
& + i2e^{i\phi_a} \cos\!\left(\frac{\theta_a}{2}\right) \sin\!\left(\frac{\theta_a}{2}\right) \left(\hat{c}_e^\dagger \hat{d}_l^\dagger + \hat{c}_l^\dagger \hat{d}_e^\dagger \right) \\
& + \cos^2\!\left(\frac{\theta_a}{2}\right) \left((\hat{c}_e^\dagger)^2 + i2\hat{c}_e^\dagger \hat{d}_e^\dagger - (\hat{d}_e^\dagger)^2 \right) \\
& + e^{i2\phi_a} \sin^2\!\left(\frac{\theta_a}{2}\right) \left((\hat{c}_l^\dagger)^2 + i2\hat{c}_l^\dagger \hat{d}_l^\dagger - (\hat{d}_l^\dagger)^2 \right) \Bigg] |0000\rangle_{ce,cl,de,dl}
\end{aligned} \tag{D.19b}
$$

and similarly for $(I \otimes (\hat{b}^\dagger)^2)|00\rangle_{ab}$. Again, the subscripts on the state vector refer to the order of listing the temporal and spatial modes, e.g. *ce* labels the early bin of the spatial output mode *c*.

We will look for coincidence detection events that correspond to projections onto the Bell-state $|\psi_-\rangle_{cd} = \frac{1}{\sqrt{2}}(\hat{c}_e^\dagger \hat{d}_l^\dagger - \hat{c}_l^\dagger \hat{d}_e^\dagger)|0000\rangle_{ce,cl,de,dl}$. Such projections correspond to a detection event in the early time-bin in one detector followed by a detection event in the late time-bin in the other detector. This projection occurs with a probability $\mathcal{P}_-(\theta_a, \phi_a, \theta_b, \phi_b) = |\ {}_{cd}\langle\psi_-|\psi(\theta_a, \phi_a, \theta_b, \phi_b)\rangle_{cd}|^2$, which can be computed by combining (D.19) with (D.17). Assuming equal mean photon numbers at the two inputs $|\alpha|^2 = |\beta|^2 \equiv \mu$ and averaging over the coherent state phases, i.e. the complex angle between α

and β, we get the expression

$$\mathcal{P}_-(\theta_a,\phi_a,\theta_b,\phi_b) \propto \frac{\mu^2 e^{-2\mu}}{8}\left[4\sin^2\left(\frac{\theta_a+\theta_b}{2}\right)+\sin^2\big(\theta_a\big)+\sin^2\big(\theta_b\big)\right.$$
$$\left.-\,2\sin\big(\theta_a\big)\sin\big(\theta_b\big)\Big(1+\cos\big(\phi_a-\phi_b\big)\Big)\right]. \qquad \text{(D.20)}$$

With this we are able to calculate the probabilities of projection onto $|\psi^-\rangle$ for different combinations of qubits at the two BS inputs, i.e. for different choices of the angles θ_x and ϕ_x. In turn, this allows us to calculate the $|\psi^-\rangle$ Bell-state measurement error rate as

$$e \equiv \frac{\mathcal{P}_-^{\parallel}}{\mathcal{P}_-^{\parallel}+\mathcal{P}_-^{\perp}}\,, \qquad \text{(D.21)}$$

where $\mathcal{P}_-^{\parallel}$ is the projection probability when the two input qubit states are identical, i.e. $\phi_a=\phi_b$ and $\theta_a=\theta_b$, while $\mathcal{P}_-^{\perp}$ is the projection probability for two orthogonal input qubit states. This is also defined in terms of count rates in (D.2) in the main text. We will now treat a number of relevant cases.

Expected and observed error rates when $\phi_a=\phi_b=0$.

Using the simplified notation this corresponds to the case were the input qubit states are of the form $|\psi\rangle=\cos\left(\frac{\theta_x}{2}\right)|e\rangle+\sin\left(\frac{\theta_x}{2}\right)|l\rangle$. When depicted on the Bloch sphere these qubits span the xz-plane. Using (D.20) we compute the projection probability as

$$\mathcal{P}_-(\theta_a,0,\theta_b,0) \propto \frac{\mu^2 e^{-2\mu}}{8}\left[4\sin^2\left(\frac{\theta_a+\theta_b}{2}\right)+\sin^2\big(\theta_a\big)+\sin^2\big(\theta_b\big)-4\sin\big(\theta_a\big)\sin\big(\theta_b\big)\right]. \qquad \text{(D.22)}$$

We are interested in the probability $\mathcal{P}_-^{\parallel}$ for the case in which the input qubits are parallel ($\theta_a=\theta_b$) and $\mathcal{P}_-^{\perp}$ for the case in which the input qubit states are orthogonal ($\theta_a=\theta_b-\pi$). Specifically, when we prepare two qubits (one at each input of the BS) in state $|e\rangle$, or two qubits in state $|l\rangle$, we expect $\mathcal{P}_-^{\parallel}=0$. The probability for observing a projection

onto $|\psi\rangle$ increases as we change θ_a (or θ_b), and reaches a maximum $\mathcal{P}_-^\perp$ if one qubit is in state $|e\rangle$ and the other one in $|l\rangle$. Hence, using the expression for the error rate above ((D.21)), we find $e_{e/l}^{(\mathrm{att})} = 0$.

We now turn to measuring the coincidence rates for all combinations of $|e\rangle$ and $|l\rangle$ input states, and thus extracting $\mathcal{P}_-^\parallel$ and $\mathcal{P}_-^\perp$, using 0.6 photons per qubit at the memory input. More precisely, we prepare the input qubit state $|e\rangle_a \otimes |e\rangle_b$ to measure $\mathcal{P}_-^{\parallel(1)}$ and then $|e\rangle_a \otimes |l\rangle_b$ to measure $\mathcal{P}_-^{\perp(1)}$. Subsequently, we prepare the input qubit state $|l\rangle_a \otimes |l\rangle_b$ to measure $\mathcal{P}_-^{\parallel(2)}$ and then $|l\rangle_a \otimes |e\rangle_b$ to measure $\mathcal{P}_-^{\perp(2)}$. These yield the average values $\mathcal{P}_-^\parallel = (\mathcal{P}_-^{\parallel(1)} + \mathcal{P}_-^{\parallel(2)})/2$ and $\mathcal{P}_-^\perp = (\mathcal{P}_-^{\perp(1)} + \mathcal{P}_-^{\perp(2)})/2$, from which we compute the experimental error rate $e_{e/l}^{(\mathrm{exp})} = 0.039 \pm 0.037$, which is near the theoretical lowest value of $e_{e/l}^{(\mathrm{att})} = 0$.

Expected and observed error rates when $\theta_a = \theta_b = \pi/2$. In this case the two input qubits are in equal superpositions of early and late bins, that is of the form $|\psi\rangle = \frac{1}{\sqrt{2}}\big(|e\rangle + e^{i\phi_x}|l\rangle\big)$. On the Bloch sphere these are qubits that lie in the xy-plane. In this case we compute

$$\mathcal{P}_-(\pi/2, \phi_a, \pi/2, \phi_b) \propto \frac{\mu^2 e^{-2\mu}}{4}\big(2 - \cos(\phi_a - \phi_b)\big)\,, \tag{D.23}$$

Thus the $|\psi^-\rangle$ Bell-state projection probability is smallest – but nonzero – when $\phi_a - \phi_b = 0$, i.e. the qubit states are parallel, and largest when the phases differ by π, i.e. the qubit states are orthogonal. Inserting these values for $\mathcal{P}_-^\parallel$ and $\mathcal{P}_-^\perp$ into (D.21) results in an expected error rate of $e_{+/-}^{(\mathrm{att})} = 0.25$.

Using again 0.6 photons per qubit, we measure the coincidence counts for $\phi_a - \phi_b = 0$ and π giving us $P_-^\parallel$ and $P_-^\perp$, respectively. From these we get an error rate of $e_{+/-}^{(\mathrm{exp})} = 0.287 \pm 0.020$, which is slightly above the theoretical bound. This indicates that either the measurement suffers from imperfections such as detector noise or the modes at the BS

are not completely indistinguishable, which in turn could be due imperfectly generated qubit states or imperfect storage of the qubit in the quantum memory. To be conservative in our assessment of our quantum memory we assume that the entire increase of the measured values of $e^{(\mathrm{exp})}$ is due to the memory fidelity being less than one.

Bounds for attenuated laser pulses stored in quantum and classical memories: We now compare the performance of our Bell-state measurement to a number of relevant bounds assuming always that any imperfections arise from the imperfect storage of the photon in the memory. We will derive bounds to the error rate in the case of one qubit being stored in either a classical memory (CM) or quantum memory (QM). To accommodate this scenario we assume that the memory performs the following operation $|\psi\rangle\langle\psi| \to F|\psi\rangle\langle\psi| + (1-F)|\psi^{\perp}\rangle\langle\psi^{\perp}|$, where F denotes the fidelity of the stored state and $|\psi^{\perp}\rangle$ is the state orthogonal to $|\psi\rangle$. For a classical memory $F^{\mathrm{CM}} = 0.667$ [[47]] whereas for a quantum memory $F^{\mathrm{QM}} = 1$.

Doing the replacement $\mathcal{P}_{-}^{\parallel} \to F\mathcal{P}_{-}^{\parallel} + (1-F)\mathcal{P}_{-}^{\perp}$ and likewise for $\mathcal{P}_{-}^{\perp}$ we can express the error rate expected after imperfect storage of one of the pulses partaking in the Bell-state measurement:

$$e = \frac{F\mathcal{P}_{-}^{\parallel} + (1-F)\mathcal{P}_{-}^{\perp}}{\mathcal{P}_{-}^{\parallel} + \mathcal{P}_{-}^{\perp}}\,, \tag{D.24}$$

where in this case the probabilities $\mathcal{P}_{-}^{\parallel}$ and $\mathcal{P}_{-}^{\perp}$ refer to those expected without the memory. Since the expected values for $\mathcal{P}_{-}^{\parallel}$ and $\mathcal{P}_{-}^{\perp}$ differ between the e/l and $+/-$ bases we treat them separately.

Beginning with the e/l basis we use (D.24) with the values from (D.22) to derive a bound for the error rate of the Bell-state measurement for one of the two qubits being recalled from a quantum or a classical memory. We find that $e_{e/l}^{(\mathrm{att})} = 1 - F$, and hence we establish the two bounds $e_{e/l}^{(\mathrm{att,QM})} = 0$ and $e_{e/l}^{(\mathrm{att,CM})} = 0.333$. This clearly shows

that a classical memory would cause a larger error rate than the $e_{e/l}^{(\mathrm{exp})} = 0.039 \pm 0.037$ measured after storage in our memory. We can also reverse the equations and estimate our memory's fidelity based on the measured error rate. In this case, inserting $e_{e/l}^{(\mathrm{exp})}$ into (D.24), we deduce the value $F_{e/l}^{\mathrm{exp}} = 0.961 \pm 0.037$.

We now turn to the $+/-$ basis. For attenuated laser pulses we insert into (D.24) the values $\mathcal{P}_{-}^{\parallel} = 1/4$ and $\mathcal{P}_{-}^{\perp} = 3/4$ computed from (D.23), which enables us to relate the error rate to the memory fidelity as $e_{+/-} = (3-2F)/4$. Thus, one obtains the theoretical lower bound on the error rate $e_{+/-}^{(\mathrm{att,QM})} = 0.250$ for an ideal quantum memory ($F^{\mathrm{QM}} = 1$) and $e_{+/-}^{(\mathrm{att,CM})} = 0.417$ with an optimal classical storage device ($F^{\mathrm{CM}} = 2/3$). We make the observation that our experimental error rate $e_{+/-}^{(\mathrm{exp})} = 0.287 \pm 0.020$ is much below the bound for a classical memory. Based on the experimental error rate $e_{+/-}^{(\mathrm{exp})} = 0.287 \pm 0.020$ we derive an experimental value for the memory fidelity of $F_{+/-}^{\mathrm{exp}} = 0.926 \pm 0.041$. The estimates of the memory fidelity $F_{e/l}^{\mathrm{exp}}$ and $F_{+/-}^{\mathrm{exp}}$ derived from our measurements in two bases are equal to within the experimental error. This together with the fact that their values are well above 0.667 reaffirms our claim that our storage device outperforms a classical memory.

We emphasize once more that we have assumed that the reduction in error rates is due solely to the memory and thus indicates the fidelity of the memory. However, this is likely not the case as imperfections in the state preparation and detector noise also contribute to the reduction in error rate.

Bounds for single photons stored in quantum and classical memories: Although we do not use single photon sources for the experiments reported here, it is interesting to determine how well our results measure up to those that could have been obtained if single photon sources had been employed. In the following we will derive the error rate for the Bell-state measurement using qubits encoded into single photons. To this end we step

back to (D.17), and note that for single photon sources all probabilities are 0 except for $p(1,1)$, which describes the probability of having a single photon at each BS input. Thus, in the output state we only need to keep the terms from (D.19a), which in turn means that the Bell-state projection probability can be written as

$$P_{-}(\theta_a,\phi_a,\theta_b,\phi_b) \propto \frac{1}{4}\left[\sin^2\left(\frac{\theta_a+\theta_b}{2}\right)+\sin^2\left(\frac{\theta_a-\theta_b}{2}\right)-\sin(\theta_a)\sin(\theta_b)\cos(\phi_a-\phi_b)\right]. \tag{D.25}$$

It is easily seen that for any two parallel input qubit states ($\theta_a = \theta_b$ and $\phi_a = \phi_b$) we get $P_{-}^{\parallel} = 0$. Therefore, irrespective of the projection probability for orthogonal input qubit states the expected error rate is always $e^{(\mathrm{sing})} = 0$, where *sing* identifies this value as belonging to the single photon case.

Gauging the effect of storing one of the single photons partaking in the Bell-state measurement in a memory is thus independent of the basis and using (D.24) we derive $e^{(\mathrm{sing,QM})} = 1 - F^{\mathrm{QM}} = 0$ and $e^{(\mathrm{sing,CM})} = 0.333$. Contrasting the error rate expected for a photon stored in a classical memory with the two values $e_{e/l}^{(\mathrm{exp})} = 0.039 \pm 0.037$ and $e_{+/-}^{(\mathrm{exp})} = 0.287 \pm 0.020$ obtained experimentally, we recognize that both are well below $e^{(\mathrm{sing,CM})}$. This means that even with a single photon source at ones disposal the error rates that we measured could not have been attained with a classical memory.

Experiments at mean photon numbers above one. In this final section we will explore in greater detail the HOM interference dependence on the angle $\phi_a - \phi_b$ between a set of equal superposition qubit states $|\psi\rangle_x = \frac{1}{\sqrt{2}}\left(|e\rangle + e^{i\phi_x}|l\rangle\right)$, which in line with the preceding sections belong to the $+/-$ basis. According to (D.23) the coincidence count rates vary as function of $\cos\left(\phi_a - \phi_b\right)$. In Fig. D.12 we show measured coincidence count rates as function of $\phi_a - \phi_b$ for a mean photon number per qubit before the memory of around 20. As expected the coincidence detection probability reaches its maximum $\mathcal{P}_{-}^{\perp}$ when two input qubits are orthogonal ($\phi_a - \phi_b = \pi$) and when they are identical ($\phi_a - \phi_b = 0$)

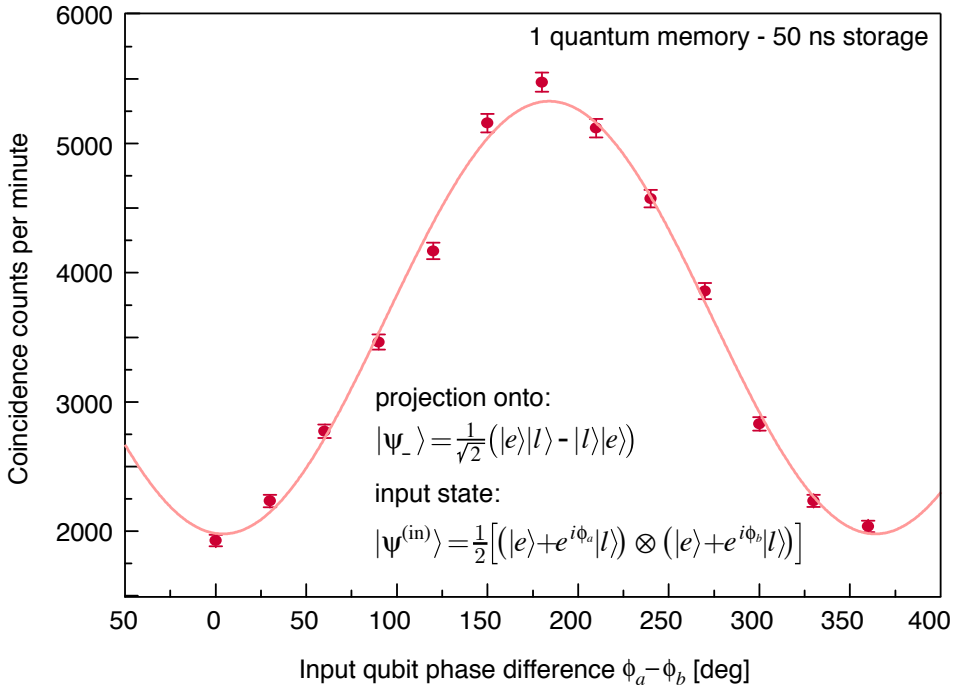

Figure D.12: Rate of projection of pairs of time-bin qubits with relative phase $\phi_a - \phi_b$ onto $|\psi^-\rangle$. Each data point was acquired over 60 s

it reaches a minimum $\mathcal{P}_-^{\parallel}$. It is natural to define a Bell-state measurement visibility as

$$\mathcal{V} = \frac{\mathcal{P}_-^{\perp} - \mathcal{P}_-^{\parallel}}{\mathcal{P}_-^{\perp}} \tag{D.26}$$

analogous to (D.1) in the main text. Using values obtained from a cosine fit to the data in Fig. D.12 yeilds $\mathcal{V}_{+/-}^{\text{exp}} = (62.9 \pm 5.2)\%$. Comparing (D.26) with (D.21) it is easily seen that $\mathcal{V}$ and e are related as $e = (1 - \mathcal{V}_{+/-})/(2 - \mathcal{V}_{+/-})$. We can then use the expected error rates to find the corresponding Bell-state measurement visibilities. Using $e_{+/-}^{att} = 0.25$ we get a theoretical value $\mathcal{V}_{+/-}^{\text{att}} = 66.7\%$. In conclusion, our experimental Bell-state measurement visibility is only slightly below and within the experimental error actually equal to the expected value.

Bibliography

[1] Sangouard, N., Simon, C., de Riedmatten, H. & Gisin, N. Quantum repeaters based on atomic ensembles and linear optics. *Rev. Mod. Phys.* **83**, 33–80 (2011).

[2] Kimble, H. J. The quantum internet. *Nature* **453**, 1023–1030 (2008). URL `http://dx.doi.org/10.1038/nature07127`.

[3] Kok, P. *et al.* Linear optical quantum computing with photonic qubits. *Rev. Mod. Phys.* **79**, 135–174 (2007). URL `http://link.aps.org/doi/10.1103/RevModPhys.79.135`.

[4] Lvovsky, A. I., Sanders, B. C. & Tittel, W. Optical quantum memory. *Nat Photon* **3**, 706–714 (2009). URL `http://dx.doi.org/10.1038/nphoton.2009.231`.

[5] Saglamyurek, E. *et al.* Broadband waveguide quantum memory for entangled photons. *Nature* **469**, 512–515 (2011). URL `http://dx.doi.org/10.1038/nature09719`. `1009.0490v2`.

[6] Clausen, C. *et al.* Quantum storage of photonic entanglement in a crystal. *Nature* **469**, 508–511 (2011). URL `http://dx.doi.org/10.1038/nature09662`. `1009.0489v2`.

[7] Saglamyurek, E. *et al.* Conditional detection of pure quantum states of light after storage in a tm-doped waveguide. *Phys. Rev. Lett.* **108**, 083602 (2012). URL `http://link.aps.org/doi/10.1103/PhysRevLett.108.083602`.

[8] Zhang, H. *et al.* Preparation and storage of frequency-uncorrelated entangled photons from cavity-enhanced spontaneous parametric downconversion. *Nat Photon* **5**, 628–632 (2011). URL `http://dx.doi.org/10.1038/nphoton.2011.213`.

[9] Specht, H. P. *et al.* A single-atom quantum memory. *Nature* **473**, 190–193 (2011). URL http://dx.doi.org/10.1038/nature09997.

[10] England, D. G. *et al.* High-fidelity polarization storage in a gigahertz bandwidth quantum memory. *Journal of Physics B: Atomic, Molecular and Optical Physics* **45**, 124008 (2012). URL http://stacks.iop.org/0953-4075/45/i=12/a=124008.

[11] Hong, C. K., Ou, Z.-Y. & Mandel, L. Measurement of subpicosecond time intervals between two photons by interference. *Phys. Rev. Lett.* **59**, 2044–2046 (1987). URL http://link.aps.org/doi/10.1103/PhysRevLett.59.2044.

[12] Kaltenbaek, R., Blauensteiner, B., Żukowski, M., Aspelmeyer, M. & Zeilinger, A. Experimental interference of independent photons. *Phys. Rev. Lett.* **96**, 240502 (2006). URL http://link.aps.org/doi/10.1103/PhysRevLett.96.240502.

[13] Beugnon, J. *et al.* Quantum interference between two single photons emitted by independently trapped atoms. *Nature* **440**, 779–782 (2006). URL http://dx.doi.org/10.1038/nature04628.

[14] Maunz, P. *et al.* Quantum interference of photon pairs from two remote trapped atomic ions. *Nat Phys* **3**, 538–541 (2007). URL http://dx.doi.org/10.1038/nphys644.

[15] Sanaka, K., Pawlis, A., Ladd, T. D., Lischka, K. & Yamamoto, Y. Indistinguishable photons from independent semiconductor nanostructures. *Phys. Rev. Lett.* **103**, 053601 (2009). URL http://link.aps.org/doi/10.1103/PhysRevLett.103.053601.

[16] Patel, R. B. *et al.* Two-photon interference of the emission from electrically tunable remote quantum dots. *Nat Photon* **4**, 632–635 (2010). URL http://dx.doi.org/10.1038/nphoton.2010.161.

[17] Flagg, E. B. *et al.* Interference of single photons from two separate semiconductor quantum dots. *Phys. Rev. Lett.* **104**, 137401 (2010). URL http://link.aps.org/doi/10.1103/PhysRevLett.104.137401.

[18] Lettow, R. *et al.* Quantum interference of tunably indistinguishable photons from remote organic molecules. *Phys. Rev. Lett.* **104**, 123605 (2010). URL http://link.aps.org/doi/10.1103/PhysRevLett.104.123605.

[19] Bernien, H. *et al.* Two-photon quantum interference from separate nitrogen vacancy centers in diamond (2011). URL http://arxiv.org/abs/1110.3329v1. 1110.3329v1.

[20] Sipahigil, A. *et al.* Quantum interference of single photons from remote nitrogen-vacancy centers in diamond. *Phys. Rev. Lett.* **108**, 143601 (2012). URL http://link.aps.org/doi/10.1103/PhysRevLett.108.143601.

[21] Felinto, D. *et al.* Conditional control of the quantum states of remote atomic memories for quantum networking. *Nat Phys* **2**, 844–848 (2006). URL http://dx.doi.org/10.1038/nphys450.

[22] Chanelière, T. *et al.* Quantum interference of electromagnetic fields from remote quantum memories. *Phys. Rev. Lett.* **98**, 113602 (2007). URL http://link.aps.org/doi/10.1103/PhysRevLett.98.113602.

[23] Yuan, Z.-S. *et al.* Synchronized independent narrow-band single photons and efficient generation of photonic entanglement. *Phys. Rev. Lett.* **98**, 180503 (2007). URL http://link.aps.org/doi/10.1103/PhysRevLett.98.180503.

[24] Chen, Y.-A. *et al.* Memory-built-in quantum teleportation with photonic and atomic qubits. *Nat Phys* **4**, 103–107 (2008). URL http://dx.doi.org/10.1038/nphys832.

[25] Yuan, Z.-S. *et al.* Experimental demonstration of a bdcz quantum repeater node. *Nature* **454**, 1098–1101 (2008). URL http://dx.doi.org/10.1038/nature07241.

[26] Weinfurter, H. Experimental bell-state analysis. *Europhysics Letters* **25**, 559–564 (1994).

[27] Mattle, K., Weinfurter, H., Kwiat, P. G. & Zeilinger, A. Dense coding in experimental quantum communication. *Phys. Rev. Lett.* **76**, 4656–4659 (1996). URL http://link.aps.org/doi/10.1103/PhysRevLett.76.4656.

[28] Bouwmeester, D. *et al.* Experimental quantum teleportation. *Nature* **390**, 575–579 (1997). URL http://dx.doi.org/10.1038/37539.

[29] Pan, J.-W., Bouwmeester, D., Weinfurter, H. & Zeilinger, A. Experimental entanglement swapping: Entangling photons that never interacted. *Phys. Rev. Lett.* **80**, 3891–3894 (1998). URL http://link.aps.org/doi/10.1103/PhysRevLett.80.3891.

[30] Afzelius, M., Simon, C., de Riedmatten, H. & Gisin, N. Multimode quantum memory based on atomic frequency combs. *Phys. Rev. A* **79**, 052329 (2009).

[31] Mandel, L. Photon interference and correlation effects produced by independent quantum sources. *Phys. Rev. A* **28**, 929–943 (1983). URL http://link.aps.org/doi/10.1103/PhysRevA.28.929.

[32] de Riedmatten, H., Afzelius, M., Staudt, M. U., Simon, C. & Gisin, N. A solid-state light-matter interface at the single-photon level. *Nature* **456**, 773–777 (2008). URL http://dx.doi.org/10.1038/nature07607.

[33] Sinclair, N. *et al.* Spectroscopic investigations of a ti:tm:linbo3 waveguide for photon-echo quantum memory. *Journal of Luminescence* **130**, 1586

– 1593 (2010). URL http://www.sciencedirect.com/science/article/pii/S0022231309006243. Special Issue based on the Proceedings of the Tenth International Meeting on Hole Burning, Single Molecule, and Related Spectroscopies: Science and Applications (HBSM 2009) - Issue dedicated to Ivan Lorgere and Oliver Guillot-Noel.

[34] Reibel, R. R., Barber, Z. W., Fischer, J. A., Tian, M. & Babbitt, W. R. Broadband demonstrations of true-time delay using linear sideband chirped programming and optical coherent transients. *Journal of Luminescence* **107**, 103 – 113 (2004). URL http://www.sciencedirect.com/science/article/pii/S0022231303002072. Proceedings of the 8th International Meeting on Hole Burning, Single Molecule, and Related Spectroscopies: Science and Applications.

[35] Tittel, W. & Weihs, G. Photonic entanglement for fundamental tests and quantum communication. *Quant. Inf. Comp.* **1**, 3–56 (2001).

[36] Afzelius, M. & Simon, C. Impedance-matched cavity quantum memory. *Phys. Rev. A* **82**, 022310 (2010). URL http://link.aps.org/doi/10.1103/PhysRevA.82.022310.

[37] Sinclair, N. *et al.* Frequency multimode quantum memory featuring recall on demand. In preparation.

[38] Afzelius, M. *et al.* Demonstration of atomic frequency comb memory for light with spin-wave storage. *Phys. Rev. Lett.* **104**, 040503 (2010). URL http://link.aps.org/doi/10.1103/PhysRevLett.104.040503.

[39] Gündoğan, M., Mazzera, M., Ledingham, P. M., Cristiani, M. & de Riedmatten, H. Coherent storage of temporally multimode light using a spin-wave atomic frequency comb memory (2013). URL http://arxiv.org/abs/1301.3048. 1301.3048.

[40] Yao, X.-C. *et al.* Observation of eight-photon entanglement. *Nat Photon* **6**, 225–228 (2012). URL http://dx.doi.org/10.1038/nphoton.2011.354.

[41] Munro, W. J., Harrison, K. A., Stephens, A. M., Devitt, S. J. & Nemoto, K. From quantum multiplexing to high-performance quantum networking. *Nat Photon* **4**, 792–796 (2010). URL http://dx.doi.org/10.1038/nphoton.2010.213.

[42] Timoney, N., Usmani, I., Jobez, P., Afzelius, M. & Gisin, N. Single-photon-level optical storage in a solid-state spin-wave memory (2013). URL http://arxiv.org/abs/1301.6924. 1301.6924.

[43] Chaneliere, T. *et al.* Storage and retrieval of single photons transmitted between remote quantum memories. *Nature* **438**, 833–836 (2005). URL http://dx.doi.org/10.1038/nature04315.

[44] Eisaman, M. D. *et al.* Electromagnetically induced transparency with tunable single-photon pulses. *Nature* **438**, 837–841 (2005). URL http://dx.doi.org/10.1038/nature04327.

[45] Moiseev, S. A. & Arslanov, N. M. Efficiency and fidelity of photon-echo quantum memory in an atomic system with longitudinal inhomogeneous broadening. *Phys. Rev. A* **78**, 023803 (2008). URL http://link.aps.org/doi/10.1103/PhysRevA.78.023803.

[46] Rarity, J. G., Tapster, P. R. & Loudon, R. Non-classical interference between independent sources. *Journal of Optics B: Quantum and Semiclassical Optics* **7**, S171 (2005). URL http://stacks.iop.org/1464-4266/7/i=7/a=007.

[47] Massar, S. & Popescu, S. Optimal extraction of information from finite quantum ensembles. *Phys. Rev. Lett.* **74**, 1259–1263 (1995). URL http://link.aps.org/doi/10.1103/PhysRevLett.74.1259.

Appendix E

Paper 5

New Journal of Physics 16, 065019 (2014)

An integrated processor for photonic quantum states using a broadband light-matter interface

Erhan Saglamyurek[1], Neil Sinclair[1], Joshua A. Slater[1], Khabat Heshami [1], Daniel Oblak[1], and Wolfgang Tittel[1]

[1]*Institute for Quantum Information Science, and Department of Physics and Astronomy, University of Calgary, 2500 University Drive NW, Calgary, Alberta T2N 1N4, Canada*

Abstract

Faithful storage and coherent manipulation of quantum optical pulses are key for long distance quantum communications and quantum computing. Combining these functions in a light-matter interface that can be integrated on-chip with other photonic quantum technologies, e.g. sources of entangled photons, is an important step towards these applications. To date there have only been a few demonstrations of coherent pulse manipulation utilizing optical storage devices compatible with quantum states, and that only in atomic gas media (making integration difficult) and with limited capabilities. Here we describe how a broadband waveguide quantum memory based on the Atomic Frequency Comb (AFC) protocol can be used as a programmable processor for essentially arbitrary spectral and temporal manipulations of individual quantum optical pulses. Using weak

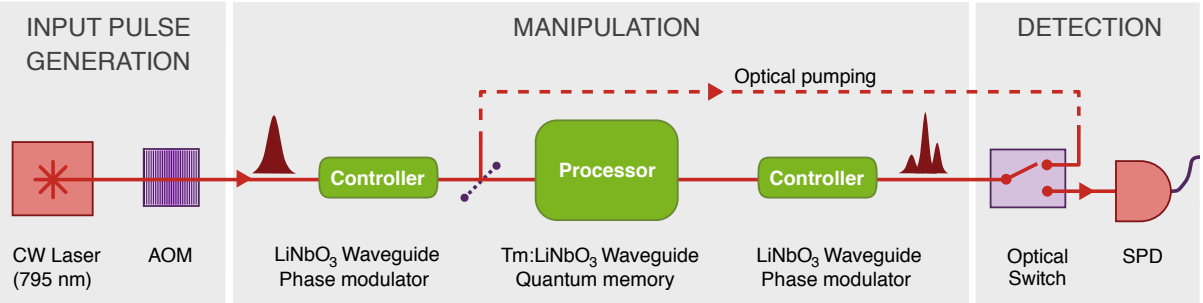

Figure E.1: Simplified diagram of experimental setup for optical pulse manipulation based on AFC processor.

coherent optical pulses at the few photon level, we experimentally demonstrate sequencing, time-to-frequency multiplexing and demultiplexing, splitting, interfering, temporal and spectral filtering, compressing and stretching as well as selective delaying. Our integrated light-matter interface offers high-rate, robust and easily configurable manipulation of quantum optical pulses and brings fully practical optical quantum devices one step closer to reality. Furthermore, as the AFC protocol is suitable for storage of intense light pulses, our processor may also find applications in classical communications.

E.1 Introduction

Since the invention of the laser, a lot of effort has been put into manipulating optical pulses for applications in science and engineering. One important application is photon-based quantum information processing, which promises unbreakable secret key distribution and unprecedented computational power [1, 2]. The realization of these applications requires coherently storing as well as manipulating quantum optical pulses in order to process and distribute quantum information [2, 3, 4]. Combining storage and manipulation in a light-matter interface that can be integrated on-chip with other photonic components reduces the complexity and thus facilitates the development of future

quantum technologies [2, 5, 6, 7]. To date there have only been a few investigations that employ a quantum storage device for coherent optical pulse manipulation [8, 9, 10, 11, 12]. However, these demonstrations feature various intrinsic limitations that impact future use in practical settings. First, all previous demonstrations rely on atomic vapor, making integration difficult. Second, most show limited processing capabilities, which restricts their use to a small number of specific applications [9, 10, 12]. Third, the bandwidths in [8, 9, 10, 11] were at most a few MHz, which, accordingly, constraints the minimum duration of the processed pulses to a few microsecond. Finally, the number of simultaneously storable (and hence processable) qubits in the quantum storage devices considered before is severely limited [8, 9, 10, 11, 12, 13].

In this paper, we propose and demonstrate a universal, large-bandwidth and multimode approach to temporal and spectral manipulation of individual quantum optical pulses – it relies on introducing a broadband quantum memory based on a Tm:$LiNbO_3$ waveguide and the Atomic Frequency Comb (AFC) protocol [14, 15] between two $LiNbO_3$ waveguide phase modulators that serve as variable frequency shifters using the serrodyne frequency-translation technique [16] (see Appendix for more details). Reversibly mapping nano-second long pulses of light onto different spectral sections of a multi-section AFC (where each spectral section is programmed to perform a different task), we demonstrate sequencing, time-to-frequency multiplexing and demultiplexing, splitting, interfering, temporal and spectral filtering, compressing and stretching as well as on-demand selective delaying. While the input pulses currently contain on average around 5–40 photons, our approach straightforwardly applies to the manipulation of individual photons or members of entangled photon pairs, as well as to pulses of light used in classical communications.

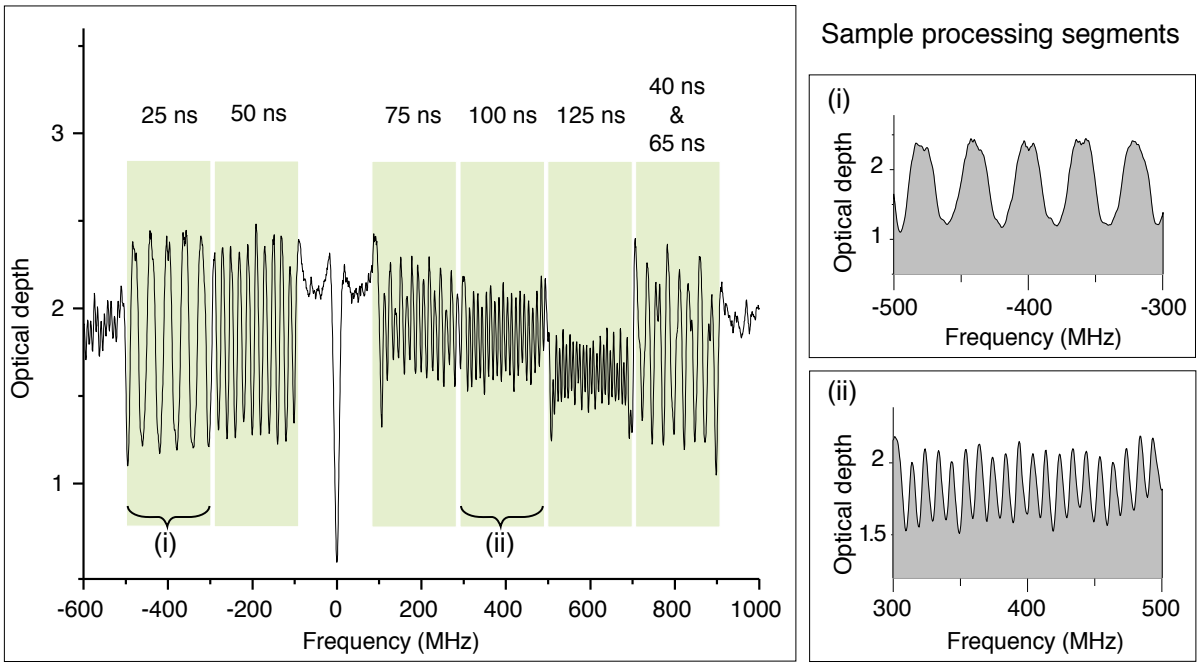

Figure E.2: Example of a programmed AFC memory used as a processor in the experiments. See main text in Section E.2 for details.

E.2 Experiment

Our experimental setup, sketched in Fig. E.1, consists of three main blocks: pulse generation, pulse manipulation, and detection. The pulse generation block features a continuous wave (CW) laser centered at 795.5 nm wavelength and an acousto-optic modulator (AOM) that is used to carve 12 ns duration pulses (measured at Full Width Half Maximum, FWHM) from the CW laser light. These pulses are heavily attenuated down to a mean photon number of $5 - 40$ photons. The pulse manipulation block is composed of a Tm:$LiNbO_3$ waveguide memory (processor) maintained at 3.5 K, and two commercial $LiNbO_3$ waveguide phase modulators (controllers) located at the input and output of the memory and kept at room temperature. We note that it may be possible to combine these three elements on a single, integrated, cryogenically cooled photonic circuit, allowing a more compact setup. The detection block contains a silicon avalanche photo diode

(Si-APD) single photon detector (SPD), an optical switch that is used to protect the detector from optical pump light while preparing the AFC, and a monolithic Fabry-Perot (FP) filter (not shown in the figure) used to demonstrate the ability to control the spectra of the retrieved pulses from the memory unit (this is further explained in Appendix). Each experimental cycle comprises three stages: AFC programming through frequency selective optical pumping (persistent spectral hole burning) for which the frequency of the CW laser light is controlled using the phase modulator placed before the memory, waiting to avoid noise from decaying atoms that were excited during the programming of the AFC, and sending, manipulating and detecting few-photon pulses. The durations of these stages are 3 ms, 2.2 ms and 5 ms, respectively. The efficiency of our AFC processor is currently limited to around 1%. As is further discussed in the Discussion and Conclusion section, this is mainly due to inefficient optical pumping during the programming stage of the AFC. For more details about the implementation, material, AFC preparation and measurements see Appendix.

In a standard AFC memory [17, 18], an inhomogeneously broadened absorption profile is tailored into a series of equally spaced absorption peaks. Photons mapped onto this spectral feature are re-emitted as so-called echoes after a time $t_{storage} = 1/\Delta$, and with a phase shift of $\phi = 2\pi\frac{\Delta_0}{\Delta}$, where Δ is the spacing between the peaks, and Δ_0 is the detuning between the carrier frequency of the input photons and the frequency of one of the peaks [1]. The retrieval process can approach unit efficiency provided that certain phase matching conditions are satisfied and variables such as AFC finesse (i.e. the ratio of the peak spacing to the peak width) and optical depth are optimum. The implementation of the AFC protocol in cryogenically cooled rare-earth ion doped crystals has already shown great promise as a quantum memory for quantum information processing applications.

[1]We note that, in the case of backward recall and assuming zero detuning, the echo picks up an additional phase of π with respect to the input. However, this is not the case for the forwards propagating echo as implemented in our experiments.

Examples include high retrieval fidelity [19], high efficiency [20], large bandwidth [14, 15], large temporal and spectral multimode storage capacity [21, 22, 23], the possibility to store time-bin and polarization qubits [15, 19, 24, 26] plus members of entangled photon pairs [14, 25] and, recently, the teleportation of photonic quantum states into a crystal [27].

When the AFC is used for processing tasks, as proposed in this study, the peak spacing in different frequency intervals is typically set to different values, resulting in storage (re-emission) times that vary as a function of frequency. An example of an AFC memory programmed as a processor is shown in Fig. E.2. In this example, the entire bandwidth is divided into six AFC segments, each having 200 MHz bandwidth. In each AFC segment, the peak spacings are set differently, yielding storage times between 25 ns and 125 ns with 25 ns increments. The right-most segment, prepared by superimposing two AFCs, is used to divide a single input pulse into two temporal modes, stored for 40 ns and 65 ns, respectively. Using this single re-configurable AFC processor, multiple processing tasks can be performed, as shown in the following [2].

E.3 Measurements and Results

Pulse Sequencing

The first example is the re-ordering of pulses in a pulse sequence, which plays an important role in synchronizing and randomly accessing quantum information in quantum repeaters and linear optics quantum computers [8]. In the standard AFC storage scheme, one is restricted to storing pulses without changing their order, as shown in Fig. E.3a [3].

[2]Note that the retrieval efficiency of each AFC segment, if programmed for different storage times, is typically different. However, as explained in Appendix, the efficiencies can be made equal at the expense of lowering the overall efficiency. This was done for the measurements depicted in Figures 3–6.

[3]Here and in the reminder of this paper, the recalled pulses (echoes) are identified by a thick outline while the transmitted parts of the incoming pulses, arising from the non-unit absorption probability of the incoming pulses, are shown in a darker color, with no outline and, for the most part, will be located

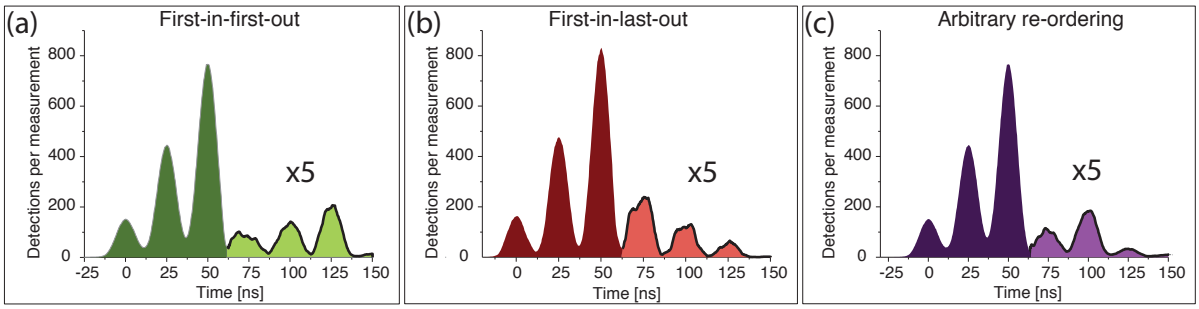

Figure E.3: Demonstration of pulse sequencing: An input pulse sequence consisting of three pulses separated by 25 ns is generated using the AOM. The pulses are prepared with 12 ns duration and the same carrier frequency but with different amplitudes. **(a)** The input pulses are all mapped onto the same AFC segment at +200 MHz detuning using the input phase modulator. After 75 ns storage they are retrieved in the same order (First-in-first-out). **(b)** The first, second and last pulses are mapped onto the AFC segments that yield 125 ns, 75 ns and 25 ns storage time, respectively. This results in the pulses being recalled in a time-reversed order with respect to the input sequence (First-in-last-out). In the measurements, the retrieval efficiency for each storage time is equalized (at the expense of lowering the overall efficiency) by choosing an appropriate magnetic field and pump intensity during the programming stage. **(c)** Similarly, by applying appropriate frequency shifts to each pulse, arbitrary time re-ordering can be obtained.

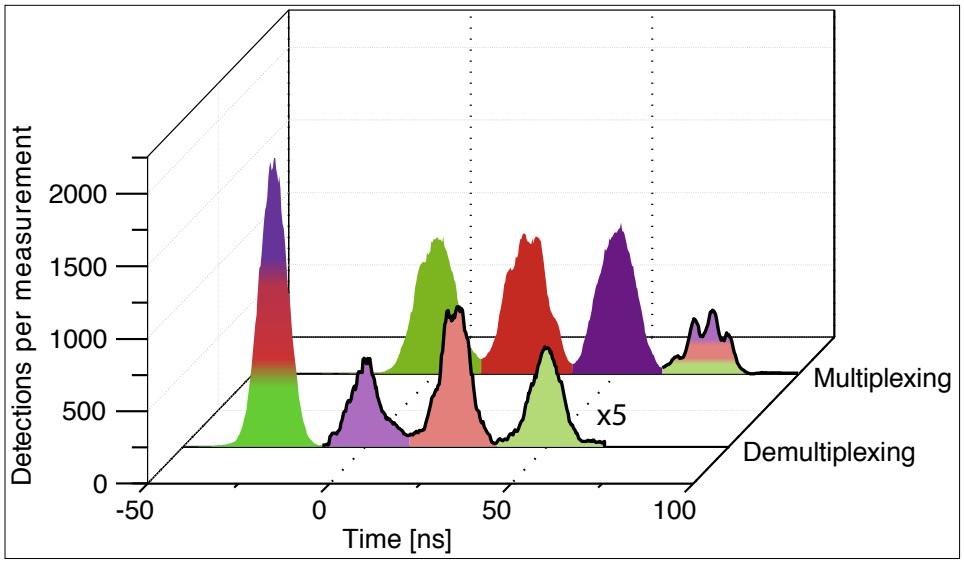

Figure E.4: Demonstration of time-to-frequency multiplexing and demultiplexing: A pulse composed of three distinct frequency modes at -400 MHz, -200 MHz and +200 MHz (represented by the three horizontal colour bands in the pulse) detunings is generated using the input phase modulator driven by a sinusoidal waveform. This multimode pulse is sent to the programmed AFC (Fig. E.2) and each frequency mode is mapped onto the corresponding AFC segment. This results in each frequency mode being retrieved at a different time, as determined by the programming of the respective AFC segment. This is illustrated in the front trace (Demultiplexing) with different colours representing the different frequency components. Next, three 25 ns-separated input pulses are prepared with center frequencies that map onto the AFC segments with +200 MHz, -200 MHz and -400 MHz detuning, respectively. This mapping allows the three recalled pulses to be merged in the same temporal mode, as shown in the back trace (Multiplexing).

To re-order the pulses in this sequence, the controller at the AFC memory input applies appropriate frequency shift to each pulse such that the pulses are mapped onto different AFC segments, resulting in the retrieved pulse sequence being reversed or arbitrarily re-ordered, as demonstrated in Fig. E.3b and c, respectively. Moreover, the center frequency of each pulse retrieved from the memory unit can be set back to its original value by the output controller, resulting in a pure time-domain manipulation (see Appendix).

Time-to-Frequency Multiplexing and Demultiplexing

The next demonstration is time-to-frequency multiplexing and demultiplexing of pulses, which is of potential interest for multiplexed quantum networks. When input pulses occupying several frequency modes and the same temporal mode are mapped onto the programmed AFC processor in Fig. E.2, they are retrieved at different times (demultiplexing) as shown in the front trace of Fig. E.4. In the same way, input pulses occupying different temporal modes can be merged into the same temporal mode (multiplexing) by applying the appropriate frequency shift to each input mode as demonstrated in the back trace of Fig. E.4.

Pulse Splitting

Splitting a pulse into separate pulses in various spectral and temporal modes is another manipulation that is possible using our processor; it allows generating high-dimensional quantum states. To demonstrate this feature, three temporal portions of an input pulse are mapped onto different AFC processor segments using the input controller. Consequently, each portion of the original pulse is retrieved in a different spectro-temporal mode, as shown in Fig. E.5. We note that it is also possible to recover the input pulse by re-processing each generated component in a subsequent system.

---

at the origin of the time axis.

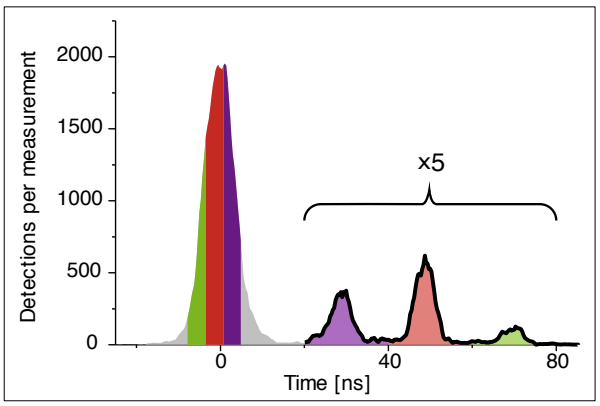

Figure E.5: Pulse splitting: Three separate temporal portions of an input pulse, indicated by the green, red and purple coloured bands are mapped to three different segments of the programmed AFC, leading to 75 ns, 50 ns and 25 ns storage times, respectively. After processing in the AFC, three spectro-temporal modes emerge as shown in the figure.

Manipulating Time-Bin and Frequency-Bin Qubit States

It is straightforward to generate and manipulate time-bin qubits using our integrated processing unit, as previously demonstrated in [15, 17, 21, 25]. In the programmed AFC processor shown in Fig. E.2, the last segment at +800 MHz detuning is prepared by superimposing two AFCs (double AFC) with different comb tooth spacings (see Fig. E.6a). When an input pulse in a well defined temporal mode is mapped onto this AFC segment, it is re-emitted in a superposition of two temporal modes with a relative phase of $\delta\phi = \phi_1 - \phi_2$, where ϕ_1 and ϕ_2 are the phase shifts introduced by each comb of the double AFC. Thus, this AFC processor segment can be used to generate any time-bin qubit state, as exemplified in Fig. E.6b.

If a single photon pulse in a superposition of two temporal modes is mapped onto the AFC segment, the photon will be re-emitted, in general, in a superposition of four temporal modes, each defined by the re-emission times of the combs and the separation of the input temporal modes. In this case, adjusting the difference between the emission times to the temporal separation of the two input modes leads to overlap between the

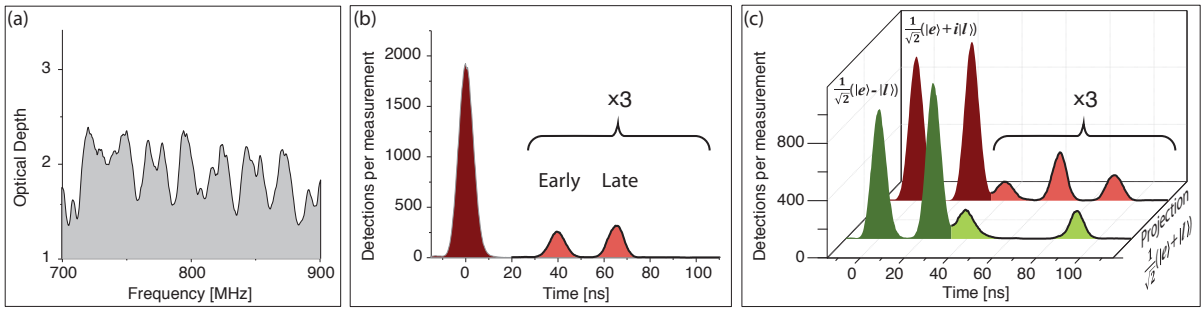

Figure E.6: Generating and Manipulating Time-Bin Quantum States: **(a)** The last segment of the programmed AFC at +800 MHz detuning (Fig. E.2) is prepared by superimposing two AFCs (double AFC) with two different comb spacings, leading to 40 ns and 65 ns storage times. **(b)** An input photon, occupying a well-defined temporal mode, is mapped to the double AFC. It is re-emitted in a superposition of two temporal modes (time bins), referred to as "early" and "late". **(c)** Storing a superposition time-bin qubit state with temporal modes separated by 25 ns (equal to the difference between the re-emission times of the superimposed AFCs) leads to the early and late input modes being overlapped in a central temporal mode after recall (see text for details). This allows performing any projection measurement onto time-bin qubit states. In the measurements represented in (c), input states $|\psi\rangle = \frac{1}{\sqrt{2}}(|e\rangle - |l\rangle)$ (front trace) and $|\psi\rangle = \frac{1}{\sqrt{2}}(|e\rangle + i|l\rangle)$ (back trace), where $|e\rangle$ and $|l\rangle$ denote the quantum state of a photon occupying the early and late temporal mode, respectively, are stored in a double AFC that projects onto $|\psi\rangle = \frac{1}{\sqrt{2}}(|e\rangle + |l\rangle)$. This results in destructive and (partially) constructive interference in the central temporal mode, respectively.

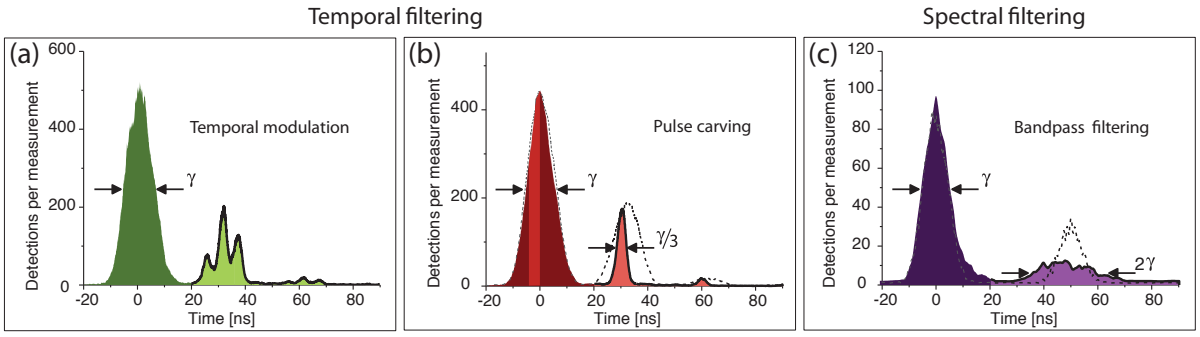

Figure E.7: Arbitrary temporal and spectral filtering: **(a)** The input phase modulator maps three selected 3 ns-long temporal portions of a 12 ns long input pulse onto an AFC segment prepared with 600 MHz bandwidth, 33 MHz peak spacing, and centered at +700 MHz detuning. This allows generating a temporally modulated pulse as seen in the figure. **(b)** The input phase modulator maps a narrow temporal portion of an input pulse onto the center of the AFC segment. This results in an echo almost three times shorter than the input pulse. The echo pulse, shown with the dashed line is obtained if the entire pulse is mapped to the same AFC. γ represents the duration of the input and transmitted pulse at FWHM. **(c)** An input pulse with nearly 70 MHz bandwidth is mapped onto an AFC segment prepared with 600 MHz bandwidth and retrieved after 50 ns (dashed line). An input pulse with the same bandwidth is mapped to an AFC with a bandwidth decreased to about 40 MHz. In this case the AFC acts as bandpass filter, yielding an output pulse with nearly twice the duration.

two central temporal modes into a single mode, as shown in Fig. E.6c. In this way, it is possible to project a time-bin qubit onto an arbitrary state [17], which resembles the use of an imbalanced Mach-Zender interferometer. Furthermore, applying the same idea used for time-to-frequency multiplexing (demonstrated in Sec. E.3), our system can easily convert a time-bin qubit to a frequency-bin qubit, which can be further manipulated using the output controller. These schemes could be useful for quantum communication protocols relying on frequency and time-bin encoding.

Arbitrary Temporal and Spectral Filtering

Our processor can also be used as a reconfigurable temporal and spectral filter. For example, this would allow tailoring single photons or matching the spectral and tempo-

ral properties of photons produced from independent sources for applications relying on two-photon interference. As opposed to the task described in the next section, filtering obviously leads to loss of photons. To demonstrate the temporal shaping capability, an AFC having a bandwidth of 600 MHz and centered at +700 MHz detuning is programmed. A 12 ns long input pulse is sent to the processing unit. If the input controller is not engaged, it remains at 0 MHz detuning and the pulse is directly transmitted as it has no spectral overlap with the AFC. However, if the input controller is engaged, the selected temporal portion (or portions) of the incoming pulse is (are) mapped onto the AFC, resulting in a temporally shaped recalled pulse as shown in Fig. E.7a. Using this idea, it is also possible to carve a narrow temporal portion from an input pulse, i.e. to generate a short pulse from a long one, as demonstrated in Fig. E.7b. Furthermore, the capability of continuously adjusting the serrodyne modulation efficiency (see Appendix) allows for arbitrary modulation of the temporal shape and intensity of an input pulse, which turns our implementation into an arbitrary optical waveform generator [28].

To demonstrate the spectral filtering capability, the bandwidth of the AFC is decreased to about 40 MHz. An input pulse with 70 MHz bandwidth is mapped onto this AFC using the input controller. The portion of the pulse spectrum that lies outside the AFC is filtered out (by being partially directly transmitted and absorbed) and the recalled pulse is emitted with smaller bandwidth and thus longer duration, see Fig. E.7c.

Pulse Compressing and Stretching

Compressing and stretching quantum optical pulses is potentially useful for increasing quantum data rates and matching bandwidths of photons to those of quantum memories [8, 11, 29]. An AFC memory is well suited for this task since it can be tailored to feature almost arbitrary chromatic dispersion, i.e. tailored in such a way that different frequency components of an input pulse are retrieved at different times. To this end, we

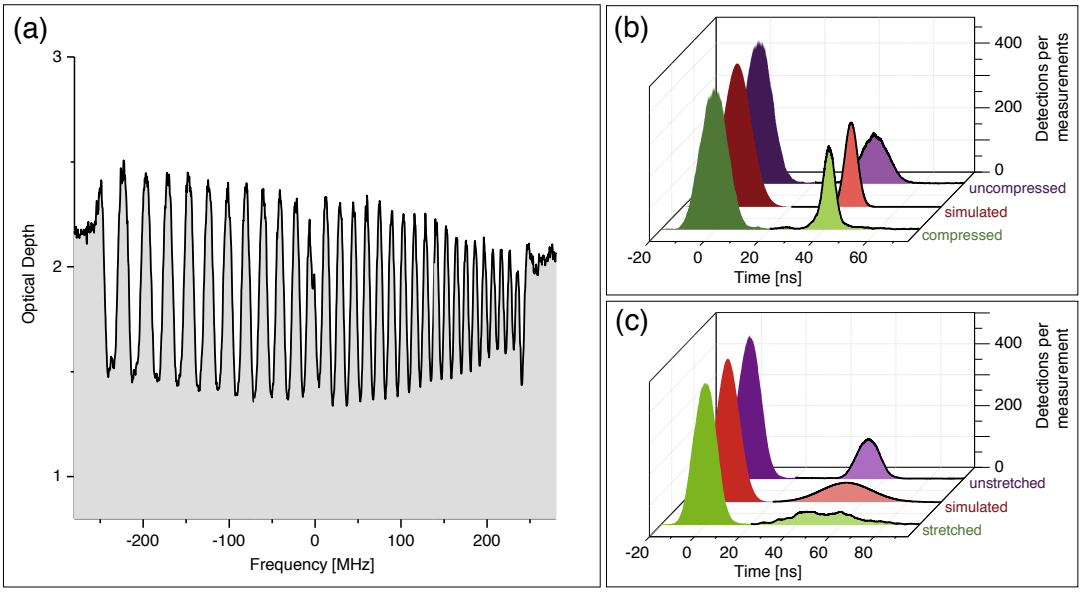

Figure E.8: Demonstration of compressing and stretching of pulses using an AFC with linearly- decreasing peak spacing: **(a)** A 500 MHz-wide AFC with linearly decreasing peak spacing from 30 MHz to 10 MHz, yielding storage times between 33 ns (at the lower frequency end of the AFC) and 100 ns (at the upper frequency end of the AFC, respectively), and thus an approximate value of $\mu = 0.14$ ns/MHz. **(b)** Using the input phase modulator, the frequency of an incoming pulse is linearly chirped from high to low at a rate of 8.3 MHz/ns, yielding $\mu r = 1.16$ (close to the optimum condition $\mu r = 1$). When this pulse is mapped onto the programmed AFC, a compressed pulse is retrieved with a compression factor of nearly 2.4, as shown in the front trace. The middle trace depicts the simulated result after scaling its intensity with respect to the experimentally obtained echo (see Appendix)– the temporal shapes are in good agreement. The back trace shows the retrieved pulse after storage using a standard AFC with equal tooth spacing. Note that the areas under the experimentally obtained curves for the standard and compressed echoes are nearly equal. **(c)** Pulse stretching is performed by applying a chirp with the same rate but different sign (i.e. from low to high frequency) and different start frequency. The resulting stretched pulse, the corresponding simulation and the re-emitted pulse from a standard AFC are shown in the front, middle and back traces, respectively.

program an AFC whose peak separation is linearly decreasing across its entire bandwidth (Fig. E.8a). To compress an input pulse, the input controller chirps the frequency of the pulse linearly from high to low, which disperses the spectrum of the pulse. When this pulse is mapped onto the AFC processor, the pulse front is stored longer than the end of the pulse, leading, under certain conditions, to the retrieval of a temporally compressed pulse as demonstrated in Figs. E.8b and E.9. Note that the output controller can be used to remove the frequency chirp in the retrieved pulse by applying a reversed linear chirp with appropriately chosen slope.

For an input pulse having a duration of τ_{in} and an AFC prepared with linearly varying peak spacing, the compression factor κ (defined to be the ratio of the duration of the input pulse to the duration of the compressed output pulse) is determined by two parameters: the spectral width of the chirped pulse, $B = \tau_{in} r$, which is controlled by the applied chirp rate, r, as well as the gradient of the programmed storage times $\mu = \frac{\delta T}{B}$. Here, δT is the difference between the storage times introduced by the AFC for the upper frequency end and the lower frequency end of the chirped pulse (see Appendix for the analysis). Note that we assume that the AFC width is at least as large as B so that the entire chirped pulse is absorbed. For maximum compression of the input pulse, τ_{in} and δT have to be equal, which is equivalent to satisfying the condition $\mu r = 1$ (this can be achieved using an appropriate chirp-rate setting). In this case, the duration of the output pulse is $1/B$ [28], and the compression factor is given by

$$\kappa = \frac{\tau_{in}}{1/B} = \delta T \cdot B = \mu B^2. \tag{E.1}$$

This equation follows straightforwardly from the definition for the storage time gradient μ. Hence, we find that, for a given storage material, the compression factor is limited by the maximally achievable storage time (which determines δT) and the storage bandwidth B (i.e. the time-bandwidth product). For instance, in our case, we have $\delta T_{max} \approx 100$ ns

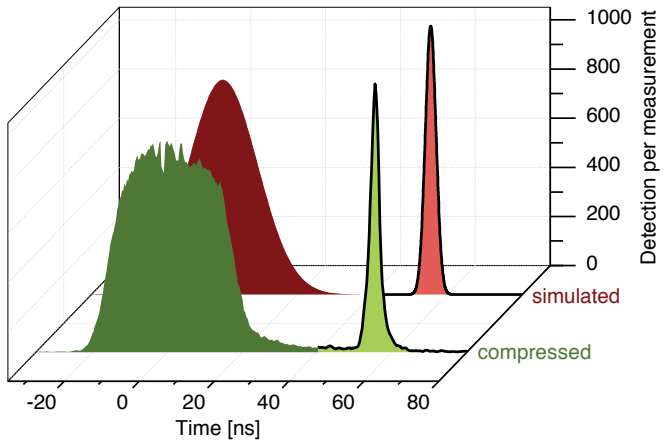

Figure E.9: Achieving high compression factors: A 2 GHz-wide AFC with linearly decreasing peak spacing from 30 MHz to 10 MHz (equivalent to a storage time gradient $\mu = 0.035$) is programmed. The frequency of an input pulse with approximately 30 ns duration is chirped from high to low at a rate of 32.9 MHz/ns, yielding $\mu r = 1.15$, and mapped onto the programmed AFC. This results in a 2.6 ns long (FWHM) echo pulse and a compression factor close to 10, as shown in the front trace. The back trace shows the simulated result assuming an input pulse having a Gaussian envelope and a similar duration to that of the actual input.

and $B_{max} \approx 10$ GHz, which allows in principle a compression factor of $\kappa_{max} \approx 1000$. We note that compression not only occurs if $\mu r = 1$, but, more generally, for $0 < \mu r < 2$ (for more information see Appendix).

Pulse stretching can be performed in a similar way by applying the input frequency chirp from low to high. When the chirped pulse is mapped onto an AFC with decreasing peak spacing, the end of the pulse is stored longer than the front, leading to a temporally stretched pulse of duration $\tau_{out} \approx \tau_{in} + \delta T = \tau_{in} + \mu B$ (an example is shown in Fig. E.8c). Hence, achieving large stretching requires programming an AFC with large μ, which, as before, is limited by the longest achievable storage time (i.e. the smallest achievable peak spacing of the AFC). In addition, the output pulse width increases with the bandwidth B of the chirped input pulse.

To finish this section, let us emphasize that the described pulse compression and de-

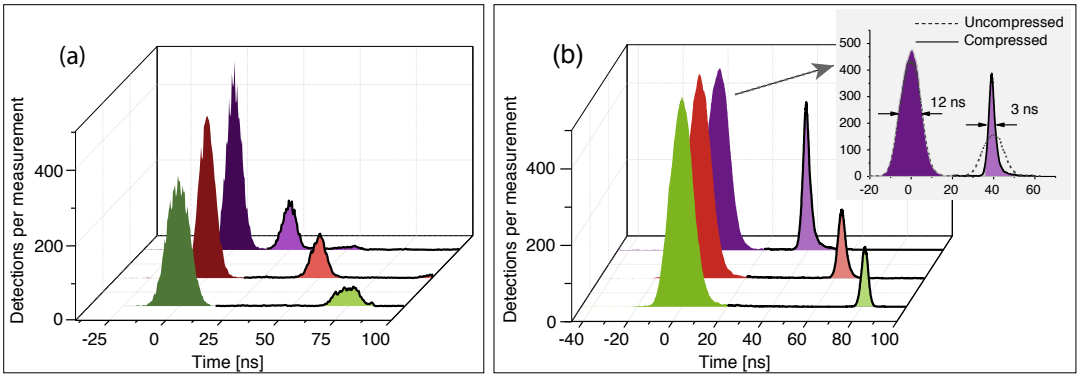

Figure E.10: Selective delaying: **(a)** The input phase modulator maps an incoming pulse to a particular segment of the programmed AFC shown in Fig. E.2 to obtain a desired delay. To achieve delay times of 25 ns, 50 ns and 75 ns, the pulses are mapped onto the segments at -400 MHz, -200 MHz and +200 MHz detuning, respectively, and are retrieved after the corresponding storage time. **(b)** A 2 GHz-wide AFC with linearly decreasing peak spacing from 30 MHz to 10 MHz is programmed. The frequency of an incoming pulse is linearly chirped from high to low as described in the previous section. This pulse is mapped onto the programmed AFC, resulting in the emission of a compressed pulse with a compression factor of nearly 4. Varying the start frequency of the chirp maps the incoming pulse to different intervals of the AFC, which allows selecting the storage time.

compression is different from the filtering process discussed in section 2.5 as, in principle, this approach can be carried out without introducing loss.

Selective Delaying

Having AFC segments with different peak spacing also allows one to select the storage time on demand without the (time demanding) need for re-programming an AFC. In our new approach, the input controller maps a pulse to a particular AFC segment shown in Fig. E.2 to achieve a desired delay, as demonstrated in Fig. E.10a. In addition, it is possible to compress the pulses during storage (as shown in the previous section) using an AFC with continuously varying peak spacing. In this case, changing the start frequency of the chirp additionally allows one to choose non-discretized storage times using appropriate frequency shifts at the input controller, as shown in Fig. E.10b and

further described in Appendix. If necessary, the emitted pulse's carrier frequency can be set back to the original frequency using the output controller. The described feature will be useful for synchronization purposes in quantum communication.

E.4 Discussion and Conclusion

An integrated optical quantum memory is an important element for future quantum communication networks and linear optics quantum computers, and employing it for the manipulation of optical pulses at the quantum level adds another direction to its potential use in quantum information processing applications. In this study, we have shown that our broadband waveguide quantum memory can be turned into a processing unit for arbitrary temporal and spectral manipulation of nanosecond-long quantum optical light pulses. Although we utilized weak laser pulses at the few photon level, our approach works equally well for laser pulses containing less than one photon on average, true single photons, or members of entangled pairs of photons. In addition, it can be used for the manipulation of strong pulses of light, as used in classical communications.

The light-matter interface presented in this paper brings several advantages over previous implementations of quantum optical pulse manipulations. First of all, its waveguide nature allows for integration with other waveguide photonic devices, e.g. currently developed lithium niobate based quantum circuits [7], which is important for practical applications. Second, as our processor relies on a large-bandwidth AFC memory and large-bandwidth electro-optic frequency shifters, it allows processing of nanosecond, and soon sub-nanosecond pulses. Third, as opposed to other quantum memory approaches [13], the number of simultaneously storable modes in the AFC approach does not depend on the optical depth of the used medium [18, 21, 22, 23]. Hence, our light-matter interface possesses a large multi-mode processing capacity. And finally, it offers a wide range of

quantum optical pulse manipulations in a single spatial mode, which makes it attractive for several quantum information processing applications [31].

However, for practical use, the total efficiency of our system (including processor and controllers) needs to be increased beyond the current sub-percent level (for some applications it needs to be close to one). The principal limitation in our current implementation stems from imperfect preparation of the AFC, which is mainly due to unfavorable relaxation dynamics in our material at 3.5 K (see Appendix). More specifically, the residual absorption background of the prepared AFCs, which can be seen in Fig. E.2, results in most of the incoming photons to be irreversibly absorbed. However, our recent observations, supplemented by those reported in [32], suggest that the relaxation dynamics change considerably when operating at lower temperature (< 1.5 K), and that this background can be eliminated almost entirely. Hence a substantial increase of the efficiency is readily achievable. In addition, to increase the system efficiency, the coupling efficiencies in and out of the phase modulators and our waveguide quantum memory need to be maximized, for instance through integration of all components on a single chip. However, to approach unit efficiency, certain not yet fully mastered techniques need to be applied. One of them requires embedding the AFC medium into an impedance matched cavity [20, 33, 34, 35] that features a resonance width compatible with broadband AFCs. Another one is to implement the AFC with additional spatial periodicity [36]. Finally, a third option is to reversibly (and with appropriate phase-matching) map the optical coherence that was excited by absorbing a quantum state onto spin states [37, 38, 39] [4].

To conclude, let us note that, while the operation wavelength cannot be chosen freely (it needs to coincide with an atomic transition in a material that allows for persistent hole burning), there is nevertheless some flexibility, in particular as no long coherence time is needed. Of particular interest are Erbium-doped materials [40, 41], due to an

[4]This method requires the availability of an additional spin state. While lacking in thulium, such levels exist in other rare-earth ions.

absorption line at telecommunication (around 1550 nm) wavelength.

Acknowledgment

The authors thank W. Sohler, M. George and R. Ricken for providing the Ti:Tm:$LiNbO_3$ waveguide, and M. P. Hedges, C. Simon, J. Jin, C. W. Thiel and W. R. Babbitt for useful discussions and help during the preparation of the manuscript. This work is supported by Alberta Innovates Technology Futures (AITF), the National Sciences and Engineering Research Council of Canada (NSERC), the Killam Trusts, and the Carlsberg Foundation.

E.5 Appendix to Paper 5

A1. Implementation

We use a cryogenically cooled Ti:Tm:$LiNbO_3$ channel waveguide quantum memory as a processor in conjunction with two commercial $LiNbO_3$ electro-optic modulators placed before and after the memory. Although in our experiments the $LiNbO_3$ phase modulators are outside the cryogenic system and connected to the input and output of the memory by single mode fibers, all components can, in principle, be implemented on a single chip. This can be achieved by fabricating a long $LiNbO_3$ channel waveguide with Thulium atoms doped only into the central part, and electrodes deposited at the beginning and end of the waveguide. Note that phase modulators similar to ours can be operated at cryogenic temperature [42].

A2. Material

The fabrication of the Tm:$LiNbO_3$ waveguide and basic spectroscopic properties of Tm atoms in this material have already been reported [43]. The waveguide used in the experiments is 10.4 mm long and 3.5 μm in diameter. The light is butt-coupled into and out of the waveguide using single mode fibers. End-to-end transmission is about 20%. The crystal temperature is kept around 3.5 K during the experiments, which results in nearly 1.5 μs coherence time on the optical $^3H_6 \leftrightarrow ^3H_4$ transition at 795.5 nm. A magnetic field of 50–130 G, depending on the measurement, is applied along the C_3 axis of the crystal in order to activate long-lived nuclear Zeeman spin level, as illustrated in Fig. A.E.1. These levels are used as shelving levels to generate persistent AFCs.

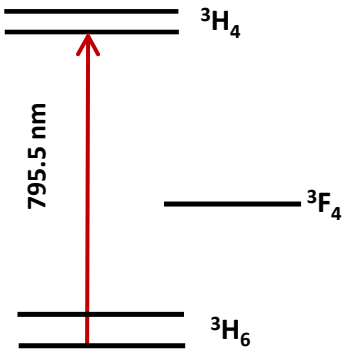

Figure E.1: Simplified energy level structure of thulium ions: The optical transition of thulium ions between the ground ($^3H_6$) and excited ($^3H_6$) electronic level is used for reversible mapping of photonic states through the AFC protocol. The lifetime of the excited level is about 80 μs. Upon application of a magnetic field, the ground and excited levels split into two sub-levels (nuclear Zeeman level) with lifetimes of the two $^3H_6$ sub-levels approaching 1 s. These levels are used as shelving states to generate persistent AFC structures through optical pumping described in Appendix.

A3. AFC preparation

Each AFC is prepared by means of frequency selective optical pumping of the inhomogenously broadened transition of Tm at 795.54 nm wavelength. As detailed previously in [14], this is achieved by simultaneously chirping the frequency and modulating the intensity of single frequency laser light. The interaction between the laser light and resonant atoms leads to excitation of the latter. The atoms may subsequently decay to the shelving level. Repeating this processes for a sufficiently long time leads to persistent spectral holes, which form the troughs of the AFC. The atoms that are not excited by the laser are left in the ground level and form the regions of high absorption (the peaks) of the AFC. Adjusting the frequency spacing Δ between the peaks (or troughs) allows setting the storage time $t_{storage}$ to $t_{storage} = 1/\Delta$.

An important point is that in the optical pumping process, reduced absorption at certain frequencies always comes with increased absorption at other frequencies, as de-

termined by the level structure. In our case, pumping atoms from one magnetic sub-level to the other magnetic sub-level results in decreased and increased absorption at frequencies whose separation is given by the difference between the excited and ground level splittings. Hence we have to adjust the magnetic field in such a way that the increased absorption and reduced absorption regions match the AFC peaks and troughs. However, this approach severely limits experiments that require different peak spacings in the prepared AFCs. Therefore, in some experimental configurations, the magnetic field is optimized so that we obtain nearly equal efficiencies from each AFC segment, at the expense of reducing the overall memory efficiency. Typically, the efficiency was reduced by a factor 2–5 from the optimum efficiency of about 0.5–2 % for a particular experiment depending on the storage time programmed.

As explained in [14] and discussed in the Discussion and Conclusion section of the main text, the low efficiencies and relatively short storage time of our memory implementation are in general due to unfavorable relaxation dynamics (arising from low branching ratio and insufficient persistent hole lifetime) and a high decoherence rate in our specific sample kept at 3.5 K. On the other hand, the results of our recent spectroscopic characterizations carried out at temperatures below 1.5 K indicate that substantial improvement in the efficiency and storage time is possible; this is supported by the observations reported in [32]. In addition, improving the fabrication of the Tm doped waveguide will also lead to better spectroscopic properties, as discussed in [44].

A4. Measurements

In each experimental cycle, optical pumping lasts for 3 ms. After the preparation of an AFC, a 2.2 ms wait time is set to eliminate any fluorescence from excited atoms, which may swamp the re-emitted pulses. During the next 5 ms, 12 ns long probe pulses are generated at a 2.7 MHz rate. The pulses are attenuated down to a mean photon

number of 5-40 and then sent into the AFC memory. As depicted in Fig. E.1, the directly transmitted, and the stored and retrieved pulses are detected by a Si-APD single photon detector with 70% detection efficiency and dark count rate of approximately 100 Hz. Given the small recall efficiency, the estimated mean photon numbers behind the memory are between 0.007 and 0.04 photons per pulse, depending on the experiment. To ensure sufficient detection statistics, each measurement is performed over $0.5 - 2.5$ minutes. In order to time-resolve and process the detection events, a time-to-digital convertor is used. The optical pumping light with 5 to 15 μW peak power is sent in backward direction to the memory (i.e. counter-propagating with respect to the probe pulses) to protect the single photon detector. Finally, an optical switch allows toggling the memory output between optical pumping and transmission towards the detector.

A5. Spectral Manipulation of Pulses Retrieved from the Memory

In most of the demonstrations reported in the main text, the center frequency or spectral distribution of the pulses are changed by the input phase modulator. The main role of the phase modulator that follows the memory unit is to undo these changes, if necessary. For example, when pulses with the same carrier frequency are re-ordered in time, their center frequencies are automatically shifted by certain amounts as explained in Section E.3 of the main text. In this case, using the output phase modulator, the frequency of the re-ordered pulses can be shifted back to their original values.

To demonstrate this capability, we add a FP filter with 80 MHz linewidth and 23 GHz free-spectral range behind the output phase modulator (see [45] for more details about the FP filter used). We generate an AFC with 600 MHz bandwidth and 33 MHz peak spacing, leading to 30 ns storage time, and tune the transmission window of the filter to the center of the AFC. First we store pulses with 12 ns duration in the prepared AFC, and detect the recalled photons after having set the frequency shift introduced by the

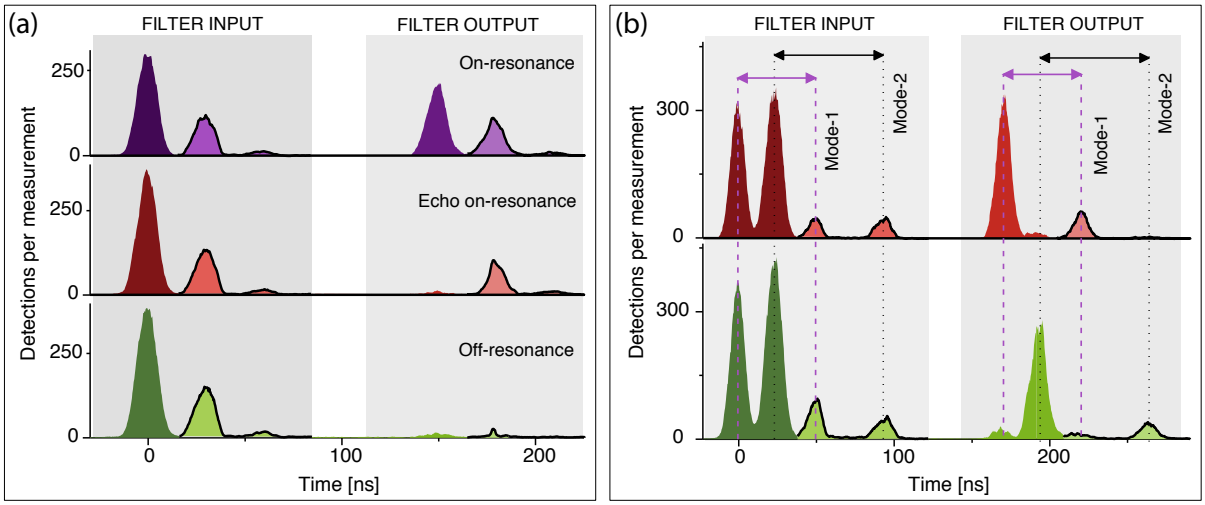

Figure E.2: Demonstration of spectral manipulation of pulses retrieved from the memory unit using the output phase modulator: **(a)** Pulses with 12 ns duration are stored in an AFC prepared with 600 MHz bandwidth and 33 MHz peak spacing. They are retrieved after 30 ns as shown on the left. The retrieved pulses are directed to the output phase modulator before going to the FP filter. The transmission window of the filter is tuned to the center of the AFC. First, no frequency shift is applied to the transmitted pulse or the echo, and both thus pass the filter, as shown in the top figure. Next, a 200 MHz frequency shift is applied to the transmitted pulse, resulting in only the echo passing the filter, as shown in the middle figure. Finally, a 200 MHz frequency shift applied to both pulses, and thus both are blocked by the filter. **(b)** Two 25 ns-separated input pulses, occupying different frequency modes, are simultaneously stored in a two-segment AFC with 50 ns and 70 ns storage times, respectively, as shown in the left part of the figure. After recall from the memory, by applying an appropriate frequency shift, we selectively retrieve one of these modes through the filter as shown in the right part.

output phase modulator to zero, as shown at the top of Fig. A.E.2a. Next we shift the frequency of the transmitted pulse by -200 MHz but leave the recalled pulse's frequency unchanged. In this case, while the transmitted pulse is blocked by the filter, the recalled pulse passes, as seen in the middle of Fig. A.E.2a. Finally we shift the frequency for transmitted and recalled pulses by 200 MHz, causing both to be rejected by the filter as shown at the bottom of Fig. A.E.2a.

In another demonstration, we prepare an AFC with two frequency segments, each having 200 MHz bandwidth centered at -100 MHz and +100 MHz detuning. We set the storage times to 50 ns and 70 ns, respectively. Next, we generate two 25 ns separated pulses with -100 MHz and +100 MHz detuning and store them simultaneously in the prepared AFC. They are retrieved after their respective storage times, as shown on the left of Fig. A.E.2b. We direct them to the phase modulator and the filter tuned to -100 MHz. Shifting the frequency by 0 MHz and +200 MHz, we can limit the output from the cavity to a single frequency mode, as illustrated on the right hand side of Fig. A.E.2b.

These experiments demonstrate that using the output phase modulator, we have full control over the processed pulses in the frequency domain. In particular, any temporal manipulation that requires the spectra of the pulses to remain unchanged, or any spectral re-distribution that protects the encoded coherent information, can be achieved with the use of this component. Moreover, as shown in [23], integrating a FP cavity into our system allows for on-demand recall with respect to the frequency domain.

A6. Theoretical Analysis of Pulse Compressing and Stretching

In this section we present a theoretical analysis for compressing and stretching optical pulses using an AFC processor. As described in Section E.3 in the main text, the frequency of an input pulse is linearly chirped and then the resulting pulse is mapped onto an AFC with a linearly varying peak spacing (Fig. E.8a), giving rise to a storage time

gradient μ. After a predetermined storage time, either a compressed or a stretched pulse emerges, depending on the applied chirp.

We describe the frequency-chirped pulse, propagating along the z-direction, before mapping onto the AFC as

$$E(z=0,t) = e(t)C(t) \tag{E.1}$$

Here, $e(t)$ is the waveform of the input pulse before chirping and $C(t) = e^{i\omega_1 t - irt^2/2}$ is the applied chirp function, where r is the chirp rate and ω_1 is the start (offset) frequency of the chirp [30].

Following the treatment carried out in [30], the first echo that is emitted from the medium of length L is expressed by

$$\tilde{E}(z=L,\omega) = C_1 e^{-i\mu(\omega-\omega_0)^2/2} e^{-ikL} \tilde{E}(0,\omega), \tag{E.2}$$

where $\tilde{E}(0,\omega) = \int dt E(z=0,t) e^{-i\omega t}$ is the Fourier transform of the chirped input pulse. Furthermore, ω_0 is the start frequency of the programmed AFC, and $|C_1|^2$ describes the efficiency of the retrieval. $|C_1|^2$ is determined by the characteristic parameters of the programmed AFC such as optical depth, the finesse and the shape of the AFC peaks but independent of the compression factor. Optimizing these parameters allows in principle approaching unit efficiency in the compression (stretching) process [30]. As seen in Eq. E.2, the AFC introduces a quadratic phase modulation at rate μ, i.e. the storage time gradient of the programmed AFC:

$$\mu = \frac{\delta T}{B}. \tag{E.3}$$

Here $\delta T = t_{storage}^{max} - t_{storage}^{min}$ describes the difference between the maximum and minimum storage time (recall that the storage time in an AFC memory is given by the inverse tooth spacing) over the bandwidth of the chirped pulse, B.

The output waveform in the time domain can be found using the Fourier transform, $E(L,t) = \frac{1}{2\pi} \int d\omega e^{i\omega t} \tilde{E}(L,\omega)$. We assume that the input waveform (before chirping) is

described by a Gaussian function of the form $e(t) = e^{-\frac{(t-t_0)^2}{2\tau_{in}^2}}$, where the Full Width at Half Maximum (FWHM) of the intensity is $2\tau_{in}\sqrt{ln(2)}$. Setting $t_0 = 0$, a lengthy but straightforward calculation yields

$$|E(L,t)|^2 \propto e^{\frac{-(t-t')^2}{\tau_{in}^2\left(\frac{\mu^2}{\tau_{in}^4}+(\mu r-1)^2\right)}}, \tag{E.4}$$

where $t' = 2\mu\omega_1 - \mu\omega_0$ is the average storage time. Note that we dropped the factor that describes the efficiency as we are only interested in the temporal shape of the recalled pulses. Eq. E.4 allows simulating the experimental results as shown in Figs E.8 and E.9 in the main article. Hence we can calculate the expected duration of the recalled pulse $\tau_{out} = \tau_{in}\sqrt{\frac{\mu^2}{\tau_{in}^4} + (\mu r - 1)^2}$, and, after comparison with the duration of the input pulse τ_{in}, we can predict the compression factor $\kappa = \tau_{in}/\tau_{out}$. Note that adjusting the start frequency of the chirp (ω_1) with respect to the start frequency of the AFC (ω_0) allows setting the storage time, as demonstrated in Section E.3.

As discussed in the main text, the optimal compression factor is obtained for $\mu r = 1$ (i.e. $\tau_{in} = \delta T$). Under this condition, the input pulse $|e(t)|^2 = e^{-\frac{t^2}{\tau_{in}^2}}$ is converted into the output pulse $|E(L,t)|^2 = e^{\frac{-(t-t')^2}{\tau_{out}^2}}$, where $\tau_{out} = \frac{\mu}{\tau_{in}}$ (from Eq. E.4), allowing us to calculate the compression factor $\kappa = \frac{\tau_{in}^2}{\mu}$. This expression shows that higher compression factors can be achieved by extending the duration of the input pulse, as demonstrated in Fig. E.9. Note that it is equivalent to $\kappa = \frac{\delta T^2}{\mu} = \mu B^2$, as described in Section E.3.

Let us finally point out that the possibility for active control of the parameter μr by adjusting the chirp rate allows one to implement compressing and stretching in a very flexible fashion. As detailed in [30], having a value of μr between 0 and 1 leads to compression (with variable compression factor) of the input pulse without changing the order of the raising and falling edge, while setting μr between 1 and 2 causes a compressed, but time-reversed output. If μr is equal to 2, time reversal of the input pulse without compression is obtained. On the other hand, setting μr larger than 2 leads

to a time-reversed stretched pulse. In addition, flipping the sign of the chirp, as described in the main text, allows one to implement stretching without time-reversal. In this case a larger μr results in increased stretching. Combining these features with the large time-bandwidth product of the AFC and the large bandwidth of existing phase modulators makes it possible to change the duration of pulses in a fully controlled manner by several orders of magnitude.

A7. Serrodyne Frequency Shifting

The serrodyne frequency shift technique [16] is an essential tool used in our experiments; it was employed in most of the described pulse manipulations and AFC preparations. The principle of this technique is to introduce a linearly varying time-dependent phase change to the light by applying a sawtooth shaped voltage to an electro-optic phase modulator. As a result of the linear phase change, the frequency of the light is shifted by the amount of the modulation frequency. The great advantage of this technique is that, in principle, all energy can be transferred to the desired frequency mode without producing side-bands. This feature allows high-bandwidth spectral manipulations of short optical pulses, which we exploited for our experiments. To generate a sawtooth modulated voltage, we use an arbitrary waveform generator (AWG) with 20 GS/s sampling rate. The output voltage of the AWG is amplified using a high-speed amplifier to achieve the 2π-voltage value of the electro-optic modulators which is necessary for providing maximum energy transfer to the desired frequency mode. Our commercial electro-optic phase modulators have 20 GHz bandwidth and feature approximately 2 dB loss. We are able to shift the light frequency by up to ± 5 GHz. Having imperfections in the applied sawtooth waveform causes imperfect energy transfer efficiency to the desired frequency mode. For instance, for a frequency shift of about 1 GHz, we maximally transfer 80% of the unmodulated light's power.

Bibliography

[1] Gisin N, Ribordy G, Tittel W and Zbinden H 2002 Quantum cryptography. *Rev. Mod. Phys.* **74**.

[2] O'Brien J L, Furusawa A and Vučković J 2009 Photonic quantum technologies. *Nature Photon.* **3,** 12: 687-695

[3] Lvovsky A I, Sanders B C and Tittel W 2009 Optical quantum memory. *Nature Photon.* **3,** 12: 706-714. .

[4] Sangouard N, Simon C, de Riedmatten H and Gisin N 2011 Quantum repeaters based on atomic ensembles and linear Optics. *Rev. Mod. Phys.* **83,** 1:3380.

[5] Sohler W, Hu H, Ricken R, Quiring V, Vannahme C, Herrmann H, Büchter D, Reza S, Grundkötter W, Orlov S, Suche H, Nouroozi R and Min Y 2008 Integrated optical devices in lithium niobate. *Opt. Photonics News* **19** 1:24-31.

[6] Martin A, Alibart O, De Micheli M P, Ostrowsky D B and Tanzilli S A 2012 quantum relay chip based on telecom integrated optics technology. *New J. Phys.* **14,** 2.

[7] Bonneau D, Lobino M, Jiang P, Natarajan C M, Tanner M G, Hadfield R H, Dorenbos S N, Zwiller V, Thompson M G and O'Brien J L 2012 Fast path and polarization manipulation of telecom wavelength single photons in lithium niobate waveguide devices. *Phys. Rev. Lett.* **108,** 053601.

[8] Hosseini M, Sparkes B M, Hétet G, Longdell J J, Lam P K and Buchler B C 2009 Coherent optical pulse sequencer for quantum applications *Nature* **461,** 241–245.

[9] Hockel D and Benson O 2010 Electromagnetically induced transparency in cesium vapor with probe pulses on the single photon level. *Phys. Rev. Lett.* **105,** 153605.

[10] Novikova I, Walsworth R L and Xiao Y 2011 EIT-based slow and stored light in warm atoms. *Laser Photon. Rev.* **6**,3, 333–353

[11] Sparkes B M, Hosseini M, Cairns C, Higginbottom D, Campbell G T, Lam P K and Buchler B C 2012 Precision spectral manipulation: A demonstration using a coherent optical memory. *Phys. Rev. X* **2,** 021011

[12] Reim K F, Nunn J, Jin X M, Michelberger P S, Champion T F, England D G, Lee K C, Kolthammer W S, Langford N K and Walmsley I A 2012 Multipulse addressing of a raman quantum memory: Configurable beam splitting and efficient readout. *Phys. Rev. Lett.* **108** 263602.

[13] Nunn J, Reim K F, Lee K C, Lorenz V O, Sussman B. J., Walmsley I A and Jaksch D 2008 Multimode memories in atomic ensembles. *Phys. Rev. Lett.* **101** 260502.

[14] Saglamyurek E, Sinclair N, Jin J, Slater J A, Oblak D, Bussières F, George M, Ricken R, Sohler W and Tittel W 2011 Broadband waveguide quantum memory for entangled photons. *Nature*, **469**, 512-515.

[15] Saglamyurek E, Sinclair N, Jin J, Slater J A, Oblak D, Bussières F, George M, Ricken R, Sohler W and Tittel W 2012 Conditional detection of pure quantum states of light after storage in a Tm-Doped waveguide. *Phys. Rev. Lett.*, **108,** 083602.

[16] Johnson L M and Cox C H 1988 Serrodyne optical frequency translation with high sideband suppression. *J. Lightwave Technol.* **6,** 1.

[17] de Riedmatten H, Afzelius M, Staudt M U, Simon C and Gisin N. 2008 A solid-state light matter interface at the single-photon level. *Nature* **456,** 773.

[18] Afzelius M, Simon C, de Riedmatten H and Gisin N 2009 Multimode quantum memory based on atomic frequency combs *Phys. Rev. A* **79** 052329.

[19] Zhou Z Q, Lin W B, Yang M, Li C F and Guo G C 2012 Realization of reliable solid-state quantum memory for photonic polarization qubit. *Phys. Rev. Let.* **108,** 19:190505.

[20] Sabooni M, Li Q, Kröll S and Rippe L 2013 Efficient Quantum Memory Using a Weakly Absorbing Sample *Phys. Rev. Lett.* **110**, 133604.

[21] Usmani I, Afzelius M, de Riedmatten H, and Gisin N 2010 Mapping multiple photonic qubits into and out of a solid-state atomic ensemble. *Nature Commun.*, **1,** 12.

[22] Bonarota M, Le Gouët J L and Chanelière T 2010 Highly multimode storage in a crystal *New J. Phys.* **13** 013013.

[23] Sinclair N, Saglamyurek E, Mallahzadeh H, Slater J A, George M, Ricken R, Hedges M P, Oblak D, Simon C, Sohler W and Tittel W 2013 A solid-state memory for multiplexed quantum states of light with read-out on demand *Arxiv:*, **1309.3202** quant-ph.

[24] Gündoğan M, Ledingham P M, Almasi A, Cristiani M and de Riedmatten H 2012 Quantum storage of a photonic polarization qubit in a solid *Phys.Rev. Lett* **108** 190504.

[25] Clausen C, Usmani I, Bussières F, Sangouard N, Afzelius M de Riedmatten H and Gisin N 2011 Quantum storage of photonic entanglement in a crystal. *Nature,* **469,** 508.

[26] Clausen C, Bussières F, Afzelius M and Gisin N 2012 Quantum storage of heralded polarization qubits in birefringent and anisotropically absorbing materials. *Phys. Rev. Lett.* **108,** 190503 (2011).

[27] Bussières F, Clausen C, Tiranov A, Korzh B, Verma V B, Nam S W, Marsili F, Ferrier A, Goldner P, Herrmann H, Silberhorn C, Sohler W, Afzelius M and Gisin N 2014 Quantum teleportation from a telecom-wavelength photon to a solid-state quantum memory. *arXiv*:**1401.6958** quant-ph.

[28] Barber Z W, Tian M, Reibel R R and Babbitt W R 2002 Optical pulse shaping using optical coherent transients. *Opt. Express,* **10,** 20:1145.

[29] Moiseev S A and Tittel W 2010 Temporal compression of quantum-information-carrying photons using a photon-echo quantum memory approach. *Phys. Rev. A* **82,** 012309.

[30] Linget H, Chanelière T, Le Gouët, J L, and Louchet-Chauvet A 2013. Time reversal of light by linear dispersive filtering near atomic resonance. *New J. Phys.*, **15**(6), 063037.

[31] Humphreys P C, Metcalf B J, Spring J B, Moore M, Jin X M, Barbieri M, Kolthammer W S Walmsley I A 2013 Linear optical quantum computing in a single spatial mode *Phys. Rev. Lett* **111**, 150501.

[32] Thiel C W, Sun Y, Böttger T, Babbitt W R and Cone R L 2010 Optical decoherence and persistent spectral hole burning in Tm:$LiNbO_3$ *J. Lumin.* **130,** 9, 1598–1602.

[33] Afzelius M and Simon C 2010 Impedance matched cavity quantum memory *Phys. Rev. A* **82**, 022310

[34] Moiseev S A, Andrianov S N and Gubaidullin F F 2010 Efficient multimode quantum memory based on photon echo in an optimal QED cavity *Phys. Rev. A* **82**, 022311.

[35] Jobez P, Usmani I, Timoney N, Laplane C, Gisin N and Afzelius M 2014 Cavity-enhanced storage in an optical spin-wave memory. *arXiv*:**1404.3489** quant-ph

[36] Tian M, Vega D and Dilles J 2013 Quantum memory based on a spatiospectral atomic comb *Phys. Rev. A* **87,** 042338.

[37] Afzelius M, Usmani I, Amari A, Lauritzen B, Walther A, Simon C, Sangouard N, Minář J, de Riedmatten H, Gisin N and Kröll S 2010 Demonstration of atomic frequency comb memory for light with spin-wave storage *Phys. Rev. Lett.* **104** 040503

[38] Timoney N, Lauritzen B, Usmani I, Afzelius M and Gisin N 2012 Atomic frequency comb memory with spin-wave storage in $^{135}Eu^{3+}$:Y_2SiO_5, *J. Phys. B: At. Mol. Opt. Phys.* **45** 124001

[39] Gündoğan M, Mazzera M, Ledingham P M, Cristiani M and de Riedmatten H 2013 Coherent storage of temporally multimode light using a spin-wave atomic frequency comb memory *New J. Phys.* **15** 045012

[40] Lauritzen B, Minář J, de Riedmatten H, Afzelius M, Sangouard N, Simon C and Gisin N 2010 Telecommunication-Wavelength solid-state memory at the single photon level. *Phys. Rev. Lett.* **104,** 080502

[41] Saglamyurek E et al 2014 A fiber-based atomic quantum memory for entangled photons at telecommunication wavelength. *In preparation*

[42] Morse J D, McCammon K G, McConaghy C F, Masquelier D A, Garrett H E, Lowry M E 1994 Characterization of lithium niobate electro-optic modulators at cryogenic temperatures *Proc. SPIE* **2150**.

[43] Sinclair N, Saglamyurek E, George M, Ricken R, La Mela C, Sohler W and Tittel W 2010 Spectroscopic investigations of a Ti:Tm:$LiNbO_3$ waveguide for photon-echo quantum memory. *J. Lumin.*, **130,** 9:1586-1593.

[44] Thiel C W, Sun Y, Macfarlane R M, Böttger T and Cone R C 2012 Rare-earth-doped $LiNbO_3$ and KTP for waveguide quantum memories. *J. Phys. B: At. Mol. Opt. Phys,* **45,** 124013.

[45] Palittapongarnpim P, MacRae A and Lvovsky A I 2012 A monolithic filter cavity for experiments in quantum optics *Rev. Sci. Instrum.* **83** 6:066101

Appendix F

Paper 6

arXiv:1510.01164 (2015), to be submitted

Cross-phase modulation of a probe stored in a waveguide for non-destructive detection of photonic qubits

Neil Sinclair[1], Khabat Heshami[2], Chetan Deshmukh[1], Daniel Oblak[1], Christoph Simon[1], and Wolfgang Tittel[1]

[1]*Institute for Quantum Information Science, and Department of Physics and Astronomy, University of Calgary, 2500 University Drive NW, Calgary, Alberta T2N 1N4, Canada* [2]*National Research Council of Canada, 100 Sussex Drive, Ottawa, Ontario, K1A 0R6, Canada*

Abstract

Non-destructive detection of photonic qubits is an enabling technology for quantum information processing and quantum communication [1, 2, 3, 4, 5, 6, 7, 8, 9, 10]. For practical applications such as quantum repeaters [11] and networks [12, 13], it is desirable to implement such detection in a way that allows some form of multiplexing as well as easy integration with other components such as solid-state quantum memories [14, 15]. Here we propose an approach to non-destructive photonic qubit detection that promises to have all the mentioned features. Mediated by an impurity-doped crystal, a signal photon in an arbitrary time-bin qubit state [16] modulates the phase of an intense probe pulse that is stored during the interaction. Using a thulium-doped waveguide in $LiNbO_3$, we

perform a proof-of-principle experiment with macroscopic signal pulses, demonstrating the expected cross-phase modulation as well as the ability to preserve the coherence between temporal modes. Our findings open the path to a new key component of quantum photonics based on rare-earth-ion doped crystals.

F.1 Introduction

The ability to detect photonic qubits non-destructively is highly desirable for photonic quantum information processing and quantum communication. For instance, it makes it possible to use precious resource states (say entangled photon pairs for quantum teleportation) only when the input photons are actually there. This is all the more essential in situations of significant loss, such as for quantum repeaters [11, 17]. Non-destructive detection of photons [6] and heralded storage of photonic qubits [8] (which, when combined with readout, is equivalent to non-destructive detection) have recently been realized in sophisticated quantum electrodynamics experiments that combine single-atom control and high-finesse cavities, and work at one specific atomic transition frequency. For practical applications it is important to have a simple and robust implementation of the same functionality but with added flexibility. In particular, it should allow for multiplexing, and be compatible with existing quantum information processing and communication components.

Here we propose a detection scheme that has all of these characteristics. The basic principle, illustrated in Fig. F.1, is based on cross-phase modulation between a weak signal and a strong probe pulse mediated by a rare-earth ion doped crystal — a technology platform whose suitability for quantum photonics has already been demonstrated [15, 18, 19, 20, 21, 22, 23, 24]. For single-photon sensitivity, the phase shift has to be greater than the quantum phase uncertainty of the probe, which is of order $1/\sqrt{N_p}$, where N_p

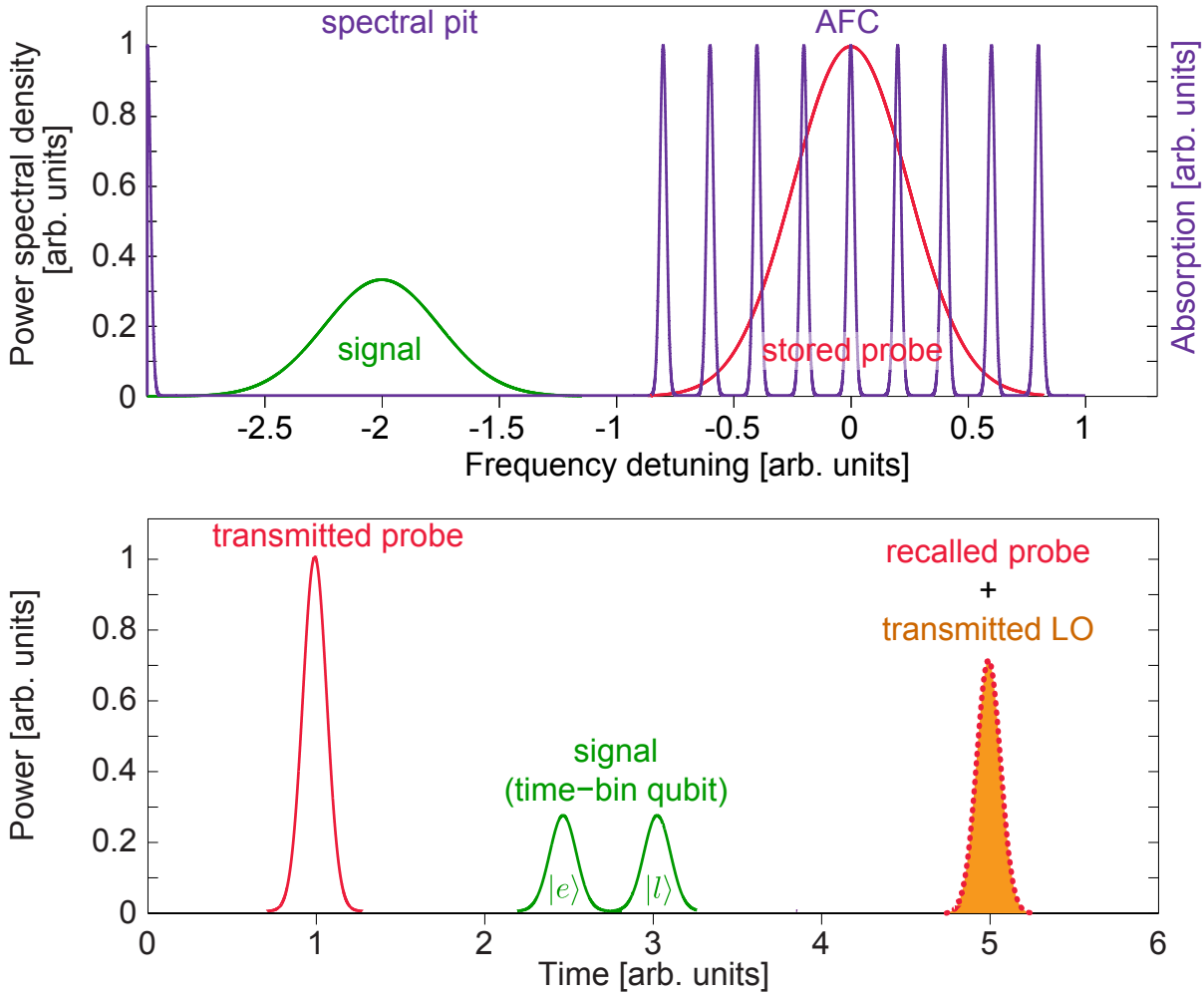

Figure F.1: Non-destructive detection of photonic time-bin qubits. A macroscopic probe pulse is stored in an atomic frequency comb (AFC) memory. The signal — a photonic time-bin qubit — propagates through a detuned transparency window and frequency shifts the atoms constituting the AFC due to the AC Stark effect. This results in a phase shift of the re-emitted probe. **a,** Spectral representation. **b,** Temporal representation. $|e\rangle$ and $|l\rangle$ denote early and late qubit modes, respectively.

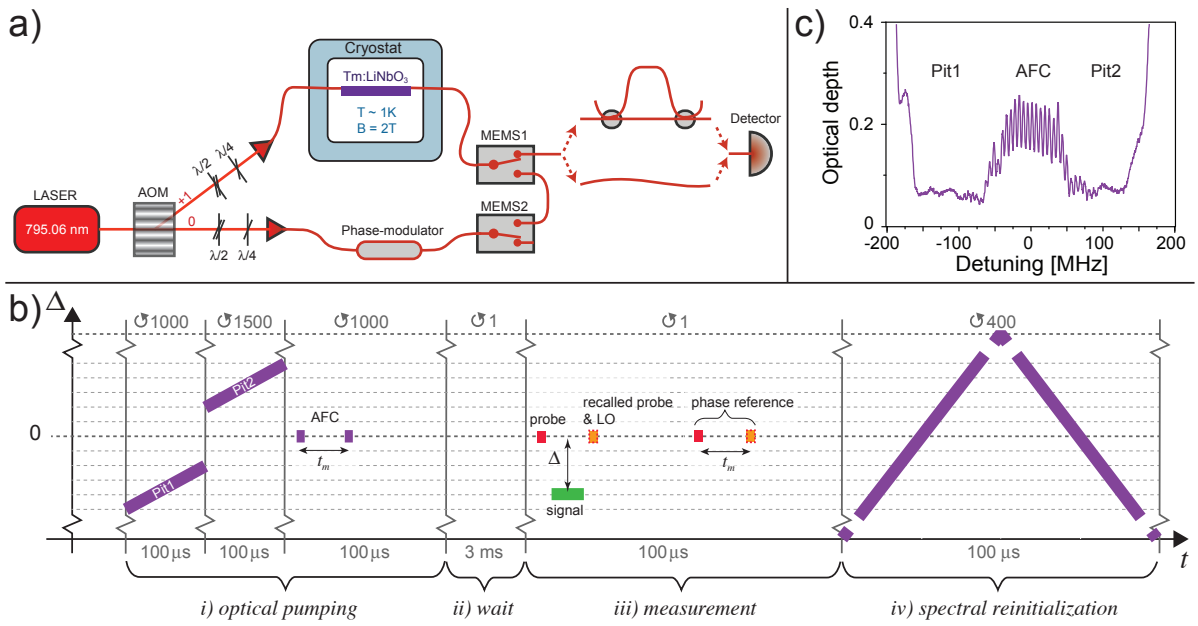

Figure F.2: Outline of the experiment. **a,** Setup. Light from a frequency-locked 795.06 nm CW-laser is intensity and frequency modulated using an acousto-optic modulator (AOM). The diffracted first-order beam is coupled via fiber into the $Tm:LiNbO_3$ waveguide, and waveplates enable adjusting its polarization to maximize the interaction with Tm ions within a single spatial mode of ∼12.5 μm diameter (characterized independently). **b,** Timing sequence. *i) Optical pumping* involves repetitive spectral pit burning at negative (-150 to -50 MHz) and positive (50 to 150 MHz) detunings for at total of 250 ms, and AFC generation using many pulse-pairs for 100 ms. (Depicted is one repetition as well as the number of repetitions per task.) *ii)* After a 3 ms *wait* time to allow excited atomic population to decay, we perform our *measurement (iii)*: A 10 ns long probe is stored in the AFC, followed by a detuned signal that is transmitted through a spectral pit. A local oscillator (LO) interferes with the probe pulse recalled after 180 ns storage. Another 200 ns later, we perform a phase reference measurement using the same sequence but excluding the signal pulse. At the memory output, a micro electro-mechanical switch (MEMS1) blocks light during optical pumping. It opens during the measurement to allow the transmission of the recalled probe pulse to the detector — either directly or via an unbalanced interferometer, depending on the measurement performed. *iv)* As the strong probe pulses modify the tailored spectral feature, we *reinitialize* the absorption line after every measurement using zeroth-order light from the AOM that is repetitively frequency-modulated over a 5-GHz range by a phase modulator. The light enters the thulium-doped waveguide through MEMS2 and MEMS1; it is blocked by MEMS2 outside the reinitialization step of 40 ms duration. **c,** Spectral feature. A 100 MHz wide AFC with a tooth separation $\Delta_m/(2\pi) = 5.5$ MHz (corresponding to a storage time of $t_m = 180$ ns) and a 100 MHz wide spectral pit on either side of the AFC.

is the number of photons in the probe. The probe is stored in an impurity-doped crystal using the atomic frequency comb (AFC) quantum memory protocol [25], and the phase shift is due to the AC Stark shift of the relevant atomic transition caused by the signal. For large detuning between signal and probe, it is given by

$$\phi = N_s \frac{1}{4\pi} \frac{\lambda^2}{n^2 A} \frac{\gamma}{\Delta}, \tag{F.1}$$

where N_s is the number of photons in the signal, λ the vacuum wavelength of the atomic transition, n the refractive index of the crystal, A the interaction cross section, γ the spontaneous decay rate from the excited state, and $\Delta/(2\pi)$ the detuning in Hz. See the Supplementary Information for a detailed derivation. Eq. (F.1) shows that the phase shift benefits from lateral confinement (small A) and small detuning, and that it increases linearly with the number of signal photons.

We emphasize that the phase shift does not depend on the exact timing of the signal, as long as it propagates through the medium while the probe is being stored. In particular, this allows one to detect the presence of a photon without affecting its qubit state, provided that the qubit is encoded in temporal modes — a very convenient and widely-used choice in quantum communication. (Note that photonic qubits can easily be converted between different types of encoding [26]).

F.2 Experiment

Our experimental set-up, sketched in Fig. F.2a, is composed of a Tm:$LiNbO_3$ waveguide quantum memory, a source for signal and probe pulses, and analyzers that allow characterizing these pulses after the waveguide-mediated interaction. We use the optical pumping sequence illustrated in Fig. F.2b to spectrally tailor the inhomogeneously broadened ${}^3H_6 \rightarrow {}^3H_4$ absorption line of Tm into a series of absorption peaks (teeth) spaced by angular frequency Δ_m (the AFC), surrounded by transparent pits (see Fig F.2c). The

bandwidth of the AFC and each of the pits is about 100 MHz, and the AFC memory storage time, given by $t_m = 2\pi/\Delta_m$, is 180 ns.

Following the spectral tailoring, we generate a probe pulse of ~ 10 ns duration whose spectrum matches the AFC. A part of the pulse is transmitted through the waveguide and a part of it is stored in the thulium ions forming the AFC. As illustrated in Fig F.2b, we then send a signal whose temporal structure, intensity and detuning w.r.t. the AFC we can vary, depending on the desired measurement. After the storage time t_m the probe pulse is re-emitted from the memory. To measure its phase change due to the interaction with the signal, we interfere it with a local oscillator (LO). See the Methods section for more details about the AFC generation and the measurement.

F.3 Measurements and Results

First, to verify the probe-phase-shift dependence given in Eq. F.1, we use a signal pulse in a single temporal mode of 130 ns duration. We vary the number of photons per pulse for nine different detunings, and record the phase shift averaged over 200 repetitions for each photon-number. As expected, we find a linear increase as a function of the number of signal photons, and that the slopes for red and blue detuning have opposite signs, as shown for two detunings in the inserts of Fig F.3. From the fitted slopes we find the phase-shifts per photon, which are shown in Fig F.3 together with the expected values. We see that the measured data closely follows the theoretical predictions derived from Eq. F.1 using λ=795 nm, n=2.3, A=$\pi\times(6.25\ \mu\text{m})^2$, γ=9.1 kHz. In particular, at +100 MHz detuning, we measure a phase shift of 1.10×10^{-9} rad/photon, which is in excellent agreement with the expected value of 1.12×10^{-9} rad/photon.

Next, we demonstrate that the probe phase shift does not depend on how the signal energy is distributed between two temporal modes, and that the signal is not affected

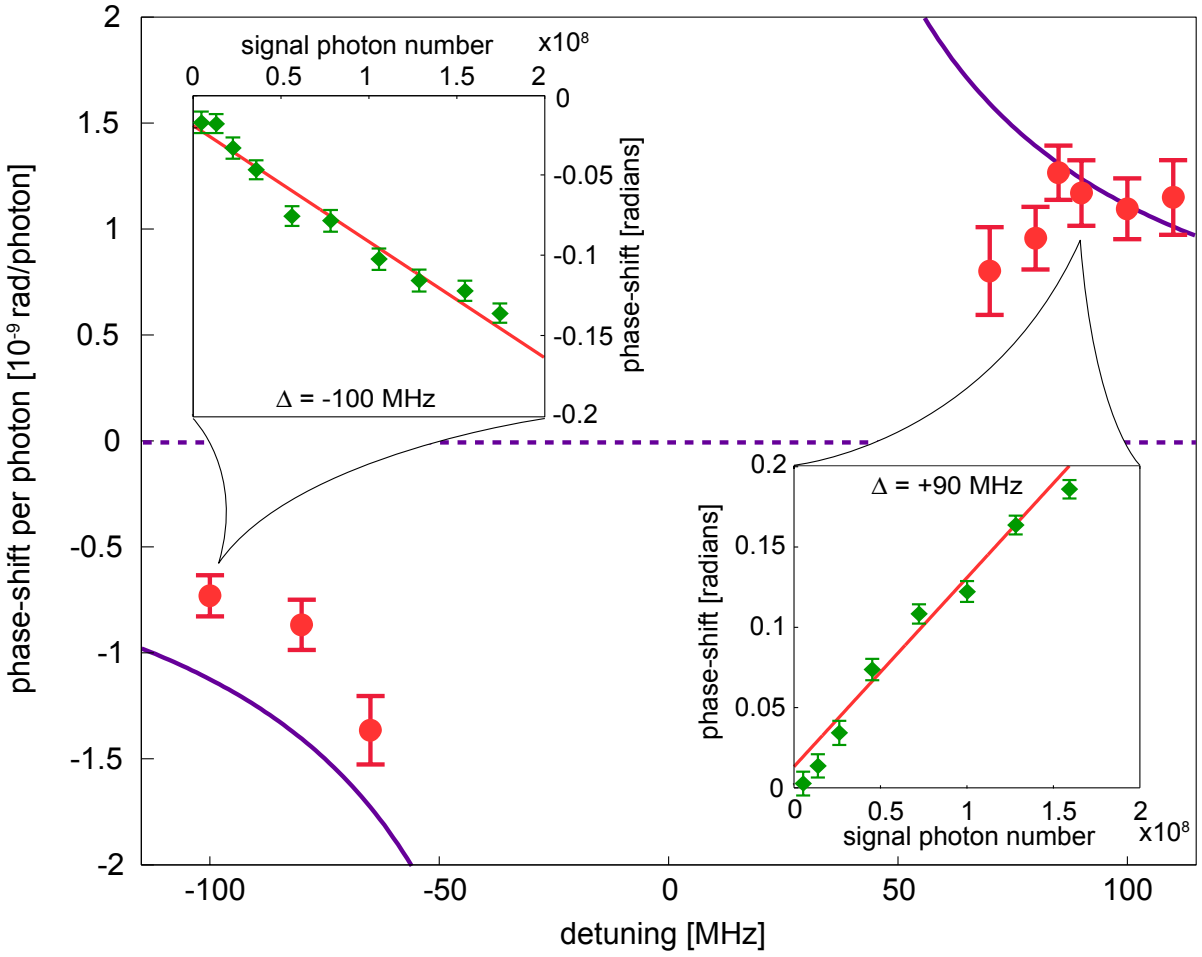

Figure F.3: Phase shift per photon for different detuning values. Expected phase shifts (purple line) according to Eq. F.1 (no fit), and experimentally obtained values (red circles) derived from linear fits to the phase shift vs. mean photon number as illustrated in the insets for two detuning values (red lines). Each data point in the insets (green diamonds) corresponds to an average over 200 repetitions. Uncertainty bars indicate the standard deviation of the average. Discrepancies between measured and predicted values are most likely due to imperfect AOM operation resulting in non-ideal signal spectra and pits (see Fig. F.2c), both of which are asymmetric w.r.t. zero-detuning.

by the measurement. Put into the context of an interaction with a single photon in a time-bin qubit state, this implies that the measurement does not project the qubit onto a specific set of basis states and thus alter it. Towards this end, we select early and late signal modes, each of 10 ns duration, separated by 18.3 ns, and featuring a detuning of +100 MHz. Keeping the total energy constant, we generate signals in which the energy is concentrated in either the early or the late mode, or in an equal superposition with either 0 or π phase-difference ('+' and '-' superpositions, respectively). The resulting probe phase shifts, averaged for each pulse sequence over 1000 repetitions, are plotted in Fig. F.4, which also includes the phase shift measured without a signal pulse. We find that, within experimental uncertainty, the phase shifts are the same irrespective of the signal state, and they clearly differ from the phase shift measured without any signal. Furthermore, to verify that our measurement preserves the signal state, we assess erroneous detections of signals prepared in various states without and with the measurement (see the Methods section for details). As shown in the inset of Fig. F.4, we find close to no change due to the cross-phase interaction, which is consistent with the fact that our scheme can measure the presence of a time-bin qubit without revealing, nor modifying, its state.

F.4 Discussion and Conclusion

While our proof-of-principle demonstration confirms the key features of the proposed scheme, a lot remains to be done before qubits encoded into individual and spectrally multiplexed photons can be detected non-destructively and without averaging. We expect that a reduction of the interaction cross section, e.g. using a small-diameter ridge waveguide, can improve the phase sensitivity by more than a factor of 100 (see Eq. F.1). Furthermore, the ratio between the radiative lifetime γ and the detuning Δ has to be increased beyond its current value of 9 kHz/($2\pi\times$65 MHz)$\sim 2.2\times10^{-5}$ — it can in prin-

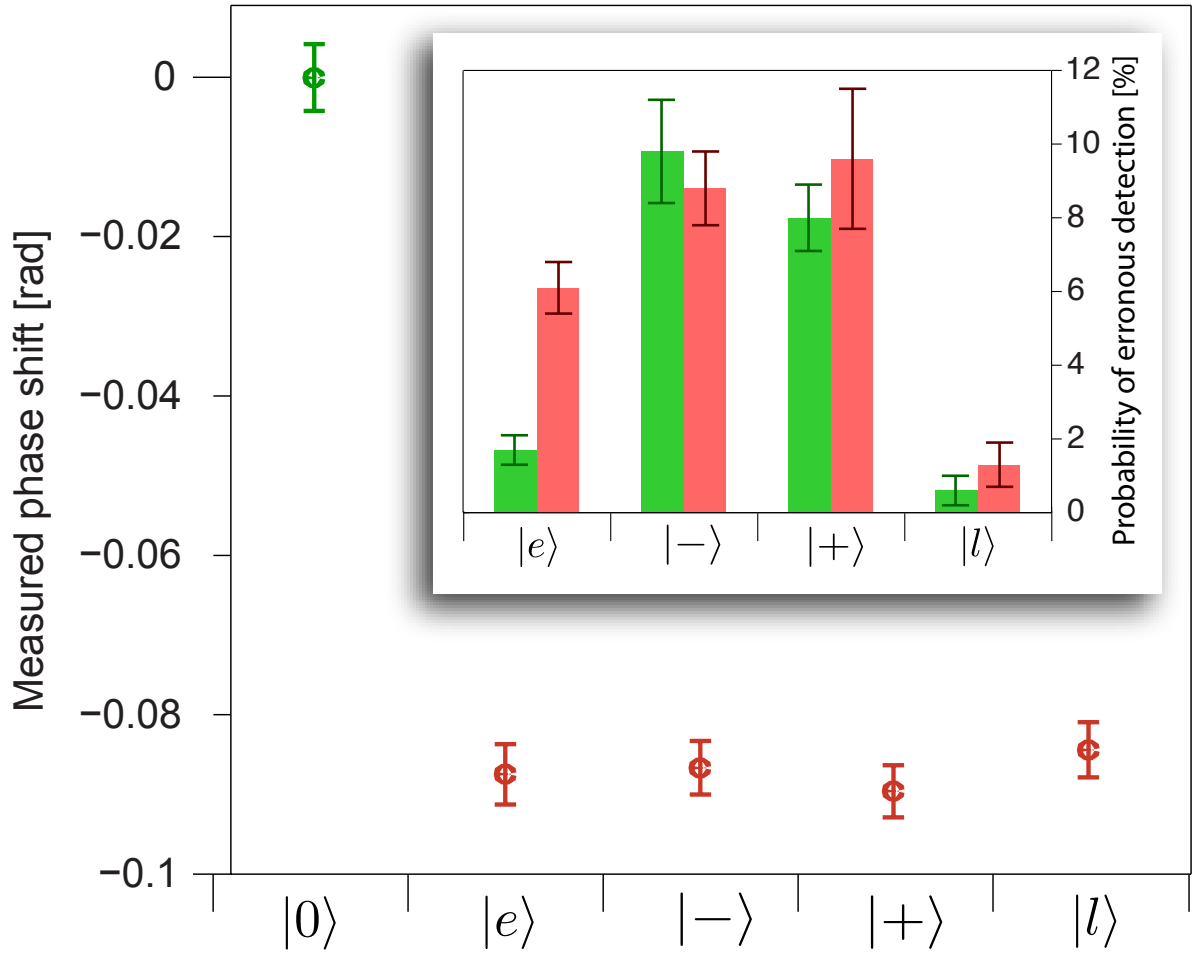

Figure F.4: State preservation for signals in different temporal modes. Probe phase shifts due to 6.9×10^7, or no, signal photons, distributed between early and late temporal modes. The labels on the x-axis refer to corresponding time-bin qubit states. Each data point shows the average over 1000 measurements, and uncertainty bars denote the standard deviation of the average. The inset shows the error rates of the different signal states before and after the measurement (error bars are calculated from shot-to-shot pulse-heights variations). There is no significant change, except for $|e\rangle$. (Increased errors are likely due to free induction decay after exciting remaining thulium atoms inside the pit, and would disappear with better hole burning. As the decay happens after absorption, only $|e\rangle$ is affected. Errors for the superposition states are caused by imperfections in the interferometer.)

ciple approach a percent. As a result of these improvements, the phase shift per photon could thus be as large as 100 μrad, which would allow single-shot detection of individual photons.

Reducing the detuning to maximize γ/Δ comes with the unwanted effects of increasing off-resonant absorption of the signal in the AFC, increasing the noise due to decay from excited atoms, and decreasing the achievable bandwidth. However, as we discuss in more detail in the Supplementary Information, these problems can be overcome in a configuration in which the population in the excited state (populated through the absorption of the strong probe in the AFC) is temporarily transferred to an auxiliary level, and in which the signal passes many times through the spectral pit during the storage of the probe (using, e.g., a cavity [22]). This makes it possible to increase the detuning and thus reduce the absorption of the signal without decreasing the number of atoms in the AFC nor the total phase shift experienced by the probe. For instance, we anticipate the nondestructive measurement to be feasible for photons of half a MHz bandwidth, using an AFC with teeth of optical depth 30 [19], and interacting approximately 900 times with the stored probe, which corresponds to a moderate-finesse cavity.

We emphasize that the cross-phase interaction in rare-earth-ion doped crystals is straightforward to generalize to multiple spectral channels, as demonstrated in the context of AFC-based optical quantum memory [23], which can extend over a total bandwidth of hundreds of GHz [27]. We also note that the present approach should allow the development of a standard (destructive) photon-number-resolving detector, for which the limitations imposed by signal loss and noise are less severe.

We believe that an improved version of our proof-of-principle demonstration will soon allow first destructive, and then non-destructive, "single shot" detection of photons. This will open the path to more efficient use of precious resources in advanced applications of quantum communication, and the heralded generation of photon-number states, including

entangled states, that do not contain often detrimental admixtures of undesired photons as, e.g., in widely-used spontaneous parametric down-conversion [28]. Finally, we note that the bandwidth of the signal in our scheme is proportional to the linewidth of the relevant atomic transition, which, in our case, is around 10 kHz. To allow the non-destructive detection of photons featuring more than of order 1 MHz bandwidth, it may therefore be interesting to investigate impurity-doped crystals with transitions that feature shorter lifetimes, e.g. Ce:YAG [29].

F.5 Methods

Spectral tailoring

We tailor the spectrum of the inhomogeneously broadened ${}^3H_6 \rightarrow {}^3H_4$ absorption line in Tm^{+3} by means of frequency-selective optical pumping of Tm-ions to another ground-state Zeeman level [27]. The Zeeman splitting in the applied 2 T field is $\sim$2.5 GHz, which sets the upper limit for the total width of our spectral feature (the AFC and two pits). However, the bandwidth of the AOM used for laser frequency modulation practically limits the total width to 300 MHz.

First, as illustrated in Fig. F.2b, we generate two spectral pits by sweeping the frequency of the laser light repeatedly over two 100 MHz wide regions separated by a spectral interval of 100 MHz. The optical depth of the remaining background is around 0.07 dB. It is irregular due to varying efficiency of the AOM with detuning. Next, we generate an AFC in between the two pits by driving the AOM using pairs of pulses that are 10 ns wide and separated by 180 ns. The resulting AFC features a bandwidth of 100 MHz and a tooth separation of $\Delta_m/(2\pi) = 5.5$ MHz, corresponding to a storage time of 180 ns. The tooth separation is chosen to match side-peaks at 11 MHz arising from the super-hyperfine interaction of thulium with niobium in the host crystal [NS *et al.*,

in preparation], and the teeth width is limited by the long-term laser linewidth (1 MHz) combined with power broadening during spectral tailoring. The teeth feature an optical depth of ∼0.1, and are sitting on a background with optical depth of ∼0.15, resulting in a recall efficiency for the probe of 0.2% [25].

The quality of our spectral feature — the background in the pits and the AFC, as well as the small optical depth of the AFC teeth — is currently limited by long-term laser frequency jitter and non-ideal spectral tailoring. It can be improved by using a laser with improved stability, and by optical pumping based on "burning back population from the side" [19]. This will allow meeting the requirements for a non-destructive measurement at the single photon level detailed in the Supplementary Information.

Measurements

Phase measurements – Assessing the cross-phase modulation relies on an interferometric measurement of the recalled probe pulse with a transmitted local oscillator (LO) in the same spatial, temporal and spectral mode, and featuring the same intensity. First, by varying the phase of the LO in the absence of a signal, we calibrate the interference visibility to 89.7%. Next, to ensure maximum measurement sensitivity, we set the phase difference between the LO and the recalled probe (still without a signal) to $\pi/2$. Taking the calibration into account, this allows us in the actual measurement to map intensities (after interfering the probe with the LO) onto phase changes of the probe. Please note that the intensity of the recalled probe does not depend on whether or not a signal is present, i.e. the calibration, taken without any signal, remains valid when the latter is present.

The precision of the phase measurements is mainly limited by long-term laser frequency instability. We estimate that fluctuations between the AFC generation and the

creation of the probe ∼3 ms later result in shot-to-shot noise of around 150 mrad. To reduce this noise, we concatenate each measurement of the AC Stark shift on the probe with a reference measurement of the probe's phase without a signal (see Fig. F.2b). Subtracting the values obtained by these two phase-measurements (with a weight given by the correlation of two subsequent measurements without signal) allows improving the single-shot phase sensitivity to around 100 mrad. This value is mainly limited by laser frequency fluctuations between the generation of the probe and LO pulses, and can be further reduced by improved laser locking. In addition, pulse intensity fluctuations and electronic noise of the photo-detector contribute ∼50 mrad of phase uncertainty. By averaging phases over j measurement repetitions, the sensitivity improves by a factor of $j^{-1/2}$. For instance, for $j = 200$, we reach a resolution of ∼7 mrad.

Qubit measurements – The variation of the signal due to the interaction with the probe is assessed as follows: for early and late signal states we measure the pulse heights in the wrong time bin, normalized to the sum of the pulse heights in both bins. For the superposition states, we pass the signal through an imbalanced fiber interferometer whose arm-length difference corresponds to 18.3 ns travel time difference. Using a piezoelectric transducer in one arm of the interferometer, we set its phase to obtain maximum constructive interference in one output, and record the normalized pulse heights in the other (the wrong) output. All measurements are done twice — once before, and once after the signal is submitted to the cross-phase interaction. Differences in the results indicate the perturbation of the signal due to the measurement.

Acknowledgements

The authors thank Erhan Saglamyurek and Mikhail Lukin for useful discussions, and acknowledge funding through Alberta Innovates Technology Futures (AITF), the Na-

tional Science and Engineering Research Council of Canada (NSERC), and the Defense Advanced Research Projects Agency (DARPA) Quiness program (contract no. W31P4Q-13-l-0004). W.T. acknowledges funding as a Senior Fellow of the Canadian Institute for Advanced Research (CIFAR).

F.6 Supplementary Information

Storage of the probe; use of additional levels

The first step in our protocol involves the storage of a classical probe field. Here, we provide a semi-classical treatment of the light-matter interaction to describe AFC storage and retrieval of the probe field (see also [30]). The total Hamiltonian describing our system is given by

$$\hat{H} = \hat{H}_0 + \hat{H}_{int}, \tag{F.1}$$

where

$$\hat{H}_0 = \sum_{j=1}^{N} \hbar\omega_{ge}^{j} \hat{\sigma}_{ee}^{j}, \tag{F.2}$$

and

$$\hat{H}_{int} = -\hbar \sum_{j=1}^{N} \left(\Omega(z,t) \hat{\sigma}_{eg}^{j} e^{-i\omega_p(t-z_j/c)} + H.c. \right). \tag{F.3}$$

Here, $\hbar\omega_{ge}^{j}$ denotes the excited state energy of atom j and ω_p is the control frequency of the probe field; $\Omega(z,t) = \frac{\mu_{eg}\mathcal{E}_p(z,t)}{2\hbar}$ is the Rabi frequency associated with the probe field ($\mathcal{E}_p$), and $\mu_{eg} = \langle e|\hat{d}.\epsilon_p|g\rangle$ is the transition dipole moment. Using the Heisenberg equation, one can find the following dynamical equations,

$$\dot{\hat{\sigma}}_{gg}(z,t;\delta) = i\Omega^*(z,t)\hat{\sigma}_{ge}(z,t;\delta) - i\Omega(z,t)\hat{\sigma}_{eg}(z,t;\delta), \tag{F.4}$$

$$\dot{\hat{\sigma}}_{ee}(z,t;\delta) = i\Omega(z,t)\hat{\sigma}_{eg}(z,t;\delta) - i\Omega^*(z,t)\hat{\sigma}_{ge}(z,t;\delta), \tag{F.5}$$

and

$$\dot{\hat{\sigma}}_{eg}(z,t;\delta) = i(\omega_0 + \delta - \omega_p)\hat{\sigma}_{eg}(z,t;\delta) + i\Omega^*(z,t)\hat{\sigma}_{ee}(z,t;\delta) - i\Omega^*(z,t)\hat{\sigma}_{gg}(z,t;\delta), \tag{F.6}$$

where

$$\hat{\sigma}_{gg}(z,t;\delta) = \frac{1}{N_z(\delta)} \sum_{i=1}^{N_z(\delta)} \hat{\sigma}_{gg}^{i}(t;\delta), \tag{F.7}$$

$$\hat{\sigma}_{ee}(z,t;\delta) = \frac{1}{N_z(\delta)} \sum_{i=1}^{N_z(\delta)} \hat{\sigma}^i_{ee}(t;\delta), \tag{F.8}$$

and

$$\hat{\sigma}_{eg}(z,t;\delta) = \frac{1}{N_z(\delta)} \sum_{i=1}^{N_z(\delta)} \hat{\sigma}^i_{eg}(t;\delta) e^{-i\omega_p(t-z_i/c)}, \tag{F.9}$$

Here, ω_0 is the central frequency of the inhomogeneously broadened atomic ensemble, ω_p is the central frequency of the probe field, and δ denotes the detuning of different modes of the ensemble with respect to its central frequency. The atomic coherence and population for atom j are determined by $\hat{\sigma}_{\nu\nu'} = |\nu\rangle^j\langle\nu'|$, where $\nu, \nu' = g, e$; $\hat{\sigma}_{\nu\nu'}(z,t;\delta)$ are collective atomic operators for all atoms in a slice of the medium for (longitudinal) position z and frequency mode δ. Note that we assume that the number of atoms in mode δ at z, $N_z(\delta)$, is much larger than 1. In addition $N_(\delta)$ characterizes a periodic absorption feature (in the frequency domain) with periodicity Δ_m that is required for AFC storage. The propagation of the probe field can be derived starting from Maxwell's equations,

$$\left(\partial_z + \frac{n}{c}\partial_t\right) \mathcal{E}_p(z,t) = \frac{i\mu_0\omega_p^2}{2k_p}\langle\hat{\mathcal{P}}_{tot}\rangle, \tag{F.10}$$

where $\mathcal{E}_p(z,t)$ is the slowly varying envelope of the probe field, $k_p = \frac{n\omega_p}{c}$, and $\langle\hat{\mathcal{P}}_{tot}\rangle$ denotes the expectation value of

$$\hat{\mathcal{P}}_{tot} = \sum_{\delta} \langle g|\hat{d}.\epsilon_p|e\rangle \frac{N(\delta)}{V} \hat{\sigma}_{ge}(z,t;\delta). \tag{F.11}$$

Equations F.4,F.5,F.6 along with Eqs. F.10,F.11 allow us to describe the dynamics of the atoms due to the probe field, when $t < T_1$ and $t > T_2$. $T_1 < t < T_2$ is the time between the probe storage and retrieval in which the evolution in perturbed by presence of the signal field; see below. Storage of a probe field carrying an average photon number N_p that is smaller than the total number of atoms N_g is expected to result in a coherent state distribution of atomic excitations. In addition, the bosonic characteristics of the

collective atomic excitation ($\hat{\sigma}_{ge}(z,t;\delta)$) can be used to evaluate the above expectation value of the total atomic polarization operator.

In the proof-of-principle experiment reported in the main text the same atomic transition is used for signal and probe fields. To minimize loss and noise for the signal, it is desirable not to have significant population in the excited state e when the signal propagates through the medium. This can be achieved either by using transitions from the same ground state to two different excited states (a V configuration), or by transferring the excited state population to another level (e.g. another ground state level or a metastable state, i.e. a Λ-type configuration) after the probe has been absorbed. The latter approach also provides a larger time window for signal propagation. Under these conditions, the signal sees an $e-g$ transition where there is no population in e, but the number of atoms in g is reduced with respect to the total initial number by the number of probe photons that were absorbed. For optimum phase sensitivity the number of absorbed photons N_p should be of order $N/2$, where N is the total number of atoms. In this case the number of atoms remaining in the ground state N_g is equal to N_p, $N_g = N_p = N/2$.

Derivation of effective Hamiltonian for cross-phase modulation

In this section, we provide the quantum-mechanical Hamiltonian for the interaction between the signal field and the atoms. For large detunings, where Δ is larger than the signal bandwidth, we derive an effective interaction Hamiltonian that will be used to find the probe phase shift with respect to the number of photons in the signal field.

The total Hamiltonian that governs the dynamics due to the presence of the signal field is given by

$$\hat{H}_{tot} = \hat{H}_0 + \hat{H}_{int} = \sum_{j=1}^{N} \hbar\omega_{ge}^{j}\sigma_{ee}^{j} + \hat{h}_{int}^{j}, \tag{F.12}$$

where

$$\hat{h}^j_{int} = -\hbar g\sqrt{\frac{L}{2\pi c}}\int d\omega \hat{a}_\omega e^{i\omega z_j/c}\hat{\sigma}^j_{eg} + \text{H.c.}. \tag{F.13}$$

The transition frequency of the j^{th} atom is ω^j_{eg}, and the atomic coherence and population operators are denoted by $\hat{\sigma}_{\nu\nu'} = |\nu\rangle^j\langle\nu'|$, where $\nu, \nu' = \{g, e\}$. The single photon coupling is given by $g = \mu_{eg}\sqrt{\frac{\omega_s}{2\hbar\epsilon V}}$, where ω_s is the central frequency of the signal and the transition dipole moment $\mu_{eg} = \langle e|\mathbf{d}\cdot\epsilon_s|g\rangle$. We define $\hat{\sigma}_{\nu\nu'}(z,t;\delta)$ as collective atomic operators for all atoms in a slice of the medium at position z and for frequency mode δ. Here, ω_s is the central frequency of the signal field. Throughout this analysis, we assume that $\omega_p = \omega_0$, where ω_0 is the central frequency of the AFC. This means that δ denotes different modes of the ensemble with respect to its central frequency.

We use the collective atomic operators that are defined in Eqs. F.7, F.8 and F.9 to re-write the interaction Hamitonian in Eq. F.13. This results in

$$\hat{H}_{int} = -\hbar g\sum_{j=1}^{N}\sqrt{\frac{L}{2\pi c}}e^{i\omega_p(t-z_j/c)}\int d\omega \hat{a}_\omega e^{i\omega z_j/c}\hat{\sigma}^j_{eg}e^{-i\omega_p(t-z_j/c)} + H.c., \tag{F.14}$$

which leads to

$$\hat{H}_{int} = -\hbar g\int dz n_z(\delta)e^{i\Delta(t-z/c)}\hat{\mathcal{E}}_s(z,t)\hat{\sigma}_{eg}(z,t;\delta) + H.c., \tag{F.15}$$

where $\hat{\mathcal{E}}_s(z,t) = \sqrt{\frac{L}{2\pi c}}e^{i\omega_s(t-z/c)}\int d\omega\hat{a}_\omega e^{i\omega z/c}$, $n_z(\delta)dz = N_z(\delta)$, $\int dz n_z(\delta) = N(\delta)$ and $\Delta = \omega_p - \omega_s$ is the detuning between the signal and probe fields.

For detunings much larger than the bandwidth of the signal field ($\Delta \gg 1/\tau_s$), we expect the dynamics of the atomic polarization ($\hat{\sigma}_{eg}(z,t;\delta)$) to be dominated by the fast rotating terms of $e^{\pm i\Delta t}$. In order to capture this effect, let us consider the dynamics of $\hat{\sigma}_{eg}(z,t;\delta)$ due to $\hat{H}_{int}$. Starting from $\dot{\hat{\sigma}}_{eg}(z,t;\delta) = \frac{i}{\hbar}\left[\hat{H}_{int}, \hat{\sigma}_{eg}(z,t;\delta)\right]$, we find

$$\dot{\hat{\sigma}}_{eg}(z,t;\delta) = -ige^{-i\Delta(t-z/c)}\hat{\mathcal{E}}^\dagger_s(z,t)\left(\hat{\sigma}_{gg}(z,t;\delta) - \hat{\sigma}_{ee}(z,t;\delta)\right), \tag{F.16}$$

which leads to

$$\hat{\sigma}_{eg}(z,t;\delta) = -ig\int_0^t dt' e^{-i\Delta(t'-z/c)}\hat{\mathcal{E}}^\dagger_s(z,t')\left(\hat{\sigma}_{gg}(z,t';\delta) - \hat{\sigma}_{ee}(z,t';\delta)\right). \tag{F.17}$$

For any state and for large detunings ($\Delta \gg 1/\tau_s$), this integral can be approximately evaluated by integrating the fast oscillating part and multiplying it by the final value of the slowly varying component. This approximation allows us to find the collective atomic polarization as

$$\hat{\sigma}_{eg}(z,t;\delta) = \frac{g}{\Delta} e^{-i\Delta(t-z/c)} \hat{\mathcal{E}}_s^\dagger(z,t) \left(\hat{\sigma}_{gg}(z,t;\delta) - \hat{\sigma}_{ee}(z,t;\delta)\right). \tag{F.18}$$

Using the above equation, in an iteration, we replace $\hat{\sigma}_{eg}(z,t;\delta)$ in Eq.F.15 to find an effective interaction Hamiltonian as follows,

$$\hat{H}_{int}^{eff} = -\frac{\hbar g^2}{\Delta} \int dz n_z(\delta) \left(\hat{\mathcal{E}}_s(z,t)\hat{\mathcal{E}}_s^\dagger(z,t) + \hat{\mathcal{E}}_s^\dagger(z,t)\hat{\mathcal{E}}_s(z,t)\right) (\hat{\sigma}_{gg}(z,t;\delta) - \hat{\sigma}_{ee}(z,t;\delta)) \tag{F.19}$$

Using the effective interaction Hamiltonian we derive the dynamical equation for the collective atomic polarization.

$$\dot{\hat{\sigma}}_{eg}(z,t;\delta) = \frac{i}{\hbar}\left[\hat{H}_0 + \hat{H}_{int}^{eff}, \hat{\sigma}_{eg}(z,t;\delta)\right] + \frac{\partial \hat{\sigma}_{eg}(z,t;\delta)}{\partial t}.$$

This leads to

$$\dot{\hat{\sigma}}_{eg}(z,t;\delta) = i\delta\hat{\sigma}_{eg}(z,t;\delta) + \frac{2ig^2}{\Delta}\left(\hat{\mathcal{E}}_s(z,t)\hat{\mathcal{E}}_s^\dagger(z,t) + H.c.\right)\hat{\sigma}_{eg}(z,t;\delta), \tag{F.20}$$

and consequently

$$\hat{\sigma}_{eg}(z,t=T_2;\delta) = e^{i\delta t} e^{i\hat{\Phi}} \hat{\sigma}_{eg}(z,t=T_1;\delta), \tag{F.21}$$

where

$$\hat{\Phi} = \int_{T_1}^{T_2} dt' \frac{2g^2}{\Delta}\left(\hat{\mathcal{E}}_s(z,t')\hat{\mathcal{E}}_s^\dagger(z,t') + \hat{\mathcal{E}}_s^\dagger(z,t')\hat{\mathcal{E}}_s(z,t')\right). \tag{F.22}$$

Note that the above dynamics describe the effects during the signal field propagation. The storage and retrieval of the probe field can be treated separately. Phase modulations due to the presence of the signal will appear in the first echo of the probe field. In addition, the total phase only depends on the total energy in the signal field and does not reveal any information about the temporal distribution of the signal field.

Phase shift per signal photon

Given Eqs. F.21 and F.23, one can find the amount of phase shift for a single photon signal propagating in the waveguide and interacting off-resonantly with the atomic polarization. The electric dipole interaction Hamiltonian can be used to relate the spontaneous emission rate of a two-level system to its transition dipole moment. For two-level atoms in a solid with dipoles oriented along a specific direction, this results in $\gamma = \frac{\mu_{eg}^2 \omega_0^3}{\pi \epsilon \hbar c^3}$. Assuming that $\lambda_s \approx \lambda_0$ we can find the phase shift due to a single photon as

$$\phi = \frac{2g^2}{\Delta}\tau_s = \frac{1}{4\pi}\frac{\lambda_0^2}{n^2 A}\frac{\gamma}{\Delta}, \tag{F.23}$$

where $\tau_s = c/L$ is the duration of the signal in vacuum and A is the cross-section area of the interaction, and λ_0 is the wavelength associated with the corresponding atomic transition in vacuum. If the population in the excited state is transferred to another ground state in order to minimize loss and noise (as discussed at the end of section I), then this expression for the phase shift has to be divided by a factor of 2 because this state is unaffected by the AC Stark shift due to the signal.

Signal loss

In this section, we analyze the signal photon loss due to its off-resonant interaction with the atoms in the AFC. In order to find a simplified description for off-resonant absorption loss, we assume that the signal detuning is larger than the inhomogenous bandwidth of the ensemble. This also guarantees that Δ is much larger than the spontaneous emission rate, γ.

For analyzing the signal loss, we treat the signal propagation using the Maxwell equation as follows

$$\left(\partial_z + \frac{n}{c}\partial_t\right)\hat{\mathcal{E}}_s(z,t) = \frac{\mu_0 \omega_0^2 \mu_{eg}}{2k_0}\sum_{\delta}\frac{N(\delta)}{V}\hat{\sigma}_{eg}(z,t;\delta), \tag{F.24}$$

where $k_0 = \frac{n\omega_0}{c}$. Given that the equations governing the single-excitation wave functions are the same as the Maxwell-Bloch equations, for evaluating the signal loss, we replace the atomic polarization and photonic annihilation operators with their corresponding wave functions. We are interested in the output signal wave function. This can be found by taking the Fourier transform of the Maxwell-Bloch equations. As a result the output signal can be written as

$$\tilde{\mathcal{E}}_s(z,\omega)|_{z=L} = e^{ik_s\chi(\omega)L}\tilde{\mathcal{E}}_s(z=0,\omega), \tag{F.25}$$

where

$$\chi(\omega) = \frac{1}{k_s}\left(-\frac{n\omega}{c} + \frac{\mu_0\omega_0^2\mu_{eg}}{2k_0}\sum_{\delta}\frac{N(\delta)}{V}\frac{i\mu_{eg}/2\hbar}{i(\omega-(\Delta+\delta))-\gamma}\right), \tag{F.26}$$

and $k_s = \frac{n\omega_s}{c}$. The imaginary part of $\chi(\omega)$ determines the loss. We can simplify the above expression by assuming $\Delta \gg \Gamma$, where $-\Gamma/2 < \delta < \Gamma/2$. In addition, the loss is expected to be uniform over the signal field spectrum when its bandwidth is smaller than the detuning ($\Delta > 1/\tau_s$). This results in a rather simple expression for the imaginary part of the response function. For $\Delta \gg \gamma$ this is given by

$$\text{Imag}(\chi(0)) = \frac{1}{k_s}\frac{1}{16\pi}\frac{N_g\lambda_0^2\gamma^2}{n^2V\Delta^2}. \tag{F.27}$$

Therefore, the intensity loss for the signal field can be derived from

$$|\mathcal{E}(L,\omega)|^2 = e^{-\zeta L}|\mathcal{E}(0,\omega)|^2, \tag{F.28}$$

where

$$\zeta L = \frac{1}{8\pi}\frac{N_g\lambda_0^2}{n^2A}\frac{\gamma^2}{\Delta^2}. \tag{F.29}$$

Requirements for single-photon sensitivity and low loss; multipass arrangement

Single photon sensitivity requires $\sqrt{\eta N_p}\phi > 1$, with ϕ given by Eq. (F.23) with an additional factor 1/2 assuming that the excited state population is transferred to another

ground state to minimize loss and noise. Here η is the retrieval efficiency of the AFC memory [30],

$$\eta = (1 - e^{-d/F})^2 e^{-\frac{\pi^2}{2\ln 2 F^2}}. \tag{F.30}$$

Assuming $N_p = N_g$ as discussed in section F.6, this puts a lower bound on the number of atoms in g,

$$N_g > \frac{1}{\eta\phi^2} = \frac{1}{\eta}\left(\frac{8\pi n^2 A\Delta}{\lambda_0^2\gamma}\right)^2, \tag{F.31}$$

and hence, using Eq. (F.29), a lower bound on the loss experienced by the signal:

$$\zeta L = \frac{N_g\lambda_0^2\gamma^2}{8\pi\eta n^2 A\Delta^2} > \frac{8\pi n^2 A}{\eta\lambda_0^2}. \tag{F.32}$$

Even for very small cross sections of order λ_0^2/n^2, this loss is $8\pi/\eta \gg 1$, which is too high for a nondestructive measurement.

This problem can be overcome by using a multipass arrangement, where m is the number of passes the signal makes through the medium. In this case the phase shift ϕ in Eq. (F.23) and the relation for the loss ζL in Eq. (F.29) are both multiplied by m. However, as a consequence of the former, the lower bound on N_g of Eq. (F.31) is multiplied by $\frac{1}{m^2}$, which finally leads to a modified bound on the total loss,

$$\zeta L > \frac{8\pi n^2 A}{m\eta\lambda_0^2}, \tag{F.33}$$

which can be much less than one for sufficiently many passes. Requiring small signal loss $m\zeta L \leq 0.1$, Eq. (F.33) gives a condition on m,

$$m > 80\pi/\eta, \tag{F.34}$$

where we have assumed a small waveguide, $A = \lambda_0^2/n^2$. Implementing $m \gg 1$ in practice requires low-loss switches. However, an analogous effect can also be achieved by using a cavity. The main difference is that a cavity enhances the signal field rather than the interaction time, which reduces the requirements on the storage time for the probe compared to a multi-pass scenario. Here we focus on the multi-pass case for simplicity.

Another condition on m follows from Eq. (F.31), which in the multi-pass case can be rewritten as

$$d > \frac{128\pi^2\Delta^2}{n_t\gamma^2 m^2\eta}, \tag{F.35}$$

where we have introduced the optical depth d, which for a small waveguide as above, and for an AFC where each tooth corresponds to one radiatively broadenend line, is related to the total number of atoms N as $N = n_t d$, where n_t is the number of teeth in the comb. In deriving Eq. (F.35) we have again assumed $N_g = N/2$. Eq. (F.35) yields a condition on the number of passes,

$$m > \frac{8\sqrt{2}\pi\Delta}{\sqrt{n_t\eta d}\gamma}. \tag{F.36}$$

We now rewrite the detuning $\Delta = f n_t F\gamma$, where $F = \Delta_m/\gamma$ is the finesse of the AFC and f is a factor greater than one that assures that the signal is sufficiently far detuned from the AFC (whose total width is $n_t F\gamma$). This yields

$$m > 8\sqrt{2}\pi f F\sqrt{\frac{n_t}{d\eta}}. \tag{F.37}$$

Eq. (F.36) also yields a condition on the number of passes as a function of the desired signal bandwidth B. For B expressed in Hz one has $B = \Delta/(2\pi f)$, where the factor f again ensures that the signal is off-resonant. This gives

$$m > \frac{16\sqrt{2}\pi^2 f B}{\sqrt{n_t\eta d}\gamma} \tag{F.38}$$

For our material system (Tm ions in Lithium Niobate, which have γ of order 9 kHz) all the above conditions are satisfied, for example, by setting $f = 3$, $d = 30$ as achieved in Ref. [31], $B = 500$ kHz, $F = 3.2$, $n_t = 110$ and $m = 930$. The latter is probably impossible for multiple passes using switches, but corresponds to only a moderate-finesse cavity [32]. For smaller bandwidth and higher optical depth smaller values of m are sufficient, but note that Eq. (F.34) implies $m > 80\pi$ under all circumstances. The bandwidth could also be increased by working with a system that has a larger γ, such as Ce ions in appropriate crystals [33] or color centers in diamond.

Bibliography

[1] Imoto, N., Haus, H. A., & Yamamoto, Y. Quantum nondemolition measurement of the photon number via the optical Kerr effect. *Physical Review A*, **32**, 2287 (1985).

[2] Matsuda, N., Shimizu, R., Mitsumori, Y., Kosaka, H., & Edamatsu, K. Observation of optical-fibre Kerr nonlinearity at the single-photon level. *Nature Photonics* **3**, 95 (2009).

[3] Bajcsy, M., Hofferberth, S., Balic, V., Peyronel, T., Hafezi, M., Zibrov, A. S., Vuletic, V., & Lukin, M. D. Efficient all-optical switching using slow light within a hollow fiber. *Physical review letters* **102**, 203902 (2009).

[4] Shiau, B. W., Wu, M. C., Lin, C. C., & Chen, Y. C. Low-light-level cross-phase modulation with double slow light pulses. *Physical review letters* **106**, 193006 (2011).

[5] Hosseini, M., Rebić, S., Sparkes, B. M., Twamley, J., Buchler, B. C., & Lam, P. K. Memory-enhanced noiseless cross-phase modulation. *Light: Science & Applications* **1**(12), e40 (2012).

[6] Reiserer, A., Ritter, S., & Rempe, G. Nondestructive detection of an optical photon. *Science*, **342**(6164), 1349 (2013).

[7] Venkataraman, V., Saha, K., & Gaeta, A. L. Phase modulation at the few-photon level for weak-nonlinearity-based quantum computing. *Nature Photonics*, **7**(2), 138 (2013).

[8] Kalb, N., Reiserer, A., Ritter, S., & Rempe, G. Heralded Storage of a Photonic Quantum Bit in a Single Atom. *Phys. Rev. Lett.* **114**, 220501 (2015).

[9] Feizpour, A., Hallaji, M., Dmochowski, G. & Steinberg, A. M. Observation of the nonlinear phase shift due to single post-selected photons. *Nature Physics* **advance online publication** (2015).

[10] Hickman, G. T., Pittman, T. B., & Franson, J. D. Low-Power Cross-Phase Modulation in a Metastable Xenon-Filled Cavity for Quantum Information Applications. arXiv preprint arXiv:1508.05993 (2015).

[11] Sangouard, N., Simon, C., De Riedmatten, H., & Gisin, N. Quantum repeaters based on atomic ensembles and linear optics. *Reviews of Modern Physics*, **83**, 33 (2011).

[12] Gisin, N., & Thew, R. Quantum communication. *Nature Photonics*, **1**(3), 165 (2007).

[13] Kimble, H. J. The quantum Internet. *Nature* **453**, 1023 (2008).

[14] Lvovsky, A. I., Sanders, B. C., & Tittel, W. Optical quantum memory. *Nature photonics*, **3**, 706 (2009).

[15] Bussières, F., Sangouard, N., Afzelius, M., de Riedmatten, H., Simon, C., & Tittel, W. Prospective applications of optical quantum memories. *Journal of Modern Optics*, **60**, 1519 (2013).

[16] Tittel, W., & Weihs, G. Photonic Entanglement for Fundamental Tests and Quantum Communication, *Quant. Inf. and Comp.* **1** (2), 03 (2001).

[17] Boone, K., Bourgoin, J. P., Meyer-Scott, E., Heshami, K., Jennewein, T., & Simon, C. Entanglement over global distances via quantum repeaters with satellite links. *Physical Review A*, **91**, 052325 (2015).

[18] Gündoğan, M., Ledingham, P. M., Kutluer, K., Mazzera, M., & de Riedmatten, H. A solid state spin-wave quantum memory for time-bin qubits. *Phys. Rev. Lett.* **114**, 230501 (2015).

[19] Hedges, M. P., Longdell, J. J., Li, Y., & Sellars, M. J. Efficient quantum memory for light. *Nature* **465**, 1052 (2010).

[20] Clausen, C., Usmani, I., Bussières, F., Sangouard, N., Afzelius, M., de Riedmatten, H., & Gisin, N. Quantum storage of photonic entanglement in a crystal. *Nature* **469**, 508 (2011).

[21] Saglamyurek, E., Sinclair, N., Jin, J., Slater, J. A., Oblak, D., Bussières, F., George, M., Ricken, R., Sohler, W., & Tittel, W. Broadband waveguide quantum memory for entangled photons. *Nature* **469**, 512 (2011).

[22] Sabooni, M., Li, Q., Kröll, S. & Rippe, L. Efficient Quantum Memory Using a Weakly Absorbing Sample. *Phys. Rev. Lett.* **110**, 133604 (2013).

[23] Sinclair, N., *et al.* Spectral multiplexing for scalable quantum photonics using an atomic frequency comb quantum memory and feed-forward control. *Physical review letters*, **113**, 053603 (2014).

[24] Saglamyurek, E., Sinclair, N., Slater, J. A., Heshami, K., Oblak, D., & Tittel, W. An integrated processor for photonic quantum states using a broadband light matter interface. *New Journal of Physics* **16**, 065019(2014).

[25] Afzelius, M., Simon, C., De Riedmatten, H., & Gisin, N. Multimode quantum memory based on atomic frequency combs. *Physical Review A* **79**, 052329 (2009).

[26] Bussières, F., Slater, J. A., Jin, J., Godbout, N., & Tittel, W. Testing nonlocality over 12.4 km of underground fiber with universal time-bin qubit analyzers, *Phys. Rev. A***81**, 052106 (2010).

[27] Sun, Y., Thiel, C. W., & Cone, R. L. Optical decoherence and energy level structure of 0.1% Tm^{3+}: $LiNbO_3$. *Physical Review B* **85**, 165106 (2012).

[28] Guha, S., Krovi, H., Fuchs, C. A., Dutton, Z., Slater, J. A., Simon, C., & W. Tittel. Rate-loss analysis of an efficient quantum repeater architecture. *Phys. Rev. A* **92**, 022357 (2015).

[29] Kolesov, R. *et al.*, Phys. Rev. Lett. **111**, 120502 (2013).

[30] M. Afzelius, C. Simon, H. de Riedmatten, and N. Gisin, Phys. Rev. A **79**, 052329 (2009).

[31] M.P. Hedges, J.J. Longdell, Y. Li, and M.J. Sellars, Nature **465**, 1052 (2010).

[32] T. Zhong, J.M. Kindem, E. Miyazono, and A. Faraon, Nature Communications **6**, 8206 (2015).

[33] R. Kolesov *et al.*, Phys. Rev. Lett. **111**, 120502 (2013).

Appendix G

Paper 7

to be submitted (2016)

A rare-earth-ion-doped waveguide based on a standard photonics technology for quantum signal processing

Neil Sinclair[1], Daniel Oblak[1], Charles W. Thiel[2], Rufus L. Cone[2], and Wolfgang Tittel[1]

[1]*Institute for Quantum Information Science, and Department of Physics and Astronomy, University of Calgary, 2500 University Drive NW, Calgary, Alberta T2N 1N4, Canada* [2]*Department of Physics, Montana State University, Bozeman, Montana 59717, USA*

Abstract

We measure properties of the 795 nm $^3H_6$ to $^3H_4$ transition of a rare-earth-ion-doped waveguide, Ti^{4+}:Tm^{3+}:$LiNbO_3$, at temperatures as low as 800 mK. Coherence and hyperfine population lifetimes up to 117 μs and 2.5 hours, respectively, are observed. They are at least one order of magnitude greater than those measured at 3 K, are the largest of any rare-earth-ion-doped solid-state waveguide yet studied, and match those observed in a bulk Tm^{3+}:$LiNbO_3$ crystal under similar conditions. Furthermore, taking advantage of these properties, we prepare a 0.5 GHz-bandwidth atomic frequency comb quantum memory of finesse >2 on a vanishing background. Finally, we measure high Rabi frequencies and calculate a transition dipole moment of $\sim 10^{-32}$ C·m, which is equivalent to that of Tm^{3+}:$LiNbO_3$. Our results show the suitability of rare-earth-doped waveguides created using industry-standard Ti-indiffusion in $LiNbO_3$ for on-chip quantum applications.

G.1 Introduction

Integrated optics offers the possibility of scalable manipulation of light due to small guiding volume and chip size, ever-improving fabrication methods, and low loss [1, 2]. These attractive features have also enabled advanced experiments and applications of quantum optics and quantum information processing, with many demonstrations using telecommunication-industry-standard Ti-indiffused $LiNbO_3$ waveguides, see e.g. [3, 4, 5, 9, 6, 7, 8] and references therein. Moreover, the ability to combine many components onto a single substrate is required for the implementation of an integrated quantum information processing node that performs local operations, interconnects, and measurements for quantum-secured computing and communications [10]. For example, a chip containing multiplexed sources of entangled photon pairs, Bell-state analyzers, photon number-resolving nondestructive photon detection, and feed-forward qubit-mode translation and selection, e.g. using frequency shifts or on-demand quantum memories, could pave the way to the development of a practical quantum repeater [11, 9, 12]. A promising avenue to this end, and to quantum information processing in general, is based on qubit interfaces using rare-earth-ion-doped (REI-doped) crystals at cryogenic temperatures [3, 15, 5, 12, 13, 14]. Thus, the development of rare-earth-ion-doped waveguide crystals constitutes an exciting and important path towards applications.

Many ground-breaking quantum optics experiments, in particular quantum memory for light [15, 13, 14], are based on cryogenically cooled REIs doped into a variety of bulk crystals. However, work employing REI-doped crystalline waveguides has, until only the past year, been restricted to $LiNbO_3$ – generally doped with thulium – into which waveguides were fabricated by means of Ti indiffusion [16, 3, 5, 9, 12]. A likely explanation for the lack of investigations using other REIs in Ti^{4+}:$LiNbO_3$ is that the first low-temperature characterization of Ti^{4+}:Tm^{3+}:$LiNbO_3$, which was performed at 3

K, revealed non-ideal properties for quantum signal processing [17]. Specifically, optical coherence and hyperfine-level lifetimes were shown to be significantly reduced compared to those of a bulk Tm^{3+}:$LiNbO_3$ crystal at the same temperature [18], possibly due to perturbations stemming from the introduction of Ti. As alternatives, several groups have recently explored the use of Y_2SiO_5 crystals together with evanescent wave-mediated planar waveguides [19], ion beam-milled photonic crystals [20], or waveguides created via femtosecond laser writing [21] – all of which guide light in unperturbed regions of the REI-doped crystal. While the results are promising, it is generally still unclear how a waveguide fabrication process affects all relevant REI properties for quantum applications and, being the topic of our study, if good properties can be retained using industry-standard Ti-indiffusion in $LiNbO_3$.

To investigate this question, we measure optical properties of the $^3H_6$ to $^3H_4$ transition of Ti^{4+}:Tm^{3+}:$LiNbO_3$ using photon echoes and spectral hole burning [22] at temperatures as low as 800 mK and with applied magnetic fields up to 600 Gauss. Remarkably, we find at least one order of magnitude improvement of critical properties (optical coherence and hyperfine population lifetimes) compared to those measured previously at 3 K [17]. Moreover, the measured properties match those observed using Tm^{3+}:$LiNbO_3$ bulk crystals under similar conditions [23], and improve upon those observed with other REI-doped waveguides [19, 20, 21]. This could mean that low temperatures reduce the impact of defects introduced into the host matrix by Ti-indiffusion, the 0.7% Tm-doping concentration, or other fabrication-induced $LiNbO_3$ matrix changes [18, 17]. Moreover, our measurements establish a ratio of coherence lifetime to ($^3H_4$) excited-state population lifetime that is greater than one [17, 24], which benefits applications in the field of cavity quantum electrodynamics [25] or employing cross-phase modulation [12]. To show key requirements for efficient quantum information processing, we burn persistent holes to transparency, and tailor a 0.5 GHz-bandwidth atomic frequency comb (AFC)

[13, 14] with a finesse of three on a vanishing absorption background. This is the first demonstration of tailored persistent spectral features on no background using a REI-doped waveguide. Finally, we measure Rabi frequencies that allow the calculation of a bulk-equivalent [18] transition dipole moment of $\sim 10^{-32}$ C·m. This establishes that waveguide fabrication does not reduce the dipole moment – an important finding in view of achieving large light-matter coupling. We note that our experiments – the first using a solid-state crystal waveguide at temperatures below 1 K – are performed at temperatures needed for other components used in advanced quantum information processing, including WSi superconducting nanowires (for high-efficiency photon counting) [26] and superconducting quantum electronic circuits that encode qubits (for further information processing) [27].

G.2 Experimental Methods

Measurements are carried out using a 15.7 mm-long Ti^{4+}:Tm^{3+}:$LiNbO_3$ waveguide. It is created by increasing the index of refraction of a ~ 4 μm-wide strip through indiffusion of Ti into the surface of a 0.9 mm-thick, 0.7% Tm-doped lithium niobate wafer [17]. The wafer is mounted inside a pulse tube cryocooler on a Cu stage attached to a GGG salt pellet that generates temperatures as low as 800 mK (measured near the crystal) via adiabatic demagnetization. Light is directed into, and out of, the waveguide using single-mode fiber butt-coupling. Transmission through the entire cryogenic setup is 10-20%, mainly limited by imperfect overlap between fiber and waveguide modes as well as reflections from the uncoated surfaces. Magnetic fields of up to 2 T are applied parallel to the crystal's c-axis using a superconducting solenoid coil. We employ an external-cavity diode laser, producing polarized light set normal to the crystal's c-axis [17, 18]. Its wavelength is tuned between 795.5 and 799.0 nm (vac.) using a diffraction grating. A 400

MHz acousto-optic modulator is employed to produce pulses as short as 50 ns for photon echo measurements, or as long as several ms for hole burning and spectral tailoring. Spectral features are probed by ramping the laser frequency using a $LiNbO_3$ waveguide phase modulator driven with a sawtooth-modulated voltage [5, 9]. Optical transmission is detected using a 1 GHz (2 MHz) AC (DC)-coupled amplified diode, digitized by an oscilloscope. Efforts are made to minimize errors due to laser power fluctuations, jitter, and noise by averaging over many experiments. Furthermore, undesired persistent spectral hole burning is mitigated by slowly sweeping the laser frequency.

G.3 Results

Long optical coherence lifetimes are a key reason why rare-earth-ion-doped crystals are employed for quantum applications [15, 13, 14]. Using a two-pulse photon echo decay, we measure the coherence lifetime T_2 of the transition at 795.6 nm under a 300 G magnetic field, at a temperature of 810 mK, and with a laser peak power inside the waveguide of $\sim$0.4 mW (set to prevent excitation-induced decoherence (EID) [28] while simultaneously ensuring the echo intensity is above the noise level). The decay, as shown in Fig. G.1, is fitted using

$$I(t_{12}) = I_0 e^{-2(\frac{2t_{12}}{T_2})^x}, \tag{G.1}$$

where t_{12} is the delay between the two excitation pulses, I_0 is the echo intensity at $t_{12} = 0$, and x describes the decay shape [29]. We find a coherence lifetime of 117 μs; the longest yet observed in any solid-state waveguide, 70 times greater than what we measured in Ti^{4+}:Tm^{3+}:$LiNbO_3$ at 3.5 K [17], and larger than the 86 μs we observed using a Tm^{3+}:$LiNbO_3$ bulk crystal at 790 mK temperature, 794.25 nm wavelength, and $\sim$150 Gauss magnetic field [23]. Temperature-dependent measurements of T_2 [24] indicate a factor of three larger direct phonon-coupling rate in the waveguide as compared to that

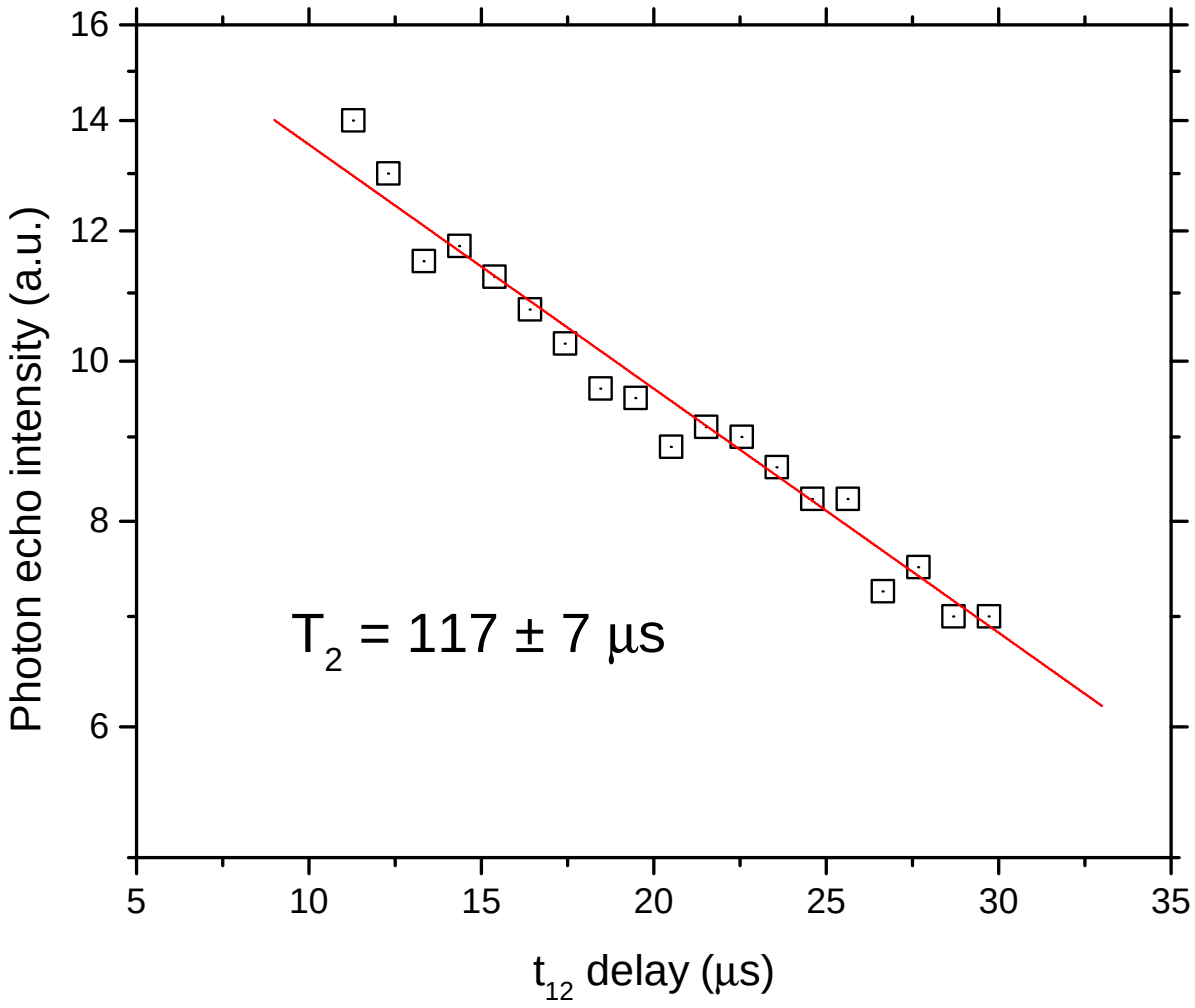

Figure G.1: Two pulse photon echo decay. Measurements at a wavelength of 795.6 nm, using 300 G magnetic field, and at a temperature of 810 mK yield a coherence lifetime of 117 μs. The decay is exponential and does not exhibit any time-dependent increase of decoherence i.e. $x = 1$ in Eq. G.1.

measured in the bulk, supporting our observed increase of coherence lifetime with lowered temperature. We expect that T_2 can be increased further by probing ions that absorb at wavelengths towards the center of the inhomogeneous line, as these ions are more characteristic of typical crystal environments than the ions currently probed. We note that the larger T_2 of the waveguide in comparison to that measured in the corresponding bulk crystal under similar conditions was not expected. This difference may be due to EID during the bulk crystal T_2 measurement, however more experiments are needed to support this claim.

In conjunction with a sufficiently-long T_2, quantum applications require the ability to spectrally tailor the absorption profile of a rare-earth-ion transition. This requires long-lived sub-levels to optically pump ions, e.g. to create transparency or efficient memories. Therefore, we measure the dynamics of the Tm hyperfine sub-levels under 600 G field, at a temperature of 850 mK, and at a wavelength of 795.5 nm using time-resolved persistent spectral hole burning. Under application of an external magnetic field, sub-levels arise due to an enhanced effective nuclear Zeeman effect from the hyperfine coupling of the ^{169}Tm spin-1/2 nucleus to the electronic states [22]. This splits both the excited and ground states into pairs ($m_s = \pm 1/2$) with a difference in energy splitting of $|\Delta_e - \Delta_g| \sim$1.4 GHz/T [18, 24], allowing optical pumping of the nuclear spin populations between hyperfine states. The resultant spectral hole in the optical absorption decays as the nuclear spin population returns to thermal equilibrium as is shown in Fig. G.2, with a simplified sub-level structure depicted in the inset. We fit the decay using a double exponential,

$$\Delta\alpha(t_d) = \Delta\alpha_a e^{-t_d/\tau_a} + \Delta\alpha_b e^{-t_d/\tau_b}, \tag{G.2}$$

where t_d is the time delay between hole burning and probing, τ_a and τ_b are two different hole lifetimes, and $\Delta\alpha_a$ and $\Delta\alpha_b$ are the relative amplitudes of the two population components present in the hole decay. We find two exponentials, similar to what we

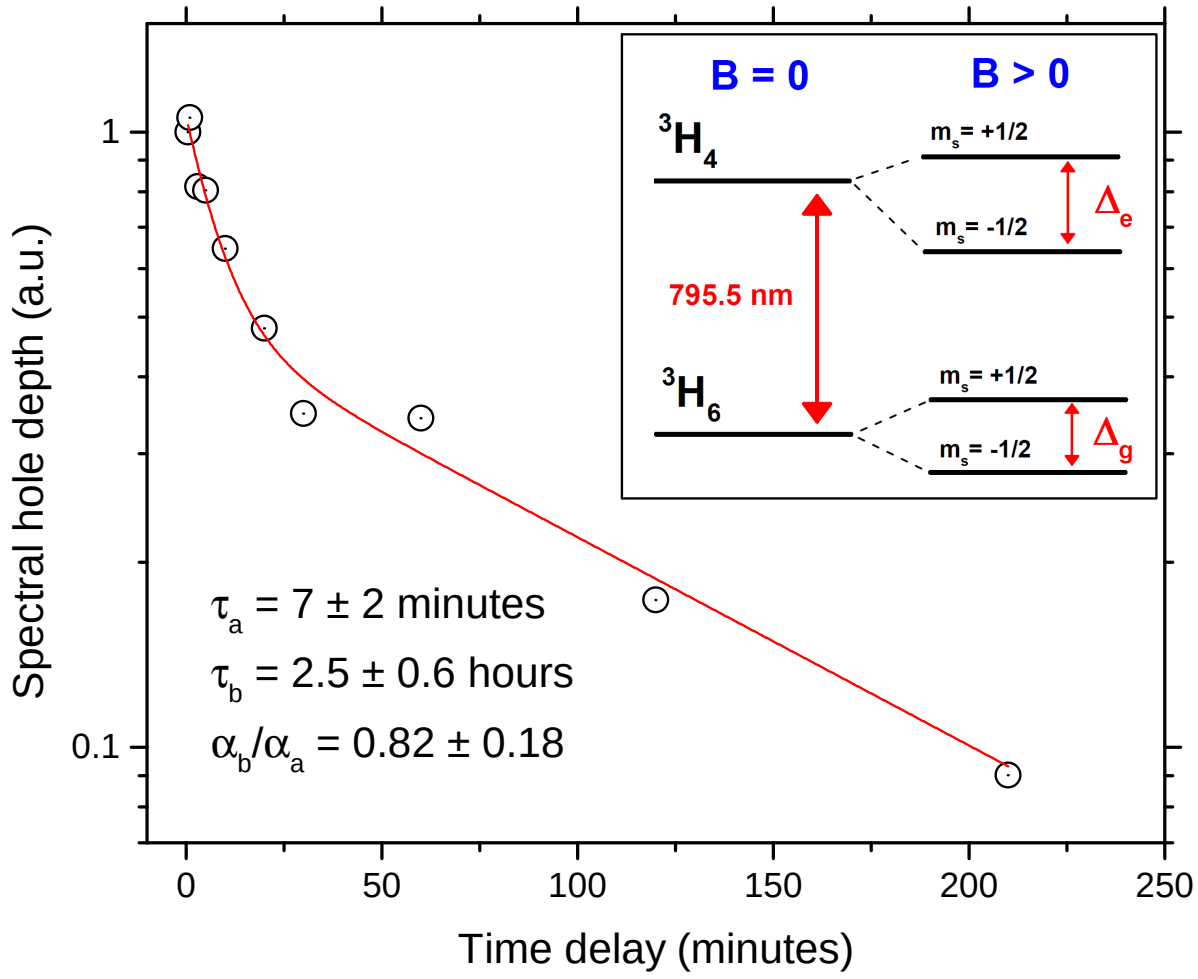

Figure G.2: Persistent spectral hole burning decay. Measurements at a wavelength of 795.5 nm, under a magnetic field of 600 G, and at a temperature of 850 mK yield a population decay that follows a double exponential. Inset: Simplified energy level diagram (not to scale) showing optically excited levels and hyperfine levels split by the applied magnetic field.

measured in this material at 3.5 K [17], except now with lifetimes of 7 minutes, and 2.5 hours. These lifetimes are two orders of magnitude increased from those measured at 3.5 K [17], and agree well with those measured using a Tm^{3+}:$LiNbO_3$ bulk crystal under similar conditions [23]. Indeed, reduction in phonon scattering due to lower temperatures predicts an increase in population lifetimes of hyperfine levels. Although we have not yet investigated the origin of the double decay, we conjecture that the 2.5-hour decay is due to ions that have a magnetic dipole oriented parallel with the applied magnetic field [18], while the 7-minute decay originates from an average of all other dipoles which are randomly oriented due to magnetic perturbations. We also believe the double decay to be independent of waveguide fabrication since a similar decay is also observed in the corresponding bulk crystal [23].

In the following we demonstrate that our Tm-doped waveguide may be used for efficient quantum applications. Going beyond what has been shown with our waveguide at 3 K and with other rare-earth-ion-doped waveguides, we take advantage of the hyperfine sub-level properties to generate a persistent spectral hole on a vanishing absorption background as shown in Fig. G.3. Specifically, at a temperature of 800 mK, wavelength of 795.5 nm, and using a 500 G magnetic field, we burn a spectral hole during several ms, wait for 100 ms, and then, with reduced laser power, sweep the laser frequency over the hole to measure its absorption profile. The laser sweep is repeated several times and then the laser frequency is tuned off-resonance to 799 nm to determine transparency. Our result is shown by the dashed curve in Fig. G.3. The width of the spectral hole is attributed to power broadening, laser jitter, and the resolution of the laser sweep (each of these contributions is verified by independent measurements). We expect that time-dependent spectral diffusion plays a minimal role here as initial measurements have shown little linewidth broadening over timescales up to $\sim$1 ms using a 300 G magnetic field and at a temperature of 800 mK, equivalent to that measured using a Tm^{3+}:$LiNbO_3$

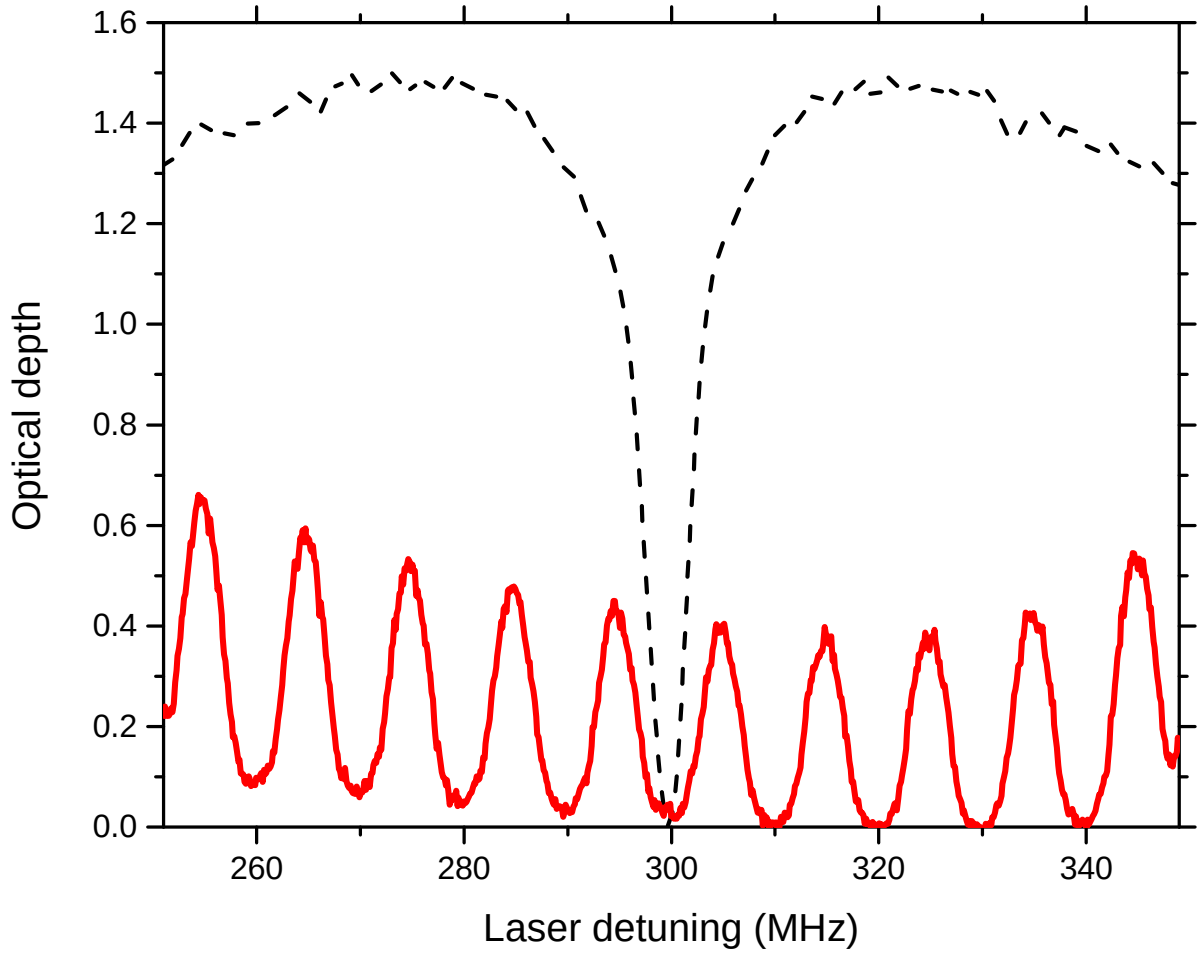

Figure G.3: A spectral hole (dashed curve) and AFC (solid curve) created under 500 G and 2 kG magnetic fields, respectively, at a temperature of 800 mK and a wavelength of 795.5 nm.

bulk crystal [23, 24]. The variance in optical depth detuned from the hole is due to laser intensity modulation from optical cavities formed by waveguide and fiber endfaces. Next we increase the magnetic field to 2 kG and then perform the aforementioned hole burning sequence at different detunings to create multiple spectral holes, each separated by 10 MHz from their neighbor. The result is a 100 MHz-bandwidth AFC programmed with a 100 ns storage time and finesse F, defined by the product of storage time and the linewidth of each tooth comprising the comb, of approximately two. Our AFC is shown by the solid curve in Fig. G.3. Note that the 100 ms wait time is >30 times greater than what we used for storage of non-classical light [3], and chosen to demonstrate AFC persistence. The small optical depth of the comb is due to both the aforementioned laser-induced broadening and excitation during the read sequence. The residual background at the AFC edges is due to anti-holes, with some asymmetry induced by the aforementioned cavity effects. The antihole inhomogeneous broadening of ∼0.5 GHz/T at this wavelength [24] is consistent with that expected in a Tm^{3+}:$LiNbO_3$ bulk crystal due to multiple Tm sites [18]. We expect the antiholes to narrow significantly at wavelengths closer to 794.3 nm [18].

To show our waveguide is suitable for high-rate applications employing AFCs beyond $F = 2$, we increase the field to 2 T, and repeat the experiment, except now preparing a 0.5 GHz-bandwidth AFC programmed with 100 ns storage time and $F = 3$. The result is shown in Fig. G.4. The short storage time, small optical depth, and small residual background is due to the same effects impacting the AFC shown in Fig. G.3, except here we intentionally choose the AFC bandwidth to be much smaller than the anti-hole splitting to have a vanishing absorption background at the AFC edges. Note that we have prepared and observed AFCs featuring a 2 GHz bandwidth and $F \leq 10$ (going beyond our previous observation of $F = 6$ [9]), however with very low optical depth (due to laser-induced broadening), and an antihole-induced background at the AFC edges.

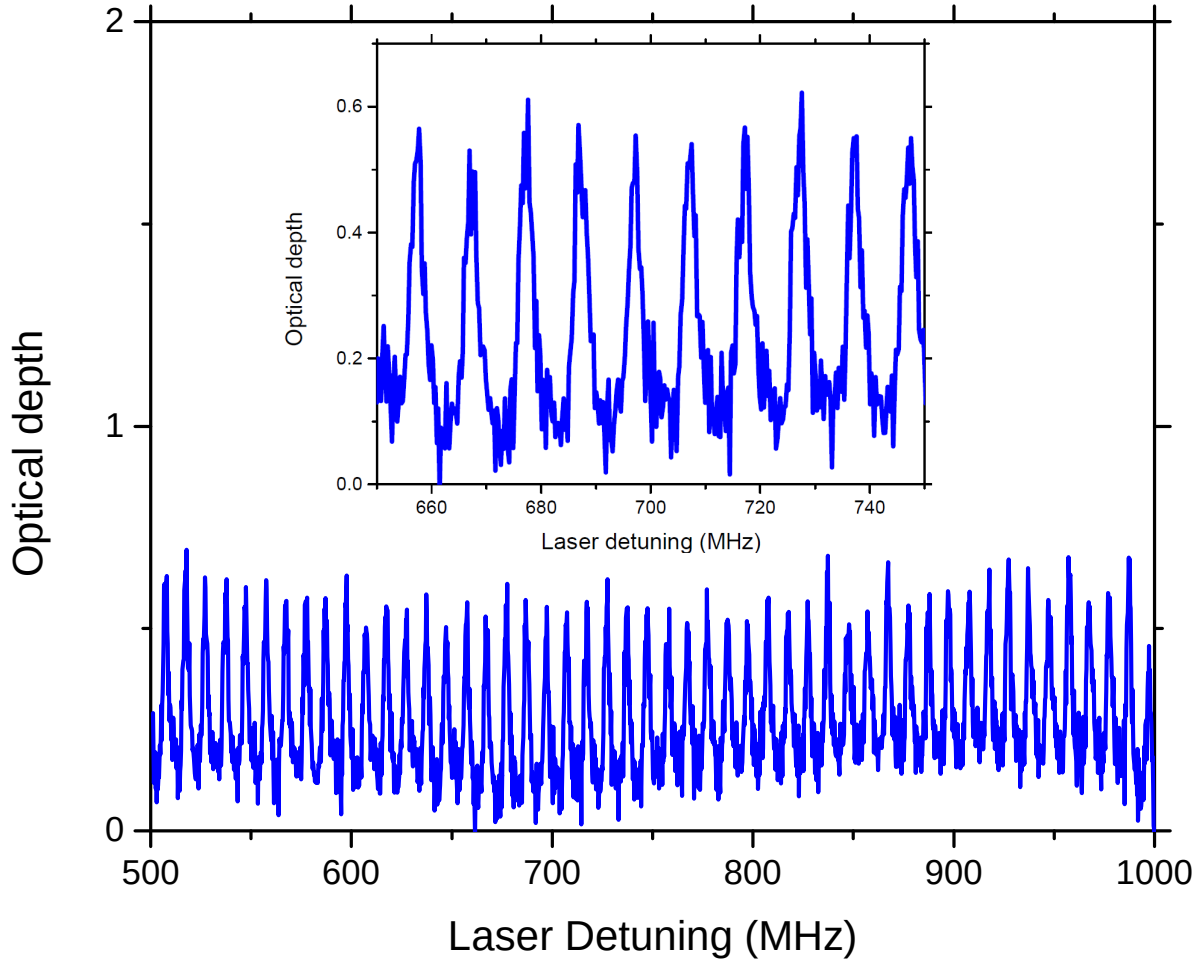

Figure G.4: A 0.5 GHz AFC prepared on a near-zero background. Inset: A 100 MHz-bandwidth section of the AFC shown in the main figure.

We expect that excitation at wavelengths closer to the center of the inhomogneous line will allow AFC bandwidths of several GHz with vanishing absorption background using fields of a few Tesla.

Due to confinement of light, a waveguide light-matter interface generally allows for higher-frequency Rabi oscillations per photon than using a bulk optics setup. Thus, waveguides are desirable for both on- and off-resonant interaction, e.g. spectral tailoring, Raman interaction, or cross-phase modulation. To these ends, we quantify the magnitude of the $^3H_6$ to $^3H_4$ transition dipole moment μ of our waveguide at a tempearture of 800 mK under zero magnetic field using both optical nutation (at a wavelength of 795.3 nm) and two-pulse photon echo excitation (at a wavelength of 795.6 nm). The strength of the light-matter coupling is scaled by a ratio of μ^2/A per photon, where A is the mode cross-sectional area. We note that the magnitude of μ must be preserved after waveguide fabrication to maintain the advantage due to smaller A. We direct a pulse into the waveguide and, after interaction, detect a coherent modulation of the pulse intensity (i.e. nutation) – see Fig. G.5a.

We observe a time-dependent decay of the nutation indicating a distribution of Rabi frequencies due to transverse (Gaussian intensity distribution) and longitudinal (coupling and propagation loss) variation in the laser intensity as well as overlap of different atomic transitions (inhomogneous broadening). The modulation is related to the effective Rabi frequency Ω. We calculate an average Ω using (i) the relative time between the beginning of the pulse and each discernible population inversion maxima and minima, and (ii) a scaling factor that depends on when the extrema occur [30]. By varying the input pulse power, we observe a linear Ω^2-dependence. We plot our results in Fig. G.5b and fit using,

$$\Omega^2 = \kappa \frac{\mu^2}{A} P, \tag{G.3}$$

where P is the estimated power in the waveguide, $\kappa = 2(n^2+2)^2/(9nc\epsilon_0\hbar^2)$ is a material

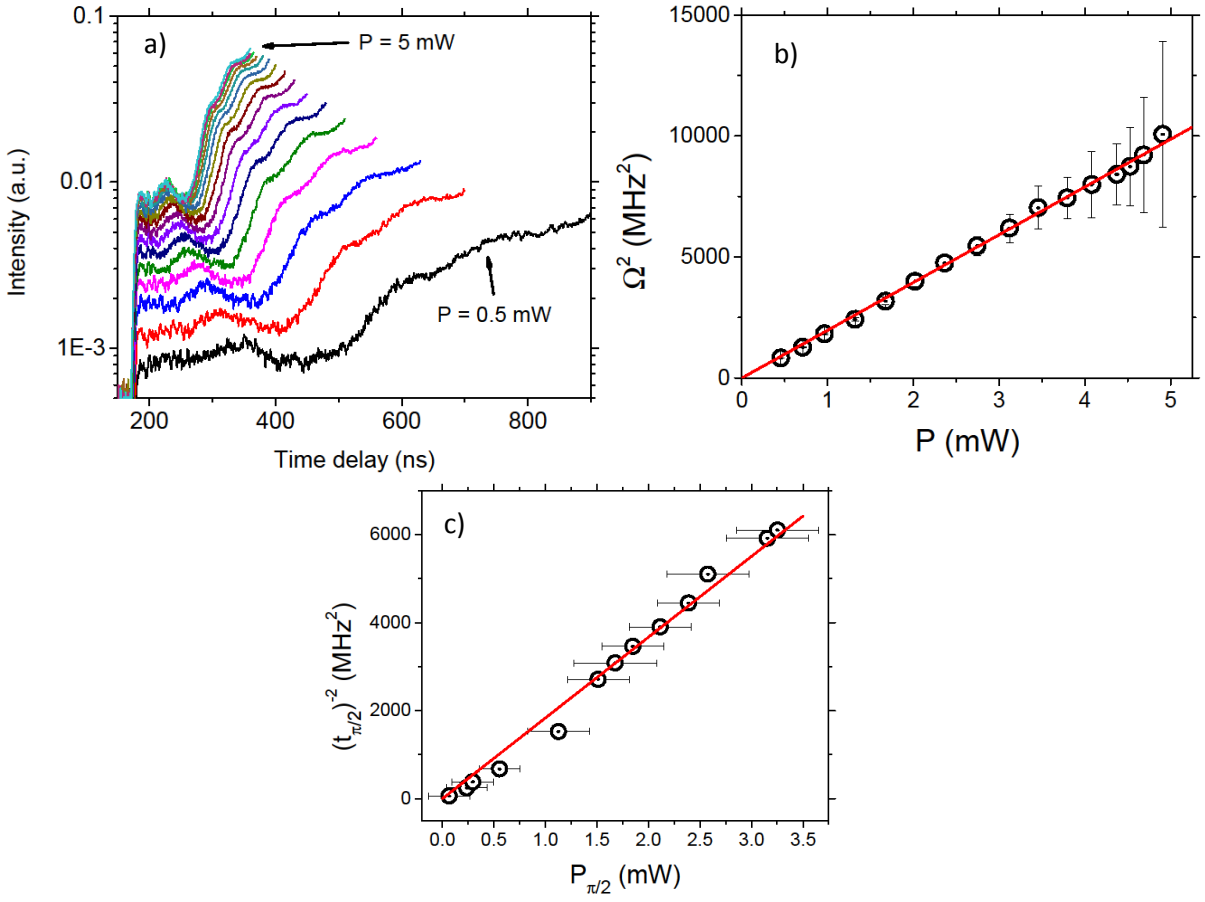

Figure G.5: Measurements of the transition dipole moment. (a) Observed optical nutation (log scale) using pulses of power P varied between 0.5 and 5 mW (shown with different colors). Curves are truncated to timescales where nutation is most visible. (b) Power dependence of Ω^2. We calculate an average Ω from each nutation using the first inversion maximum and minimum, and the second and third inversion maxima. (c) Pulse duration and power dependence from two-pulse photon echo experiments.

constant [28], n is the index of refraction, and $A \approx \pi\ (6.25\ \mu\text{m})^2$ is estimated from independent beam-waist measurements. A fit of the curve reveals an average $\bar{\mu} = (3.7 \pm 0.4) \times 10^{-32}$ C·m, agreeing well with the 4×10^{-32} C·m observed using a Tm^{3+}:$LiNbO_3$ bulk crystal [18]. This dipole moment is one of the largest of all rare-earth-ion optical transitions that have been studied [22, 25].

To confirm our result, we perform a series of two-pulse echo excitation measurements where we restrict the second excitation pulse to have identical peak power $P_{\pi/2}$ and twice the duration $t_{\pi/2}$ of the first pulse. By increasing $P_{\pi/2}$, the condition of excitation using $\pi/2$- and π-pulses is found by observing a maximal echo intensity, and is repeated for varying $P_{\pi/2}$ and $t_{\pi/2}$. Using the area theorem $\pi/2 = \Omega t_{\pi/2}$ [28] and $P \equiv P_e$, we plot and fit our data to Eq. G.3 (see Fig. G.5c) giving $\bar{\mu} = (7.3 \pm 0.1) \times 10^{-32}$ C·m, which is comparable with our nutation measurements.

G.4 Conclusion

Using temperatures only a few Kelvin less than those typically employed for optical quantum processing using rare-earth-ion-doped crystals [13, 14], we measure dramatically improved spectroscopic properties of Ti^{4+}:Tm^{3+}:$LiNbO_3$ compared to previous work at 3 K [17], with performance surpassing other rare-earth-ion-doped waveguides [19, 20, 21], and properties matching that of a corresponding bulk Tm^{3+}:$LiNbO_3$ bulk crystal [18, 23] despite the potential of light interacting with ions that reside within a Ti-modified host matrix. Our results advance the development of low-loss quantum light-matter integrated circuits using industry-standard materials and shed light on the relationship between rare-earth-ion properties and crystal modification. However, more detailed investigation of other important properties of our waveguide, such as field-dependent spectral diffusion beyond 1 ms time delays and wavelength-dependent characteristics, are needed for

optimal implementations and further understanding of any potential fabrication-induced modification of spectral properties due to either Ti-indiffusion or rare-earth doping.

Acknowledgment

We thank E. Saglamyurek and C. Deshmukh for discussions and help with early investigations, and M. George, R. Ricken, and W. Sohler for the waveguide fabrication. We acknowledge funding through Alberta Innovates Technology Futures (AITF), the Natural Sciences and Engineering Research Council of Canada (NSERC), the US National Science Foundation (NSF) under award nos. PHY-1415628 and CHE-1416454, and the Montana Research and Economic Development Initiative. Furthermore, W.T. acknowledges support as a Senior Fellow of the Canadian Institute for Advanced Research (CIFAR).

Bibliography

[1] W. Sohler, H. Hu, R. Ricken, V. Quiring, C. Vannahme, H. Herrmann, D. Büchter, S. Reza, W. Grundkötter, S. Orlov, H. Suche, R. Nouroozi, and Y. Min, Opt. Photon. News **19**, 24-31 (2008).

[2] M. Bazzan and C. Sada, Appl. Phys. Rev. **2**, 040603 (2015).

[3] E. Saglamyurek, N. Sinclair, J. Jin, J. A. Slater, D. Oblak, F. Bussières, M. George, R. Ricken, W. Sohler and W. Tittel, Nature **469**, 512-515 (2011).

[4] S. Tanzilli, A. Martin, F. Kaiser, M.P. De Micheli, O. Alibart, and D.B. Ostrowsky, Laser & Photonics Rev. **6**, 115143, (2012).

[5] E. Saglamyurek, N. Sinclair, J. A. Slater, K. Heshami, D. Oblak, and W. Tittel, New J. of Physics **16**, 065019 (2014).

[6] D. Bonneau, et al., Phys. Rev. Lett. 108, 053601 (2012).

[7] J. Carolan, C. Harrold, C. Sparrow, E. Martín-López, N. J. Russell, J. W. Silverstone, P. J. Shadbolt, N. Matsuda, M. Oguma, M. Itoh, G. D. Marshall, M. G. Thompson, J. C. F. Matthews, T. Hashimoto, J. L. OBrien, and A. Laing, Science **349**, 711-716 (2015).

[8] T. Meany, M. Gräfe, René Heilmann, A. Perez-Leija, S. Gross, M.l J. Steel, M. J. Withford, and A. Szameit Laser & Photonics Rev. **9**, 363384, (2015).

[9] N. Sinclair, E. Saglamyurek, H. Mallahzadeh, J. A. Slater, M. George, R. Ricken, M. P. Hedges, D. Oblak, C. Simon, W. Sohler, and W. Tittel, Phys. Rev. Lett. **113**, 053603 (2014).

[10] H. J. Kimble, Nature **453**, 1023-1030 (2008)

[11] N. Sangouard, C. Simon, H. de Riedmatten, and N. Gisin, Rev. Mod. Phys. **83**, 33 (2011).

[12] N. Sinclair, K. Heshami, C. Deshmukh, D. Oblak, C. Simon, and W. Tittel, arXiv:1510.01164 (2015).

[13] F. Bussières, N. Sangouard, M. Afzelius, H. de Riedmatten, C. Simon & W. Tittel, J. Mod. Opt. **60**, 18 (2013).

[14] H. de Riedmatten and M. Afzelius, in *Engineering the Atom-Photon Interaction Springer*, edited by Ana Predojević and Morgan Mitchell (Springer, 2015), Chap. 9.

[15] W. Tittel, M. Afzelius, T. Chanelière, R. L. Cone, S. Kröll, S. A. Moiseev and M. Sellars, Laser & Photonics Reviews **4**, 244 - 267 (2010).

[16] M. U. Staudt, S. R. Hastings-Simon, M. Nilsson, M. Afzelius, V. Scarani, R. Ricken, H. Suche, W. Sohler, W. Tittel, and N. Gisin, Phys. Rev. Lett. **98**, 113601 (2007). M. U. Staudt, M. Afzelius, H. de Riedmatten, S. R. Hastings-Simon, C. Simon, R. Ricken, H. Suche, W. Sohler, and N. Gisin, Phys. Rev. Lett. **99**, 173602 (2007).

[17] N. Sinclair, E. Saglamyurek, M. George, R. Ricken, C. La Mela, W. Sohler, and W. Tittel, J. Lumin. **130**, 1586-1593 (2010).

[18] Y. Sun, C. W. Thiel, and R.L. Cone, Phys. Rev. B **85**, 165106 (2012). C.W. Thiel, Y. Sun, T. Böttger, W.R. Babbitt, and R.L. Cone, J. Lumin **130**, 1598 (2010). C. W. Thiel, Y. Sun, R. M. Macfarlane, T. Böttger, and R. L. Cone, Journal of Physics B: Atomic, Molecular and Optical Physics **45**, 12 (2012).

[19] S. Marzban, J. G. Bartholomew, S. Madden, K. Vu, and M. J. Sellars, Phys. Rev. Lett. **115**, 013601 (2015).

[20] T. Zhong, J. M. Kindem, E. Miyazono, and A. Faraon, Nature Communications **6**, 8206 (2015).

[21] G. Corrielli, A. Seri, M. Mazzera, R. Osellame, and H. de Riedmatten, arXiv:1512.09288 (2015).

[22] R. M. Macfarlane and R. M. Shelby, in *Spectroscopy of Solids Containing Rare Earth Ions*, edited by A. A. Kaplianskii and R. M. Macfarlane (North Holland, Amsterdam, 1987), Chap. 3.

[23] C. W. Thiel et al., in preparation.

[24] N. Sinclair et al., in preparation.

[25] D. L. McAuslan, J. J. Longdell, and M. J. Sellars, Phys. Rev. A **80**, 062307 (2009).

[26] F. Marsili, V. B. Verma, J. A. Stern, S. Harrington, A. E. Lita, T. Gerrits, I. Vayshenker, B. Baek, M. D. Shaw, R. P. Mirin, and S. W. Nam. Nature Photon. **7**, 210214 (2013).

[27] Z.-L. Xiang, S. Ashhab, J. Q. You, and F. Nori, Rev. Mod. Phys. **85**, 623 (2013). C. O'Brien, N. Lauk, S. Blum, G. Morigi, M. Fleischhauer, Physical review letters **113**, 063603 (2014), Y.-H. Chen, X. Fernandez-Gonzalvo, J. J. Longdell, arXiv:1512.03606 (2015).

[28] C. W. Thiel, R. M. Macfarlane, Y. Sun, T. Böttger, N. Sinclair, W. Tittel and R. L. Cone, Laser Physics **24**, 106002 (2014).

[29] W. B. Mims, Phys. Rev. **168**, 370 (1968).

[30] Y. Sun, G. M. Wang, R. L. Cone, R. W. Equall, and M. J. M. Leask, Phys. Rev. B **62**, 15443 (2000). A. Louchet, J. S. Habib, V. Crozatier, I. Lorgeré, F. Goldfarb,

F. Bretenaker, J.-L. Le Gouët, O. Guillot-Noël, and P. Goldner, Phys. Rev. B **75**, 035131 (2007).

Appendix H

Copyright permissions

This appendix states the copyright permissions required to include Papers 1-7 in this thesis.

Papers 1-5 are published in journals that grant me permission to use these papers in my thesis. Proof of this permission is shown via screen-shots from the appropriate websites. Paper 6 is uploaded to a pre-print server where only a 'right to distribute' is granted and not a copyright as is the case with journals; a screen-shot is included that describes this. Consequently, I can distribute Paper 6 without requiring permission. Paper 7 is unpublished. All website addresses are shown in the corresponding screen-shots. Permission from all co-authors has been granted via e-mail communication. Copies of these emails are shown.

H.1 Permissions from journals and the arXiv pre-print server

Papers 1 and 2

Proof of copyright is shown in Fig. H.1. Note that the required copyright credit lines are indicated at the start of Papers 1 and 2. A credit line is written as follows: Reprinted (abstract/excerpt/figure) with permission from [FULL REFERENCE CITATION]. Copyright (YEAR) by the American Physical Society.

Papers 3 and 4

Proof of copyright is shown in Fig. H.2.

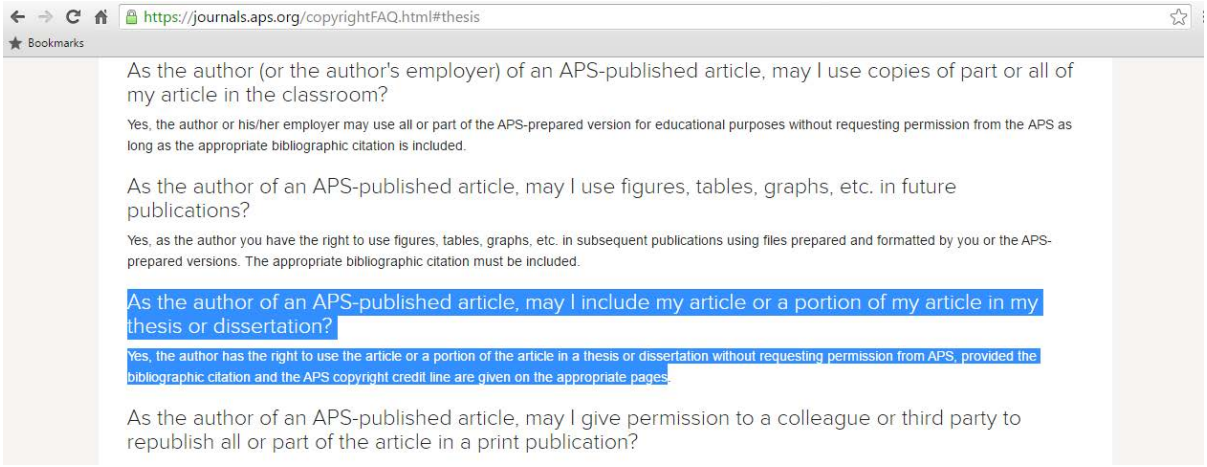

Figure H.1: Proof of copyright for Papers 1 and 2. They are published in Physical Review Letters, a journal of the American Physical Society (APS).

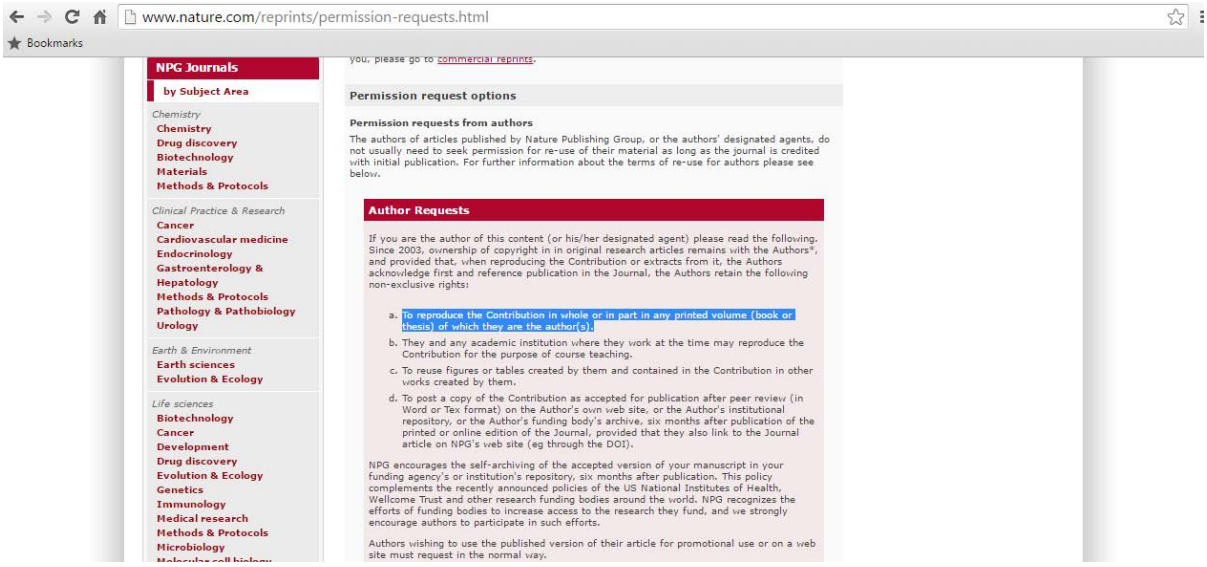

Figure H.2: Proof of copyright for Papers 3 and 4. Paper 3 is published in Nature, Paper 4 in Nature Communications. Both papers have the same copyright permissions because they are both part of the Nature Publishing group.

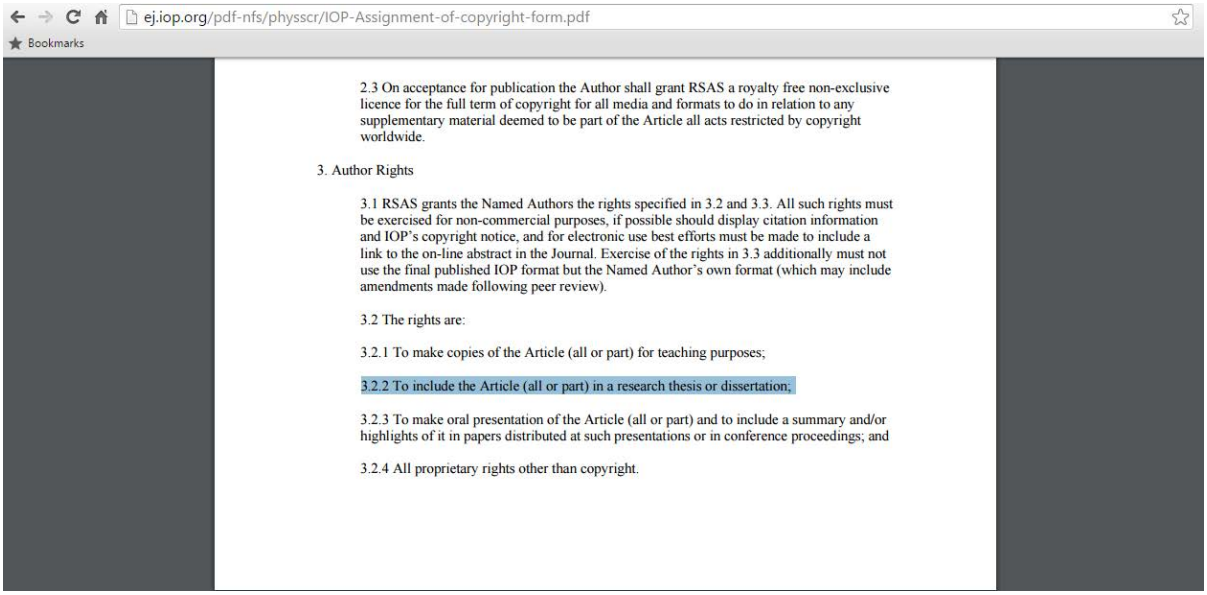

Figure H.3: Proof of copyright for Paper 5. This paper is published in the New Journal of Physics, a journal of the Institute of Physics (IOP).

Paper 5

Proof of copyright is shown in Fig. H.3. IOP's copyright notice is described below in italic font.

References to IOP mean the Institute and/or IOP Publishing as appropriate. References to this website are to the specific IOP website from which the user is linking to this Copyright statement. Please read the following Copyright statement carefully as your access to and use of this website will be deemed as acceptance of its terms. This Copyright statement was last updated on 18 April 2012. The material featured on this website is subject to IOP copyright protection unless otherwise indicated. Subject to subscriber status, reasonable amounts of IOP copyright-protected material (other than logos) may be reproduced, distributed or communicated to others free of charge in any format or media for the purposes of research for a non commercial purpose or for private study or for internal circulation within an organization. This is subject to the material being reproduced accurately and not used in a misleading context. Where any IOP

Paper 6

The arXiv's proof of 'right to distribute' is shown in Fig. H.4. Note that Paper 6 is not published but only uploaded to the arXiv pre-print server. The arXiv does not acquire copyrights as a journal does.

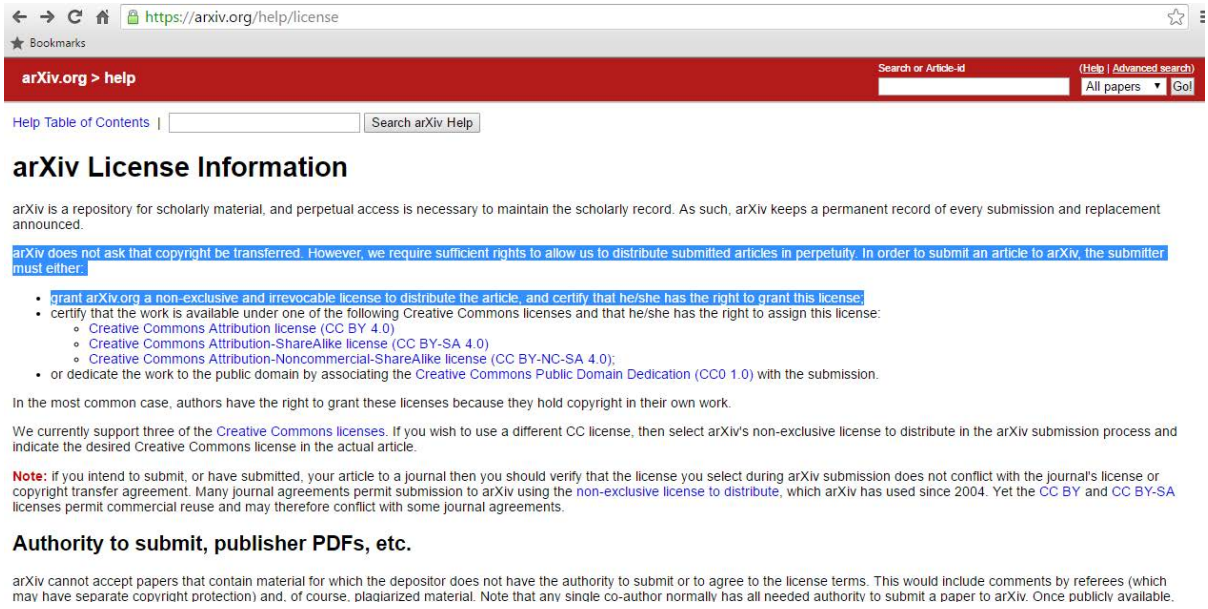

https://arxiv.org/help/license

Bookmarks

arXiv.org > help

Search or Article-id (Help | Advanced search) All papers Go!

Help Table of Contents | Search arXiv Help

arXiv License Information

arXiv is a repository for scholarly material, and perpetual access is necessary to maintain the scholarly record. As such, arXiv keeps a permanent record of every submission and replacement announced.

arXiv does not ask that copyright be transferred. However, we require sufficient rights to allow us to distribute submitted articles in perpetuity. In order to submit an article to arXiv, the submitter must either:

- grant arXiv.org a non-exclusive and irrevocable license to distribute the article, and certify that he/she has the right to grant this license;
- certify that the work is available under one of the following Creative Commons licenses and that he/she has the right to assign this license:
  - Creative Commons Attribution license (CC BY 4.0)
  - Creative Commons Attribution-ShareAlike license (CC BY-SA 4.0)
  - Creative Commons Attribution-Noncommercial-ShareAlike license (CC BY-NC-SA 4.0);
- or dedicate the work to the public domain by associating the Creative Commons Public Domain Dedication (CC0 1.0) with the submission.

In the most common case, authors have the right to grant these licenses because they hold copyright in their own work.

We currently support three of the Creative Commons licenses. If you wish to use a different CC license, then select arXiv's non-exclusive license to distribute in the arXiv submission process and indicate the desired Creative Commons license in the actual article.

Note: if you intend to submit, or have submitted, your article to a journal then you should verify that the license you select during arXiv submission does not conflict with the journal's license or copyright transfer agreement. Many journal agreements permit submission to arXiv using the non-exclusive license to distribute, which arXiv has used since 2004. Yet the CC BY and CC BY-SA licenses permit commercial reuse and may therefore conflict with some journal agreements.

Authority to submit, publisher PDFs, etc.

arXiv cannot accept papers that contain material for which the depositor does not have the authority to submit or to agree to the license terms. This would include comments by referees (which may have separate copyright protection) and, of course, plagiarized material. Note that any single co-author normally has all needed authority to submit a paper to arXiv. Once publicly available,

Figure H.4: Proof of the arXiv's 'right to distribute' is shown.

H.2 Permissions from co-authors

Wolfgang Tittel see Fig. H.5.

Daniel Oblak see Fig. H.6.

Christoph Simon see Fig. H.7.

Chetan Deshmukh see Fig. H.8.

Félix Bussières see Fig. H.9.

Morgan P. Hedges see Fig. H.10.

Hassan Mallazadeh see Fig. H.11.

Jeongwan Jin see Fig. H.12.

Joshua A. Slater see Fig. H.13.

Erhan Saglamyurek see Fig. H.14.

Khabat Heshami see Fig. H.15.

Rufus L. Cone see Fig. H.16.

Charles W. Thiel see Fig. H.17.

Wolfgang Sohler see Fig. H.18.

Raimund Ricken see Fig. H.19.

Mathew George see Fig. H.20.

Re: permission

Wolfgang Tittel

Sent: Monday, May 9, 2016 12:20 PM

To: Neil Sinclair

Cc:

Hello Neil,

I agree that you include the following research papers - all of which include me as a co-author - into your thesis:

- Spectral multiplexing for scalable quantum photonics using an atomic frequency comb quantum memory and feed-forward control, Phys. Rev. Lett. 113, 053603 (2014).
- Conditional detection of pure quantum states of light after storage in a waveguide, Phys. Rev. Lett. 108, 083602 (2012).
- Broadband waveguide quantum memory for entangled photons, Nature 469, 512-515 (2011).
- Two-photon interference of weak coherent laser pulses recalled from separate solid-state quantum memories, Nature Communications 4, 2386 (2013).
- An integrated processor for photonic quantum states using a broadband light-matter interface, New J. Phys. 16 065019 (2014).
- Cross-phase modulation of a probe stored in a waveguide for non-destructive detection of photonic qubits, arXiv:1510.01164.
- A rare-earth-ion-doped waveguide based on a standard photonics technology for quantum signal processing, unpublished.

Best,
Wolfgang

Figure H.5: Email from Wolfgang Tittel granting me permission to publish Papers 1-7, all of which he is a co-author.

Re: permission
Daniel Oblak

Sent: Monday, May 9, 2016 12:16 PM
To: Neil Sinclair

To whom it may concern,

I hereby give my permission to publish the papers listed below as part of Neil Sinclair's Ph.D. thesis.

Best regards
Daniel Oblak

> On May 9, 2016, at 12:14 , Neil Sinclair wrote:
>
> Wolfgang and Daniel,
>
> Please permit me to publish the following papers in my thesis:
>
> Spectral multiplexing for scalable quantum photonics using an atomic frequency comb quantum memory and feed-forward control, Phys. Rev. Lett. 113, 053603 (2014).
> Conditional detection of pure quantum states of light after storage in a waveguide, Phys. Rev. Lett. 108, 083602 (2012).
> Broadband waveguide quantum memory for entangled photons, Nature 469, 512-515 (2011).
> Two-photon interference of weak coherent laser pulses recalled from separate solid-state quantum memories, Nature Communications 4, 2386 (2013).
> An integrated processor for photonic quantum states using a broadband light-matter interface, New J. Phys. 16 065019 (2014).
> Cross-phase modulation of a probe stored in a waveguide for non-destructive detection of photonic qubits, arXiv:1510.01164.
> A rare-earth-ion-doped waveguide based on a standard photonics technology for quantum signal processing, unpublished.

Figure H.6: Email from Daniel Oblak granting me permission to publish Papers 1-7, all of which he is a co-author.

Re: permission

Christoph Simon

Sent: Monday, May 9, 2016 12:08 PM
To: Neil Sinclair

Hi Neil,
you have my permission.
Christoph

On Mon, May 9, 2016 at 12:05 PM, Neil Sinclair wrote:

> Christoph,
>
> Please permit me to publish the following papers in my thesis:
>
> Cross-phase modulation of a probe stored in a waveguide for non-destructive detection of photonic qubits, arXiv:1510.01164
> Spectral multiplexing for scalable quantum photonics using an atomic frequency comb quantum memory and feed-forward control, Phys. Rev. Lett. 113, 053603 (2014)
>
> Thanks,
> Neil

Figure H.7: Email from Christoph Simon granting me permission to publish Papers 1 and 6, both of which he is a co-author.

From: Chetan Deshmukh
Sent: Monday, May 9, 2016 12:08 PM
To: Neil Sinclair
Subject: Re: permission

Hi Neil,

Yes, you have my permission to publish Cross-phase modulation of a probe stored in a waveguide for non-destructive detection of photonic qubits, arXiv:1510.01164 in your PhD thesis.

Regards
Chetan

Figure H.8: Email from Chetan Deshmukh granting me permission to publish Paper 6, of which he is a co-author.

Félix Bussières

Sent: Wednesday, May 11, 2016 1:43 PM
To: Neil Sinclair

Hi Neil,

I agree to the publication of the papers "Conditional detection of pure quantum states of light after storage in a waveguide" and "Broadband waveguide quantum memory for entangled photons" for your thesis.

Best wishes,
Félix

On 09/05/16 20:46, Neil Sinclair wrote:
> Hi Felix,
>

>
> At this point the university needs your permission to publish our papers in my thesis in order for me to graduate. Replying to this email is sufficient. Do you permit me to publish the following papers in my thesis?
>
> Conditional detection of pure quantum states of light after storage in a waveguide, Phys. Rev. Lett. 108, 083602 (2012).
> Broadband waveguide quantum memory for entangled photons, Nature 469, 512-515 (2011).
>
> Apologies for the inconvenience,
> Neil
>

Figure H.9: Email from Félix Bussières granting me permission to publish Papers 2 and 3, both of which he is a co-author.

Re: permission
Morgan Hedges

Sent: Monday, May 9, 2016 1:06 PM
To: Neil Sinclair

Of course! Publish away.

Morgan

On Mon, May 9, 2016 at 2:41 PM, Neil Sinclair wrote:
> Hi Morgan,
>
> As you know, I have just defended my thesis. At this point the university administration needs your permission to publish our paper in my thesis in order for me to graduate. Replying to this email is sufficient
> Do you permit me to publish the following paper in my thesis?
>
> Spectral multiplexing for scalable quantum photonics using an atomic frequency comb quantum memory and feed-forward control, Phys. Rev. Lett. 113, 053603 (2014).
>
> Sorry about the inconvenience,
> Neil

Figure H.10: Email from Morgan P. Hedges granting me permission to publish Paper 1, of which he is a co-author.

Re: permission
Hassan Mallahzadeh

Sent: Monday, May 9, 2016 12:55 PM
To: Neil Sinclair

Hi Neil,

Certainly you can publish the paper in your thesis.

Sincerely,
Hassan

On Mon, May 9, 2016 at 12:27 PM, Neil Sinclair wrote:
> Hi Hassan,
>
> In case you didn't know, I have just defended my thesis. At this point the university administration needs your permission to publish our paper in my thesis in order for me to graduate. Replying to this email is sufficient. Do you permit me to publish the following paper in my thesis?
>
> Spectral multiplexing for scalable quantum photonics using an atomic frequency comb quantum memory and feed-forward control, Phys. Rev. Lett. 113, 053603 (2014).
>
> Thanks,
> Neil

Figure H.11: Email from Hassan Mallahzadeh granting me permission to publish Paper 1, of which he is a co-author.

RE: permission
Jeongwan Jin

Sent: Monday, May 9, 2016 3:11 PM
To: Neil Sinclair

Hi Neil,

Absolutely I do.

Cheers,
Jin

From: Neil Sinclair
Sent: Monday, May 09, 2016 2:35 PM
To: Jeongwan Jin
Subject: permission

Hi Jin,

As you know, I have just defended my thesis. At this point the university administration needs your permission to publish our papers in my thesis in order for me to graduate. Replying to this email is sufficient. Do you permit me to publish the following papers in my thesis?

Conditional detection of pure quantum states of light after storage in a waveguide, Phys. Rev. Lett. 108, 083602 (2012).
Broadband waveguide quantum memory for entangled photons, Nature 469, 512-515 (2011).
Two-photon interference of weak coherent laser pulses recalled from separate solid-state quantum memories, Nature Communications 4, 2386 (2013).

Thanks,
Neil

Figure H.12: Email from Jeongwan Jin granting me permission to publish Papers 2-4, all of which he is a co-author.

Re: permission
Joshua Slater

Sent: Monday, May 9, 2016 12:47 PM
To: Neil Sinclair

Dear Neil,

I certainly permit you to publish the following papers in your thesis:
Spectral multiplexing for scalable quantum photonics using an atomic frequency comb quantum memory and feed-forward control, Phys. Rev. Lett. 113, 053603 (2014).
Conditional detection of pure quantum states of light after storage in a waveguide, Phys. Rev. Lett. 108, 083602 (2012).
Broadband waveguide quantum memory for entangled photons, Nature 469, 512-515 (2011).
Two-photon interference of weak coherent laser pulses recalled from separate solid-state quantum memories, Nature Communications 4, 2386 (2013).
An integrated processor for photonic quantum states using a broadband light-matter interface, New J. Phys. 16 065019 (2014).

Sincerely,

Joshua Slater

Figure H.13: Email from Joshua A. Slater granting me permission to publish Papers 1-5, all of which he is a co-author.

Re: permission
Erhan Saglamyurek

Sent: Monday, May 9, 2016 12:58 PM
To: Neil Sinclair

Hi Neil,

Yes, I permit you to publish the listed papers in your thesis.

Cheers

Erhan

On May 9, 2016 12:19 PM, "Neil Sinclair" wrote:
> Hi Erhan,
>
> As you know, I have just defended my thesis. At this point the university administration needs your permission to publish our papers in my thesis in order for me to graduate. Replying to this email is sufficient. Do you permit me to publish the following papers in my thesis?
>
> Spectral multiplexing for scalable quantum photonics using an atomic frequency comb quantum memory and feed-forward control, Phys. Rev. Lett. 113, 053603 (2014).
> Conditional detection of pure quantum states of light after storage in a waveguide, Phys. Rev. Lett. 108, 083602 (2012).
> Broadband waveguide quantum memory for entangled photons, Nature 469, 512-515 (2011).
> Two-photon interference of weak coherent laser pulses recalled from separate solid-state quantum memories, Nature Communications 4, 2386 (2013).
> An integrated processor for photonic quantum states using a broadband light-matter interface, New J. Phys. 16 065019 (2014).
>
> Thanks,
> Neil

Figure H.14: Email from Erhan Saglamyurek granting me permission to publish Papers 1-5, all of which he is a co-author.

permission
Heshami, Khabat

Sent: Monday, May 9, 2016 12:04 PM
To: Neil Sinclair

Dear Dr. Sinclair,

I am writing to state that I permit the following papers that we co-authored to be published in your PhD thesis.

1) Cross-phase modulation of a probe stored in a waveguide for non-destructive detection of photonic qubits, arXiv:1510.01164
2) An integrated processor for photonic quantum states using a broadband light-matter interface, New J. Phys. 16 065019 (2014)

Best regards,
Khabat Heshami

Figure H.15: Email from Khabat Heshami granting me permission to publish Papers 5 and 6, both of which he is a co-author.

Re: permission
Cone, Rufus

Sent: Monday, May 9, 2016 11:35 AM
To: Neil Sinclair

Dear Neil,

This email is to give you permission to publish that paper / manuscript in your Ph.D. Thesis for University of Calgary.

Sincerely,
Rufus

_____
From: Neil Sinclair
Sent: Monday, May 9, 2016 11:32:49 AM
To: Thiel, Charles; Cone, Rufus
Subject: permission

Dear Charles and Rufus,

As you know I have recently defended my thesis. In order for it to be processed by administration, I need an email stating that you permit our paper 'A rare-earth-ion-doped waveguide based on a standard photonics technology for quantum signal processing' to be published in my thesis.

Apologies for the inconvenience,
Neil

Figure H.16: Email from Rufus L. Cone granting me permission to publish Paper 7, of which he is a co-author.

Re: permission
Charles Thiel

Sent: Monday, May 9, 2016 12:26 PM
To: Neil Sinclair;

Hi Neil,

Yes, you have my permission to include this paper in your thesis.

Charles

On 5/9/2016 11:32 AM, Neil Sinclair wrote:
> Dear Charles and Rufus,
>
> As you know I have recently defended my thesis. In order for it to be processed by administration, I need an email stating that you permit our paper 'A rare-earth-ion-doped waveguide based on a standard photonics technology for quantum signal processing' to be published in my thesis.
>
> Apologies for the inconvenience,
> Neil.

Figure H.17: Email from Charles W. Thiel granting me permission to publish Paper 7, of which he is a co-author.

Re: need permission to include joint papers into Neil's thesis
Wolfgang Sohler

Sent: Thursday, May 12, 2016 1:40 AM
To: Neil Sinclair
Cc:

Dear Neil,

of course, we grant you the permission to include the following papers in your thesis:

- Spectral multiplexing for scalable quantum photonics using an atomic frequency comb quantum memory and feed-forward control, Phys. Rev. Lett. 113, 053603 (2014).
- Conditional detection of pure quantum states of light after storage in a waveguide, Phys. Rev. Lett. 108, 083602 (2012).
- Broadband waveguide quantum memory for entangled photons, Nature 469, 512-515 (2011).
- Two-photon interference of weak coherent laser pulses recalled from separate solid-state quantum memories, Nature Communications 4, 2386 (2013).

With best regards

Wolfgang Sohler

Figure H.18: Email from Wolfgang Sohler granting me permission to publish Papers 1-4, all of which he is a co-author.

> Dear Mr. Ricken,
>

>
> I am currently submitting my Ph.D. thesis. Since you are the co-author of several of my papers, my university requires your permission to publish the following papers in my thesis:
>
> - Spectral multiplexing for scalable quantum photonics using an atomic frequency comb quantum memory and feed-forward control, Phys. Rev. Lett. 113, 053603 (2014).
> - Conditional detection of pure quantum states of light after storage in a waveguide, Phys. Rev. Lett. 108, 083602 (2012).
> - Broadband waveguide quantum memory for entangled photons, Nature 469, 512-515 (2011).
> - Two-photon interference of weak coherent laser pulses recalled from separate solid-state quantum memories, Nature Communications 4, 2386 (2013).
>
> Do you grant me permission to publish the above papers in my thesis?
>

> Sincerely,
> Neil Sinclair
> University of Calgary

Dear Mr. Sinclair,
you have from my side the permission to publish the papers.

Sincerely
Raimund Ricken

Figure H.19: Email from Raimund Ricken granting me permission to publish Papers 1-4, all of which he is a co-author.

Re: URGENT message for Prof. Mathew George
Mathew George

Sent: Thursday, May 12, 2016 12:43 AM
To: Neil Sinclair

Dear Neil Sinclair,

Glad to hear from you.

I have no objections in including the materials presented the the articles cited below, in your Ph.D. thesis.

- Spectral multiplexing for scalable quantum photonics using an atomic frequency comb quantum memory and feed-forward control, Phys. Rev. Lett. 113, 053603 (2014).
- Conditional detection of pure quantum states of light after storage in a waveguide, Phys. Rev. Lett. 108, 083602 (2012).
- Broadband waveguide quantum memory for entangled photons, Nature 469, 512-515 (2011).
- Two-photon interference of weak coherent laser pulses recalled from separate solid-state quantum memories, Nature Communications 4, 2386 (2013).

Best regards,
Mathew George

Figure H.20: Email from Mathew George granting me permission to publish Papers 1-4, all of which he is a co-author.